NMR CHARACTERIZATION OF METAL NANOPARTICLE FORMATION, STRUCTURE, AND PERFORMANCE

by

Lauren Elizabeth Marbella

B. S., Duquesne University, 2009

M. S., University of Pittsburgh, 2012

Submitted to the Graduate Faculty of

The Kenneth P. Dietrich School of Arts and Sciences in partial fulfillment

of the requirements for the degree of

Doctor of Philosophy

University of Pittsburgh

2016

UNIVERSITY OF PITTSBURGH

DIETRICH SCHOOL OF ARTS AND SCIENCES

This dissertation was presented

by

Lauren E. Marbella

It was defended on

July 26, 2016

and approved by

Dr. Sunil K. Saxena, Professor, Department of Chemistry

Dr. David H. Waldeck, Professor, Department of Chemistry

Dr. Stefan Bernhard, Associate Professor, Department of Chemistry

Dissertation Advisor: Dr. Jill E. Millstone, Associate Professor, Department of Chemistry

NMR CHARACTERIZATION OF METAL NANOPARTICLE FORMATION, STRUCTURE, AND PERFORMANCE

Lauren E. Marbella, PhD

University of Pittsburgh, 2016

Prof. Jill E. Millstone

NMR CHARACTERIZATION OF METAL NANOPARTICLE FORMATION, STRUCTURE, AND PERFORMANCE

Lauren E. Marbella, PhD

University of Pittsburgh, 2016

Analytical methods with high chemical, spatial, and temporal resolution are crucial to understanding and controlling nanoparticle properties as well as translating these discoveries into society-shaping technologies. However, approaches for the characterization of solid inorganic materials and solution phase molecular species are often disparate. One powerful technique to address this gap is nuclear magnetic resonance (NMR) spectroscopy, which can facilitate routine, direct, molecular-scale analysis of nanoparticle formation and morphology *in situ*, in both the solution and solid phase. This dissertation describes the application of NMR to study metal nanoparticle formation, structure, and performance with unprecedented chemical detail.

In Chapter 1, the dissertation is introduced by highlighting recent developments in the application of NMR spectroscopy to the study of noble metal nanoparticle growth, surface chemistry, and physical properties. In Chapter 2, the formation of bimetallic Au-Cu nanoparticles is studied by solution NMR techniques (in conjunction with mass spectrometry and X-ray absorption spectroscopy) to reveal the chemical mechanisms driving metal atom distribution in the final particle. Building on hypotheses tested in Chapter 2, Chapter 3 describes one of the first syntheses of Au-Co alloys at any length scale with fully tunable compositions. The magnetic and optical properties of the resulting Au-Co nanoparticle alloys are evaluated with NMR and photoluminescence spectroscopies, respectively, and are found to exhibit both high relaxivity and high brightness, making them ideal bimodal imaging agents.

Building on these studies of nanoparticle formation, NMR spectroscopy is then used to study final particle structure and physical properties. In Chapter 4, NMR is used to probe ligand shell architectures on phosphine-terminated Au nanoparticles and allow the identification of ^{31}P-^{197}Au coupling for the first time in nanoparticle systems – a feature which may ultimately be used to study previously NMR-inaccessible nuclei such as ^{197}Au. This utility is highlighted in Chapter 5 where the impact of local and global crystallographic environments in Au nanoclusters are probed using ^{31}P NMR. In Chapter 6, solid-state NMR is used to characterize the emergence of metallic behavior in degenerately doped $Cu_{2-x}Se$ nanoparticles as well as to reveal the structural evolution of the particle as a function of this doping.

TABLE OF CONTENTS

LIST OF TABLES

LIST OF FIGURES

ACKNOWLEDGMENTS

I would like to start by thanking my advisor, Jill Millstone. Throughout my Ph. D. work, she has provided a constant source of enthusiasm, diligence, and creativity that I aspire to replicate. From Jill, I have learned to become a better scientist in every aspect of research, from experimental design to communicating my work in the most effective way through writing and presenting. Her unwavering support has provided me with countless rewarding opportunities that have allowed me to grow as an individual and a scientist. Overall, I am incredibly thankful to have had her as my advisor and explore a new realm of nanochemistry together.

In addition to my advisor, I would like to thank my committee members, who have continued to support me throughout my graduate studies. I also thank all of the members of the Millstone lab, past and present, and our collaborators. I have been lucky to work together with all of you on various exciting projects and have your input in my research. I cherish the fact that we all close and are able to be both productive in the lab and have fun hanging out together – it is truly unique. I'd particularly like to thank Michael Hartmann, who has simultaneously served as my support system, one of my best friends, and an invaluable colleague – both in terms of scientific feedback and inspiration. I am also grateful to have formed a network in both the nanoscience and NMR community who have given me support, advice, and friendship.

Finally, I would like to thank my friends and family, especially my parents and my sister. You have led me to work hard and encouraged me to pursue my interest in science to the fullest extent while supporting me in any and every way possible. Your love and support has undoubtedly helped me get where I am today.

1.0 NMR TECHNIQUES FOR NOBLE METAL NANOPARTICLES

(Portions of this work were published previously and are reprinted with permission from Marbella, L. E. and Millstone, J. E. *Chem. Mater.*, **2015**, *27*, 2721-2739.

1.1 INTRODUCTION

Nuclear magnetic resonance (NMR) spectroscopy is a transformational molecular characterization tool that requires little perturbation of the analyzed system, while providing exceptional detail about the chemical environments of constituent atomic nuclei. These features make NMR especially well-suited for in situ analysis of chemical structure, reactions, and even dynamics in some cases. With this versatility, it is not surprising that NMR analysis has been applied to a wide variety of systems[1] ranging from large biomolecules[2] to lithium batteries,[3] in addition to its daily analytical use in organic synthesis laboratories. The chemical resolution possible using NMR is particularly attractive for characterizing both the formation and final architecture of noble metal nanoparticles (NMNPs). To understand why NMR is promising for these studies one must clarify both what one may want to determine about NMNP systems as well as the unique capabilities of NMR in metallic materials.

Analytical targets in the study of NMNPs range from tracking molecular precursors during NP formation to particle surface reorganization during catalytic reaction and many aspects of particle architecture, electronic properties, and surface chemistry in between. Nanoparticle systems often involve a hard-soft matter interface between the solid surface of the particle core and pendant ligands (species ranging from monoatomic ions to large macromolecules). This interface includes many parameters of interest including surface element composition, ligand shell composition, and ligand shell architecture. However, each of these features is difficult to resolve using classic surface and materials characterization strategies such as electron microscopy or photoelectron spectroscopy techniques.

Here, we highlight reports, including examples from our laboratory, in which NMR has provided crucial insights into NMNP formation, morphology, and physical properties. First, we briefly outline key NMR concepts in the study of NMNPs including NMR phenomena such as the Knight shift and Korringa behavior. In Section 1.2, we discuss NMR analyses of NMNP formation and growth, and give examples of studies that monitor either resonances of the ligand (Section 1.2.1) or NMR-active metal nuclei within the metal precursors (Section 1.2.2). In the remainder of the Perspective, we discuss final nanoparticle characterization both of the particle itself (Section 1.3) as well as its resulting physical properties (Section 1.4). In each section, we focus on NMR techniques that are generally accessible to the synthetic nanochemistry community. We also consider instrumental and physical limitations of NMR for studying NMNPs where appropriate. At the end of each section, we include results obtained using more advanced NMR equipment and techniques. While these studies may require more expertise to execute, the results obtained are of broad interest and therefore we highlight the method and the results.

1.1.1 Basic Concepts for Metal Nanoparticle NMR Spectroscopy

Here, we outline selected NMR concepts that are chosen to be useful for interpreting the results summarized in this dissertation, as well as for appreciating the scope of possible contributions using NMR spectroscopy in NMNP systems. In particular, we focus on phenomena unique to NMR of metals, adsorbates on metals, and nuclei at a hard-soft matter interface.

Consider an NMR spectrum of ^{195}Pt nuclei in Pt nanoparticles or a ^{1}H NMR spectrum of H_2 molecules adsorbed to their surface. In both cases, conduction electrons in the Pt metal will have a dramatic influence on the resulting NMR spectra because of nuclear coupling to conduction electrons at the particle surface (defined as hyperfine coupling). In bulk metals, it is well-known that hyperfine coupling of nuclear spins to the unpaired conduction electrons in the metal results in a dramatic change in NMR frequency termed the Knight shift, K. Observation of the Knight shift was first reported in 1949 when W. D. Knight noticed that the NMR signal for Li, Na, Al, Cu, and Ga metals resonated at a different frequency from that of the same element in a nonmetallic environment (chloride salts).[4]

Like chemical shift, the Knight shift is sensitive to the local electronic environment surrounding the nucleus, and the magnitude of the shift is a sensitive probe of the electronic structure of metals, semiconductors, and superconductors.[5] Therefore, exciting experiments such as probing the change from molecular to metallic electronic structure in NMNPs is possible using NMR techniques. Further, metallic properties can be studied by evaluating the Korringa behavior of materials through NMR measurements. In the Korringa relation,[6] K is related to the temperature, T, at which the NMR measurement is performed and the longitudinal relaxation time constant, T_1, of the material where K^2TT_1 is a constant. As a result, T_1 and T^{-1} display a linear relationship with one another.[7] NMR nuclei that exhibit this temperature correlation with

T_1 suggest metallic electronic structure within the material analyzed. Both the slope of the temperature dependent relaxation as well as the magnitude of the Knight shift can give information about the evolution of particle electronic structure as a function of particle size, shape, composition, and surface chemistry.[5]

Surface chemistry is particularly interesting because NMNPs prepared by wet chemical techniques are often capped with organic molecules. By combining the unique impact of metal conduction electrons on ligand nuclei with traditional NMR spectroscopy techniques, NMR investigation of these capping ligands can provide detailed insight into properties of the particle core (e.g., electronic structure, atomic composition, or compositional architecture) as well as important aspects of its ligand shell including ligand identity, arrangement, and dynamics.

For each nucleus observed, the measured resonance will be influenced by both "macroscopic" and "microscopic" forces acting on it.[8] At the macroscopic level, the homogeneity and strength of the applied magnetic field, molecular tumbling, and magnetic susceptibility of the material can each influence observed spectral features. Many NMR techniques have been developed to either mitigate the impact of these macroscopic effects or to leverage them as in solid-state NMR (ssNMR). "Microscopic" factors include the electronic environment of the nuclei as well as the influence of neighboring nuclear and electronic spin interactions. These microscopic interactions may be deduced from several spin-1/2 NMR figures of merit, including chemical shift, lineshape/linewidth, relaxation times, and various anisotropic interactions (e.g. chemical shielding anisotropy (CSA), dipolar coupling, etc.).

For a given chemical environment, several of these spectroscopic parameters may be influenced simultaneously. Further, because NPs incorporate components from both molecular chemistry (e.g., organic capping ligands) and solid phase materials (e.g., metallic core), methods

may be used or combined from both traditional solution phase NMR characterization as well as more advanced ssNMR techniques. In order to ascertain how different spectral features arise in spectra obtained from these techniques, we begin by discussing a traditional solution phase spin-1/2 1D NMR spectrum and focus on a single nuclear site, *j*. In a typical spectrum of a small molecule, sharp resonance lines of chemical shift, $\delta_{iso,j}$, are observed at a frequency (in ppm) that is proportional to the external magnetic field, B_0.

$$\omega_{0,j} = \gamma_j B_0 \left(1 + \delta_{iso,j}\right) \quad (1)$$

In equation 1, $\omega_{0,j}$ is the chemically shifted Larmor frequency for site *j*, and γ_j is the gyromagnetic ratio of nucleus *j*. Here, the direction of the external magnetic field is in the z-direction of a three-coordinate axis. Each nuclear site may exhibit a unique chemical shift as the result of differences in chemical shielding.[9] The chemical shielding interaction is composed of both a diamagnetic and a paramagnetic contribution that results in frequency shifts.[10] The magnitude of the chemical shielding depends on the molecular electronic structure and the orientation of the molecule with respect to B_0.[11] In solution, rapid reorientation of the small molecule with respect to B_0 allows it to sample all orientations on a time scale that averages the CSA and dipole-dipole coupling interactions to zero. This averaging results in an isotropic chemical shift and sharp resonance lines in the solution phase NMR experiment (Figure 1A).

However, a static ^{13}C ssNMR spectrum of the same small molecule shows a broad powder pattern. This apparent loss in spectral features is due to anisotropic spin interactions such as CSA and dipole-dipole coupling which are not averaged out in the solid state because of restricted molecular motion. In theory, the effects of both CSA and dipole-dipole coupling can be removed from ssNMR spectra via magic-angle spinning (MAS) in combination with high power decoupling (Figure 1B).

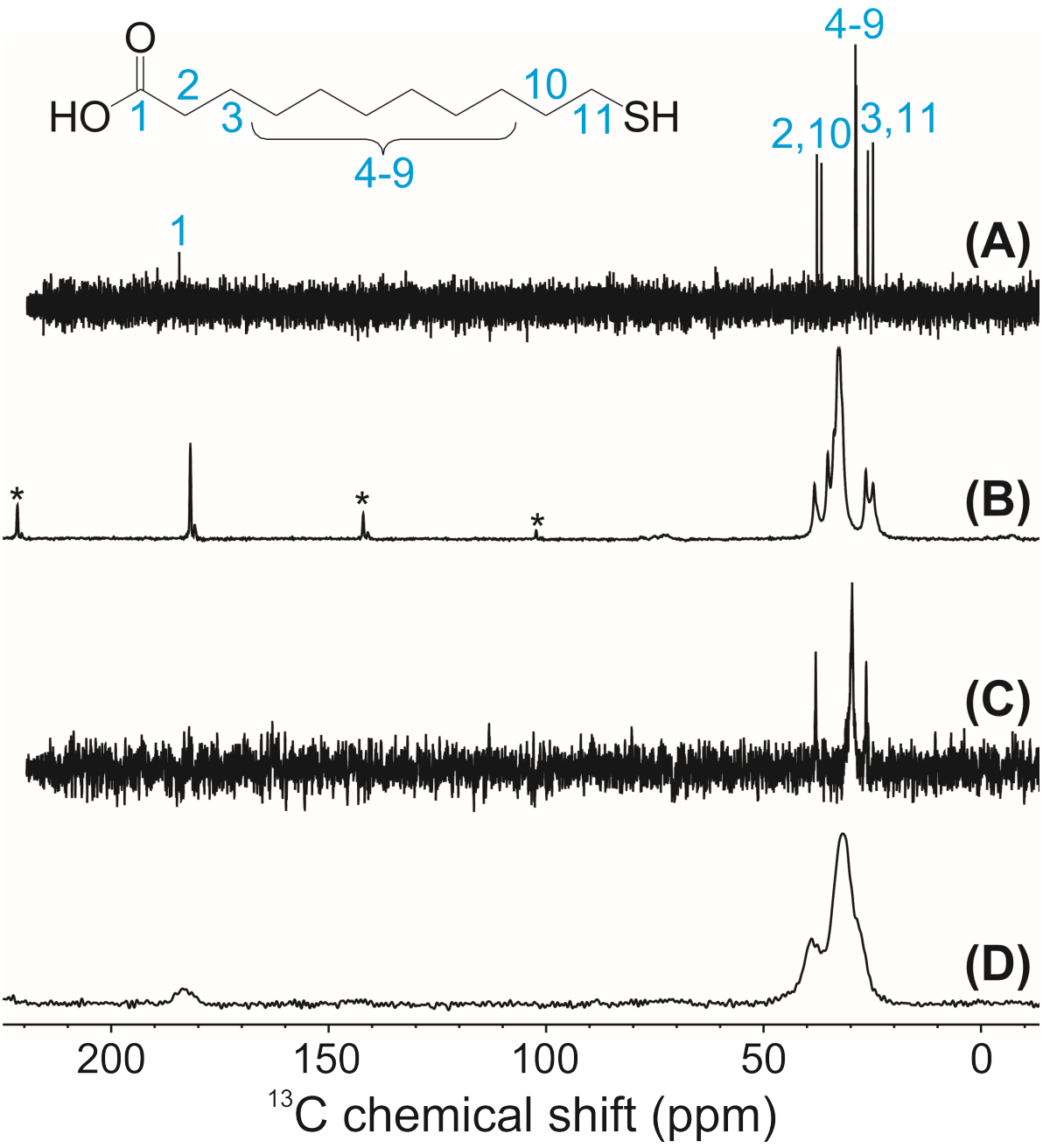

Figure 1. 1D ^{13}C NMR spectra of 11-mercaptoundecanoic acid in (A) D_2O, (B) the solid state with MAS = 5 kHz and ^{1}H decoupling = 80 kHz, (C) D_2O appended to Au NPs (d = 2.2 nm), and (D) the same NPs in the solid state. Asterisks in (B) denote spinning sidebands from moderate MAS speeds = 5 kHz

When small molecules are attached to a metal nanoparticle, they are at the interface between solution and a solid support. Therefore, if the same small molecule depicted in Figure 1A is appended to a AuNP and the same 1D ^{13}C NMR spectrum is recorded, several spectral differences will be apparent: line broadening of the resonances is observed, the chemical shift may be altered, and some resonances may disappear completely (Figure 1C). These changes become more dramatic when the particles are dried to a solid state (Figure 1D). For spin-1/2 nuclei, such as the ^{13}C solution phase spectra in Figure 1C, the spin interactions that arise from being in a more "solid-like" environment can be briefly explained as a reintroduction of anisotropic spin interactions. For example, CSA can arise from the different frequencies associated with each different orientation of the same molecule with respect to B_0, even if the particle exhibits identical crystallographic binding sites. If the molecule does not reorient at a rate greater than the absolute magnitude of the CSA (which can be the case when attached to a nanoparticle substrate because of restricted molecular motion and slower tumbling), inhomogeneous line broadening is observed in the NMR spectrum.

Likewise, dipole-dipole coupling can also be a source of line broadening and is the through-space interaction between the induced magnetic moments of neighboring spins. Measuring dipole-dipole coupling constants can provide detailed information about the structure and arrangement of ligands attached to NMNPs in both the solid and solution phase. For example, the effect of dipole-dipole coupling on nuclear spin relaxation results in nuclear Overhauser effects that can be measured by NMR and provide information on the distances between nuclei (termed nuclear Overhauser effect spectroscopy (NOESY)). Using specialized pulse sequences, spin interactions can be selectively reintroduced to learn about the molecular

environment of nanoparticle capping ligands, including the degree of crystallinity, orientation, and supramolecular architecture.

Depending upon the size of the underlying nanoparticle, molecular tumbling of pendant ligands may be greatly reduced. The attenuation of molecular tumbling rates via attachment to relatively large particle surfaces results in a reintroduction of CSA and dipole-dipole coupling spin interactions as discussed above (*N.B.* other sources of line broadening are ignored here for simplicity). Changes in the magnitude of spin interactions (*e.g.*, by fixing molecules in close proximity or near a metal center) can also influence the spin-lattice relaxation (or longitudinal relaxation, T_1) and spin-spin relaxation (or transverse relaxation, T_2). Here, T_1 is defined as the time constant for spins to reach thermal equilibrium in the presence of B_0. Similarly, T_2 is the time constant that describes the dephasing of spin polarization associated with single quantum coherences in the transverse plane. In particular, T_2 is related to the observed NMR full width at half-maximum (fwhm) by the following equation:

$$fwhm = \frac{1}{\pi T_2} \quad (2)$$

Another spin interaction that will be mentioned is the quadrupolar interaction. Quadrupolar nuclei are nuclei with spin > 1/2 and can have either integer or half-integer spins. In these cases, the nucleus exhibits a quadrupole moment which is coupled to the surrounding electric field gradient, producing the quadrupolar interaction. Quadrupolar interactions are commonly characterized by nuclear quadrupolar coupling constants. It is important to note that, in many systems, especially solids where molecular motion is restricted, the magnitude of quadrupolar coupling can surpass the magnitude of the dipole-dipole coupling interactions, producing NMR lineshapes that are dominated by quadrupolar interactions.[12] In the first Chapter,

we will focus mainly on the quadrupolar interaction as it applies to deuterium NMR spectroscopy, where deuterium is spin-1 and has a relatively small quadrupole moment.

1.2 NUCLEAR MAGNETIC RESONANCE CHARACTERIZATION OF METAL NANOPARTICLE FORMATION AND GROWTH

During the formation of NMNPs, both chemical change and phase transformations occur. Following the evolution of molecular precursors into a final NP solid phase requires methods that can capture chemical and physical transformations in real time with molecular resolution. NMR approaches to study growth have employed a broad range of techniques, as well as combined NMR with other analytical methods such as thermogravimetric analysis (TGA), Raman spectroscopy, and differential scanning calorimetry (DSC). To study NMNP growth, both the nuclei of NP ligands as well as the metal nuclei themselves can be monitored.

1.2.1 NMR Observation of Nanoparticle Ligand Resonances during Synthesis

First, we consider the use of NMR to monitor the chemical environment, reaction rates, and dynamics of ligands used in NMNP syntheses. One nanochemical reaction mechanism that has benefited significantly from NMR analysis is the two-phase Brust-Schiffrin synthesis.[13] Briefly, this synthesis involves the transfer of aqueous $HAuCl_4$ into an organic solvent such as toluene via a "phase transfer agent" such as tetraoctylammonium bromide (TOAB), and a thiolated ligand (RSH) solubilized in the organic phase. A reducing agent such as $NaBH_4$(aq) is introduced and thiolate-terminated AuNPs are produced (diameter, $d \approx$ 1-5 nm).[13] In general, the

mechanism of formation is thought to begin by an initial reduction of Au(III) species to Au(I) via oxidation of RSH ligands. The resulting species are then fully reduced by $NaBH_4$ and particle nucleation is induced. On the basis of dynamic light scattering (DLS) measurements and the sensitivity of the final product size to metal:RSH ratio, it has been thought that metal-sulfur bond formation occurred after RSH addition and that polymeric Au(I)-thiolate species were the active precursor to thiolate-capped NPs produced via the two-phase approach.

Using 1D ^1H NMR analyses of precursors at various Au:RSH ratios, Lennox and co-workers found that, after thiol addition, Au(III) is indeed reduced to Au(I) and that RSH is oxidized to the disulfide but that there was no evidence of metal-sulfur bond formation prior to the introduction of $NaBH_4$ (Figure 2A, B).[14] Instead, Lennox postulates the formation of TOA^+-$[AuX_2]^-$ species and supports this assignment via chemical shift differences in the TOA^+ resonances after the addition of $HAuCl_4$ and its transfer to the organic phase. TOA^+ proton resonances (protons on the carbons adjacent to the nitrogen) were consistent with fast anion exchange between coordination of TOA^+ to $[AuX_2]^-$ and Br^-. Similar metal-surfactant precursors were subsequently identified for analogous Ag and Cu two-phase NP syntheses.[14]

This work led to a proposed "inverse micelle mechanism" by Tong and co-workers[15] where the metal ion coordination complex is sequestered in an inverse micelle of TOAX (X = Br^- or Cl^-). Both the size of the micelle and the chemical environment inside play crucial roles in the ultimate size and stability of AuNPs formed, even in the absence of an RSH ligand. Tong et al. support this mechanism via both NMR and synthesis experiments. Using 1D ^1H NMR, the authors follow the water resonance and show chemical shift values consistent with sequestration of water inside a TOAX micelle[16] or other supramolecular architecture. Further, the TOA^+-$[AuX_2]^-$ precursor could be prepared in high purity according to a literature procedure,

eliminating the need for RSH reduction of TOA^+-$[AuX_4]^-$. Then, the thiolated capping ligand could be added post-$NaBH_4$ addition and indistinguishable particles could be obtained for Au, Ag, or Cu cores (Figure 2C).

This particle formation pathway differs from observations in a one-phase synthesis[17,18] involving the same reagents with the exception of the phase transfer agent TOAB, which is no longer needed and typically omitted. In the one-phase synthesis, metal-sulfur bonds are observed before $NaBH_4$ addition, which is consistent with results from our own laboratory. Cliffel and co-workers studied the one-phase aqueous synthesis of tiopronin-capped AuNPs and used a combination of ^{1}H NMR, TGA, matrix assisted laser desorption ionization mass spectrometry (MALDI-MS), and pair distribution function (PDF) analysis to identify precursor species.[19] The authors showed that a possible precursor to AuNPs in the tiopronin synthesis was a Au(I)-thiolate tetramer with distinct optical signatures, and these observations are consistent with theoretical predictions of "prenucleation" species.[20,21] Interestingly, features of the Au(I)-thiolate tetramer are also present in the final colloid (d = 2-3 nm), suggesting that the intermediates may also be present as capping moieties on the particle surface. Studies of analogous syntheses using phosphine-based ligands have been studied using ^{31}P ssNMR spectroscopy and indicate that Au(I) ligand complexes also form prior to reduction and subsequent particle formation.[22]

Taken together, these NMR studies suggest that there are fundamental differences between the formation pathways of small NMNPs (d = 1-5 nm) synthesized by one-phase and two-phase methods, despite the seemingly similar protocols. These distinctions are important contributions to establishing well-controlled, easily tailored, and high yielding NMNP syntheses.

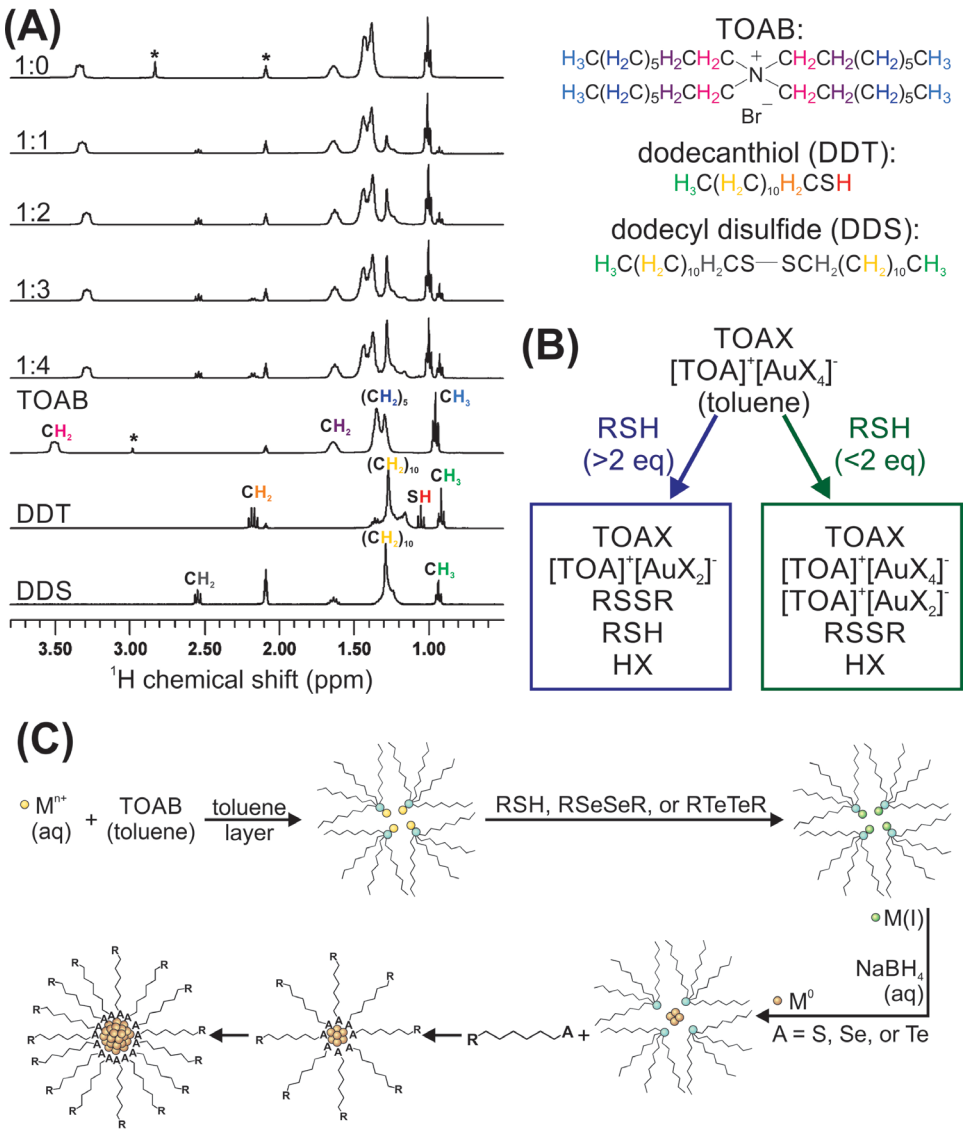

Figure 2. (A) ^{1}H NMR spectra of TOAX + TOA^{+}-[AuX$_4$]$^{-}$ titrated with increasing equivalents of dodecanethiol (DDT) from top to middle as well as spectra of pure TOAB, DDT, and dodecyl disulfide free in solution. (B) Diagram describing possible nanoparticle precursors in the first two steps of a two-phase Brust-Schiffrin synthesis based on spectra in (A). (C) Proposed scheme for nanoparticle formation based on similar NMR analyses to (A) and Raman spectroscopy. (A) and (B) adapted with permission from ref 14. Copyright 2010 American Chemical Society. (C) adapted with permission from ref 15. Copyright 2011 American Chemical Society

Another canonical NMNP synthesis studied by solution phase ^{1}H NMR is the citrate reduction of Au(III) at elevated temperature (~100 °C), commonly referred to as the Turkevich[23] or Frens[24] method. In this synthesis, citrate acts as both a reducing agent for Au(III) as well as a capping ligand for the final NPs. By altering either the solution pH (and presumably the speciation of both the Au precursor and/or the reduction potential of the citrate) or the ligand to metal ratio, the final particle size and size distribution can be modified (d ~10 to 100 nm). In order to correlate variations in precursor chemistry with particle products, Bruylants and co-workers monitored the Turkevich synthesis at constant citrate:Au(III) ratio (5:1) at various pH values (pH = 3, 4.5, 7, 9, and 12) using a combination of UV-visible absorption and NMR spectroscopy as a function of time.[25]

In this work, the authors identified that the narrowest particle size distribution was obtained from reactions performed at pH 7. At pH 7, a majority of the citrate ligand was found by ^{1}H NMR to be deprotonated (pK_a = 3.1, 4.8, 6.4) and the Au species was present as $[AuCl_2(OH)_2]^-$ as determined by UV-visible spectroscopy. Under these conditions, dicarboxyacetone appeared in the ^{1}H NMR spectrum within 1 min of reaction initiation, where dicarboxyacetone is the primary oxidation product of citrate and itself a reducing agent. However, when the reduction of Au cations is performed with dicarboxyacetone alone, particle size distribution increases, indicating that the reaction is sensitive to kinetics and/or progresses by a different route than when using citrate.

In addition to the appearance of the dicarboxyacetone peak, a new, broad peak at the base of the free citrate peaks was observed. 2D ^{1}H-^{1}H correlation spectroscopy (COSY) analysis indicated that the peaks were consistent with citrate in fast exchange with two different chemical environments on the NMR time scale. When the diffusion coefficients of the various citrate

peaks were measured by diffusion ordered spectroscopy (DOSY), citrate aggregates containing Au atoms (either Au(I) or Au(0); not yet known) were observed.[25]

These Au-citrate aggregates are consistent with the supramolecular metal-ligand assemblies proposed to explain nucleation and growth of AuNPs using the Turkevich approach.[23] NMR techniques may also be used to follow NMNP syntheses that use a gas reduction approach. In one example, Chaudret et al. characterize AuNP formation (d = 4.7 ± 0.9 nm) using a combination of solution phase and ssNMR techniques to monitor the CO(g)-reduction of a gold precursor in the presence of amine-functionalized capping ligands.[26] Solution phase ^{1}H NMR measurements showed that the reaction shared mechanistic features with the one-phase Brust-Schiffrin synthesis. For example, after combining hexadecylamine (HDA) with Au(I)Cl(tetrahydrothiophene) (THT), a Au(I)Cl-HDA coordination complex is formed. Resulting spectral features support this assignment including the disappearance of the triplet from the protons on the carbon adjacent to the amine group, coincident appearance of new resonances that correspond to Au(I)Cl-HDA, and the appearance of resonances that correspond to free THT. After reduction of the Au(I)Cl-HDA complex by CO(g), AuNPs are formed and were characterized using ssNMR MAS techniques (to mitigate spectral line-broadening due to the increasing size of the NP core). ^{13}C ssNMR spectroscopy indicated that, after reduction, 1,3-dihexadecylurea was formed via carbonylation of HDA. As a result, the final particle product was terminated with a binary ligand shell composed of both amine and carbamide ligands.

NMR has also been used to investigate how early NP nuclei may be stabilized but continue to grow. Studying an IrNP system, Finke and co-workers used a combination of ^{1}H and ^{2}H NMR spectroscopy to understand how ionic liquid media are able to stabilize transition metal NPs by monitoring the ionic liquid chemistry during synthesis.[27] The authors found that Ir(0)

NPs (d = 2.1 nm) reacted with imidazolium-based ionic liquids in order to form surface-bound carbenes, suggesting that chemical reaction of the solvent can create molecular stabilizers for the growing particle surface. Solvent and other reaction byproducts have been implicated as stabilizing agents in other NP syntheses as well. For example, Polte et al.[28] have shown that borate byproducts may stabilize Au and Ag NPs on the time scale of hours during and after their formation when using $NaBH_4$ as a reductant in the absence of other ligand reagents.

In addition to determining the chemical evolution of ligand precursors and their role in particle growth, NMR has also been used to probe the role of capping ligands in the emergence of particle shape. For example, Gordon and co-workers used ^{1}H-^{13}C cross-polarization (CP)-MAS NMR spectroscopy to determine the surface composition of poly(vinylpyrrolidone) (PVP, MW = 29 kDa)-capped Ag-Pt nanocubes and octahedral (d = 6-8 nm) before catalytic evaluation.[29] As may be expected, when more Ag precursor is added to the synthesis, more Ag is incorporated into the final particle architecture. For each new composition, dramatically different ^{1}H-^{13}C CP-MAS NMR spectra are observed, each of which deviates from the spectrum of pure PVP. Upon increasing Ag addition to the final particle, ^{13}C resonances that correspond to hydrocarbons and amines begin to appear. At the same time, characteristic ^{13}C resonances of PVP, specifically those from the 5-membered ring in the polymer repeat unit, disappear. Combined, these results suggest that Ag promotes bond cleavage to form hydrocarbon and amine fragments from the original PVP ligand - an interesting observation of changes in ligand chemistry initiated by the forming particle itself. Importantly, these spectroscopic changes in ligand chemistry as a function of Ag addition correlated not only with alloy composition but also with overall alloy shape, suggesting that metal-PVP reactions may bias surface growth rates and influence the final particle morphology.

1.2.2 NMR Observation of Metal Nuclei during Synthesis

In addition to observing ligand chemistry during the steps of NMNP synthesis, NMR-active metal nuclei allow direct observation of metal precursor behavior as well. Unfortunately, while 100% naturally abundant, the large quadrupole moment of the ^{197}Au nucleus precludes direct observation via NMR with current methods, although coupling to heteroatoms, such as ^{31}P, has been reported.[30] Luckily, other metal nuclei have more favorable NMR properties, such as ^{195}Pt and $^{109/107}$Ag. While Ag NMR holds promise for understanding silver NP precursor chemistry, both isotopes suffer from low sensitivity because of low gyromagnetic ratios and therefore generally require specialized low-gamma probe hardware for NMR observation. Further, Ag nuclei typically exhibit extremely long T_1 values (on the order of hours) making data acquisition time-consuming.

Despite these difficulties, understanding the magnetic resonance properties of inorganic silver compounds, many of which are NP precursors, is an area of active research[31] and the applications to NP synthesis are beginning to be explored. For example, Liu, Saillard, and co-workers have used a combination of NMR spectroscopies (^{1}H, ^{2}H, ^{31}P, ^{77}Se, and ^{109}Ag), UV-vis, ESI-MS, FTIR, TGA, elemental analysis, single crystal X-ray diffraction, and density function theory (DFT)) to monitor the conversion of Ag(I) salts into hydride-centered Ag clusters (number of atoms ranging from 7 to 10) and larger Ag NPs (d = 30 nm).[32] Here, ^{109}Ag NMR was used to locate the hydrogen atom within the Ag clusters. Figures of merit such as the coupling constant between Ag and H were consistent when measured either by ^{1}H NMR or ^{109}Ag NMR ($J_{\text{H-Ag}}$ = 39.4 Hz and $J_{\text{Ag-H}}$ 39.7 Hz, respectively) indicating a robust structure assignment.

To date, the majority of work studying NMNP formation via NMR of metal nuclei has focused on Pt and specifically on Pt precursors. One of the first studies was reported by Murphy

and co-workers and used a combination of solution phase ^{195}Pt, ^{1}H, and ^{13}C NMR to determine the dynamics of ligand exchange between $[PtCl_4]^{2-}$ and poly(amidoamine) (PAMAM) dendrimers during dendrimer-mediated PtNP synthesis.[33] ^{195}Pt NMR, in particular, was used to identify the speciation of the metal precursor upon binding to the dendrimer as well as track Pt precursor uptake into the template branches. The goal of the study was to understand the chemical environment of the Pt(II) precursor (starting material = K_2PtCl_4) before reduction to Pt(0) by $NaBH_4$ in the presence of either generation 2 (G2-OH) or generation 4 (G4-OH) PAMAM dendrimers. In both G2-OH and G4-OH cases, the ^{195}Pt NMR signal intensity assigned to $[PtCl_4]^{2-}$ decreased, while new peaks arose as Cl^- ligands were replaced by nitrogen-containing sites from within the dendrimer. On the basis of chemical shift analyses, the number and type of nitrogen substitution could be deduced, with each successive amine substitution leading to a chemical shift change of -261 ppm and each successive amide substitution leading to a chemical shift change of -333 ppm.

In addition to chemical shift distribution, the total Pt(II) signal could also provide information about the sample. For example, in the case of G2-OH, 50% of the total ^{195}Pt NMR signal disappeared during uptake, and this decrease was attributed to a black Pt(0) precipitate that formed during the course of uptake (~2 days). In the G4-OH system no precipitate is observed over 10 days, but the ^{195}Pt NMR signal intensity is attenuated by ~80%, indicating that the discrepancy may be due to signal dephasing of Pt nuclei in areas of restricted molecular motion such as inside the dendrimer or from aggregation of more than one dendrimer. Overall, the authors found that Pt(II) uptake, speciation, and reactivity was a complex result of the dendrimer architectures, correlating with both the impact of ligand exchange about the Pt(II) center as well the sterics of the dendrimer as a whole.

Recently, we have studied the role of Pt(IV) speciation on reaction pathways in Pt-containing, mixed metal NP syntheses. Specifically, we examined the influence of Pt(IV) speciation on the deposition of Pt metal onto colloidal AuNP substrates (Figure 3).[34] Here, Pt(IV) speciation was controlled by adding NaOH to the H_2PtCl_6 precursor solution which we used as a strategy to control the extent of Pt hydrolysis that occurs in aqueous solutions of H_2PtCl_6. We then monitored the resulting ligand substitution of the Pt center as a function of pH via solution phase ^{195}Pt NMR spectroscopy.

Monitoring ligand substitution of these complexes via ^{195}Pt NMR is particularly attractive because chemical shift assignment can be supported by isotopologue analysis of the pendant chloride ligands. In this analysis, the isotopologue distribution of ^{35}Cl/^{37}Cl species in the $[PtCl_6]^{2-}$ and $[PtCl_xL_y]^{n-}$ (where L = H_2O or OH^-) can be extracted from deconvolution of NMR peaks (Figure 3A, insets). Specifically, at high field strengths (B_0 = 14.1 T), ^{37}Cl substitution leads to an upfield shift of ~0.17 ppm.[35] The relative populations of isotopologues in the spectra directly correlate with the natural abundance of the respective chlorine isotopes. Further, for monosubstituted $[PtCl_5L]^{n-}$ species, resolution of both $^{35/37}$Cl isotopologues and isotopomers is possible (isotopomers are represented by the same color in the peak fitting in Figure 3). This analysis provides both a spectroscopic fingerprint for Pt(IV) complexes in solution as well as a relative quantification of various Pt species in solution.[36]

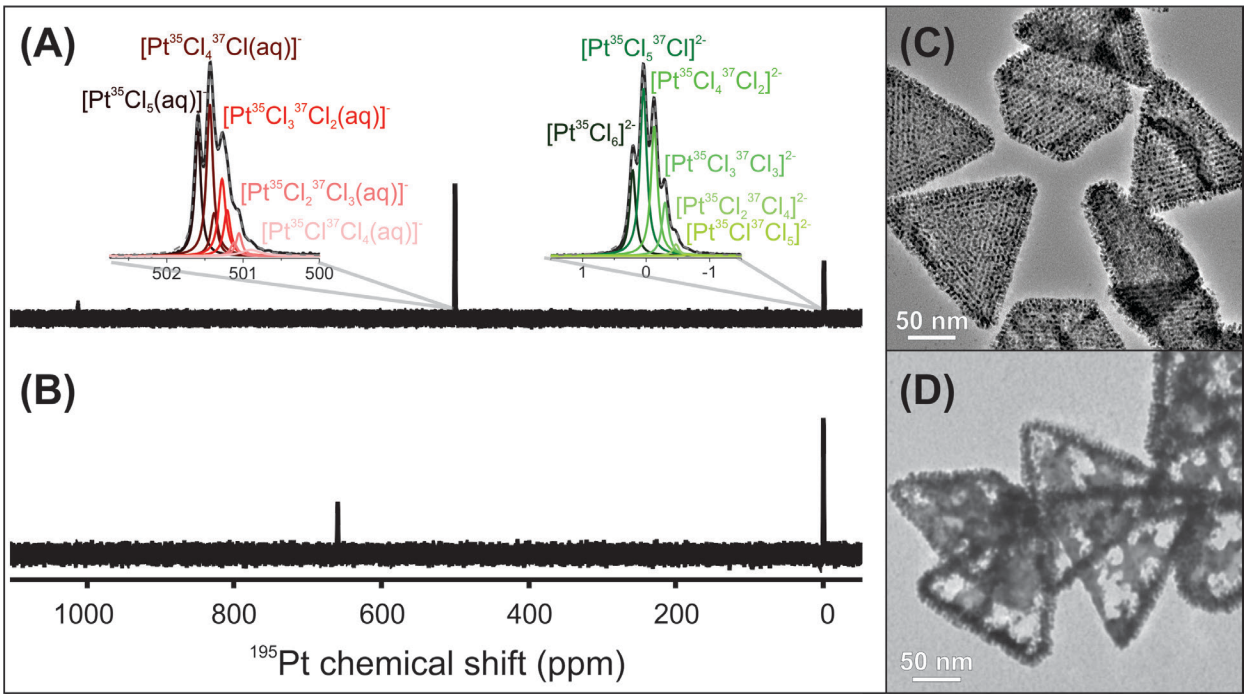

Figure 3. ^{195}Pt NMR spectra of Pt(IV) precursor solutions at pH 1.8 (A) and 8.6 (B). Corresponding TEM images of particle motifs of Pt deposition on Au nanoprism substrates when Pt(IV) precursor solution pH is 1.8 (C) and 8.6 (D). Insets in (A) show ^{195}Pt NMR chemical shift assignments for monosubstituted species $[PtCl_5(aq)]^-$ (left) and $[PtCl_6]^{2-}$ (right) using isotopologue analysis at B_0 = 14.1 T. In the case of monosubstitution, isotopomers could also be resolved upon peak fitting. Black lines represent experimental spectra, colored lines represent the peak fits for each isotopologue and/or isotopomer, and dashed gray lines represent the sum of the peak fit. Adapted with permission from ref 34. Copyright 2014 American Chemical Society

Ultimately, Pt(IV) speciation was found to correlate well with final NP morphologies, and the pH of the original Pt(IV) precursor solution was a reliable method to modulate this speciation parameter. Particularly interesting was the impact of speciation at high precursor solution pH. At pH 8.6, 67% of the Pt(IV) complexes are $[PtCl_6]^{2-}$ and 33% are the monosubstituted $[PtCl_5(OH)]^2$. When Pt(IV) precursor solutions at this pH are used for Pt deposition on the AuNP substrates, the majority of AuNPs are oxidized via a galvanic replacement mechanism and the synthesis results in the formation of framelike Au-Pt alloy nanostructures (Figure 3D). Conversely, when Pt(IV) precursor solution pH is low, reduction of the metal cation occurs primarily via externally added reducing agent oxidation (in this case, ascorbic acid), as evidenced by lack of oxidation in the Au nanoprism substrate (Figure 3C). The difference in Pt(IV) reduction pathway is consistent with previous electrochemical studies of $[PtCl_6]^{2-}$ in water, which find that OH^- substituted halide complexes are more readily reduced.[37] Therefore, controlling Pt(IV) speciation (and thereby metal precursor reduction potential) is a synthetic handle with which to mediate whether Pt(IV) reduction will occur via oxidation of the small molecule reducing agent (leading to deposition on top of the existing particle substrate) or through oxidation of existing NPs in solution (leading to cage-like, hollow, or "frame" nanostructures). These insights provide important mechanisms for tunability in the synthesis of Pt-containing NP products which are of interest in many applications including fuel cells[38] and data storage.[39]

Overall, the literature suggests that unprecedented, molecular- scale information can be gained by using NMR to monitor the chemical conversion of NP precursors in both the solution and the solid phase, under diverse reaction conditions, and for several different metal identities.

These insights should lead to a deeper understanding of NMNP synthesis mechanisms and ultimately provide a robust foundation for future NP synthesis design.

1.3 NUCLEAR MAGNETIC RESONANCE CHARACTERIZATION OF NOBLE METAL NANOPARTICLES

In addition to providing critical insights into the formation of NMNPs, NMR techniques may also be used to understand several aspects of the final nanoparticle architecture. NMR stands out here, because it is able to resolve molecular architectures at the surface of the solid phase nanoparticle. In this section, we discuss the use of NMR techniques to elucidate features of both the nanoparticle core and the nanoparticle ligand shell with high spatial and chemical resolution.

1.3.1 Metal Nanoparticle Surface Chemistry: Small Molecule Ligand Shells

1.3.1.1 Ligand Identity and Quantity

An important aspect of ligand shell characterization is monitoring the process and final products of ligand exchange. These studies require the ability to evaluate both ligand identity as well as quantity. NMR spectroscopy is particularly well-suited for these requirements, because of the chemical resolution offered by chemical shift and the direct relationship between NMR signal integration and spin population. Indeed, solution phase ^{1}H NMR spectroscopy has been used to quantify the type and amount of ligands on quantum dots and metal oxide nanoparticles,[40-43] and similar approaches have been used to assess the relative ratios of ligands in mixed monolayer systems appended to NMNPs.[44-47] However, in order to achieve quantitative results, NMNP

cores typically must be digested due to line broadening effects that become increasingly problematic at larger particle sizes (*vide supra*).[48,49] Perhaps more importantly, with all bulk ligand quantification strategies to date (including those using NMR), the accuracy of ligand density values is fundamentally limited by the size distribution of the nanoparticle cores analyzed.

Using NMR to monitor ligand exchange in real time was performed without particle digestion to gain information on ligand exchange. At very small particle sizes (generally <200 atoms), ligand exchange can be monitored on intact particles with relatively well-resolved NMR spectra due to the rapid tumbling in solution, similar to that of small molecules. Yarger and co-workers used solution-phase ^{1}H NMR to observe ligand exchange on triphenylphosphine (PPh_3)-capped AuNPs (d = 1.8 nm) with both d_{15}-PPh_3 or Au(I)(d_{15}-PPH_3)Cl in CD_2Cl_2.[50] Under ambient conditions, both d_{15}-PPh_3 and Au(d_{15}-PPh_3)Cl showed similar kinetics with ligand exchange rate constants (0.17 and 0.20 min^{-1}, respectively) extracted from time-dependent ^{1}H NMR spectroscopy. In both cases, Au(I)(PPh_3)Cl was removed from the particle surface and replaced with the incoming ligand. Further analysis with ^{31}P NMR of the tethered PPh_3 groups was consistent with Au(0) and/or Au(I) phosphine complexes, indicating that Au-phosphine complexes, rather than simply PPh_3, was the capping ligand in these systems.

Recently, we have exploited the quantitative capabilities of ^{1}H NMR spectroscopy to describe both the identity and absolute quantity of ligands before and after ligand exchange on commonly used pseudospherical AuNPs (d = 13 and 30 nm).[51] The method is a widely applicable approach to quantify ligand shell compositions using a combination of transmission electron microscopy (TEM), inductively coupled plasma mass spectrometry (ICP-MS), and ^{1}H NMR spectroscopy (Figure 4). The accuracy associated with this methodology was verified by

comparison of ligand quantities between several techniques using specialized ligands designed specifically to be analyzed via several approaches. First, a selenol-functionalized ligand was synthesized and appended to the AuNP surface. After particle digestion, the sample ligand solution was analyzed by two methods: ^{1}H NMR as described in Figure 4 and ICP-OES (optical emission spectrometry) for analysis of Se atom concentrations. Using multiple modes of statistical analysis to compare values obtained from these two techniques, both ^{1}H NMR and ICP-OES were found to yield statistically equivalent ligand values within a 95% confidence interval. Quantification can also be performed by the addition of a high purity internal standard with a known number of protons and concentration, such as dimethylmalonic acid (DMMA), or by using ERETIC (electronic reference to access in vivo concentrations) techniques[52] for ligand concentration evaluation in a single spectrum, eliminating the need to construct a calibration curve. To demonstrate this point, we also conducted ^{1}H NMR ligand quantification experiments using DMMA. Similar to the comparison with ICP-OES, we found that both approaches showed statistical agreement (no difference within 95% confidence interval).

Using the approach outlined in Figure 4, we found that ligand addition mechanisms are strongly influenced by intermolecular interactions within the ligand shell itself. We expect these findings will have implications for both routine surface characterization of AuNPs as well as for generating highly tailored surface chemistries that optimize particle functionality in applications such as multivalent biomolecular interactions or catalytic reactions.

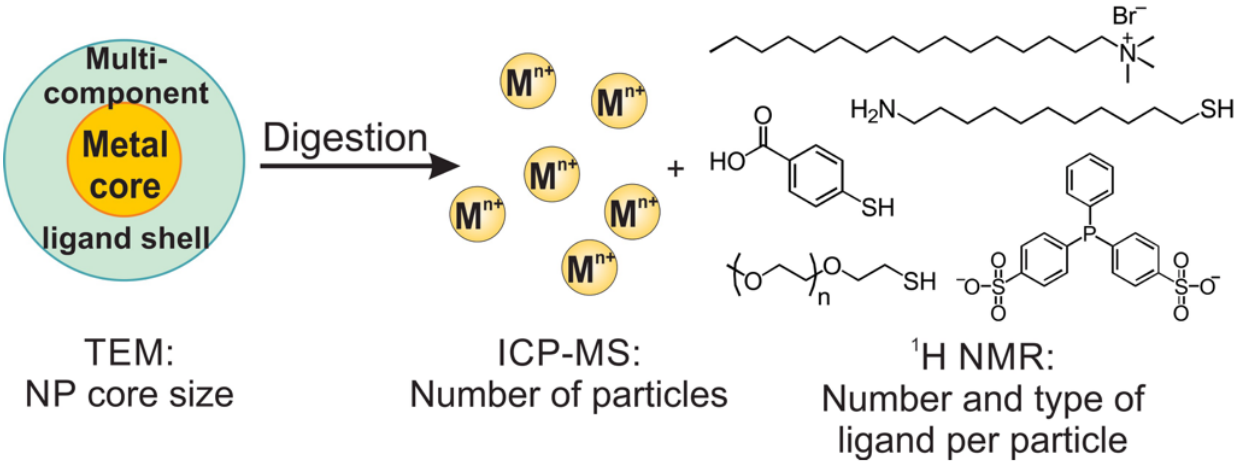

Figure 4. General procedure to analyze the number and type of ligands present on a nanoparticle. Nanoparticle core size and total metal atom concentration are used together to determine the nanoparticle concentration. Adapted with permission from ref 51. Copyright 2015 American Chemical Society

1.3.1.2 Ligand Shell Morphology

Under conditions where the ligand is still appended to the nanoparticle surface, spatial information, including the average local chemical environment of the ligands as well as overall ligand architectures adopted on-particle, may be studied. The observation of ligand shell architectures is a particularly exciting application of NMR spectroscopy, because resolution of ligand shell morphology is difficult to observe with traditional materials characterization techniques (*vide supra*).

Two of the fundamental driving forces behind the formation of various ligand shell morphologies are chemical interactions between individual ligands and chemical interactions between ligands and the nanoparticle surface. A variety of NMR techniques can be used to probe these interactions. For example, 1D and 2D ^{1}H high resolution (HR)MAS NMR techniques showed the presence on π-π stacking between aromatic ligands appended to a AuNP surface (orientation of the π-π stacking with respect to the particle surface was not resolved).[53] One may also systematically monitor ligand position by using either the particle surface itself[54] or site-specific paramagnetic lanthanide labels,[55,56] both of which act as a spectroscopic ruler by dephasing resonances closest to the unpaired electron (for more information about distance-dependent NMR signal dephasing using a variety of methods, the reader is referred to the work of Solomon[57] and Bloembergen[58]). Both strategies have been used to assess parameters such as protein-nanoparticle binding sites on specific residues[54] and molecular position-mapping of organic capping ligands,[55,56] respectively.

Although limited distances (~5 Å) can be measured with solution phase NMR techniques, detailed structural information on various ligand shell architectures and arrangement can still be ascertained. Recently, Stellacci and co-workers presented a ^{1}H NMR method to

determine ligand shell morphologies by predicting ^{1}H chemical shift trends as a function of ligand shell composition (also measured with ^{1}H NMR, but with digested particles) in combination with NOE cross peak patterns (Figure 5).[59] Using this method, the authors were able to determine the difference between randomly mixed, Janus, and patchy ligand shell morphologies on AuNPs (d = 2-5 nm) capped by binary mixtures of aromatic and aliphatic molecules. Further, ^{1}H NMR line narrowing of specific ligand resonances provided spectroscopic evidence for structural defects associated with particular morphologies.

To extract architectural information from this combination of 1D ^{1}H NMR spectra and NOE patterns, two important experimental conditions must be met. First, the binary ligand shell composition must be tunable across all composition space (i.e., from 0 to 100% of each ligand). This control is needed in order to observe the changes in chemical shift associated with the ligand mixtures as shown in Figure 5A-C. Second, the ^{1}H NMR resonances of the constituent ligands must be well-resolved to observe the cross-peaks shown in Figure 5D-F (i.e., distinct and preferably very well-resolved from one another on the chemical shift spectrum). The first limitation can be overcome as a more robust understanding of ligand shell chemistry evolves, with a significant amount of progress attributed to the information gained from NMR studies (*vide supra*). Additionally, the need to study mixed ligand systems with well-resolved resonances can be mitigated by moving to higher field strengths and/or other observable nuclei with larger chemical shift ranges than traditional ^{1}H NMR, such as ^{31}P or ^{13}C.

Additional spatial information on nanoparticle ligand shells can be gained by using advanced ssNMR techniques, such as rotational echo double resonance (REDOR).[60] Strong dipolar couplings between neighboring nuclei lead to broad NMR lines in the solid state that can be averaged out with MAS. Due to long-range order observed in solids, selective reintroduction

of dipolar couplings with REDOR allows for the measurement of much longer distances between nuclei (~25 Å) than in the solution phase, in which dipolar couplings are averaged out by molecular tumbling.

One example of this technique was used to distinguish between bilayer formation via a disulfide linkage vs a hydrogen bonding interaction with important implications for cysteine-mediated protein binding to AuNP surfaces. Here, Gullion and co-workers used $\{^{1}H\}^{13}C\{^{15}N\}$ REDOR to selectively reintroduce heteronuclear dipolar couplings on uniformly labeled ^{13}C, ^{15}N L-cysteine and L-cystine capped-AuNPs (d = 6.6 nm).[61] REDOR measurements along with ^{1}H-^{13}C CP-MAS NMR analysis showed that the thiol-group of the L-cysteine molecule was chemisorbed to the Au surface and formed an initial ligand layer. Thiol anchoring of the initial monolayer exposed charged amino and carboxyl groups on the zwitterionic L-cysteine, to which a second L-cysteine layer coordinated via hydrogen bonding. ^{1}H MAS analysis indicated that the outer layer of L-cysteine molecules interacting with the chemisorbed inner layer exhibit large amplitude motion about the carbon-carbon bonds.[62] Comparison to L-cystine-functionalized AuNPs indicated that L-cysteine was not absorbed as the disulfide analogue. While these results are significant for protein-attachment strategies to AuNPs, their more important impact is in establishing REDOR as a powerful approach to resolve long-range interactions within the NMNP ligand shell, analogous to structural detail that has been transformative in structural biology.

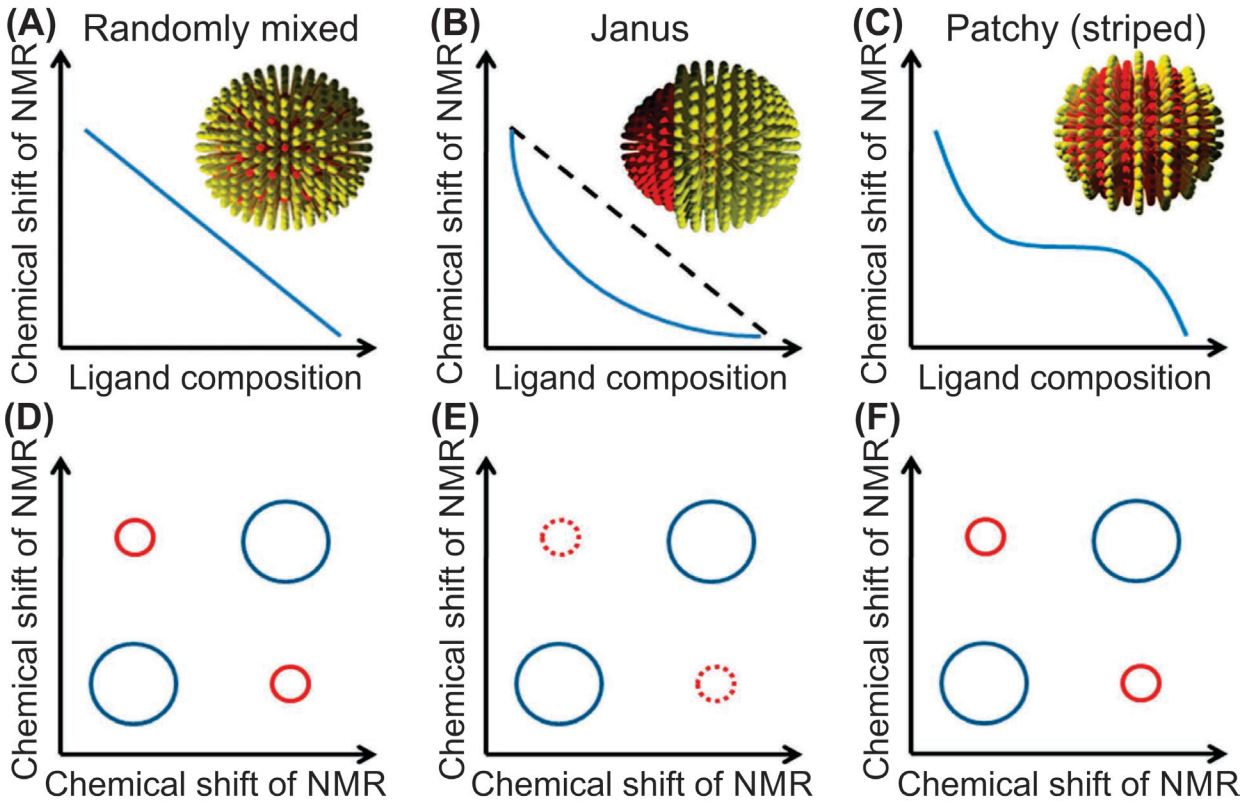

Figure 5. Ligand shell arrangements and morphologies can be assessed by combining solution phase ^{1}H chemical shift with NOE analysis. (A), (B), and (C) represent the predicted chemical shift patterns as a function of ligand composition. (D), (E), and (F) represent the predicted NOE cross-peak patterns as a function of randomly mixed, Janus, and patchy ligand shell morphologies. Reproduced with permission from ref 60. Copyright 2012 Nature Publishing Group

1.3.1.3 Ligand Shell Structural Dynamics

In addition to probing the identity, quantity, and arrangement of ligands on metal NP surfaces, NMR techniques are also useful to probe variations in structure (e.g., as a function of temperature) and dynamics of the NP ligand shell with atomic site resolution within the ligand.[63]

For example, by simply measuring the ^{13}C NMR chemical shift values of ligand resonances appended to a nanoparticle, the crystallinity of alkanethiol ligand shells can be estimated. This strategy takes advantage of ^{13}C chemical shifts that are particularly sensitive to trans- and gauche-conformational changes for ligands tethered to solid surfaces. Under MAS conditions in the solid state, all-trans conformations for interior methylenes resonate at 33-34 ppm and gauche conformations appear between 28-30 ppm.[64] As expected, in solution a dynamic equilibrium between trans and gauche conformations is typically observed and leads to an averaged ^{13}C chemical shift of 29-30 ppm, consistent with chemical shift averaging observed in other equilibrium processes monitored by NMR. More detailed information on alkyl chain dynamics, relative molecular mobilities, and the degree of crystallinity can be measured with a combination of ^{13}C and ^{1}H T_1 relaxation measurements, ^{13}C-^{1}H heteronuclear dipolar dephasing experiments (Figure 6B), and 2D ^{13}C-^{1}H wide-line separation ssNMR experiments.[65]

Using the strategies above, chain ordering trends on AuNPs (d = 2-5 nm) as a function of alkyl chain length have been evaluated.[65] In all cases, the thiol moiety is anchored to the AuNP surface, which is evident from NMR signal dephasing at ^{13}C positions adjacent to the thiol. When the alkanethiol chain length is < C_8, the ligand shells show dynamics similar to that of the solution phase (*N.B.* this does not imply rapid exchange with solution phase ligands), indicating that a high population of gauche conformers is present at short chain lengths. On the other hand, when the alkanethiol chain length is increased to C_{18}, the ligand shell displays a high degree of

conformational order from large-amplitude motion about the chain axes in a mostly trans conformation. The increased conformational order was proposed to be a result of chain intercalation in the solid state with neighboring particles (Figure 6A).

Surprisingly, ssNMR analyses also revealed a non-negligible population of gauche conformers concentrated at chain termini in C_{18} thiol-capped AuNPs, a detail that was not apparent from FTIR analysis alone. While also a bulk measurement of the average, NMR has the distinct advantage of providing ^{13}C chemical shift resolution of specific carbon sites and different electronic environments along the alkane chain. Further, phase transitions observed via DSC corresponded to reversible alkyl chain disordering, as determined by variable temperature (VT) ^{1}H-^{13}C CP-MAS experiments. These results were later confirmed and expanded by Lennox and co-workers using a combination of DSC, FTIR, and ^{2}H ssNMR.[66]

In addition to crystallinity and chain ordering trends in alkanethiol-capped AuNPs, the influence of terminal-alkyl functional groups on these architectures was studied using similar methods. Both conformational order and thermal stability have been studied for several chain lengths and functional groups including alcohols,[65] carboxylic acids,[67] phosphonic acids,[68] and sulfonic acids.[68] In general, the authors found that hydrogen bonding imparted a higher degree of conformational order and thermal stability compared to methyl-terminated analogues.

Solid-state NMR techniques were used to resolve not only interactions at the ligand-solvent interface but also to provide important insight into ligand-particle bonding at the hard-soft matter interface. To describe in similar structural detail the metal-sulfur binding motif present in AuNPs, Lennox, Reven, and co-workers investigated the Au-SR interaction using ssNMR techniques for both long- (C_{14}) and short-chain (C_4) alkanethiols.[69] Site-selective ^{13}C isotopic labeling was used to enhance and resolve the ^{13}C NMR resonances at positions C_1 and

C_2, closest to the thiol group. On the basis of chemical shift comparison to the free ligands, the C_1 and C_2 positions were both found to undergo extensive line broadening and downfield shifts of 18 and 12 ppm, respectively. The changes in chemical shift upon coordination to AuNPs were consistent with strongly adsorbed organosulfur species.

Here, metal-specific NMR features were helpful in clarifying the origin of these changes in chemical shift. For example, the observed chemical shifts could arise from coupling of the $^{13}C_1$ and $^{13}C_2$ resonances to the conduction electrons on the AuNP surface. However, the T_1 values did not exhibit a linear relationship with temperature. This lack of Korringa behavior indicated that the resonances experienced little, if any, Knight shift contribution to the observed NMR chemical shift. Further comparison to analogous diamagnetic Au(I)-thiolates showed similar changes in chemical shift at the C_1 and C_2 position to those observed in the nanoparticle system. Taken together, the absence of Korringa behavior and similarity to Au(I)-thiolate chemical shifts, ruled out a metallic contribution and suggested the origin of chemical shift change was from the presence of a Au-thiolate bond at the particle surface.

Once the origin of the chemical shift difference was assigned, the source of line broadening was evaluated. The fwhm of both the C_1 and C_2 resonances of the thiolate-capped AuNPs were both broadened significantly (fwhm = 1000-1300 Hz). As mentioned in Section 1.1, MAS techniques eliminate contributions from CSA as well as isotropic bulk magnetic susceptibility sources of broadening. Upon MAS, the line widths of C_1 and C_2 were reported to narrow only slightly, indicating that the contribution to the line broadening was the result of a distribution of isotropic chemical shifts. A hole burning experiment confirms the heterogeneous line broadening of C_2, which is likely the result of a chemical shift distribution from chemisorption of the thiol on various crystallographic sites of the AuNPs. These distributions in

ligand-particle bonding environments are then assigned to the impact of a highly faceted particle surface (i.e., different crystallographic facets produce distinct environments for ligand and metal nuclei) as well as deviations in particle shape. Likewise, crystallographic variation in chemisorption sites was also independently found to cause heterogeneous line broadening in ^{31}P and ^{1}H resonances on triphenylphosphine-capped AuNPs (d = 1.8 nm), as determined by ^{31}P and ^{1}H hole burning experiments.[50] Both studies indicate that changes in line width and chemical shift upon particle attachment are primarily the result of heterogeneous line broadening mechanisms from a distribution of chemical environments on various surface facets.

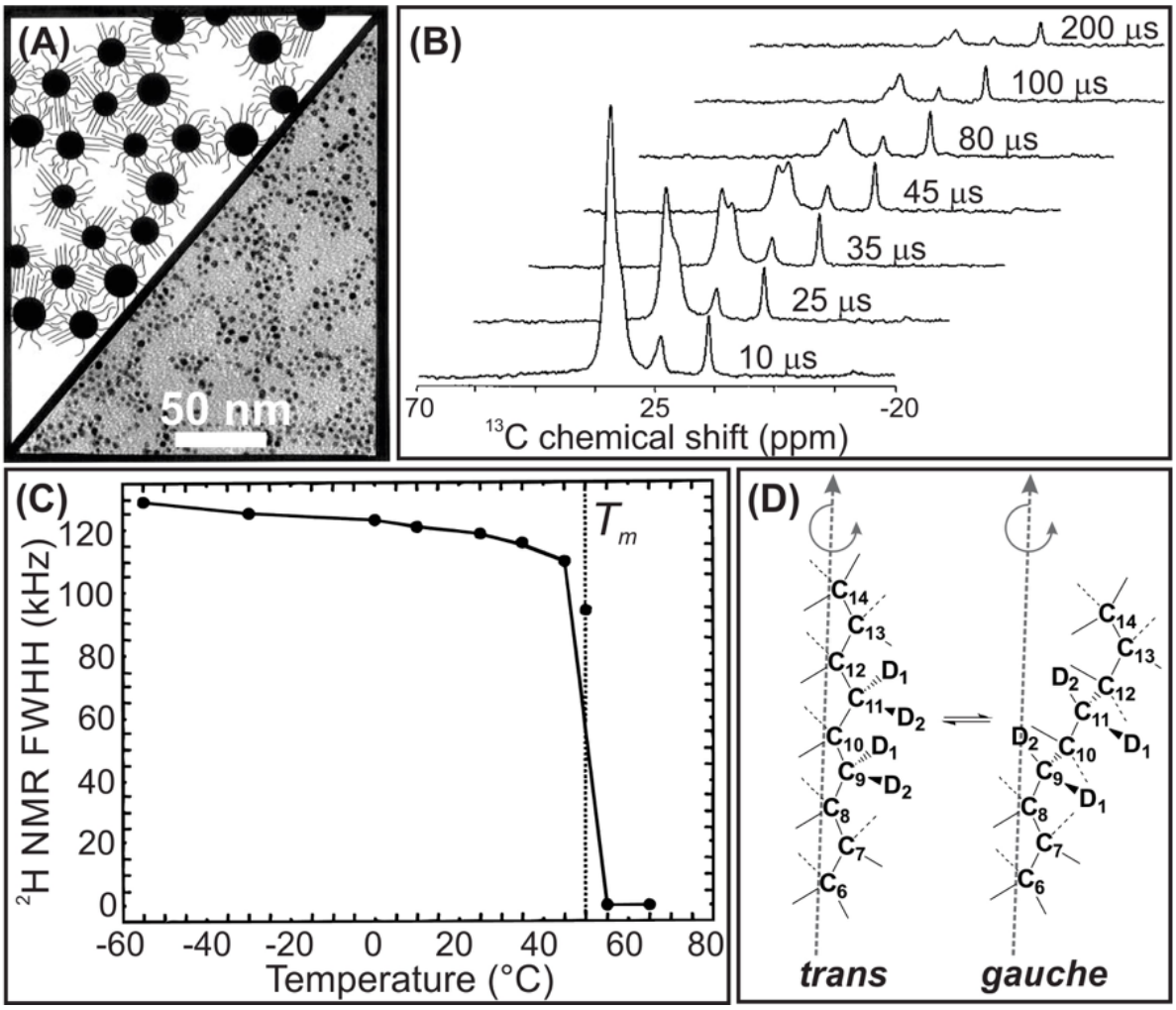

Figure 6. (A) Scheme of possible nanoparticle interactions and corresponding TEM image of octadecanethiol-terminated AuNPs and (B) ^{13}C-^{1}H dipolar dephasing measurements of the NPs shown in (A). (C) Correlation of static ^{2}H NMR lineshapes with phase transitions measured with DSC (T_m). (D) Scheme of trans and gauche methylene confomers in equilibrium as measured by ^{2}H NMR spectroscopy. (A) and (B) adapted with permission from ref 65. Copyright 1996 American Chemical Society. (C) and (D) adapted with permission from ref 66. Copyright 1997 American Chemical Society

In both instances, NMR was able to provide unprecedented insight into the processes contributing to line broadening and chemical shift changes of the resonances closest to the ligand anchoring moiety on NMNPs. Further, there are notable cases in which NMR spectroscopy of the ligand shell may provide information about the chirality of the ligand arrangement or even the underlying particle itself. Using a combination of 1D and 2D solution phase ^{1}H NMR techniques, Jin, Gil and coworkers demonstrated that glutathione-terminated $Au_{25}(SG)_{18}$ clusters exhibit two different types of surface thiolate binding modes, consistent with previous NMR spectroscopy and X-ray crystallography results for $Au_{25}(SCH_2CH_2Ph)_{18}$.[70] Alterations in ^{1}H chemical shift as a result of underlying Au nanocluster chirality were also examined,[71] similar to methods used in traditional organic synthesis. In both cases, the ^{1}H NMR chemical shift behavior is sensitive to the surrounding electronic environment, which includes the electronic structure and bonding environment of the nucleus. Therefore, changes in the handedness of a molecule can be detected by neighboring spin positions and is observed as a change in chemical shift, making NMR observables valuable for assessing chirality or non-chirality of small, molecule-like nanoclusters.

In the case of small, noble metal clusters (<200 atoms) it is important to note that interesting and often unexpected magnetic properties can arise.[72] For example, Maran and coworkers have shown that paramagnetic $Au_{25}L_{18}$ clusters exhibiting −1, 0, and +1 charges show marked shifts in ^{1}H and ^{13}C NMR properties based on cluster charge (L = $S(CH_2)_2Ph$).[73] Depending on the overall diamagnetic or paramagnetic character of the cluster, it may be appropriate to characterize the material with both NMR and electron paramagnetic resonance (EPR) spectroscopies.[74]

More advanced NMR techniques such as deuterium NMR spectroscopy can be used to enhance both spatial and chemical resolution in structure and dynamics studies of NMNP ligand shells. Unlike ^{13}C and ^{1}H NMR spectroscopies, ^{2}H NMR spectroscopy directly probes quadrupolar ^{2}H coupling, and in the case of many solids, the NMR spectrum is dominated by the ^{2}H quadrupolar interaction.[10,75] ^{2}H quadrupolar coupling is a parameter that is a physical representation of the amplitude and symmetry of molecular motion present at each deuterated site, providing exceptional structural information. These methods are routinely exploited for polymeric materials[76] and similar approaches can be applied to study the structure and dynamics of the ligand shell of both phosphine-[77] and thiolate-capped NMNPs.[66]

In one example, VT static ^{2}H ssNMR was used in combination with DSC and FTIR to study site-specifically deuterated (position 1 and 10-13) and perdeuterated (2-18) octadecanethiol-capped AuNPs. These particles were then used to study the molecular origin of several thermodynamic phenomena such as ligand shell melting transitions.[66] Here, Lennox and co-workers used ^{2}H NMR to show that alkanethiols attached to AuNP surfaces undergo rapid trans-gauche bond isomerization and axial chain rotation, consistent with observations deduced from previous ^{13}C and ^{1}H NMR studies (*vide supra*, Figure 6A,D). The phase transition detected by DSC was found to arise from a thermally induced transformation from a predominantly trans chain conformation to a largely disordered state. ^{2}H NMR spectroscopy was able to definitively demonstrate that chain melting originates from a population of gauche bonds that begin in the chain termini and increasingly progress to the middle of the chain with increasing temperature (Figure 6C). However, monitoring the thermal behavior of ^{2}H resonances at position 1 indicated that conformational order is maintained adjacent to the anchoring sulfur atom. The detailed, molecular description that emerged from these studies was in good agreement with previously

observed trends for octadecanethiols in 2D SAMs as well as lipid membrane systems and gave an unprecedented structural foundation for the emergent thermodynamic properties of alkanethiol SAMs on AuNPs.

1.3.2 Metal Nanoparticle Surface Chemistry: Adsorbed Gases

In this section we highlight studies of gas adsorption onto substrates that evaluate the behavior of the gas, including location and geometry of binding sites as well as diffusion coefficients. These experiments are of particular interest to the catalytic community and have been used primarily to elucidate the structure and properties of NMNPs that lead to effective catalysts. In Section 1.3.3.3, we will address experiments that use adsorbed gases to probe the underlying properties of the metal nanoparticle core.

Pioneering studies on hydrogen adsorbed to a variety of NMNPs as well as an overview of several reactions including hydrogenation of benzene, methanation reactions, and the scission of C_2H_2 and C_2H_4 species on nanoparticle surfaces are covered in Slichter's 1986 review.[78] The reader is referred to this review and the references therein for a comprehensive perspective on the seminal works in this field. Here, we focus on more recent advances using NMR spectroscopy to study adsorbed species on NMNP surfaces.

Using VT 1D and 2D ^{1}H NMR, Pruski and co-workers adsorbed hydrogen gas onto SiO_2-supported RuNP catalysts and showed that three different species of hydrogen gas could be identified at the metal surface.[79] One of the hydrogen species exhibited strong adsorption properties, while the other two showed high molecular mobility. These three species likely represented disassociated H species, weakly bound H_2, and H_2 in rapid exchange with the environment. Further examination of the adsorption properties of deuterium on NP surfaces has

clarified some ambiguity in proton dynamics and binding sites in these systems. For example, surface ^{2}H species have been observed, as well as deuterons within the metal NP itself and the presence of mobile and/or reactive hydrides on ligand-capped RuNP systems. Chaudret and co-workers were able to distinguish between different crystallographic adsorption sites on the NP surface (i.e., fcc vs hcp, bridge vs linear) by pairing experimentally observed ^{2}H NMR quadrupolar coupling constants and asymmetry parameters of $^{2}H_2(g)$ adsorbed on RuNPs to the values predicted with DFT calculations.[80] This combination can be extended to determine the effect of ^{2}H adsorption on co-adsorbates, including changes in ligand chemistry, differences in coverage saturation, or variation in metal surface structure.

NMR has also been used to directly monitor the diffusion of adsorbed gases on the surface of metal NPs. Early work included determining various binding sites and exchange of ^{13}CO on RhNPs supported on alumina[81] and ^{13}CO diffusion on PtNPs.[78] Later, using VT ^{13}C and ^{2}H NMR spectroscopy, Oldfield, Wieckowski, and co-workers found that CO diffusion on PtNPs followed Arrhenius behavior and extracted both an activation energy and pre-exponential factor (6.0 ± 0.4 kcal/mol and $1.1 \pm 0.6 \times 10^{-8}$ cm^2/s, respectively).[82] The proposed mechanism for CO diffusion was exchange between different CO populations driven by a chemical potential gradient. This study introduced a new method to quantitatively correlate diffusion of surface adsorbates to catalytic activity and should be amenable to the study of other adsorbed species and metal surfaces.

In a related study, the authors used a combination of ^{13}CO electrochemical NMR and cyclic voltammetry (CV) to investigate the origin of Ru promoted electro-oxidation of MeOH on PtRuNP catalysts.[83] NMR results revealed two different types of ^{13}CO on the catalysts, one population on pure Pt sites and another population on Pt-Ru islands. Surprisingly, no exchange

was observed between different CO populations, and these observations were supported by CV measurements. Detailed analysis of ^{13}C chemical shift changes and Korringa behavior between the two CO populations suggested that Ru weakens the Pt-CO bond, resulting in increased CO oxidation rates. The combination of NMR spectroscopy and electrochemistry provided unprecedented insight into CO tolerance and promotion in bimetallic NP catalysts.

1.3.3 Metal Nanoparticle Core Characterization

1.3.3.1 Nanoparticle Size

A basic property of any nanoparticle is its size. NMR is a useful tool to measure the hydrodynamic radius of metal nanoparticles and can provide an important complement to traditional nanoparticle sizing techniques, such as electron microscopy and DLS. Similar to DLS, NMR signal can be used to determine nanoparticle size via analysis of particle diffusion. Specifically, NMR uses pulsed-field gradient (PFG) techniques to extract diffusion coefficients of well-dispersed species in solution diffusing according to Brownian motion only. Under these conditions, the hydrodynamic size is calculated by rearranging the Stokes-Einstein equation:

$$D = \frac{k_B T}{6\pi\eta R_H} \quad (3)$$

where D is the diffusion coefficient, k_B is the Boltzmann constant, T is temperature, η is viscosity of the solvent, and R_H is the hydrodynamic radius of the diffusing species.

However, unlike DLS, NMR provides the added benefit of chemical resolution. In ^{1}H (or other nuclei of interest) DOSY, a pseudo-2D NMR experiment is performed that separates NMR signals according to their diffusion coefficient. Murray and co-workers presented one of the first accounts of ^{1}H DOSY to measure the hydrodynamic size of Au colloids[84] and extended this

approach to systematically study the size dependent ^{1}H DOSY signatures of AuNPs with core sizes ranging from 1.5 to 5.2 nm.[48] Here, the authors also noted a correlation between nanoparticle core size and the fwhm of the ^{1}H NMR spectra, which was a result of the slower molecular tumbling and reduced correlation time (and, hence, decreased T_2 values) for larger particle sizes. Using changes in NMR spectral breadth as a function of particle size may be particularly useful for systems that are not amenable for DOSY analysis, such as dendrimer-encapsulated nanoparticles.[85] It is worth noting that DOSY analysis can be combined with NOE techniques to use NMNPs as a platform for NMR-based chemosensing of small molecules in solution as reported by Mancin and co-workers.[86,87]

Building upon earlier work, Kubiak and co-workers reported a convenient nanoparticle sizing technique using ^{1}H DOSY measurements in deuterated organic solvents.[88] The sizes measured with DOSY compared well with results obtained from TEM for AuNPs ranging in size from d = 2-5 nm. Nanoparticle size distributions were extracted from the data using the continuous method CONTIN.[89] An important contribution of this study is the use of an internal standard for the calibration of nanoparticle sizing. The use of an internal standard mitigates experimental error while simultaneously simplifying data processing. Here, an internal standard with both a well-defined hydrodynamic size and ^{1}H NMR resonances well-resolved from that of the nanoparticle ligand resonances is added to the sample before ^{1}H DOSY measurement. Common examples of internal standards include ferrocene for organic solvents and dioxane for aqueous media. During the experiment, the diffusion coefficients of both the internal standard and the nanoparticle-bound ligands are measured. The hydrodynamic radius of the nanoparticle can then be calculated from equation 4:

$$R_{NP} = \frac{D_{ref}}{D_{NP}} R_{ref} \quad (4)$$

where RNP is the hydrodynamic radius of the nanoparticle, D_{ref} is the diffusion coefficient of the reference molecule as measured by ^{1}H DOSY, DNP is the diffusion coefficient of the ligands bound to the nanoparticle as measured by ^{1}H DOSY, and R_{ref} is the known hydrodynamic radius of the reference molecule in the solvent of interest. The measurement of relative diffusion coefficients minimizes error from changes in sample temperature, viscosity, instruments, independent measurements, and fluctuations during data acquisition. In our laboratory, we have found that this method can be extended to measure the hydrodynamic size of a range of metal nanoparticle compositions in polar and nonpolar solvents, and that sizes obtained match well with those measured by TEM.[90,91]

Further, we have also found that, by changing the chain length of capping ligand on the nanoparticle surface, we are able to tune and detect corresponding changes in hydrodynamic radius using ^{1}H DOSY. Likewise, Häkkinen and coworkers found that the apparent diffusion coefficient and hydrodynamic size of Au nanoclusters (144 and 102 Au atoms) capped with *para*-merpcaptobenzoic acid (*p*MBA) in aqueous solution depends strongly on the counterion of the deprotonated *p*MBA$^-$ capping ligand.[92] DFT calculations revealed that competing hydrogen bonding interactions and ion-pairing between the *p*MBA$^-$, Na^+, NH_4^+, acetic acid, and water molecules affected the hydrodynamic size of the Au nanoclusters.

Despite these successes, measuring nanoparticle size becomes more challenging and time-consuming with larger particle diameters due to the NMR line broadening effects observed from slower tumbling at larger sizes. It may be that ^{1}H DOSY is most useful at size ranges where alternate sizing techniques, such as TEM imaging, becomes less useful (due to both instrument and sample limitations). It is also important to note that NMR is a population-averaged technique, meaning that ^{1}H DOSY could introduce a bias toward larger particle sizes when

performing sizing measurements, assuming that larger diameter particles contain more capping ligands than smaller ones. However, with these caveats in mind, the combination of ^{1}H DOSY, TEM, and UV-vis can provide robust and sometimes otherwise inaccessible information on the average size of metal nanoparticles.

1.3.3.2 Nanoparticle Core Properties Observed Using Metal Nuclei

Here, we discuss NMR spectroscopy of metal nuclei contained within the nanoparticle itself. These experiments reveal detail both about the nanoparticle physical architecture as well as its electronic structure. For a comprehensive discussion on the theory and history of metal NMR to study particles and clusters, we refer the readers to a classic review by van der Klink and Brom from 2000.[93] Likewise, the quantum dot and metal oxide communities have leveraged direct NMR observation of nuclei that compose the nanomaterial to learn about details such as surface architecture[94] and particle electronic structure[95] as a function of size. For metals, ^{109}Ag,[96-100] ^{103}Rh,[101] and ^{63}Cu[102-105] NMR of small metal nanoparticles have all been reported, but ^{195}Pt is the most well-studied nucleus, because of favorable NMR properties such as relatively high natural abundance (33.8%) and moderate gyromagnetic ratio. Here, we focus on reports of ^{195}Pt NMR with the note that techniques outlined for Pt may be extended to other NMR active metal nuclei as both instrumentation and methodology continue to advance.

Although ^{195}Pt NMR had been used previously to study a range of PtNP systems,[106] Slichter and co-workers reported one of the first observations of size dependent spectral changes in ^{195}Pt NMR line shape as a function of metal core diameter.[78,107,108] This exciting result was confirmed by van der Klink and co-workers who also reported a broad ^{195}Pt NMR line shape spanning 2.5 MHz at 8.5 T from surface to core resonances in the presence of additional adsorbates.[109-111] *Ab initio* calculations suggested that the ^{195}Pt NMR shift in the surface Pt

species compared to the core was the result of a gradual decrease in the d-like Fermi-level local density of states (E_f-LDOS) upon moving from the inside of the particle to its surface.[112] Further, Slichter and co-workers found that ^{195}Pt NMR line shape was a function of particle size and adsorbate identity.[107] As particle size decreased, the ^{195}Pt NMR peak corresponding to bulk Pt metal also decreased. Likewise, when the particles were coated with adsorbates, a surface peak was observed in the region where diamagnetic ^{195}Pt species are typically observed. When the surface of the particles was "cleaned" (heat treated to remove adsorbed molecules), the peak disappeared. Additionally, the frequency of the ^{195}Pt NMR surface peak was dependent upon the chemical identity of the adsorbate.

In order to extract more quantitative information from wideline static ^{195}Pt NMR lineshapes, Bucher and co-workers developed a layer model,[109,113] which assumes a pseudospherical particle shape, and each population-weighted layer of Pt atoms contributes to a specific NMR frequency (Figure 7A).[114] In this model, the average Knight shift of a given layer, n, can be written as follows:

$$K_n = K_\infty + (K_0 - K_\infty)e^{(-n/m)} \quad (5)$$

where K_0 is the Knight shift of the surface, K_∞ is the Knight shift of bulk Pt, and m is the "healing length". Here, the healing length is a probe of how strongly the more "molecule-like" surface is able to influence the metallic Knight shift of the interior Pt atoms. The healing length will vary with particle diameter, but Oldfield, Wieckowski, and co-workers have demonstrated that healing length can also depend on the electronegativity of adsorbates (*vide infra*).[115]

The difference in healing length can be seen in the shift of NMR frequency as a function of PtNP core diameter (Figure 7B). As the population of surface atoms increases, the population of surface species present in the spectrum increases accordingly. Likewise, to examine the

influence of Pt core diameter ($d \approx$ 1-5 nm) on catalytic behavior, Watanabe, Oldfield, Wieckowski, and co-workers used ^{195}Pt NMR analysis to study the oxygen reduction reaction (ORR) in an electrochemical environment.[116] Surprisingly, ^{195}Pt NMR line shape and T_1 relaxation analysis indicated that surface Pt atoms showed similar electronic structure, regardless of core size, and thus had negligible effect on ORR rate constants. This work indicated that the electronic structure of the surface Pt species alone may dictate catalytic behavior, rather than changes in particle size (it is important to note that at NP sizes where the number of surface atoms dominates the total atom population of the particle, these two effects (core size vs surface structure) may be indistinguishable).[117]

In addition to the influence of particle size on E_f-LDOS, the influence of particle surface chemistry has also been examined using ^{195}Pt NMR. For example, comparison of ^{195}Pt NMR lineshapes, chemical shifts, and T_1 relaxation behavior of clean, K-, and Li-impregnated PtNP catalysts revealed that alkali metal impregnation increased E_f-LDOS at surface Pt sites by 10-15%.[118] This result was in contrast to H_2 adsorption, which was shown to diminish E_f-LDOS at Pt surface sites. The spatial resolution available with ^{195}Pt NMR analysis also indicated that the alkali metals add to the surface of the PtNPs and do not diffuse to the particle interior. These data provided a structural basis for proposed mechanisms of alkali metal promotion in PtNP catalysts.

Holding PtNP core size constant ($d \approx$ 2.5 nm), Oldfield, Wieckowski, and co-workers systematically investigated the influence of a variety of adsorbates (H, O, S, CN^-, CO, and Ru) on ^{195}Pt NMR figures of merit.[115] Here, the authors found that the Knight shift of interior Pt atoms remained unchanged, regardless of surface chemistry. However, the Knight shift of the surface and subsurface Pt sites varied over ~11 000 ppm and showed an increasing downfield shift as the electronegativity of the adsorbate increased. Similarly, in two independent reports, Pt

atoms bound to organic capping ligands exhibited no Knight shift and did not show typical Korringa behavior, while Pt atoms at the core exhibited metallic properties.[119,120]

Another class of relevant Pt-containing nanostructures that are particularly difficult to characterize are small multimetallic architectures (d = 1-3 nm) containing Pt and at least one other metal. In these materials, the number as well as the position of the constituent metal atoms are crucial to their optical, catalytic, and magnetic properties. Methods such as X-ray absorption techniques as well as ssNMR can provide comprehensive information on metal nanoparticle architectures. NMR has the advantage of being more accessible and therefore can provide real-time analysis of ongoing experiments. Especially in the case of ^{195}Pt NMR, the electronic structure at both the surface and core of the nanoparticle can be determined by direct observation of the metal nucleus as described in pure Pt NPs above.

One of the first reports of ^{195}Pt NMR to probe bimetallic nanoparticles investigated Pt-Rh NPs and correlated the results with metal segregation observed in EDS.[121] Further investigations used ^{195}Pt NMR to understand the changes in E_f-LDOS of catalytically active PVP-coated Pt-Pd nanoparticles. Here, van der Klink and co-workers showed that the E_f-LDOS of the interior Pt atoms varied strongly with % Pt composition, similar to observations in bulk Pt-Pd alloys.[122] The authors suggested that the changes in E_f-LDOS were also present at the surface of the NPs and were responsible for changes in catalytic behavior as a function of composition in Pt-Pd particles.

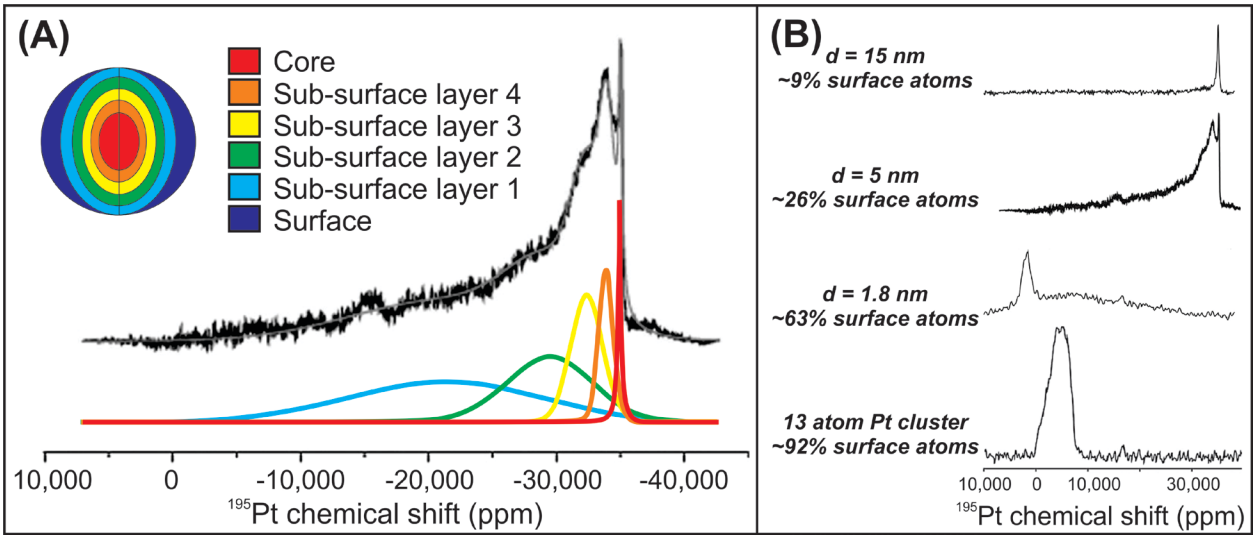

Figure 7. (A) Wideline ^{195}Pt NMR spectrum of 5 nm carbon-supported PtNPs showing deconvolution as a function of atom position. (B) Change in ^{195}Pt NMR line shape as a function of PtNP core diameter and % surface atoms. Adapted with permission from ref 114. Copyright 2013 Royal Society of Chemistry

In a separate report, Oldfield, Wieckowski, and co-workers used a combination of TEM, electrochemistry, and ^{195}Pt NMR spectroscopy to investigate the effect of heat treatment on bimetallic Pt-Ru nanoparticle alloys (d = 2-3 nm).[83,123] Upon heat treatment at 600 °C, the ^{195}Pt NMR signal of Pt-Ru NPs shifted upfield, consistent with Pt migration to the interior of the particle.[83] This structural change resulted in a decrease in catalytic activity and was also consistent with a decrease in the number of Pt atoms on the surface of the NP. When the original sample was instead subjected to heat treatment at 220 °C in H_2(g), CO tolerance and methanol oxidation reactivity both increased, consistent with increased metallic Ru at the particle surface. At the same time, ^{195}Pt NMR resonances exhibited a change in Korringa product, T_1T, consistent with a decrease in E_f-LDOS of the Pt. Taken together, the changes in catalytic behavior and ^{195}Pt NMR properties led to the proposal of a Ru-rich core with a Pt-Ru alloy overlayer as a result of heat treatment at 220 °C in H_2(g). Later, Tong and co-workers expanded this approach to include ^{195}Pt NMR shift analysis for spatial distribution of Pt atoms in Pt-Ru nanoparticle alloys[124] as well as to probe electronic structure in other bimetallic compositions, including Pt-Au NPs.[125]

Recently, Hanna and co-workers investigated a series of Pt_3X (where X = Sn, Al, Sc, Nb, Ti, Hf, and Zr) bimetallic nanoparticles with ^{195}Pt NMR spectroscopy.[114] Here, the authors also used ssNMR analysis of the heteronuclei present in the Pt_3X alloys, which provided multi-element information comparable to powder X-ray diffraction (XRD) techniques (XRD was also performed and correlated to the NMR results). Multinuclear NMR comparison with XRD facilitated assessment of bimetallic NP composition, size, relative order/disorder, and electronic structure. This study highlights the insight that can be achieved by combining NMR techniques with traditional materials characterization tools.

Despite its broad utility, routine acquisition of wide-line NMR spectra can be technically demanding. The inherent difficulty in acquiring ^{195}Pt NMR of Pt-containing nanoparticles lies in the fact that the static lineshapes often span several megahertz, making uniform broadband excitation challenging. Several approaches have been used to reconstruct ultra-wideline patterns, including spin echo height spectroscopy (SEHS), variable offset cumulative spectroscopy (VOCS),[126] and field sweep Fourier transform (FSFT) spectroscopy.[114] The development of methods such as wideband uniform rate smooth truncation-Carr-Purcell Meiboom-Gill (WURST-CPMG)[127] promise to greatly reduce the time and sensitivity burden associated with collecting ultra-wide-line spectra, while accurately replicating lineshapes. Importantly, the advent of broadband excitation and sensitivity enhancement techniques, such as FSFT and WURST-CPMG, suggest the opportunity to explore more exotic metal elements such as ^{105}Pd and ^{197}Au NMR as well as dramatically expand the characterization of Pt-containing NP systems.

1.3.3.3 Nanoparticle Core Properties Observed via Adsorbate Nuclei

Above, we describe the use of NMR to directly observe nuclei in the nanoparticle core. However, NMR of the adsorbate may also provide information about the morphology and electronic structure of the NP. For example, certain adsorbates such as ^{13}CO exhibit a Knight shift and corresponding Korringa behavior as a result of mixing between the adsorbate molecular orbitals and the transition metal d-band.[78]

Slichter and co-workers conducted a large body of foundational work examining adsorbates on the surface of metal particles.[78,128] In 1985, ^{13}CO adsorption on PtNPs was found to shift the ^{13}C resonance to much higher frequency (~200 ppm from the unbound CO resonance).[129] The authors suggested that this large shift was a Knight shift, and therefore the result of polarization of electron spins. This assignment was supported by the observation of

Korringa behavior, and specifically the temperature dependent T_1 of the ^{13}CO molecule. Additionally, the E_f-LDOS on the C atom was determined from electron spin resonance measurements on CO radicals. Slichter and co-workers went on to measure the T_1 behavior of ^{13}CO adsorbed on a variety of small metal particle compositions including Ru, Pd, Rh, Os, and Ir and were able to draw similar conclusions.[78]

A quantitative correlation between the Knight shift of chemisorbed ^{13}CO and the E_f-LDOS on the surface of Pt and Pd nanoparticles was the subject of a later report by Oldfield, Wieckowski, and co-workers.[130] In this work, the authors investigate the NMR properties of ^{13}CO adsorbed to PtNP and PdNP catalysts in an electrochemical environment. The data compared the ^{13}C Knight shift, E_f-LDOS values from DFT calculations and NMR measurements of four systems: ^{13}CO adsorbed onto M_7CO clusters (where M = Pt or Pd),[130] ^{13}CO adsorbed onto oxide-supported PtNPs in a dry environment,[78,109] ^{13}CO adsorbed onto carbon-supported PtNPs in a wet electrochemical environment,[130] and ^{13}CO adsorbed onto oxide-supported PdNPs in a dry environment (Figure 8).[131,132] The linear relationship in Figure 8 was supported by trends in nanoparticle size as well as IR measurements of particle-bound CO.[130,133] The authors suggested that the linear correlation between the Knight shift of chemisorbed CO, K_{13CO}, and the clean E_f-LDOS of the transition metal substrate followed the form:

$$K_{13CO} = a \cdot LDOS \quad (6)$$

where a ~11 (±2) ppm/Ry^{-1} atom^{-1} for Pt and Pd.

While observation of the ^{195}Pt NMR resonance from the PtNP catalyst can serve as a direct probe of the E_f-LDOS of the metal nanoparticle, direct NMR observation of metals such as ^{105}Pd nuclei remains challenging. However, ^{13}CO may be used as a probe of the underlying PdNP. Specifically, the authors measured the Knight shift and T_1 values of linear and bridge

^{13}CO adsorbed onto the surface of PdNPs as a function of temperature.[131] These results are important because they suggest that the NMR behavior of the ligand nuclei bound to a metal surface can be used to probe the metal electronic properties, even in the case of NMR-silent metals. The correlation of ligand nuclei with metal core electronic properties dramatically expands the utility of NMR to understand the behavior of catalytic and photoactive nanomaterials.

Both theoretical[134] and experimental NMR[135] studies provide evidence that, indeed, adsorbates other than ^{13}CO can probe the metallic and structural properties of nanoparticles. For example, Kitagawa and co-workers used $^{2}H_2(g)$ to examine morphology changes in bimetallic NPs. In these studies, the authors used ^{2}H NMR spectroscopy to distinguish between core-shell and alloyed architectures of Pd-Pt,[136] Pd-Au,[137] and Ag-Rh[138] nanoparticles, morphologies which could be tuned as a function of atomic composition.

Tong and co-workers used ^{77}Se NMR to examine the influence of selenol-terminated ligands on underlying AuNP electronic properties. In this case, results indicated changes in both the chemical shift and the temperature dependent T_1 relaxation rate of the Se nucleus, consistent with strong coupling to electrons on the Au surface.[139] The NMR behavior observed in this case is consistent with a possible Knight shift contribution to the ^{77}Se NMR resonance. Unfortunately, analogous ^{33}S NMR experiments are not suitable for routine assessment of thiol-binding environments because ^{33}S exhibits unfavorable NMR properties such as a moderate quadrupole moment (-6.78×10^{-30} m^2), low natural abundance (0.76%), and low gyromagnetic ratio (2.06×10^7 rad T^{-1} s^{-1}). However, based on the work presented by Tong and co-workers, ^{77}Se NMR of selenol-capped nanoparticles is a promising alternative probe of the NMNP metallic properties.

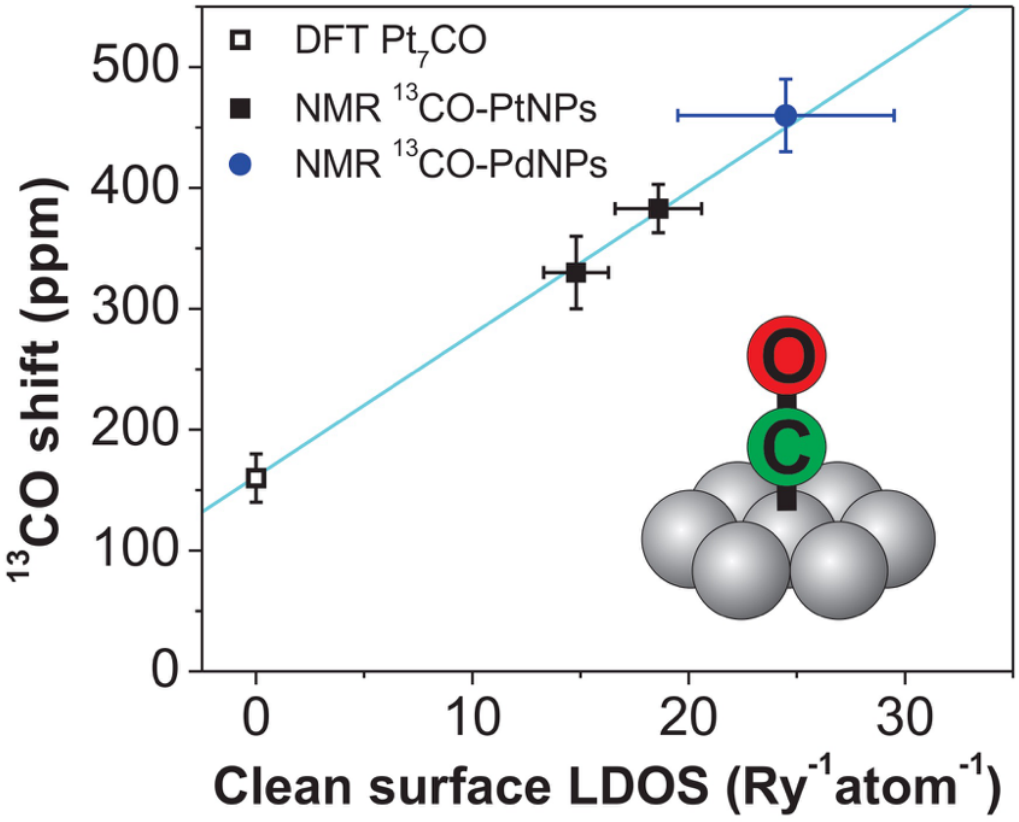

Figure 8. ^{13}CO Knight shift as a function of "clean surface" LDOS based on *ab initio* calculations of CO adsorbed on Pt_7 clusters (open black square) and experimental NMR measurements of ^{13}CO adsorbed on Pt (closed black squares) and Pd (closed blue circle) nanoparticle substrates. Adapted with permission from ref 130. Copyright 1999 American Chemical Society

1.4 USING NMR TO ASSESS NANOPARTICLE PERFORMANCE

Because of its broad accessibility and its ability to analyze NMNPs in situ, NMR may be uniquely well-suited to monitor NMNP performance in certain applications. Here, we give examples of how NMR spectroscopy can provide robust structure-function correlations between NMNP architecture and its utility in applications such as bioimaging and heterogeneous catalysis.

1.4.1 Magnetic Properties

NMR techniques can be used to measure figures of merit for magnetic resonance imaging (MRI) contrast agents. The principles that apply to metal nanoparticle systems are identical to other contrast agents and are not discussed in detail here. Briefly, in order to ascertain the efficacy of an MRI contrast agent, T_1 and T_2 relaxation rates of surrounding media are measured as a function of metal or nanoparticle concentration using standard inversion-recovery and CPMG pulse sequences, respectively. The slope of the resulting relationship between T_1 or T_2 relaxation rate vs concentration is referred to as the relaxivity value, r_1 or r_2, respectively, which can be used to compare between different contrast agents.

In addition to MRI, NMR measurements can provide a fundamental understanding of the magnetic susceptibility in colloids. The NMR-based Evans' method[140] is a particularly attractive technique to measure magnetic susceptibility because it can be used to rapidly evaluate the magnetic properties of NPs in solution (the entire colloid is analyzed), it does not require a large amount of material (~1 nmol NPs), and it is a relatively simple, widely accessible procedure (1D ^{1}H NMR acquisition, performed on any NMR instrument). Importantly, the Evans' method is

also more tolerant of surrounding diamagnetic materials appended to the NP surface (e.g., small molecule ligands), in contrast to other susceptibility measurements such as superconducting interference quantum device (SQUID) measurements.

In the Evans' method, the mass magnetic susceptibility is measured by comparing the ^{1}H NMR chemical shift of a solution containing the magnetic colloid and a standard with that of the pure standard (if suitable, the solvent can serve as the standard). The comparison can be made using a coaxial insert inside an NMR tube, with the inner tube containing pure standard and the outer tube containing both the standard and the colloid of interest. This experimental approach allows acquisition of both species in a single 1D ^{1}H NMR spectrum. The difference in ^{1}H NMR frequency between the standard in the colloidal solution and the pure standard is related to the total mass susceptibility by a modified Evans' method equation:[141]

$$\chi_{tot,g} = \frac{3\Delta f}{4\pi f m} + \chi_0 \quad (7)$$

Here, $\chi_{tot,g}$ is the total mass susceptibility, Δf is the frequency difference in Hz, f is the operating frequency of the spectrometer, m is the mass of magnetic species in 1 mL of solvent, and χ_0 is the mass susceptibility of the solvent. The Evans' method has been used to rapidly assess the magnetic properties of superparamagnetic metal oxides and inorganic complexes and has started to be used to evaluate the susceptibility of binary metal nanoparticles, including Au-Ni[142] and Au-Co.[91]

Chandler and co-workers used the Evans' method to determine the room-temperature, solution-phase magnetic susceptibility of Au-Ni nanoparticles (d = 3 nm) and also measured these values using SQUID measurements.[142] In this study, temperature-dependent SQUID measurements >10 K were difficult to obtain because of the diamagnetic contribution from excess dendrimer template, alkanethiols, and residual solvent necessary to stabilize the bimetallic

structures. Here, the Evans' method provided an alternative to measure the net magnetic susceptibility at room temperature without perturbing sample integrity.

In Chapter 3, we describe the use of the Evans' method to determine the composition-tunable magnetic properties of Au_xCo_yNPs as a function of % Co incorporated in the final NP.[91] By increasing the concentration of Co in the final NP, the mass susceptibility of the NPs was tunable from -3.9×10^{-7} to 112.6×10^{-7} cm^3/g (Figure 9). All measurements were performed at room temperature, in D_2O, with nanoparticle quantities of ~1 nmol NPs. Spectral acquisition was typically complete within 30 s, allowing high throughput analysis of many samples and compositions with little demand on material quantity.

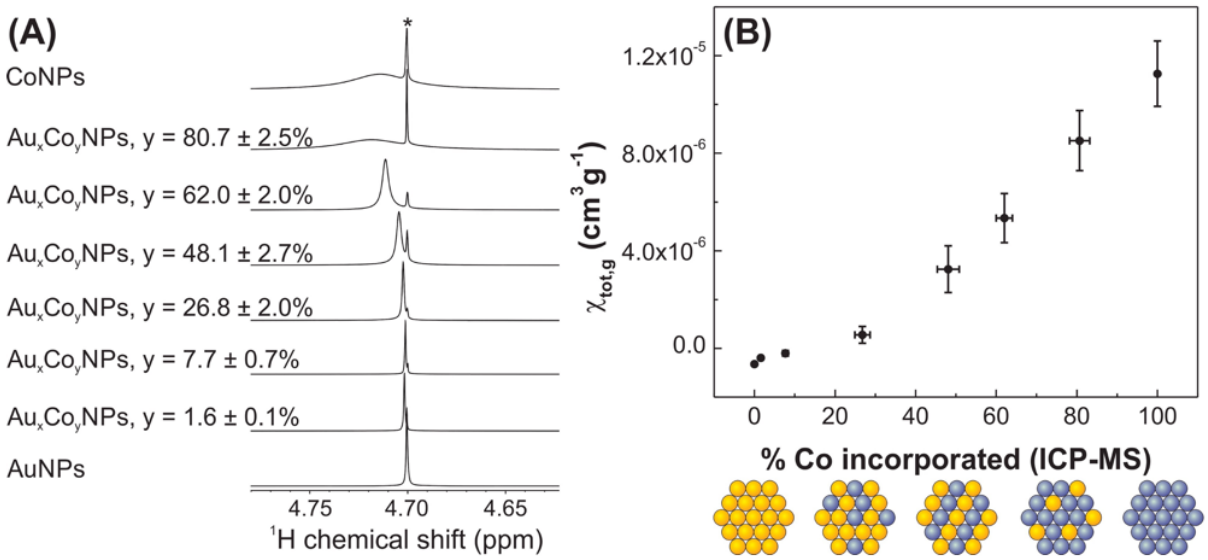

Figure 9. (A) Evans' method ^{1}H NMR spectra of the HDO peak in pure D_2O (asterisk) and the HDO peak in D_2O containing various colloidal compositions. (B) Mass susceptibility as a function of % Co incorporated in Au_xCo_yNP alloys, as measured from the Evans' method spectra in (A). Yellow circles = Au atoms. Blue circles = Co atoms. Adapted with permission from ref 91. Copyright 2014 Wiley-VCH Verlag GmbH & Co. KGaA

In the previously described analysis, the total mass susceptibility is comprised of both the diamagnetic and paramagnetic contribution. If the molecular weight, *M*, of the nanoparticle is known, the paramagnetic contribution can be extracted by converting the mass susceptibility to molar susceptibility according to equation 8 and subtracting the diamagnetic contribution using Pascal's constants[143] (equation 9).

$$\chi_{tot,mol} = M\chi_{tot,g} \quad (8)$$

$$\chi_{para,mol} = \chi_{tot,mol} - \chi_{dia,mol} \quad (9)$$

$$\mu^{eff}\sqrt{8\chi_{para,mol}T} \quad (10)$$

From here, the effective magnetic moment, μ^{eff}, per nanoparticle can be calculated according to equation 10, using elemental analysis of particle concentrations. However, figures of merit such as blocking temperature, saturation magnetization, and extent of hysteresis must be determined using alternate magnetic characterization techniques such as SQUID. Yet, because SQUID is technically more demanding than NMR, NMR measurements of magnetic properties are an attractive complement and/or alternative for many NMNP investigations, including rapid screening in materials development for applications such as data storage, bioimaging, and supercomputing.

1.4.2 Catalytic Behavior

In addition to providing rapid, high throughput information on the magnetic properties of NMNPs, NMR can also be used to explore catalytic behavior. Several examples in the literature use NMR to monitor reactions on metal nanoparticle catalysts, some of which were highlighted in Section 1.3.2. Recently, Tsang and co-workers have used NMR to monitor reactant turnover in

heterogeneous catalysis, but have also correlated changes in ^{13}C chemical shift of chemisorbed formic acid with catalytic figures of merit. Specifically, the authors found that ^{13}C chemical shift of adsorbed formic acid was related to the work function of the surface and the specific activity for a variety of carbon supported and PVP-coated colloids with both monometallic and bimetallic core@shell compositions (Figure 10).[144]

Previously, the authors provided evidence that ^{13}C-labeled formic acid can probe the electronic properties of Ru particle surfaces.[145] In this study, the authors introduce an oxygen spacer between the ^{13}C label and the particle surface and were able to eliminate the line broadening from Knight shift effects (e.g., those observed with ^{13}CO probe molecules). This approach was extended to several other monometallic and bimetallic NP systems. For ^{13}C-labeled formic acid adsorbed to PVP-coated PdNPs, four separate resonances were observed (Figure 10A). The peak at 165.89 ppm was assigned to weakly adsorbed formic acid that was in rapid exchange with free formic acid, leading to an average chemical shift. The remaining ^{13}C resonances, 165.42, 165.69, and 165.95 ppm, were assigned to monodendate, "multimonodentate" (see Figure 10A for molecular structure), and bridging formate adsorbed to the particle surface, respectively. ^{13}C NMR spectral assignment was correlated with FTIR spectroscopy results.

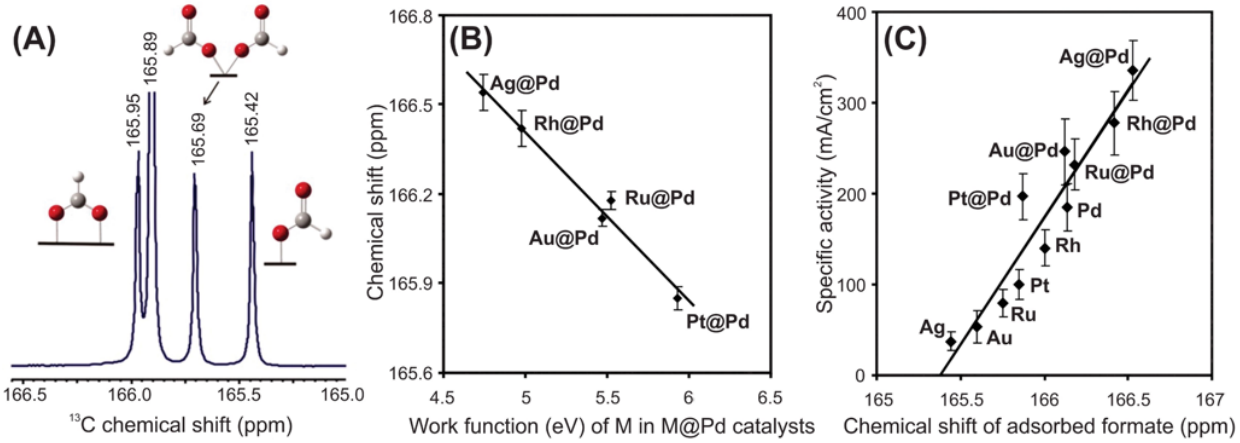

Figure 10. (A) Solution phase ^{13}C NMR spectrum of ^{13}C-labeled formic acid adsorbed to PVP-coated PdNPs. Distinct chemical shifts can be observed for each binding motif. (B) ^{13}C chemical shift of adsorbed bridging formic acid as a function of the workfunction of the core metal in core@shell, M@Pd catalysts. (C) Specific activity of various monometallic and bimetallic catalysts as a function of ^{13}C chemical shift of adsorbed bridging formate on the surface. Adapted with permission from ref 145. Copyright 2011 American Association for the Advancement of Science

Remarkably, even in the presence of an oxygen spacer, DFT calculations suggested a significant degree of overlap of the 2s and 2p orbitals of the ^{13}C atom with metal d-electrons when formate was in a bridging conformation. Linear trends were observed between ^{13}C chemical shift of the bridging formate on the NP surface and the d-band center, work function (Figure 10B), and specific activity (Figure 10C) of the underlying catalysts. Similar trends were observed for a variety of metal types, particle sizes, and compositions, emphasizing the breadth of information gained by using NMR spectroscopy for routine NP performance evaluation.

1.5 OUTLOOK

From the work highlighted in the preceding sections, it is clear that NMR spectroscopy has broad utility in the field of NMNPs, both in terms of the NMR techniques available and the NMNP properties measured.

Yet, it is also clear that there are challenges to capitalizing on this utility. The first barrier is low and largely logistical: many researchers trained and participating in nanoparticle studies are not also trained in the use of NMR as an analytical tool and likewise many experts in NMR spectroscopy are not active in nanomaterials research. This is changing rapidly as the utility of NMR in day-to-day nanochemistry work (e.g., particle sizing or ligand shell characterization) becomes apparent. Second, as mentioned previously, all NMR studies suffer from the inherent low sensitivity of Zeeman splitting. There are ongoing efforts to overcome this disadvantage with high field instrumentation, specialized hardware and pulse sequences,[146,147] and techniques such as dynamic nuclear polarization.[148] Many of these strategies have already been used successfully in the field of structural biology, and it is likely that these advances can also be

applied to the study of NMNPs. Finally, beyond basic 1 and 2D NMR techniques, both the technical and conceptual challenges of NMR spectroscopy increase steeply. For example, experiments that combine electrochemistry and NMR within a single instrument are beyond the capabilities of many but the most expert NMR researchers. In these cases, the results presented in this dissertation combined with growing advances across the NMR and materials communities, have the potential to encourage expanded collaboration between the two disciplines so that, together, we can ask the most pressing scientific questions and answer them using the most accurate and efficient tools available.

2.0 DESCRIPTION AND ROLE OF BIMETALLIC PRENUCLEATION SPECIES IN THE FORMATION OF SMALL NANOPARTICLE ALLOYS

(Portions of this work were published previously and are reprinted with permission from Marbella, L. E.; Chevrier, D. M.; Tancini, P. D.; Shobayo, O.; Smith, A. M.; Johnston, K. A.; Andolina, C. M.; Zhang, P.; Mpourmpakis, G.; Millstone, J. E. *J. Am. Chem. Soc.*, **2015**, *137*, 15852-15858. Copyright 2015 American Chemical Society.)

2.1 INTRODUCTION

Both the composition and relative position of atoms in bimetallic nanoparticles (NPs) are crucial determinants in the electronic structure of the resulting materials.[149-151] This electronic structure, especially at the particle surface, significantly impacts emergent properties including catalytic behavior,[152] optical signatures,[153,154] and magnetic phenomena.[155] For example, the presence and position of even a single metal atom substitution have been demonstrated to dramatically influence emergent properties such as particle bandgap and plasmonic features.[156-160] These remarkable structure-property relationships drive an intriguing synthetic holy grail: atom-level control of multimetallic nanostructures.

Yet, developing these molecular mechanisms of nanoparticle formation is challenging because the formation of colloidal metal NPs often involves not only chemical change (e.g., metal cation reduction) but also phase change (i.e., particle nucleation). For example, species distinct from both the initial molecular reagents as well as the final NP architecture have recently been observed during the formation of monometallic noble metal NPs[19,161] as well as during the formation of quantum dots.[162] The existence of these "prenucleation species" is intriguing because it suggests NP formation pathways such as multiple-step nucleation or aggregation-induced particle formation. Ultimately, controlling the structure of these species may lead to major advances in the atom-scale control of particle chemistries and create both new routes to and also types of alloys,[91,163] semiconductor compounds,[164] and other nanoparticle solids.

Here, we report the identification and description of bimetallic metal-thiolate prenucleation species in the aqueous synthesis of thiol-capped bimetallic NPs and demonstrate the impact of these precursors on final NP composition and composition architecture. Specifically, we consider the formation of small (diameter, d ~2 nm) Au_xCu_yNP alloys. This metal combination is widely studied in both nanoclusters[151,156,165,166] and larger NPs,[167-169] incorporates both noble and 3d transition metals, and is known to exhibit composition-dependent optoelectronic behaviors.[90,156,159,165] Therefore, characterization of molecular mechanisms in these syntheses has the potential to impact a wide variety of synthetic approaches to multimetallic NP formation as well as to enhance our understanding of fundamental chemical phenomena driving metal mixing behavior across length scales.

2.2 EXPERIMENTAL

2.2.1 Materials and Methods

Hydrogen tetrachloroaurate(III) trihydrate ($HAuCl_4 \cdot 3H_2O$, 99.999%), copper(II) nitrate hemipentahydrate ($Cu(NO_3)_2 \cdot 2.5H_2O$, >99.99%), copper(II) chloride ($CuCl_2$, ≥99%), sodium chloride (NaCl, 99.5%), tetraoctylammonium bromide (TOAB, 98%), O-(2-mercaptoethyl)-O′-methylhexa(ethylene glycol) (OEGSH, ≥95% oligomer purity, CAS: 651042-82-9), hexanes (98%), toluene (99.8%), absolute ethanol, and dodecanethiol (DDT, ≥98%) were purchased from Sigma-Aldrich (St. Louis, MO). Poly(ethylene glycol) methyl ether thiol (PEGSH, average M_n = 1 kDa) was purchased from Laysan Bio, Inc. (Arab, AL). Deuterium oxide (D_2O, 99.9%), toluene-d_8 (99.5%), benzene-d_6 (99.5%), and ethanol-d_6 (99%) were purchased from Cambridge Isotope Laboratories, Inc. (Tewksbury, MA). All reagents were used as received unless otherwise indicated. NANOpure (Thermo Scientific, ≥18.2 MΩ·cm) water was used to prepare all aqueous solutions. Before use, all glassware, including NMR tubes, and Teflon-coated stir bars were washed with aqua regia (3:1 ratio of concentrated HCl and HNO_3 by volume) and rinsed thoroughly with water. *Caution: aqua regia is highly toxic and corrosive and requires proper personal protective equipment. Aqua regia should be handled in a fume hood only.*

2.2.2 Preparation of Mono- and Bimetallic Prenucleation Species

The preparation of prenucleation species is identical to the first steps of mono- and bimetallic nanoparticle syntheses described previously.[90] Briefly, 188 μL total volume of 20.0 mM $HAuCl_4$ and $Cu(NO_3)_2$ at various initial molar ratios (*vide infra*) were added to 4.29 mL of water. While

stirring, 376 μL of 10.0 mM PEGSH solution was added and immediately analyzed by each of the following methods: nuclear magnetic resonance (NMR), X-ray photoelectron spectroscopy (XPS), X-ray absorption spectroscopy (XAS), and matrix-assisted laser desorption ionization-time-of-flight-mass spectrometry (MALDI-TOF-MS).

2.2.3 Aqueous Au_xCu_yNP Syntheses

The one-phase, room temperature aqueous Au_xCu_yNP synthesis has been described previously.[90] Briefly, 188 μL total volume of 20.0 mM $HAuCl_4$ and 20.0 mM $Cu(NO_3)_2$ at various initial molar ratios were added to 4.29 mL of water. Then, 376 μL of 10.0 mM of PEGSH or OEGSH was added while stirring. Immediately after ligand addition, 450 μL of 20.0 mM $NaBH_4$ was injected to produce Au_xCu_yNPs. The NPs were allowed to age for 1 h prior to purification by washing five times in 30 kDa molecular weight cutoff filters (Amicon Ultra centrifugal filter units, EMD Millipore) at 4000 rcf for 15 min.

2.2.4 Two-Phase Au_xCu_yNP Syntheses

Here, Au_xCu_yNPs were synthesized by a modified Brust-Schiffrin synthesis[13] as described by Tong and co-workers.[15] We further modified the procedure to produce bimetallic Au-Cu nanoparticles. First, 700 μL total volume of aqueous 0.1421 M $HAuCl_4$ and 0.1421 M $CuCl_2$ (at various molar ratios) were added to 10 mL of 0.030 M TOAB in toluene while stirring. The two-phase reaction mixture was heated to 80 °C for 30 min to facilitate phase transfer of metal ion precursor species into the organic phase. The toluene phase changed from clear to red or dark orange, depending on the initial molar ratio of Au:Cu. After 30 min, the aqueous layer was

removed, and the reaction mixture containing TOAB and metal salt precursors was allowed to cool to room temperature for an additional 30 min. An aliquot was removed for ICP-MS analysis to determine the total amount of metal transferred to the organic phase.

Once the reaction mixture returned to room temperature, 71.9 μL of neat DDT (density = 0.845 g/mL at 25 °C) was added and stirred for 1 h. The reaction mixture changed from a deep red or dark orange to clear upon addition of DDT (complete color change within 10 s). After 1 h, 1.0 mL of 1.0 M ice-cold, freshly prepared $NaBH_4$ was injected into the rapidly stirring solution and allowed to stir for 4 h before purification.

In order to purify the resulting Au_xCu_yNPs, the organic phase was washed with water (3 × 15 mL). The crude NP product was concentrated by removing the toluene under reduced pressure at 40 °C via rotary evaporation. The crude product was then resuspended in 30 mL of absolute ethanol, sonicated, and placed in the freezer to allow precipitation of the purified DDT-capped nanoparticle product overnight. The precipitate was subsequently washed three times with absolute ethanol and resuspended in hexanes for further analysis.

2.2.5 NMR Spectroscopy

For all solution phase NMR analyses, the one-phase prenucleation species were prepared by combining 400 μL water, 50.0 μL D_2O, 20.0 μL of 20.0 mM $HAuCl_4$:$Cu(NO_3)_2$, 40.0 μL 10.0 mM PEGSH. *N.B.* The ratio $HAuCl_4$:$Cu(NO_3)_2$ is tuned such that the total concentration of metal solution added is 20.0 mM. The precursors present in a two-phase nanoparticle synthesis were investigated by combining 1.0 mL toluene-d_8 with 70.0 μL 0.1421 M metal salt (*vide supra*) in D_2O at the desired initial molar ratio of $HAuCl_4$:$CuCl_2$. After stirring for 30 min at 80°C, the aqueous layer was removed and the toluene-d_8 layer was evaluated with ^{1}H NMR spectroscopy.

To determine whether or not any metal thiolate complexes were formed in the next step of the synthesis, the resulting solutions were also analyzed using ^{1}H NMR spectroscopy techniques after the addition of 7.19 μL of dodecanethiol (0.030 M in toluene).

^{1}H NMR spectra were recorded on a Bruker Avance III 600 MHz spectrometer with a broadband fluorine observe (BBFO) Plus probe. The temperature was calibrated by monitoring the chemical shift of 80% ethylene glycol in DMSO-d_6 and temperature control was maintained at T = 25°C using a Bruker BVT3000 variable temperature system unless otherwise noted. Single pulse ^{1}H spectra were acquired after a π/2 pulse (typical pulse lengths ~10 μs) in order to reference the chemical shift to water at 4.7 ppm prior to water suppression.

^{1}H NMR diffusion spectra were recorded with a stimulated echo bipolar pulsed field gradient sequence with WATERGATE for water suppression.[170,171] The maximum gradient strength of the gradient coil was found to be 0.48 T/m after calibration with "doped water" (1% H_2O in D_2O and 0.1% $CuSO_4$), which has a diffusion coefficient of 1.91 × 10^{-9} m^2/s at 25 °C. The response of the NMR signal integration, I, to variation in gradient strength, g, is described by the Stejskal Tanner equation[172]:

$$\frac{I}{I_0} = exp\left(-g^2\gamma^2\delta^2\left(\Delta - \frac{\tau}{2} - \frac{\delta}{8}\right)\cdot D\right) = exp(-kD) \quad (11)$$

Where I_0 is the integral in the absence of gradients, τ is the time between bipolar gradient pulses, γ is the gyromagnetic ratio of the observe nucleus, δ is the length of the gradient pulse, D is the measured diffusion coefficient, and k represents the grouped experimental parameters. For samples containing the pre-nucleation species, it is evident from 1D ^{1}H NMR and 2D ^{1}H-^{13}C heteronuclear single quantum correlation (HSQC) NMR analyses (*vide infra*) that there is more than one PEG-containing species present in solution. For example, for the methylene units in the ethylene glycol repeat unit of the PEG species, it was necessary to fit the diffusion data for the

precursor solutions to a biexponential decay rather than a single exponential to extract diffusion coefficients. In these cases, the NMR signal integration was fit to the following modified equation to allow for more than one diffusion coefficient to be extracted:

$$\frac{I}{I_0} = Aexp\left(-kD_{fast}\right) + Bexp(-kD_{slow}) \quad (12)$$

Where the prefactors *A* and *B* represent the relative populations contributing to the fast and slow diffusion coefficients.

For ^{1}H diffusion measurements used to estimate the hydrodynamic size of the final nanoparticles, the NMR signal was fit to a single exponential decay. Hydrodynamic diameters were extracted from experimental data using our previously reported method.[91] For OEGSH/PEGSH-capped nanoparticles in aqueous solution, dioxane was used as a reference molecule (R_H = 0.212 nm)[173] while for DDT-capped nanoparticles in benzene-d_6, the residual solvent (R_H = 0.254 nm)[174] was used as a reference molecule of known hydrodynamic size.

For ^{1}H-^{13}C HSQC spectroscopy analyses, the pre-nucleation species were concentrated and prepared in pure D_2O as follows: 200 µL of 200 mM $HAuCl_4$:$Cu(NO_3)_2$ was combined with 400 µL of 100 mM of PEGSH and loaded into a 5 mm NMR tube for analysis. ^{1}H-^{13}C HSQC experiments were performed using ^{1}H-^{13}C INEPT (insensitive nuclei enhanced by polarization transfer) transfer and garp (globally optimized alternating-phase rectangular pulses) ^{1}H decoupling during acquisition. At least 2048 and 128 complex data points were acquired in the direct and indirect dimension, respectively.

2.2.6 MALDI-TOF-MS

A stock solution of 20 mg/mL super DHB (9:1 mixture of 2,5-dihydroxybenzoic acid: 2-hydroxy-5-methoxybenzoic acid) and/or DHB (2,5-dihydroxybenzoic acid) was prepared in 50 mM NaCl, depending on the ligand to be analyzed. The preparation of the pre-nucleation species was scaled down for matrix assisted laser desorption ionization mass spectrometry (MALDI-TOF-MS) analysis. Here, reagents were added in the following order: 429 μL water, 18.8 μL total volume of 20 mM $HAuCl_4$:$Cu(NO_3)_2$, and 37.6 μL of 10 mM PEGSH or OEGSH and quickly vortexed for ~5 seconds. A 10 μL aliquot of the resulting solution was combined with 20 μL of either super DHB or DHB solutions, respectively, and quickly vortexed for ~5 seconds. Two μL of this combined sample and matrix solution were immediately dropcast onto a 100 well MALDI plate and air-dried. MALDI-TOF-MS spectra were recorded using a PerSeptive Biosystems Voyager-DE Pro time-of-flight mass spectrometer with an accelerating voltage of 25,000 V in positive mode. No signals were observed in negative mode.

2.2.7 XPS

Immediately after preparation of prenucleation species, the solutions were flash frozen and lyophilized to remove the solvent. Once dry, the products were resuspended in 20 μL of absolute ethanol and dropcast onto clean (for ultra-high vacuum conditions)[169] 1 cm × 1 cm silicon (*p*-doped (boron)) wafers (University Wafer, Boston, MA). A bulk Cu_2S sample was purchased from Ted Pella, Inc. (Redding, CA) for comparison to samples. X-ray photoelectron spectroscopy (XPS) was performed using an ESCALAB 250XI XPS with a monochromated, micro-focused Al Kα X-ray source (spot size = 400 μm). Survey and high resolution spectra

were collected with a pass energy of 150 eV and 50 eV, respectively. No argon ion sputtering was used prior to sample analysis of pre-nucleation species to minimize ion-induced sample damage. All XPS spectra were charge referenced to the adventitious carbon 1s peak at 284.8 eV.

Dry, purified nanoparticle powders were dropcast from either absolute ethanol (one-phase NPs) or hexane (two-phase BPs) onto clean (for ultra-high vacuum conditions)[169] 1 cm × 1 cm silicon (*p*-doped (boron)) wafers (University Wafer, Boston, MA). X-ray photoelectron spectroscopy (XPS) and Auger electron spectroscopy (AES) was performed using an ESCALAB 250XI XPS with a monochromated, micro-focused Al Kα X-ray source (spot size = 200 μm). Survey and high resolution spectra were collected with a pass energy of 150 eV and 50 eV, respectively. Spectra were collected both with and without Ar ion sputtering (500 eV, 10 seconds) prior to sample analysis. All XPS and AES spectra were charge referenced to the adventitious carbon 1s peak at 284.8 eV.

2.2.8 X-ray Absorption Spectroscopy

Pre-nucleation species measured with X-ray absorption spectroscopy (XAS) at the Au L_3-edge and Cu K-edge were prepared as described above and in the experimental section of the main text. One-phase Au_xCu_yPEGSH nanoparticle precursors were measured in the aqueous phase under ambient conditions. Au_xCu_yPEGSH NPs were measured in the solid-phase under ambient conditions. XAS data for Au_xCu_yPEGSH NPs were collected in transmission mode at the MR-CAT (Sector 10) beamline of the Advanced Photon Source, Argonne National Laboratory (Lemont, IL, USA). Two-phase DDT-capped Au_xCu_yNP samples were measured in the solid-phase at 90 K. XAS data for Au_xCu_yDDT NPs were collected in transmission mode at the

CLS@APS (Sector 20) beamline of the Advanced Photon Source, Argonne National Laboratory (Lemont, IL, USA).

Background subtraction, scan averaging, energy calibration, XANES normalization, and EXAFS fitting were all performed using the WinXAS 3.1 software package. The amplitude reduction factor (S_0^2) was fixed at 0.9 for Au L_3-edge EXAFS fitting and at 0.95 for Cu K-edge EXAFS fitting, which were determined using Au and Cu foil references and fixing the first shell metal-metal scattering coordination number at 12. Theoretical phase and scattering amplitudes for all scattering paths used in EXAFS fitting were simulated using the FEFF8.2 computational package.[175] E_0 shift values were sometimes correlated for EXAFS fitting to reduce the number of varying parameters. A k-range of ~3.0-12 $Å^{-1}$ was used for the Fourier transformation to R-space (i.e., EXAFS spectrum) for Au L_3-edge data and a k-range of 3.0-10.0 $Å^{-1}$ was used for Cu K-edge data. Uncertainties in EXAFS fitting parameters were computed from off-diagonal elements of the correlation matrix and weighted by the square root of the reduced chi-squared value obtained for the simulated fit. The amount of experimental noise from 15-25 Å in R-space was also taken into consideration for each EXAFS spectrum.[176]

2.2.9 Electron Microscopy

An aliquot of the purified NP solution was diluted 1:100 with water for one-phase particles or hexane for two phase particles, prior to drop casting onto thin film (<10 nm) molybdenum 400 mesh carbon grids (Pacific Grid Tech, Inc.). Samples were allowed to air dry followed by drying under vacuum for at least 24 h. Bright field, HRTEM and STEM characterization was performed using a JEOL JEM-2100F equipped with a Gatan GIF-Tridiem or Orius camera and Oxford Inca

EDS detector operating at 200 kV (NanoScale Fabrication and Characterization Facility, Petersen Institute of NanoScience and Engineering, Pittsburgh, PA).

2.2.10 Inductively Coupled Plasma Mass Spectrometry

ICP-MS analysis was performed using an argon flow with a Nexion spectrometer (PerkinElmer, Inc.). An ultrapure aqua regia solution was prepared with a 3:1 ratio of hydrochloric acid (Sigma-Aldrich > 99.999% trace metal basis): nitric acid (Sigma Aldrich, > 99.999% trace metal basis), a portion of which was diluted with NANOpure water for a 5% v/v aqua regia matrix. A small aliquot of the purified nanoparticle samples was digested with ~100 μL of ultrapure, concentrated aqua regia in a 10 mL volumetric flask and diluted to volume with the 5% aqua regia solution. A small aliquot of the reaction mixtures prior to $NaBH_4$ addition was also removed for ICP-MS analysis to measure the initial molar ratio of the synthetic solution. The unknown Au and Cu concentrations were determined by comparison to a 5-point standard calibration curve with a range of 1-30 ppb prepared from a gold standard for ICP (Fluka, TraceCERT 1001 ± 2 mg/L Au in HCl) and a copper standard for ICP (Fluka, TraceCERT 1000 ± 2 mg/L Cu in HNO_3), respectively, and diluted in the 5% aqua regia matrix. The ICP standards were measured 5 times and averaged, while all unknown samples were measured in triplicate and averaged. An 8 minute flush time with 5% aqua regia matrix was used between all runs, and a blank was run before every unknown sample to confirm removal of all residual metals.

2.2.11 Absorption Spectroscopy

UV-vis spectra of the final nanoparticles were collected using a Cary 5000 spectrophotometer (Agilent, Inc.). Baselines were collected using H_2O and hexanes as reference solutions for one-phase PEGSH/OEGSH-capped and two-phase DDT-capped nanoparticles, respectively.

2.3 RESULTS AND DISCUSSION

2.3.1 Prenucleation Species Identification and Characterization

Aqueous Au_xCu_y nanoparticles are synthesized using four reagents: a thiolated capping ligand, the two metal ion precursors, and a reducing agent. At synthetic concentrations, a mixture of the capping ligand and metal ion precursors was evaluated using 1D ^{1}H NMR and ^{1}H diffusion measurements prior to introduction of the reducing agent (Figure 11). Once combined, and in the absence of additional reducing agent, oxidation of the thiol moiety is observed. As may be expected, the extent of thiol oxidation is dependent on both the molar ratio of ligand to metal ion as well as the molar ratio of the two metal ion precursors at constant thiol to total metal ion ratios. Oxidation of the thiol moiety is indicated by the shift of the ^{1}H triplet from the α-CH_2 group (with respect to sulfur, α) from 2.73 to 2.94 ppm (^{1}H adjacent to a disulfide, α').[177] In all ^{1}H diffusion measurements, the peak labeled α' exhibited a single-exponential decay. However, in all precursor solutions, ^{1}H diffusion decay curves for peak β exhibited a biexponential decay, from which two diffusion coefficients could be extracted. One diffusion coefficient corresponds to PEG-disulfide (Figure 11a, open squares), and the other diffusion coefficient corresponds to a

higher molecular weight species (Figure 11a, closed triangles). Calibration with molecular weight standards indicates that the mass of the slowest diffusing species is approximately ~4-5 kDa - too large for a PEG-disulfide species alone and consistent with the formation of metal-thiolate structures (Figure 11).

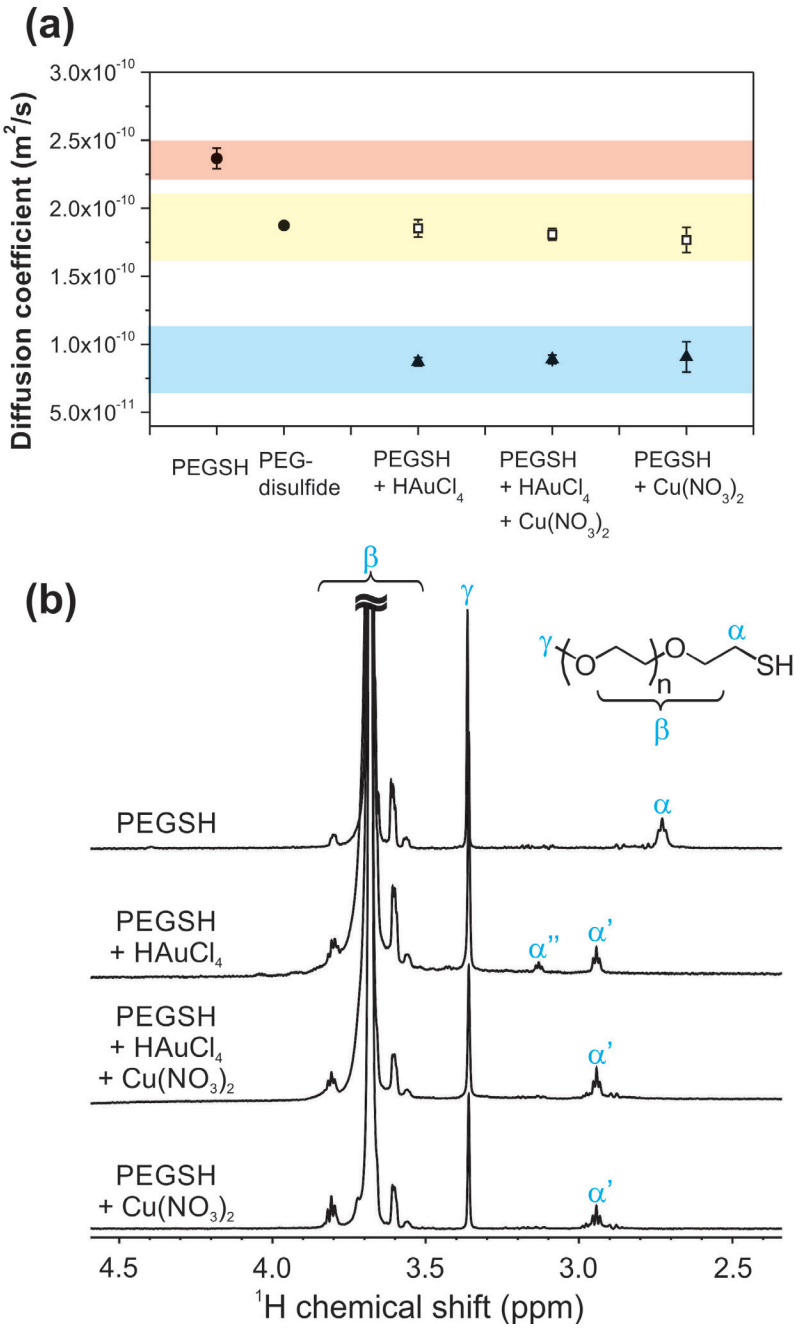

Figure 11. (a) Diffusion coefficient of species from (b) measured by integration of the (O-CH_2-CH_2)$_n$ repeat units of the PEG species, β. (b) ^{1}H NMR spectra recorded at 14.1 T of 0.78 mM PEGSH alone in solution and in the presence of 0.78 mM $HAuCl_4$, $HAuCl_4$:$Cu(NO_3)_2$ 50:50, and $Cu(NO_3)_2$ (the solvent for all solutions is 90% H_2O, 10% D_2O) at 25 °C

Mass spectrometry analysis of the resulting products supports these assignments. In the case of the monometallic 100% $HAuCl_4$ + PEGSH, a high molecular weight species is observed with a center of mass at 5222.76 m/z that corresponds to the Na^+ adduct of Au_4L_4 (Figure 12, L = PEGSH, calculated m/z = 5222.88). As Cu is added to the precursor solution, the peak center of mass shifts to lower m/z values, consistent with the incorporation of a lighter element. These assignments are supported by control experiments using an oligomer analogue of the PEGSH ligand, where peak shifts correspond directly to the replacement of Au with Cu (Δ133.42 m/z, Figures 13).

In all bimetallic syntheses described above, the predominant species present are assigned to a tetranuclear, bimetallic complex. To support this structure assignment, metal atom oxidation state and binding environments were analyzed using XPS and XAS. In all cases, when either metal precursor (Au or Cu) is reduced to the +1 oxidation state, the metal atom is bound to sulfur, consistent with the observations and assignments in MS and NMR. However, we note that for mixed metal solutions both XPS and XAS measurements show that the majority of Cu species remain in the +2 oxidation state after ligand addition (~80-90% remains Cu(II) depending on Au to Cu ratios).

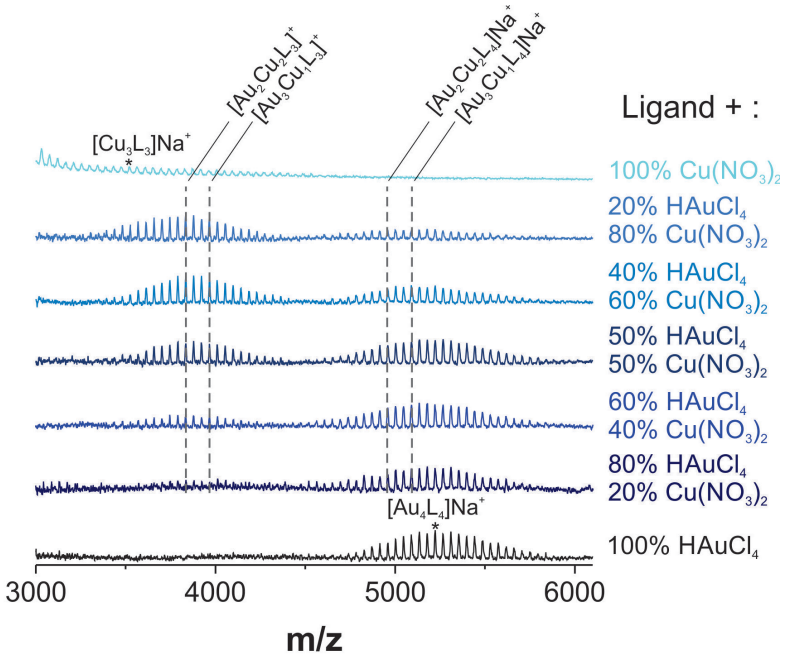

Figure 12. MALDI-TOF-MS of PEGSH in the presence of various molar ratios of $HAuCl_4$:$Cu(NO_3)_2$

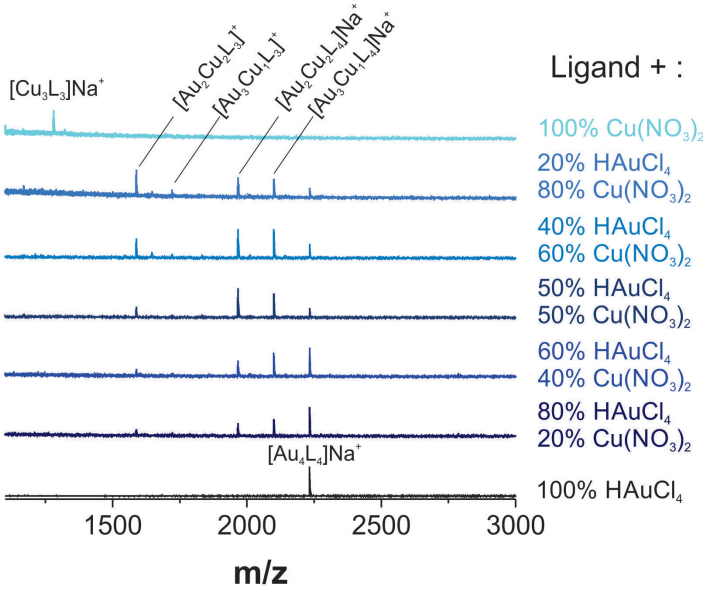

Figure 13. MALDI-TOF-MS of OEGSH in the presence of various molar ratios of $HAuCl_4$:$Cu(NO_3)_2$

The limited reduction of $Cu(NO_3)_2$ impacts the metal atom ratios within the mixed metal-thiolate prenucleation species and is important in the targeted design of these structures (*vide infra*). For example, at initial molar ratios of 4:1 Cu(II):Au(III), the observed metal-thiolate complexes correspond to Au-rich prenucleation species (Figure 12-14). Density functional theory (DFT) simulations help to clarify these observations. When the starting oxidation states of the metals are both +1, a pure Au metal-thiolate complex is the least energetically favorable of the possible complexes, and instead, mixed-metal or Cu-rich species are preferred (Figure 15). In practice, due to the low concentration of Cu(I) in these reactions, we observe a higher population of Au-rich prenucleation structures. However, even at low concentrations of Cu ions, mixed-metal thiolate complexes form at readily observed concentrations, consistent with DFT predictions (Figure 12-14).

Taken together, these results indicate that metal mixing in small NP alloys begins before the nucleation process is initiated. Instead, alloying at this length scale may rely on "premixing" of metals that occurs via formation of multinuclear complexes between metal ion precursors and ligands during the early stages of NP formation. Interestingly, these results are consistent with other examples where mixed metal precursors are crucial to obtain otherwise immiscible metal alloys.[178,179]

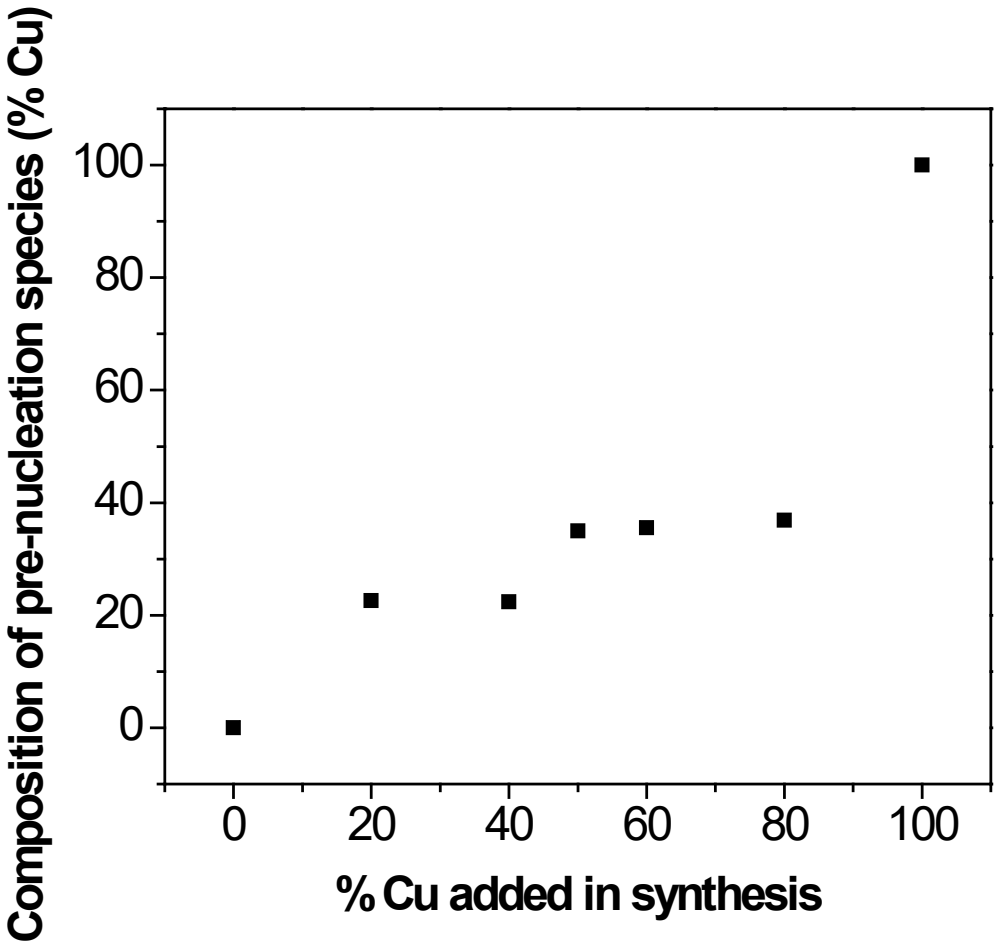

Figure 14. Composition of prenucleation species based on the population of Cu-containing species observed in MALDI-TOF-MS of OEGSH + metal salt precursor as a function of % Cu added in the synthesis

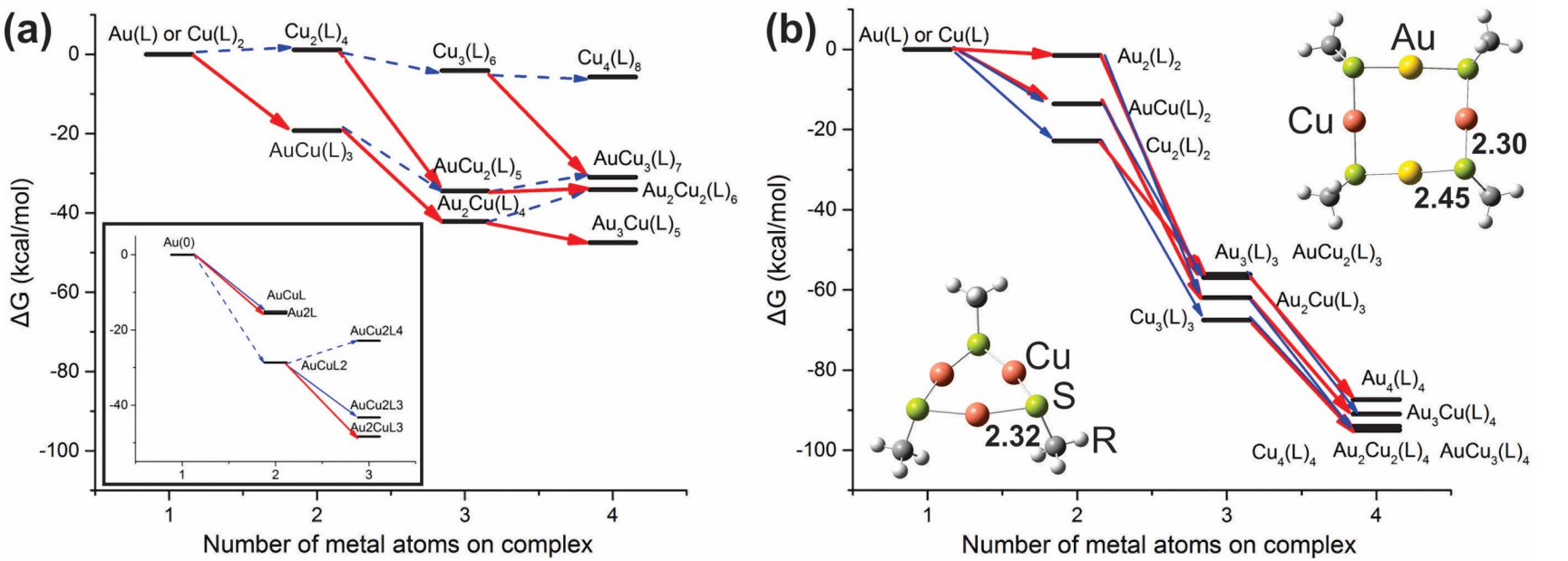

Figure 15. DFT calculated free energy growth pathway of (a) mono-thiolated Au (Au(L)) reacting with double-thiolated Cu ($Cu(L)_2$) and (b) mono-thiolated Au reacting with mono-thiolated Cu (Cu(L)) up to the formation of tetramers. The inset graph on the left shows select reactions of a metallic Au (Au(0)) with Au(L), Cu(L) and $Cu(L)_2$. Red and blue solid arrows represent the addition of a mono-thiolated Au and Cu species, respectively, whereas the dotted blue lines indicate the addition of a double-thiolated Cu species. Negative ΔG values denote exothermicity. Molecular structures on the right show low energy structures of $Cu_3(L)_3$ and $Au_2Cu_2(L)_4$ prenucleation complexes where L = SCH_3. The numbers illustrated in the structures are bond distances in Å

2.3.2 Impact of Prenucleation Species on Final Nanoparticle Composition and Composition Architecture

In order to test the hypothesis that the mixed metal-thiolate structures influence the formation of Au-Cu nanoparticle alloys, we compared the bimetallic nanoparticle products obtained from our one-phase, aqueous synthesis described above to a standard, two-phase Brust-Schiffrin synthesis (2PBSS).[13] This comparison is useful because multiple groups have demonstrated that in the 2PBSS metal-thiolate bonds do not form prior to introduction of reducing agent and subsequent NP nucleation.[15,180,181] Therefore, if the mixed-metal thiolate species we describe are important for alloy formation, one will observe significant differences in the final NP composition architecture (e.g., alloy vs core-shell motifs) depending upon whether a one- or two-phase synthesis is used. (We note that while it is obvious that two different preparations may yield two different products, these syntheses share significant similarity (*vide infra*). By exploiting their fundamental difference - the presence or absence of metal-thiolate prenucleation species, we target the chemical underpinnings of these differences both in the current report and in all Brust-Schiffrin derived syntheses.)

In order to facilitate comparison between our observations and previous work on two-phase syntheses, we compared 1D ^{1}H NMR and ^{1}H diffusion measurements of the prenucleation species present in a traditional 2PBSS in toluene to the prenucleation species observed in an analogous one-phase Brust-Schiffrin synthesis using a 50:50 Au:Cu initial metal ion ratio (Figure 16). In these controls, dodecanethiol rather than PEGSH serves as the capping ligand, and the phase transfer agent, TOAB, is present in both the 2PBSS and “one-phase” analogue in ethanol (to ensure solubility of all reagents).

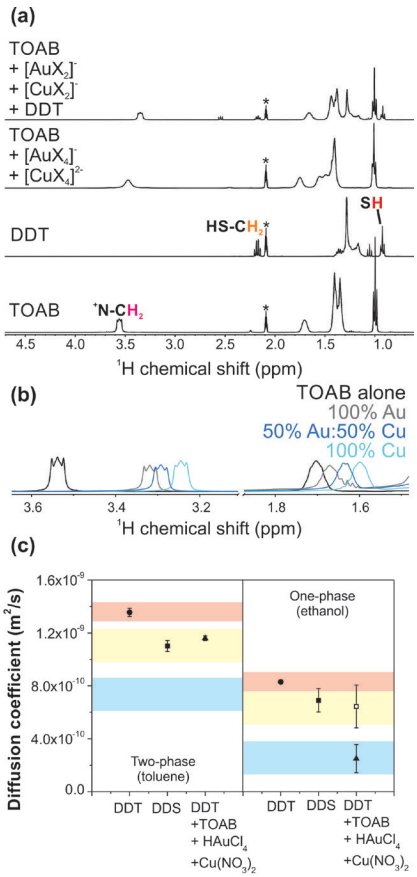

Figure 16. (a) ^{1}H NMR spectra comparison of TOAB, DDT, TOAB + $[AuX_4]^-$ + $[CuX_4]^{2-}$, and TOAB + $[AuX_2]^-$ + $[CuX_2]^-$ + DDT recorded at 14.1 T and 25 °C. Asterisk denotes residual solvent signal. (b) ^{1}H NMR spectra depicting the shift in protons both one (δ = 3.6-3.2 ppm) and two positions (δ = 1.8-1.5 ppm) away from the quaternary ammonium as the counterion on TOA^+ is changed from Br^- (black) to a mixture of Br^- and $[AuX_2]^-$ (gray), a combination of $[AuX_2]^-$ and $[CuX_2]^-$ (blue), or $[CuX_2]^-$ (cyan). (c) The left column shows diffusion coefficients of the species present in a typical two- phase synthesis shown in the top spectra of (a) while the right column depicts the diffusion coefficients present in solution for the same species in deuterated ethanol (one-phase synthesis analogue) obtained via integration of the DDT ^{1}H resonances $(CH_2)_n$, n = 2-10, at δ = 1.3 ppm. *N.B.*: differences observed in diffusion coefficients for the same molecules (e.g., DDT alone) are a result of the difference in solvent viscosities

Consistent with previous reports,[15,180] ^{1}H NMR and diffusion measurements of the 2PBSS prenucleation species revealed that no metal-sulfur bonds were formed prior to $NaBH_4$ addition (Figure 3). Instead, metal halide anions coordinate to the ammonium headgroups on the $[TOA]^+$ inverse micelle as indicated by the chemical shift change of the nearby resonances, indicating fast anion exchange between the metal halide complexes and free halides. Further, in the case of the paramagnetic metal precursor, Cu(II), distance-dependent ^{1}H signal dephasing[57,58] is observed for resonances closest to the quaternary ammonium (Figure 16a). This distance-dependent dephasing is apparent from the broadening of the resonances closest to the quaternary ammonium, whereas the terminal methyl remains narrow, consistent with the formation of an encapsulating, inverse micelle structure.[16]

Upon addition of DDT, the signal dephasing is eliminated in reaction mixtures containing Cu, indicating that the Cu(II) in these micelles has been reduced to diamagnetic Cu(I) (Figure 16a). The increased spectral resolution after the addition of DDT allows anion composition on the micelle interior to be determined. Comparison between three reaction mixtures - 100% Au, 50:50 Au:Cu, and 100% Cu - shows a gradual shift in the ^{1}H resonance adjacent to the quaternary ammonium, suggesting a change in anion composition inside the micelle (Figure 16b). This observation is consistent with micelles that contain both metals but do not form larger metal-thiolate structures like those observed in either one-phase synthesis.

Comparison of the ^{1}H diffusion coefficients of the $(CH_2)_n$ (n = 2-10) ^{1}H resonances on the DDT ligand shows a dramatic difference between one- and two-phase preparations (Figure 16c). No larger thiolate structures are detected in a two-phase toluene synthesis, but in a one-phase analogue, larger thiolates are observed, as they are in the one-phase aqueous synthesis (*vide supra*). Indeed, over the course of the experiment, a white precipitate was observed in the

ethanol reaction mixtures, but not in the toluene mixtures, as would be expected in the formation of metal-thiolate coordination polymers.

2.3.3 Resulting Nanoparticle Composition Architectures are Different between the Two Methods

In the one-phase synthesis, structures consistent with alloyed NPs are obtained. In the two-phase synthesis, XAS and XPS data indicate that metal-segregated NPs are formed. For all preparation methods, final NP size, composition, and composition architecture were characterized by ICP-MS, STEM-EDS point spectra, HRTEM, XAS, XPS, PFG-SE NMR, and Auger electron spectroscopy (AES).

Particle diameters were consistent between one- and two-phase methods, and on average, core diameters were ~1.9 ± 0.2 nm (Figures 17-20). EXAFS comparison of low-Cu content NPs from the one- (14% Cu) and two-phase (12% Cu) syntheses showed differences in the spatial distribution of Cu atoms within the NP depending on synthetic route (Figure 21, Table 1). One-phase AuNPs exhibited a short Au-Au bond length from the relatively small size of the Au core (d = 2.2 ± 0.5 nm) and a high Au-S CN, suggesting dense thiol coverage of the particle surface. Fitting results for one-phase Au_xCu_yNPs show a small amount of Au-Cu bonding from the Au L_3-edge (CN_{Au-Cu} = 0.30) and Cu K-edge (CN_{Cu-Au} = 1) EXAFS. The Au-Cu or Cu-Au bond distances range from 2.73 to 2.8 Å, indicating that Cu and Au are mixed in the nanoparticle core (Figure 22a). The difference in Au-Au CN between AuNPs and Au_xCu_yNPs prepared via the same one-phase method also supports the addition of Cu into the NP core.

Bonding at the surface of the one-phase NPs is also consistent with metal mixing. Au-S and Cu-S bond lengths and Au-S and Cu-S CN values indicate that both elements are present in

the ligand layer. Interestingly, Au-S and Cu-S CN values are higher in the one-phase bimetallic case, as compared to the 100% AuNPs from the same preparation, which indicates possible changes in the metal-ligand binding motif, for example, from the "staple"[182,183] to "mount" motif.[166,184,185]

For the two-phase NPs, XAS analysis indicates metal segregated architectures. Au L_3-edge EXAFS fitting results show a slightly lower Au-Au CN for 100% AuNPs when compared to the Au-Au CN in the 50:50 Au_xCu_yNPs. The two-phase Au_xCu_yNPs show the presence of Cu primarily in the ligand layer, as indicated by the high Cu-S CN and absence of Au-Cu bonding from the Au L_3-edge EXAFS (Figure 22b). A longer Au-S bond of 2.43 Å and higher Au-Au CN indicate that less Au is found in the ligand layer. A small amount of intermetallic bonding could be resolved from the Cu K-edge, but not from the Au L_3-edge, likely due to the low concentration of these bonds and segregation of Au and Cu - consistent with a single interface between Au and Cu in a core-shell motif.

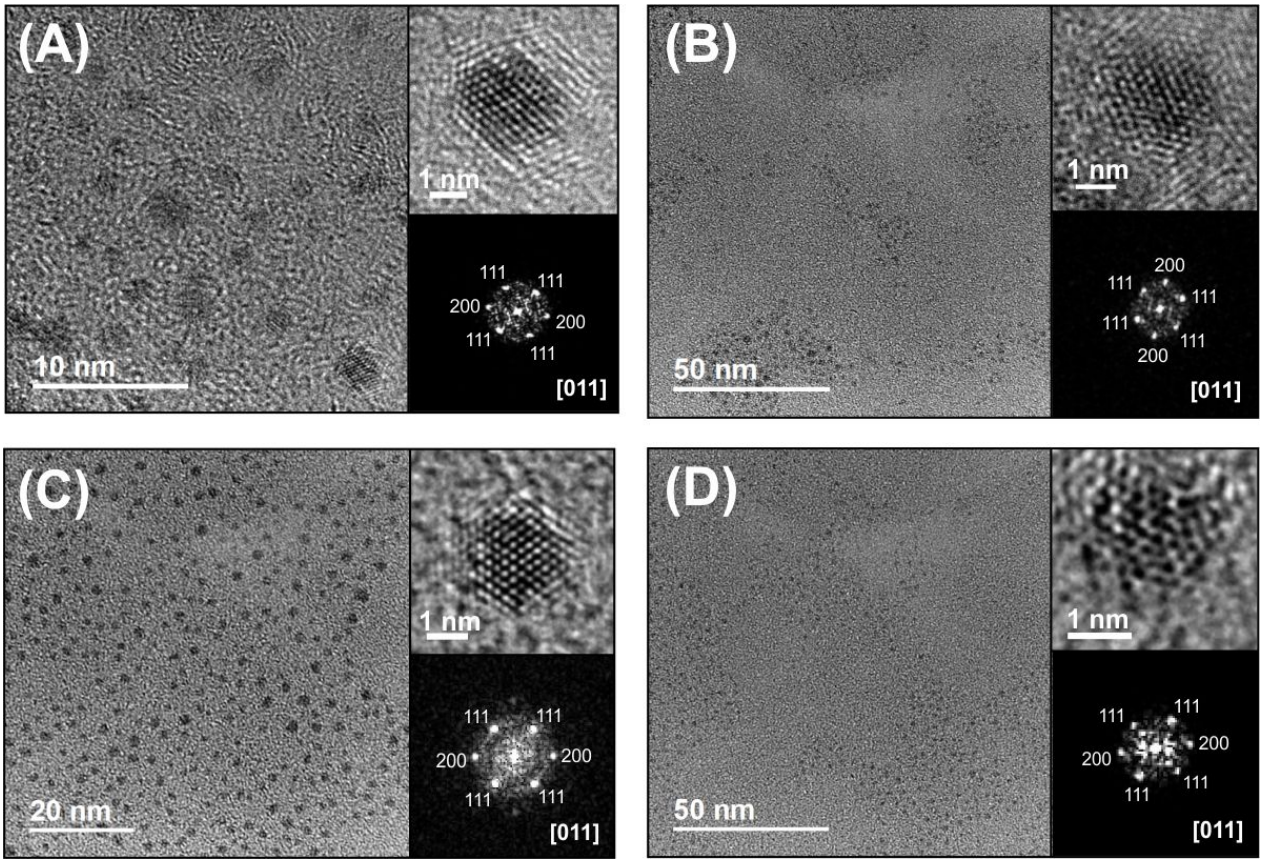

Figure 17. HRTEM micrographs for OEGSH-capped nanoparticles including an extended view, close-up of an individual particle, and the corresponding indexed FFT for (A) AuNPs (B) Au_xCu_yNPs (y = 21% Cu) (C) Au_xCu_yNPs (y = 49% Cu), and (D) Au_xCu_yNPs (y = 82% Cu)

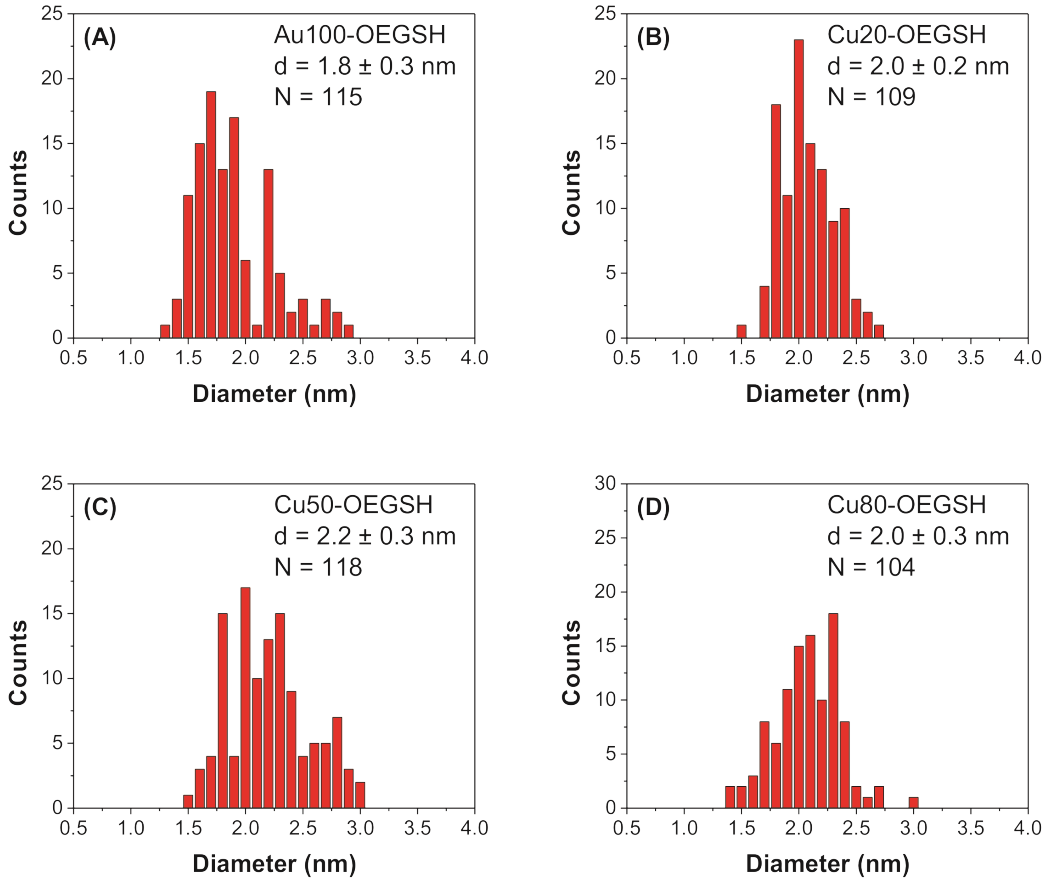

Figure 18. Histograms of one-phase OEGSH-capped nanoparticle size distributions based on HRTEM micrographs for A) Au, B) Au_xCu_yNPs (y = 21% Cu), C) Au_xCu_yNPs (y = 49% Cu), and D) Au_xCu_yNPs (y = 82% Cu). N represents the number of particles used for size determination and *d* represents average diameter ± the standard deviation

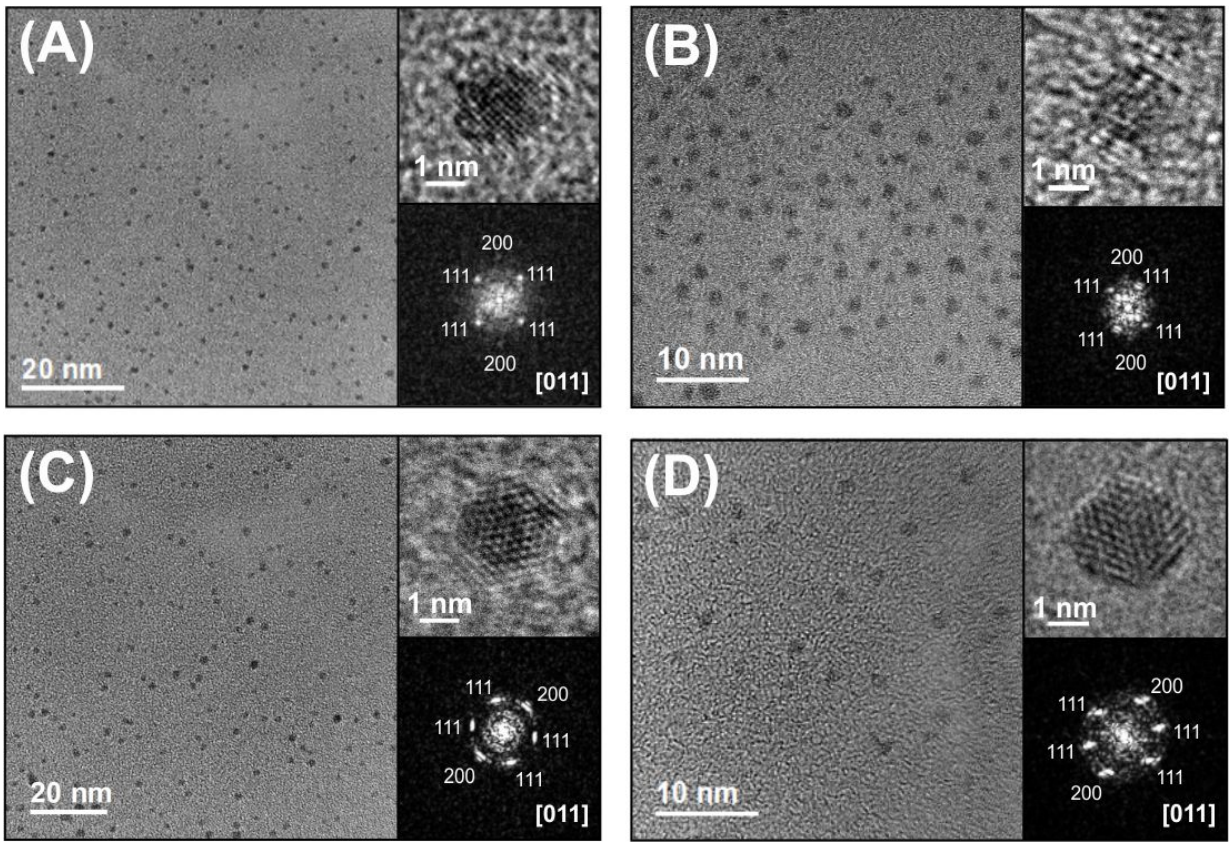

Figure 19. HRTEM micrographs for DDT-capped nanoparticles including an extended view, close-up of an individual particle, and the corresponding indexed FFT for (A) AuNPs (B) Au_xCu_yNPs (y = 12% Cu) (C) Au_xCu_yNPs (y = 24% Cu), and (D) Au_xCu_yNPs (y = 53% Cu). % Cu was measured by ICP-MS

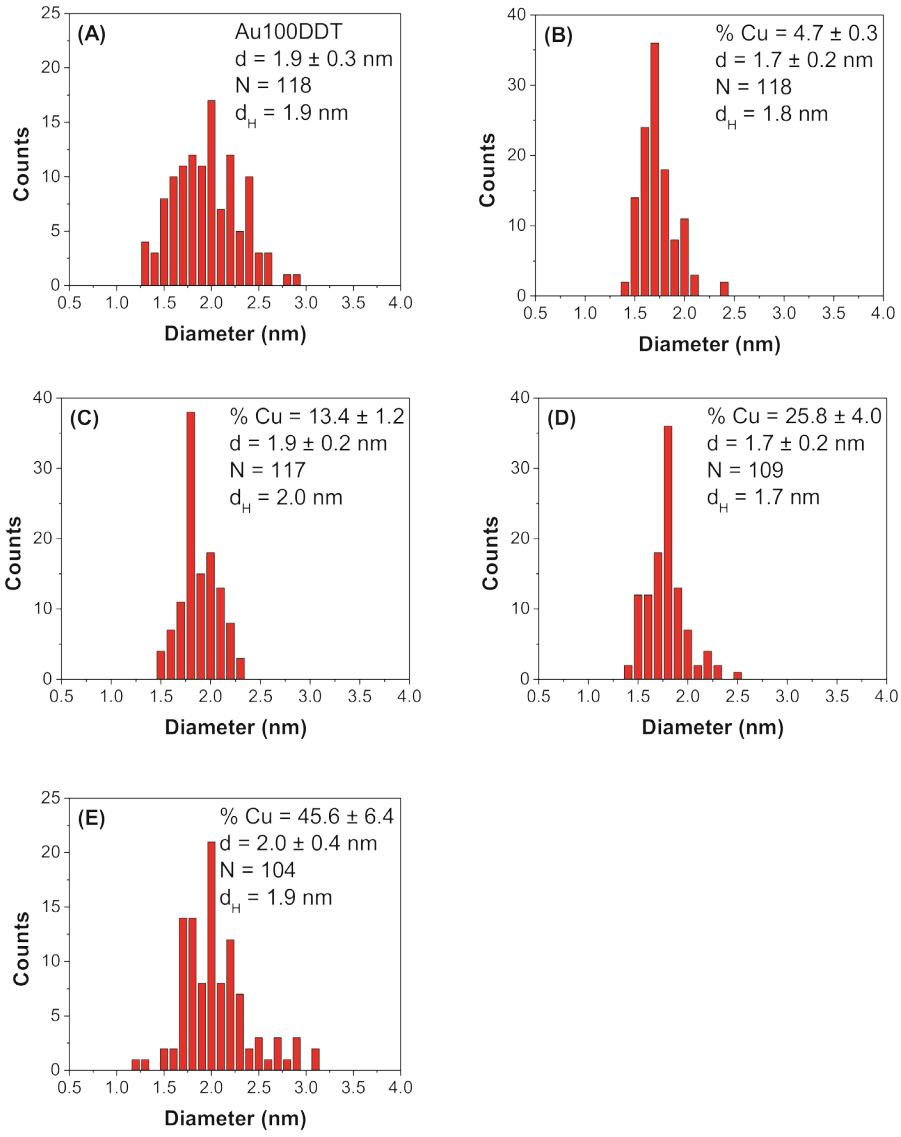

Figure 20. Histograms of two-phase DDT-capped NP size distributions based on HRTEM micrographs for A) 100% Au, B) y = 4.7 ± 0.3 % Cu, C) y = 13.4 ± 1.2 % Cu, D) y = 25.8 ± 4.0 % Cu, and E) y = 45.6 ± 6.4 % Cu. N represents the number of particles used for size determination, *d* represents average diameter ± the standard deviation, and d_H is the hydrodynamic size measured with ^{1}H PFG NMR

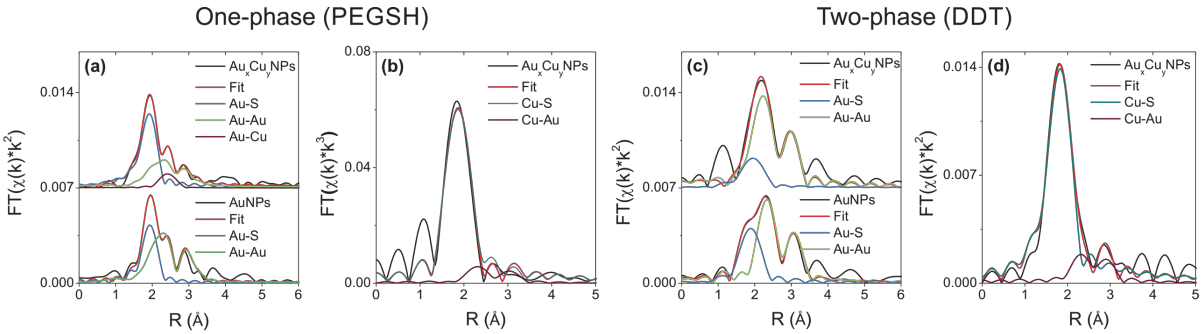

Figure 21. Fitted EXAFS spectra for one-phase Au- and Au_xCu_y-PEGSH NPs at the (a) Au L_3-edge and (b) Cu K-edge. Fitted EXAFS spectra for two-phase Au- and Au_xCu_y-DDT NPs at the (c) Au L_3-edge and (d) Cu K-edge

Table 1. Au L_3-Edge and Cu K-Edge EXAFS Fitting Results for PEGSH- and DDT-Capped NPs

Sample	Path	CN	R (Å)	σ^2 (Å^2)	ΔE_0 (eV)
Au-PEGSH capped NPs	Au-S	0.6(1)	2.323(8)	0.003(1)	-1.5(9)
	Au-Au	7(1)	2.79(1)	0.015(1)	-1.5(9)
Au_xCu_y-PEGSH capped NPs (y = 14%)	Au-S	1.1(1)	2.327(8)	0.0040(6)	-0.7(4)
	Au-Au	3.5(7)	2.75(1)	0.011(3)	-0.7(4)
	Au-Cu	0.3(2)	2.73(2)	0.006(5)	-0.7(4)
	Cu-S	1.6(5)	2.27(3)	0.007(4)	-2(5)
	Cu-Au	1(1)	2.8(1)	0.01(1)	0(2)
Au-DDT capped NPs	Au-S	0.8(1)	2.334(5)	0.001(1)	1.4(7)
	Au-Au	5.8(5)	2.843(5)	0.0063(6)	1.4(7)
Au_xCu_y-DDT capped NPs (y = 12% Cu)	Au-S	0.8(4)	2.43(4)	0.005(4)	-1(2)
	Au-Au	7(3)	2.81(2)	0.007(4)	-1(2)
	Cu-S	2.5(3)	2.26(1)	0.007(1)	0(2)
	Cu-Au	1(1)	2.76(2)	0.007(7)	2(3)

The differences in particle morphology observed in XAS were also observed in high-resolution Cu 2p, Au 4f XPS spectra and Cu $L_3M_{45}M_{45}$ AES analysis as a function of various Au-Cu compositions. In all one-phase Au_xCu_yNPs, a binding energy shift in the Au $4f_{7/2}$ and Cu $2p_{3/2}$ peak is observed as a function of composition (Figures 23 and 24) and is a hallmark of alloying both at the nanoscale and in the bulk.[186] Further, Cu $L_3M_{45}M_{45}$ AES is consistent with the formation of small metal particles[187] and the presence of both elements distributed throughout the particle (Figure 25). The AES and XPS spectra were used to determine the modified Auger parameter for all NP compositions, which ranged from 1851.7 to 1850.0 eV (from 100% Cu to 10% Cu), generally decreasing with increasing Au content, also consistent with Au-Cu alloys.[188] In particular, 100% CuPEGSH-capped NPs exhibited two distinct peaks in the Cu $L_3M_{45}M_{45}$ AES spectra, with one Auger parameter consistent with metallic Cu (1851.7 eV) and one Auger parameter consistent with Cu-S bonds likely from the particle surface (1849.3 eV).

Conversely, XPS and AES analysis of the 2PBSS particles is consistent with metal segregation for all Au-Cu compositions. High-resolution XPS showed little to no binding energy shift for either the Au $4f_{7/2}$ or the Cu $2p_{3/2}$ regions as a function of composition (Figures 24 and 26). Cu $L_3M_{45}M_{45}$ AES peak position (modified Auger parameter is 1848.7 and 1849.6 eV, respectively) and line shape indicate that at both 12 and 24% Cu the majority of Cu is present in the ligand layer as Cu-S (Figure 27) (*N.B.* the modified Auger parameter for a Cu_2S standard was measured at 1849.8 eV and is sensitive to nonstoichiometric phases[189]) Indeed, for a particle of $d \sim 2$ nm and Cu concentrations of 12-21%, it is possible that all Cu atoms are located in the ligand shell.

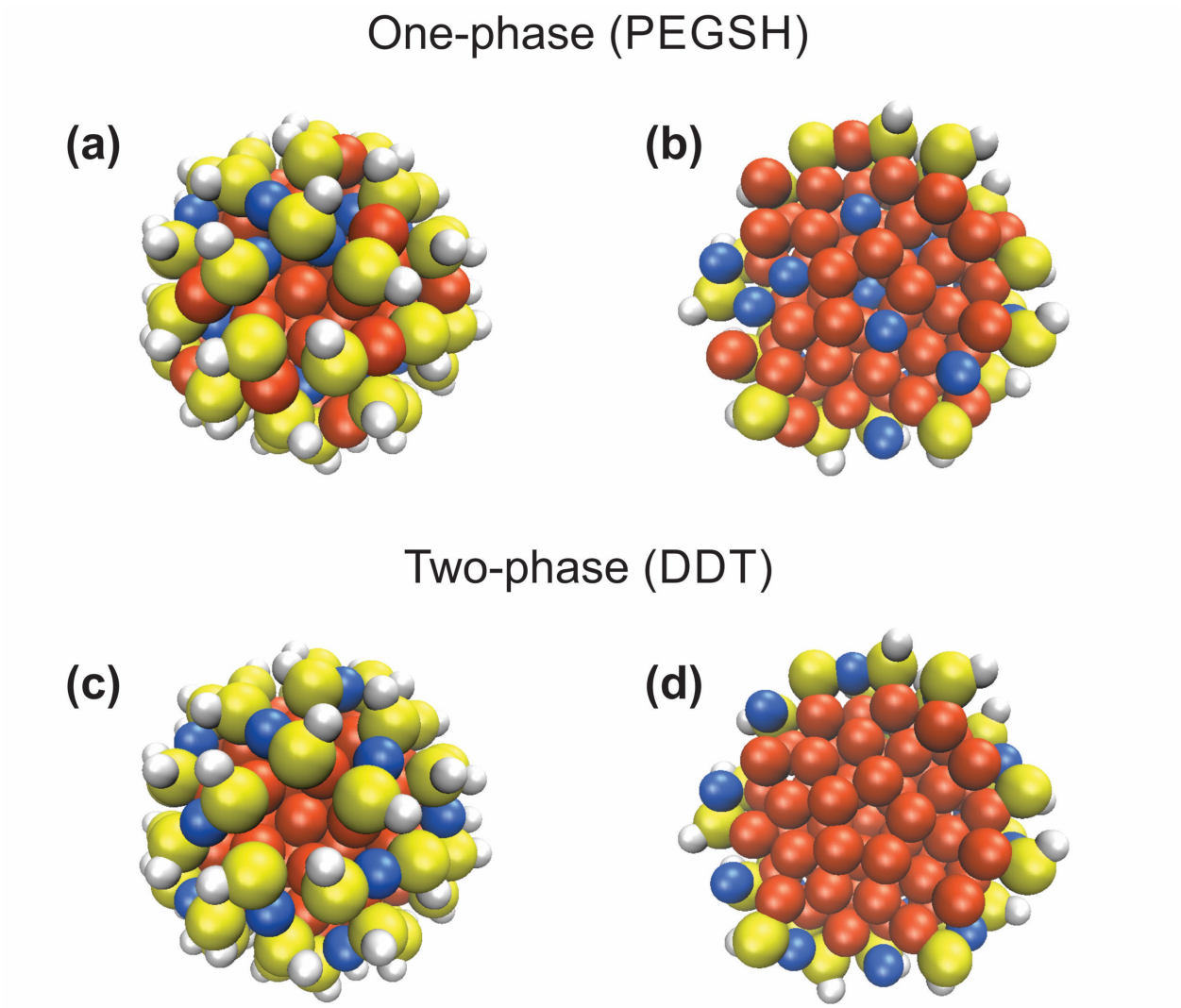

Figure 22. Cartoon of final nanoparticle architectures resulting from one-phase PEGSH (a, b) and two-phase DDT (c, d) syntheses. Full particles (a, c) and corresponding cross sections (b, d) are presented and illustrate differences in the spatial distribution of metal atoms resulting from the two approaches. Orange = Au, blue = Cu, yellow = S, and white = H. The ligands are represented as SH groups only, for clarity

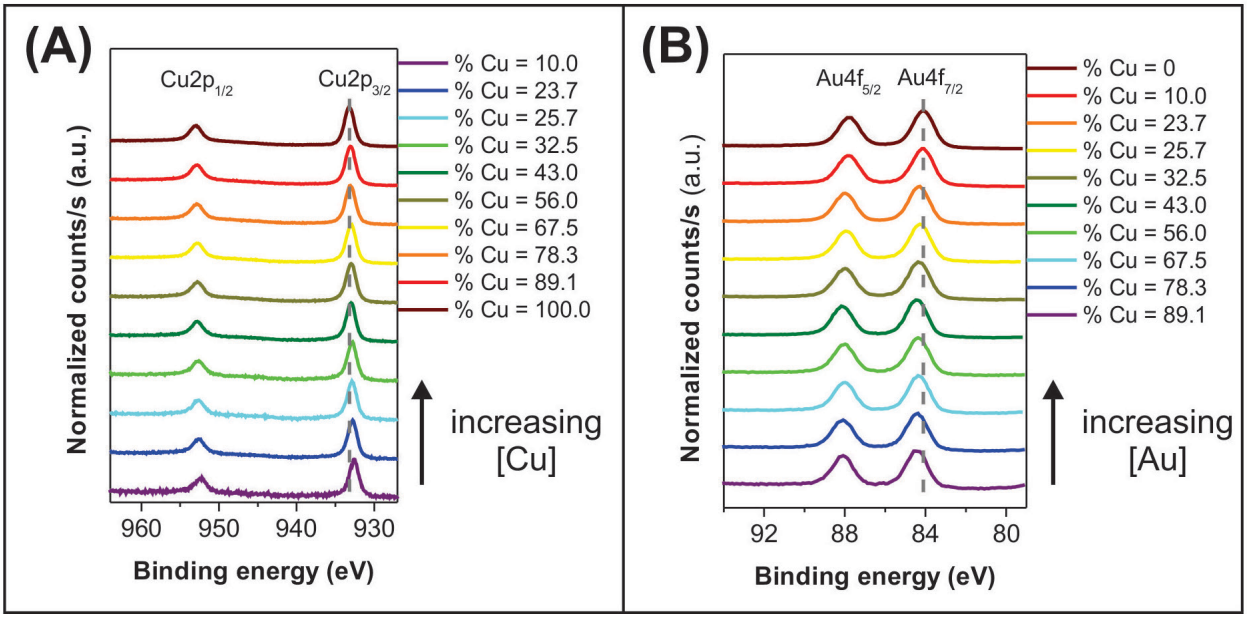

Figure 23. High resolution XPS of Cu2p (A) and Au4f (B) regions for one-phase PEGSH-capped Au_xCu_yNPs with various amounts of Cu from y = 0 to y = 100%. The gray dotted line represents the binding energy of the pure metal nanoparticle

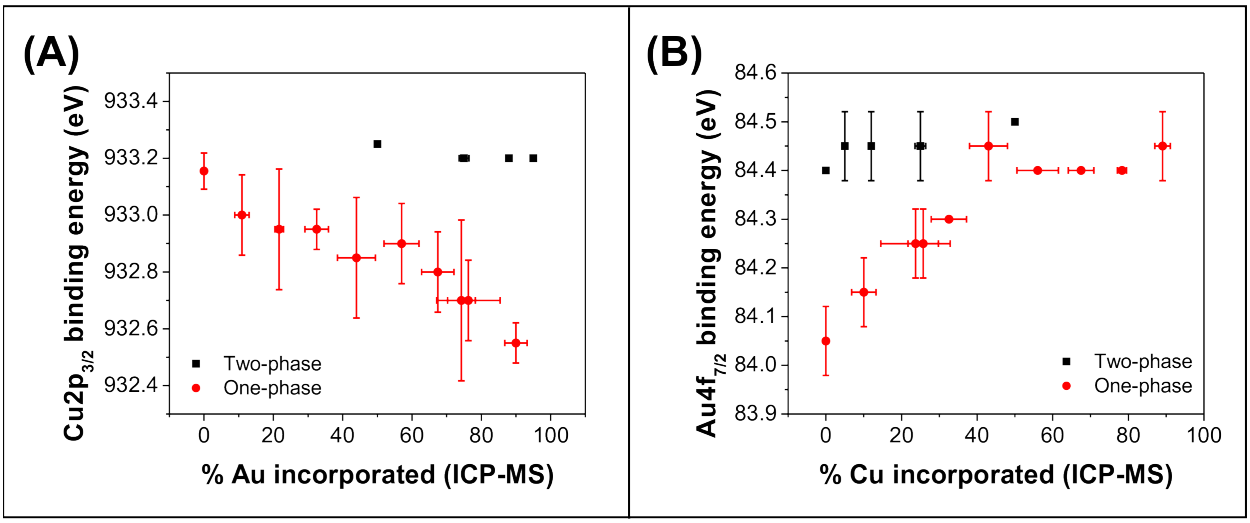

Figure 24. Binding energy of $Cu2p_{3/2}$ (A) and $Au4f_{7/2}$ (B) as a function of % Au and % Cu incorporation in the NP, respectively. Error bars represent the standard deviation of 3 independent trials

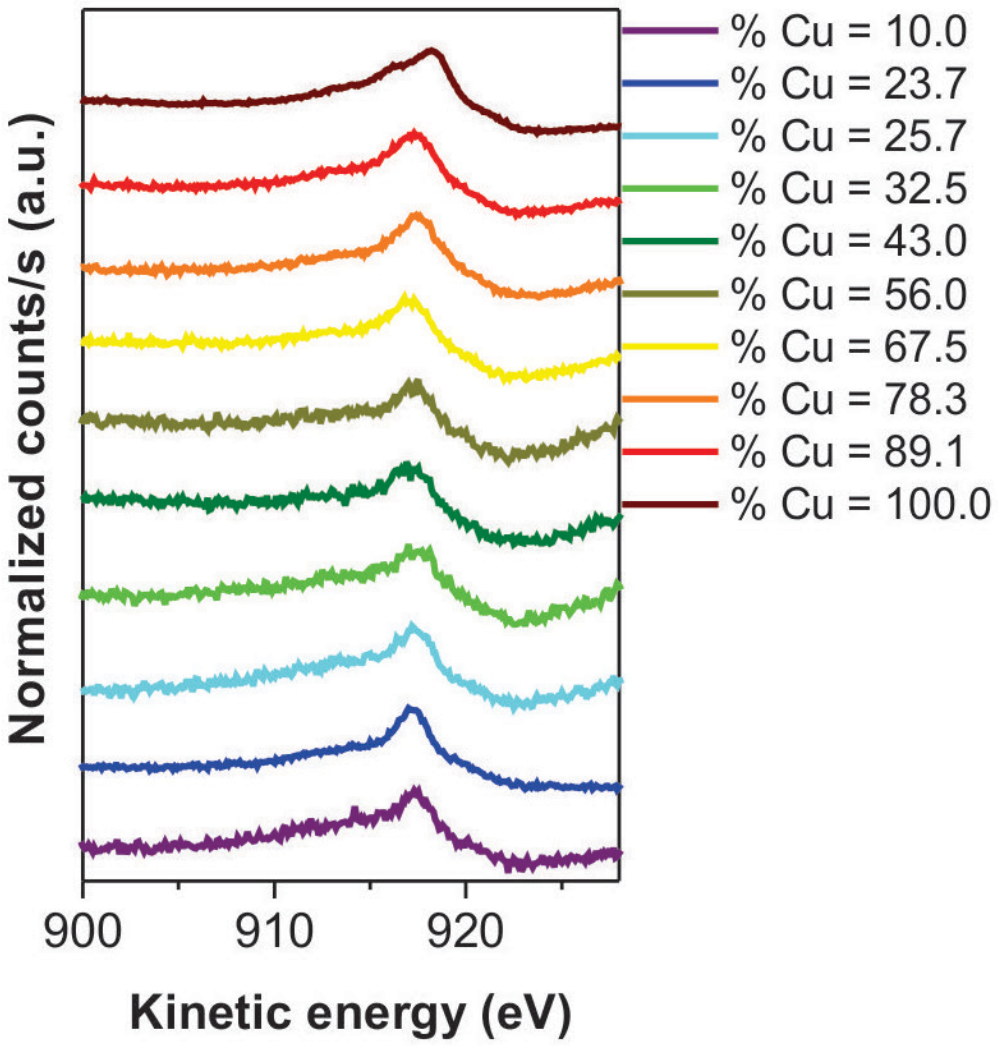

Figure 25. Cu $L_3M_{45}M_{45}$ AES of one-phase PEGSH-capped Au_xCu_yNPs

As expected, when the % Cu is increased, Cu begins to migrate to the particle interior. In the Cu $L_3M_{45}M_{45}$ AES spectra of 42% Cu incorporation for a two-phase particle, two distinct peaks can be observed: one corresponding to Cu-S and one corresponding to metallic Cu (modified Auger parameters of 1849.1 and 1850.7 eV, respectively; Figures 27 and 28).

2.4 CONCLUSIONS

In summary, we report a description of prenucleation species present in both one-phase and two-phase bimetallic NP syntheses. We find that one-phase syntheses form multinuclear metal-thiolate complexes and characterize these species using NMR, MS, XPS, and XAS techniques as well as by first-principles calculations. These mixed-metal prenucleation species are found to play a critical role in obtaining alloyed NPs of Au and Cu. Conversely, in two-phase syntheses, where metal-thiolate prenucleation species are not present, transition metal incorporation is likely dictated by the reduction rate of the original metal cation reagents (and their aqueous speciation products) which ultimately results in the formation of core-shell architectures. Taken together, these data suggest that final atom positions within a NP may be tuned by manipulating the chemical structure of species present in the reaction prior to NP nucleation. Ultimately, these correlations point toward synthetic approaches that may achieve unprecedented control over multimetallic NP architectures.

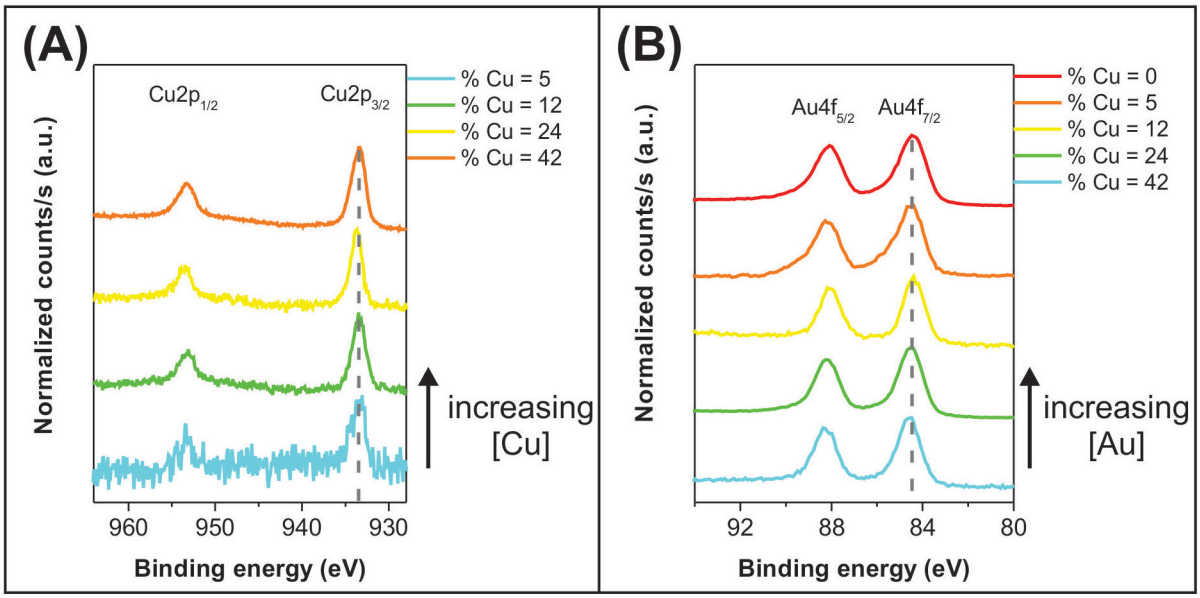

Figure 26. High resolution XPS of Cu2p (A) and Au4f (B) regions for two- phase DDT-capped Au_xCu_yNPs. The gray dotted line represents the binding energy of the highest incorporation composition nanoparticle

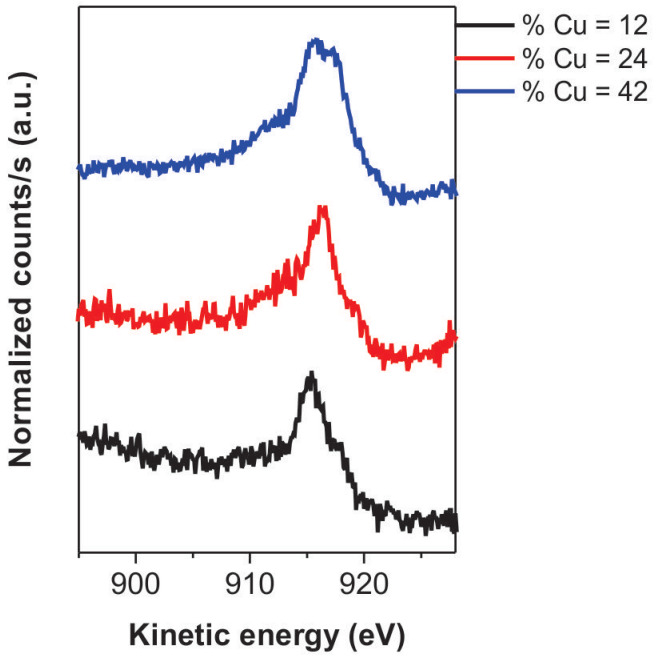

Figure 27. Cu $L_3M_{45}M_{45}$ AES of two-phase DDT-capped Au_xCu_yNPs

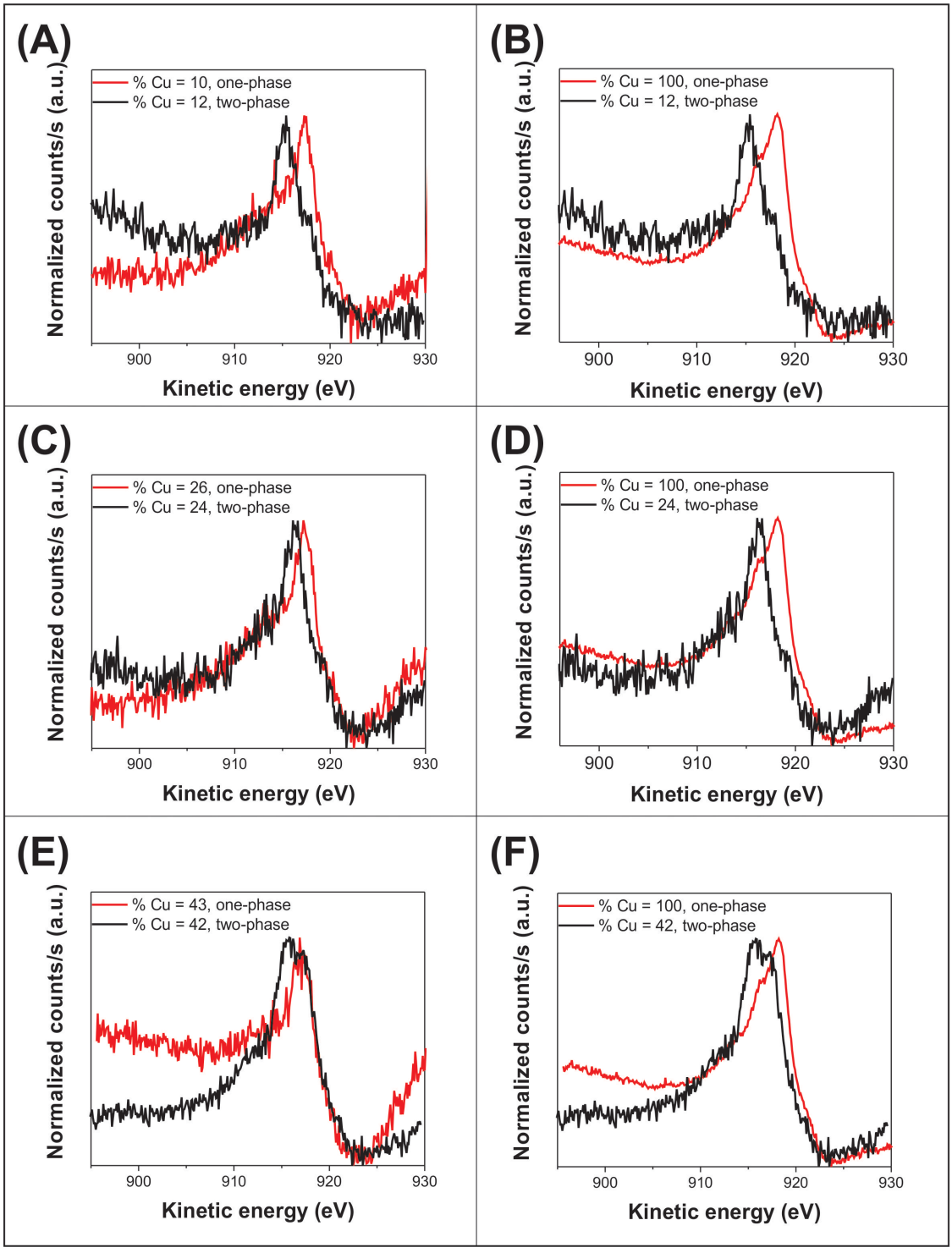

Figure 28. Cu $L_3M_{45}M_{45}$ AES comparison of two-phase (black) Au_xCu_yNPs to (A, C, E) one-phase (red, left column) Au_xCu_yNPs of similar composition as well as comparison to (B, D, F) one-phase (red, right column) 100% CuNPs

3.0 GOLD-COBALT NANOPARTICLE ALLOYS EXHIBITING TUNABLE COMPOSITIONS, NEAR-INFRARED EMISSION, AND HIGH T_2 RELAXIVITY

(Portions of this work were published previously and are reprinted with permission from Marbella, L. E.; Andolina, C. M; Smith, A. M.; Hartmann, M. J.; Dewar, A. C.; Johnston, K. A.; Daly, O. H.; Millstone, J. E. *Adv. Funct. Mater.*, **2014**, *24*, 6532-6539. Copyright 2014 Wiley-VCH Verlag GmbH & Co. KGaA, Weinheim.)

3.1 INTRODUCTION

The now canonical relationship between nanoparticle morphology and nanoparticle physical properties is remarkable and continues to produce an inspiring suite of new materials,[190-194] physical insights,[195-201] and technological capabilities.[202-207] In the case of metallic nanoparticles, the majority of these advances have been made with particles comprised of a single element.[191-194,198-200,202-204,206] Yet, centuries of metallurgy indicate that a vast new dimension of particle properties and applications may emerge with the creation of alloyed nanoparticle colloids.[208-210] Further, in applications with narrow tolerance for particle dimensions and/or surface chemistry (e.g., biologic or catalytic applications)[211-216] accessing a diversity of nanoparticle behaviors from a single composition is challenging. To address this challenge, a variety of multimetallic

nanoparticles have been synthesized including core-shell, hollow, Janus, and alloyed morphologies.[153,217-219]

One attractive class of alloys is the combination of noble metals with more earth-abundant transition metals. These metal mixtures have generated considerable interest for cost reduction and/or performance enhancement of precious metal catalysts[220-223] as well as for stabilization (e.g., from oxidation) of ferromagnetic elements such as Fe and Co in materials for data storage[39] and theranostic applications.[224-226] Optical properties can also be enhanced via alloying.[227] For example, we have reported the composition-tunable near-infrared (NIR) photoluminescence (PL) properties of gold-copper (Au_xCu_y) nanoparticle alloys (diameter, d = 2-3 nm).[90] Combining the optical features of Au with ferromagnetic (in the bulk) elements such as Ni, Co, or Fe is an opportunity to leverage several of these effects within a single particle architecture.

However, bulk phase diagrams indicate that Au is largely immiscible with each of these metals at temperatures below 400 °C.[228-230] In the case of cobalt, the immiscible behavior is dramatic, with no miscibility or intermetallic states predicted below 400 °C across all composition space.[229] Likewise, simulations for surface alloys of Au and Co consistently predict segregation behavior for both Au host-Co solute and Co host-Au solute surfaces.[231,232] Yet, some reports indicate that materials at the nanometer length scale may deviate significantly from these trends. At particle sizes between 95-2590 atoms, Nørskov and co-workers have reported that particle size alone can influence metal segregation behaviors.[233] More recently, Schaak and co-workers have developed a spectrum of preparations for the formation of nanocrystalline alloyed materials, which are analyzed to be representative of $L1_2$ intermetallic states.[234,235] In particular, the authors use metal diffusion at 250 °C to create Au_3Ni, Au_3Fe, and Au_3Co particles with

dimensions ranging from ~10-30 nm. Interestingly, these intermetallics are not predicted by bulk phase diagrams, and instead were one of the first indications that nanoscale colloids may form a greater diversity of alloyed architectures than has previously been observed in the bulk.

Here, we use a combination of rapid metal ion reduction and surface chemistry-based strategies to form small (d = 2-3 nm), discrete, composition-tunable gold-cobalt nanoparticle (Au_xCo_yNP) alloys at room temperature in water. This approach produces Au_xCo_yNPs across a wide range of compositions (0 to 100% Co) and indicates a new pathway to synthesize these previously inaccessible alloys. The resulting particles exhibit composition- tunable magnetic susceptibility as well as some of the highest reported values for T_2 relaxivity as compared to superparamagnetic iron oxide nanoparticles (SPIONs) in a similar size range.[236] At the same time, the particles retain attractive optical features associated with Au at this length scale, specifically, bright NIR emission. Tuning composition, we then identify optimum architectures for bimodal imaging properties, while maintaining particle size and surface chemistry.

3.2 EXPERIMENTAL

3.2.1 Materials and Methods

Hydrogen tetrachloroaurate(III) trihydrate ($HAuCl_4 \cdot 3H_2O$, 99.999%), cobalt(II) nitrate hexahydrate ($Co(NO_3)_2 \cdot 6H_2O$, >99.99%), sodium borohydride ($NaBH_4$, 99.99%), dimethyl sulfoxide (DMSO, > 99.9%), were obtained from Sigma-Aldrich and used as received. Poly(ethylene glycol) methyl ether thiol (average M_n = 1000 Da) was obtained from Laysan Bio, Inc. or Sigma-Aldrich and used as received. Deuterium oxide (D_2O) and DMSO-d_6 were

purchased from Cambridge Isotope Laboratories, Inc. and used as received. NANOpure (Thermo Scientific, >18.2 MΩ·cm) water was used to prepare all solutions unless otherwise indicated. Before use, all glassware and Teflon coated stir bars were washed with aqua regia (3:1 ratio of concentrated HCl and HNO_3 by volume) and rinsed thoroughly with water. *Caution: Aqua regia is highly toxic and corrosive and requires proper personal protective equipment. Aqua regia should be handled in a fume hood only.*

3.2.2 Synthesis of Au_xCo_yNPs

Au_xCo_yNP alloys were synthesized by co-reduction of $HAuCl_4$ and $Co(NO_3)_2$ with $NaBH_4$ at room temperature in an aqueous solution containing the capping ligand, poly(ethylene glycol) methyl ether thiol (PEGSH, average M_n = 1000 Da). Reagents were added to a glass vial, while stirring, in the following order: water (4.29 mL), $HAuCl_4$ (188-X µL, 20.0 mM), $Co(NO_3)_2$ (X mL, 20.0 mM), PEGSH (375 µL of 10.0 mM), and $NaBH_4$ (450 µL of 20.0 mM). The total concentration of metal cations was held constant while the molar ratio of Au and Co was varied. The initial molar ratio of Co to Au was varied from 0-100%, while maintaining the same total metal, capping ligand, and reducing agent concentrations.

3.2.3 Nanoparticle Purification

The entire contents of the NP synthesis were transferred to Amicon Ultra – 4 Ultracel 10 kDa molecular weight cutoff centrifugal filters (Merck Millipore Ltd.). Samples were purified from excess PEGSH and metal salts using an Eppendorf 5804 or 5804R centrifuge with swing bucket rotor (A-44-4) (Eppendorf, Inc.) with a force of 4000 rcf at 20 °C for 12-15 min. The resulting

concentrated particles (typically ~50 μL in water) were diluted in the concentrator tube to a volume of 3 mL with water. The loose pellet was resuspended by gentle mixing using a pipette prior to re-centrifugation. This washing procedure was repeated 5 times. Purified Au_xCo_yNPs were then characterized by electron microscopy techniques, UV-visible spectroscopy, ICP-MS, XPS, photoluminescence, and ^{1}H NMR techniques.

3.2.4 Electron Microscopy

Samples were prepared for electron microscopy by drop casting an aliquot of purified NP solution (diluted 1:10 or 1:100 with water) onto ultra-thin (3-5 nm) carbon type A 400 mesh copper grids (Ted Pella, Inc.). Samples were allowed to slowly air dry for at least 10 h followed by drying under vacuum. Bright field, HRTEM and STEM characterization was performed using a JEOL JEM 2100F equipped with a Gatan GIF-Tridiem camera and Oxford Inca EDS detector operating at 200 kV (NanoScale Fabrication and Characterization Facility, Petersen Institute of NanoScience and Engineering, Pittsburgh, PA).

3.2.5 Size Determination by NMR

Pulsed field gradient stimulated echo (PFGSE) ^{1}H NMR measurements were performed on a Bruker 500 Ultrashield magnet with an Avance III 500 Console or a Bruker 600 Ultrashield magnet with an Avance III 600 Console (Bruker Biospin, Billerica, MA) at 298 K. Au_xCo_yNPs NMR samples were lyophilized, resuspended in DMSO-d_6, and loaded in a 5 mm NMR tube for measurement. ^{1}H NMR diffusion spectra were acquired on a broadband fluorine observe probe using a stimulated echo bipolar pulsed field gradient pulse sequence.

3.2.6 XPS

XPS was performed using a Thermo Scientific K-Alpha with monochromatic Al Kα X-rays (RJ Lee Group, Inc., Monroeville, PA). Survey and high resolution spectra were collected with a pass energy of 200 eV and 50 eV, respectively. Lyophilized NPs were resuspended in absolute ethanol and drop cast onto silicon wafers (University Wafer, Boston, MA). Prior to XPS collection, samples were sputtered for 30 seconds with an argon ion gun. All XPS spectra were measured with a 400 μm X-ray spot size. High resolution XPS spectra were charge referenced to the adventitious hydrocarbon C1s peak at 284.8 eV.

3.2.7 ICP-MS

ICP-MS analysis was performed using an Argon flow with a Nexion spectrometer (PerkinElmer, Inc.). An ultrapure aqua regia solution was prepared with a 3:1 ratio of hydrochloric acid (Sigma Aldrich > 99.999% trace metal basis): nitric acid (Sigma Aldrich, > 99.999% trace metal basis), a portion of which was diluted with NANOpure water for a 5% v/v aqua regia matrix. An aliquot of the purified nanoparticle samples was digested with ≈100 μL of ultrapure, concentrated aqua regia in a 10 mL volumetric flask, and diluted to volume with the 5% aqua regia solution. The unknown Au and Co concentrations were determined by comparison to a 5-point standard calibration curve with a range of 1-30 ppb prepared from a gold standard for ICP (Fluka, TraceCERT 1001 ± 2 mg/L Au in HCl) and a cobalt standard for ICP (Fluka, TraceCERT 1000 ± 2 mg/L Co in HNO_3), respectively, and diluted in the 5% aqua regia matrix. The ICP standards were measured 5 times and averaged, while all unknown samples were measured in triplicate and

averaged. An 8 minute flush time with 5% aqua regia matrix was used between all runs, and a blank was run before every unknown sample to confirm removal of all residual metals.

3.2.8 Magnetic Susceptibility Measurements

Mass magnetic susceptibility for NPs were recorded on a Bruker 600 Ultrashield magnet (14.1 T) with an Avance III 600 Console or a Bruker 700 Ultrashield magnet (16.4 T) with an Avance III 700 Console (Bruker Biospin, Billerica, MA) equipped with a BVT3000 and BCU05 variable temperature unit, respectively. ^{1}H NMR spectra were collected at 298 K using the Evans' method.[140] Au_xCo_yNPs were synthesized, purified and the concentrated NP pellet was lyophilized. The mass of the dried NPs was recorded and resuspended in 1 mL of D_2O and loaded into a 5 mm NMR tube along with an internal sealed capillary tube of pure D_2O. A 1D ^{1}H NMR spectrum of each sample was recorded with 16 transients. ^{1}H NMR chemical shifts were referenced to the HDO peak from the capillary at 4.7 ppm. Typical 90° radiofrequency pulses were ~9 μs for ^{1}H NMR spectra, and were processed using Bruker Topspin 3.0 and iNMR. The distance in Hz between the residual HDO peak of the pure D_2O and the HDO peak of the D_2O containing the Au_xCo_y colloidal suspension (experimental ^{1}H NMR spectra shown in Figure 29) was measured and used to calculate the magnetic susceptibility (see Chapter 1, Section 1.4.1 for calculation details).

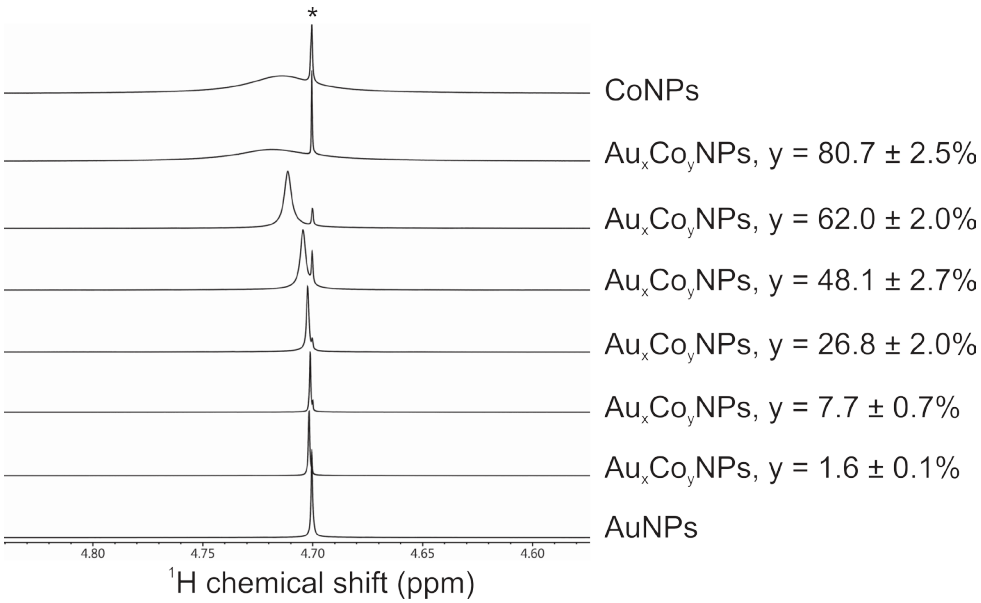

Figure 29. Stack plot of ^{1}H NMR spectra from Au_xCo_yNPs recorded for the Evans method. The asterisk represents the HDO ^{1}H NMR peak from pure D_2O in the capillary tube. As % Co increases, the distance between the HDO peaks from solvent inside the capillary vs. solvent inside the colloidal suspension increases. The HDO peak from the colloid also experiences dephasing as % Co increases as a result of T_2 relaxation enhancement line-broadening: fwhm = $(\pi T_2)^{-1}$

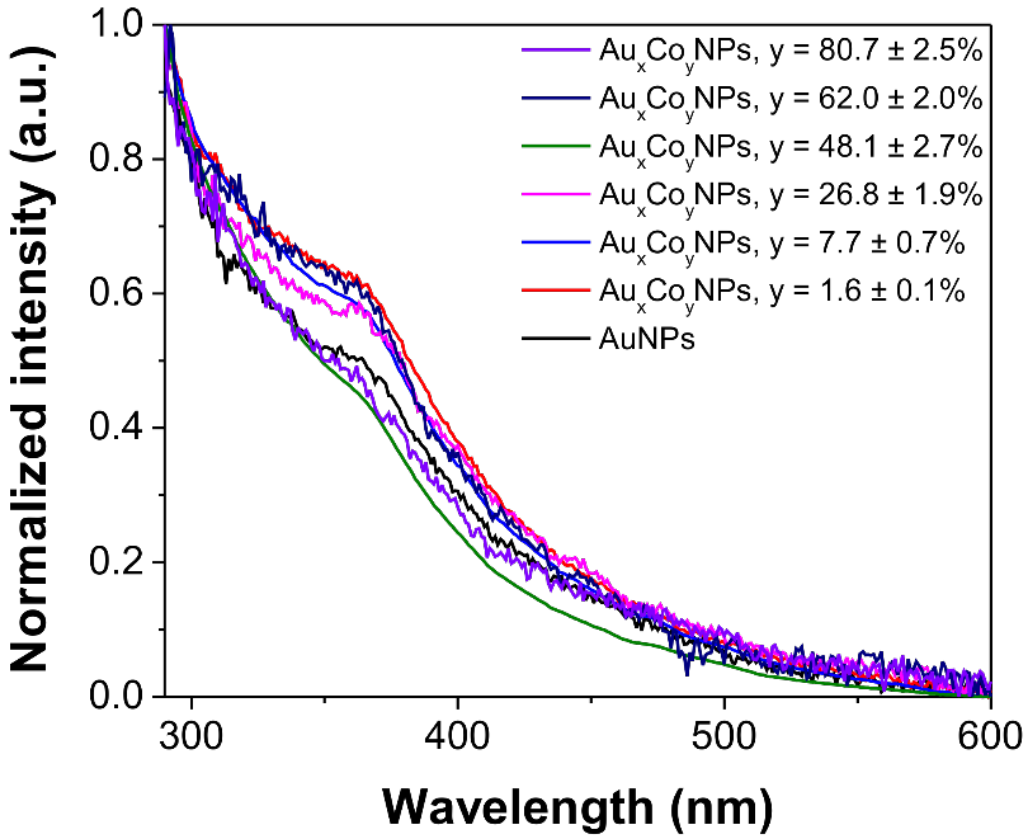

Figure 30. Normalized excitation spectra of Au_xCo_yNPs in water at 25 °C, λ_{EM} = 950 ± 40 nm

3.2.9 Absorption Spectroscopy: Molar Extinction Coefficient

Nanoparticle extinction coefficients were calculated using the UV-vis-NIR spectrum of the NPs after purification. Spectra were taken using a Cary 5000 UV-vis-NIR (Agilent, Inc.). UV-vis measurements were collected of nanoparticle suspensions diluted in D_2O using 1.0 cm quartz cuvettes (Hellma, Inc.).

3.2.10 Photoluminescence: Quantum Yield and Brightness

NP suspensions in D_2O were prepared from the purified Au_xCo_yNP stocks at concentrations ≤ 0.25 abs at 340 nm determined by UV-Vis. Emission spectra were acquired on a HORIBA Jobin Yvon IBH FluoroLog-322 spectrofluorometer equipped with a Hamamatsu R928 detector for the visible domain; DSS-IGA020L (Electro-Optical Systems, Inc.) detector for the NIR domain and a temperature controller using 1.0 cm × 0.4 cm quartz cuvettes (Hellma, Inc). A 780 nm NIR cut-on filter (Newport FSQ-RG780, Newport Corporation, Inc.) was used to block the excitation source. The quantum yields in the NIR region were determined by the optically dilute method. Excitation spectra of the purified Au_xCo_yNPs were collected using an emission slit of 20 nm centered at 950 nm with an excitation slit of 5 nm. Spectra were collected in 1 nm increments using an integration time of 0.4 s from 290-600 nm and the NIR cut-on (780 nm) filter was used to filter the emission (Figure 30). Excitation spectra have been corrected for lamp power fluctuations and the instrument response.

3.2.11 Relaxivity Measurements

Longitudinal (T_1) and transverse (T_2) relaxation time measurements were collected for five dilutions of each sample at 37 °C using an inversion recovery pulse sequence and the Carr-Purcell-Meiboom-Gill (CPMG) spin echo pulse sequence, respectively. Relaxation measurements were collected at both 20 MHz (0.47 T) on a Bruker mq20 minispec NMR analyzer and 300 MHz (7 T) on a Bruker DRX 300 MHz magnet. In order to minimize radiation damping effects at 7 T, the NPs were suspended in 50/50 H_2O/D_2O and the probe was de-tuned prior to measurement. All relaxivity measurements were performed in triplicate (three independent syntheses of each composition), with ICP-MS analysis of each sample for exact metal concentration.

3.3 RESULTS AND DISCUSSION

In a typical experiment, Au_xCo_yNP alloys were synthesized by co-reduction of $HAuCl_4$ and $Co(NO_3)_2$ with $NaBH_4$ at room temperature in an aqueous solution containing the capping ligand, poly(ethylene glycol) methyl ether thiol (PEGSH, average M_n = 1000 Da). $NaBH_4$ is an attractive reducing agent because it is water soluble, can reduce both metal precursors,[13,237] and in pure metal nanoparticle syntheses (e.g. Au and Ag), the oxidized byproducts are not known to influence the reaction. We choose a thiolated ligand, because they are associated with the synthesis of small, stable Au nanoparticles.[13] A PEG moiety is chosen for water solubility and biocompatibility. The initial molar ratio of Co to Au was varied from 0-100% Co, while maintaining the same total metal, capping ligand, and reducing agent concentrations. All

nanoparticle products were characterized using UV-visible spectroscopy, inductively coupled plasma mass spectrometry (ICP-MS), X-ray photoelectron spectroscopy (XPS), photoluminescence spectroscopy, transmission electron microscopy (TEM), and ^{1}H nuclear magnetic resonance (NMR) techniques. Figures of merit from these studies are listed in Table 2. Figure 31 shows high-resolution transmission electron microscopy (HRTEM) images of Au_xCo_yNPs (x = 100% - y; y = 26.8 ± 2.0% Co as measured by ICP-MS; see Figure 33 for HRTEM of additional Au_xCo_yNP compositions). In all cases, Au_xCo_yNPs are observed as pseudospherical, discrete, and crystalline nanoparticles with average metallic core diameters between 2.1-2.3 nm and a standard deviation of <20% (Figure 31-34). The hydrodynamic diameter of the Au_xCo_yNPs was calculated from the diffusion coefficient as measured by pulsed-field gradient stimulated echo (PFGSE) ^{1}H NMR. The hydrodynamic diameters of all Au_xCo_yNPs are 4.1-4.3 nm, consistent with a 2.1-2.3 nm metallic core diameter capped with a monolayer of random coil PEGSH (M_n = 1000 Da).

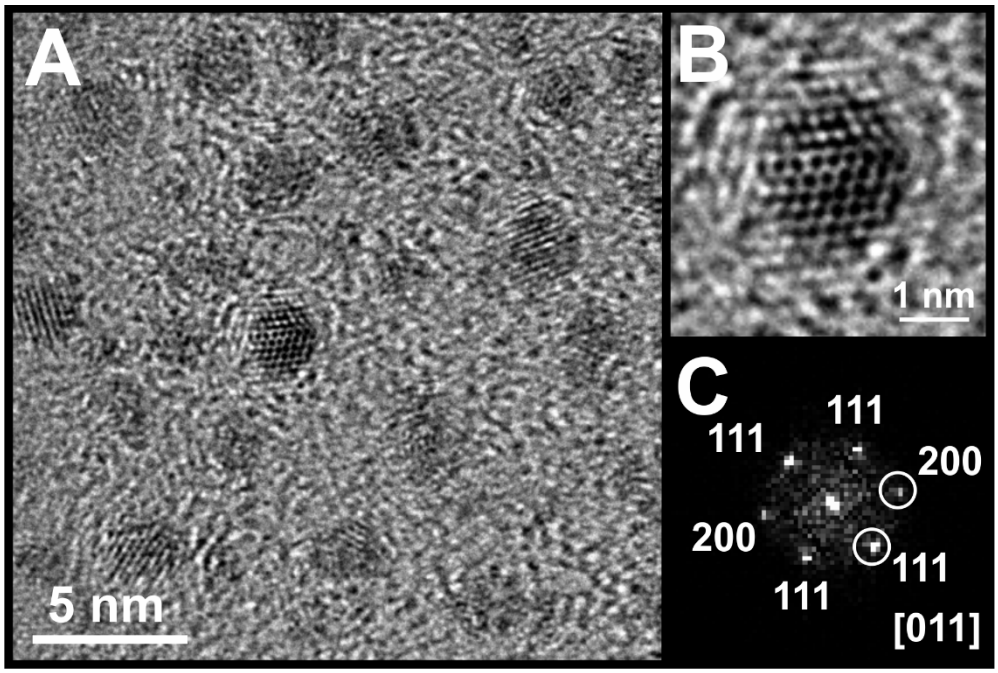

Figure 31. A) HRTEM image of Au_xCo_yNPs (y = 26.8 ± 2.0%). B) Magnified image of an individual Au_xCo_yNP and C) the corresponding FFT

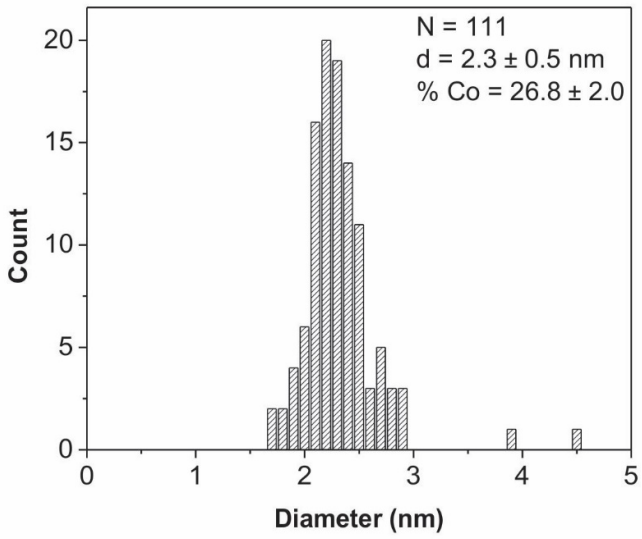

Figure 32. Histograms of Au_xCo_yNPs size distributions based on HRTEM micrographs for y = 26.8 ± 2.0%. N represents the number of particles used for size determination; *d* represents average diameter ± the standard deviation of the average

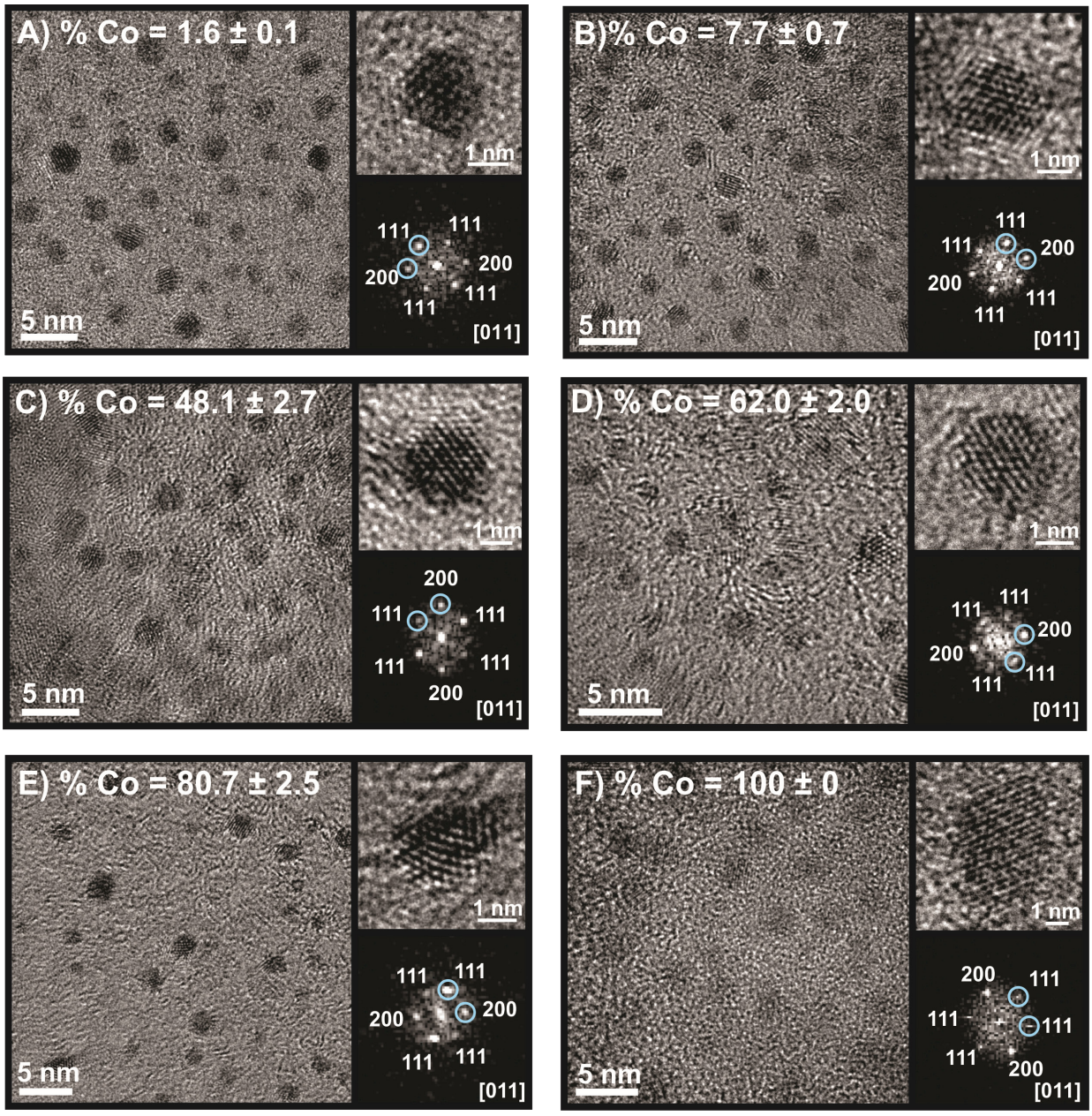

Figure 33. HRTEM micrographs for the following Au_xCo_yNP alloy compositions A) y = 1.6 ± 0.1%, B) y = 7.7 ± 0.7%, C) y = 48.1 ± 2.7%, D) y = 62.0 ± 2.0%, E) y = 80.7 ± 2.5%, and F) y = 100 ± 0%, including a wideview, close-up of an individual particle, and the corresponding indexed FFT used to determine average lattice constant

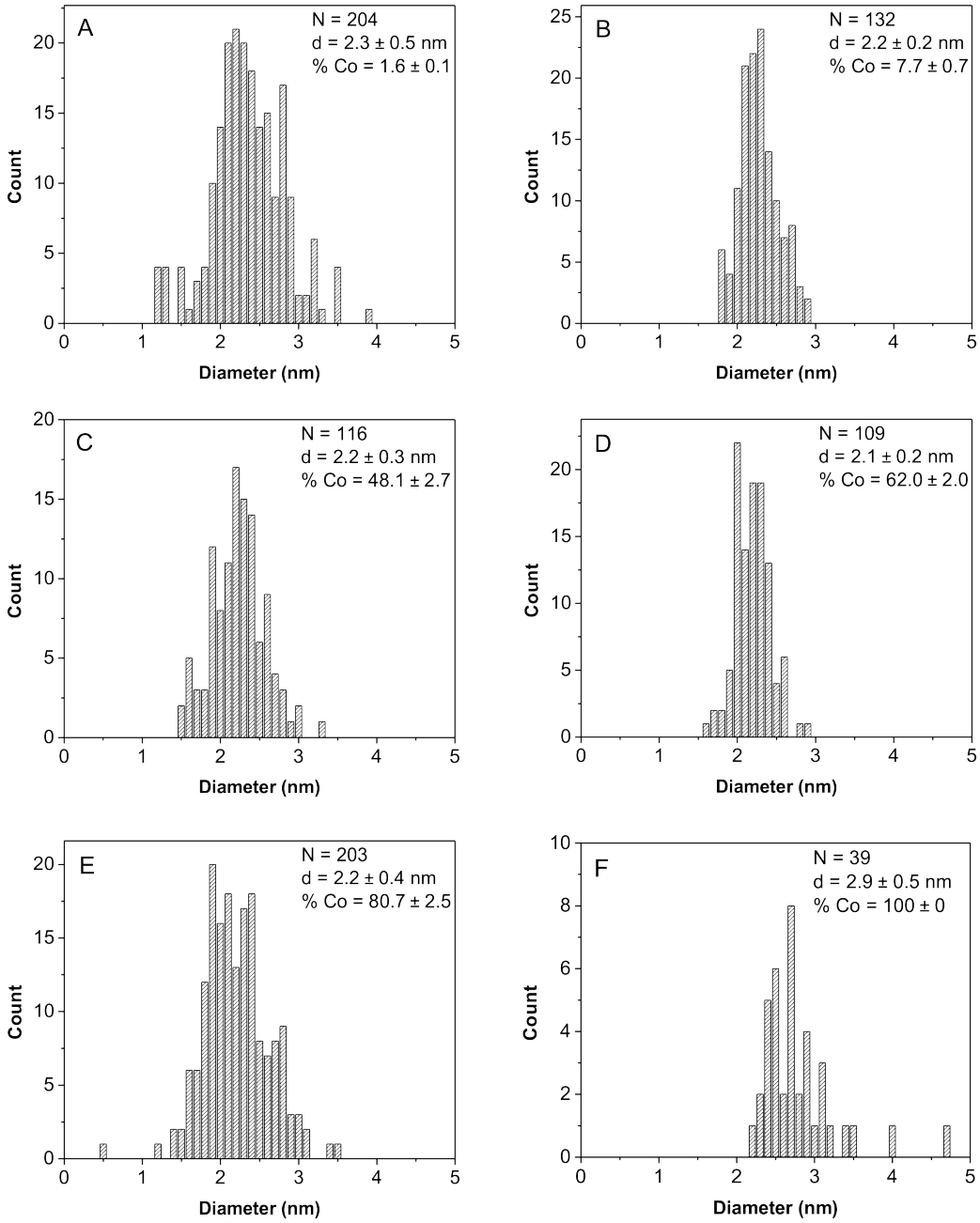

Figure 34. Histograms of Au_xCo_yNPs size distributions based on HRTEM micrographs for A) y = 1.6 ± 0.1%, B) y = 7.7 ± 0.7%, C) y = 48.1 ± 2.7%, D) y = 62.0 ± 2.0%, E) y = 80.7 ± 2.5%, and F) y = 100 ± 0. N represents the number of particles used for size determination; *d* represents average diameter ± the standard deviation of the average

To assign the composition and composition morphology of the resulting particles, we use a combination of several techniques. First, we analyze particle crystallographic features using HRTEM. The bulk lattice constant of Au_{fcc}, a = 4.079 Å and the bulk lattice constant of metallic Co_{hcp}, a = 2.503 Å, c = 4.061 Å or Co_{fcc}, a = 3.545 Å.[238] Therefore, regardless of the overall crystal system adopted by the particle, as % Co increases, the particle lattice constant(s) are expected to decrease with respect to either bulk Au or the lattice constant of a pure Au particle of this size (100% AuNPs = 3.96 Å, Table 2). Initially, our results follow this trend where increasing Co incorporation leads to a decrease in observed particle lattice constants (Table 2). However, as the % Co incorporation reaches a threshold (>60%), the observed lattice constants begin to increase. This increase is likely due to the formation of a cobalt oxide, which may be expected since our synthesis is conducted in air and in water (this assignment is supported by XPS analysis, *vide infra*, and Figure 35). Importantly, no core-shell architectures are observed in either HRTEM or scanning transmission electron microscopy (STEM) analysis (Figure 36), and the distribution of lattice constants is not bimodal, indicating that there are not two populations of particles each comprised of only one metal.

Table 2. Size, composition, photoluminescence, and magnetic property analysis of Au_xCo_yNPs

Initial molar ratio added (% Co)	NP composition (% Co) ICP-MS	Lattice constant (Å) HRTEM	NP size (nm) HRTEM	NP size (nm) PFG NMR	ε at 360 nm ($\times 10^5$ $M^{-1}cm^{-1}$)	Φ ($\times 10^{-3}$)	Brightness ($M^{-1}cm^{-1}$)	$\chi_{tot,g}$ ($\times 10^{-6}$ $cm^3g_{NPs}^{-1}$)	r_2 ($mM_{Co}^{-1}s^{-1}/mM_{NP}^{-1}s^{-1}$) **7T**
0	0 ± 0	3.96 ± 0.05	2.2 ± 0.5	4.1 ± 0.1	9.3 ± 2.3	0.40 ± 0.02	374	-0.65 ± 0.00	NA
50	1.6 ± 0.1	3.85 ± 0.03	2.3 ± 0.5	4.2 ± 0.1	12.6 ± 4.8	2.29 ± 0.49	2884	-0.39 ± 0.04	NA
60	7.7 ± 0.7	3.70 ± 0.03	2.2 ± 0.2	4.3 ± 0.3	8.7 ± 1.2	2.80 ± 0.64	2430	-0.20 ± 0.05	1.5/49
70	26.8 ± 2.0	3.75 ± 0.04	2.3 ± 0.5	4.3 ± 0.1	4.6 ± 1.1	3.00 ± 0.15	1373	0.55 ± 0.34	2.4/209
80	48.1 ± 2.7	3.73 ± 0.03	2.2 ± 0.3	4.1 ± 0.3	9.2 ± 1.8	2.52 ± 0.36	2322	3.24 ± 0.96	6.8/1750
85	62.0 ± 2.0	3.88 ± 0.05	2.1 ± 0.2	4.3 ± 0.4	6.1 ± 0.9	0.50 ± 0.26	305	5.34 ± 1.01	11/3650
90	80.7 ± 2.5	3.90 ± 0.05	2.2 ± 0.4	4.3 ± 0.1	7.1 ± 0.1	0.30 ± 0.16	211	8.51 ± 1.23	NA
100	100 ± 0	4.79 ± 0.05	2.9 ± 0.5	4.9 ± 0.1	NA	NA	NA	11.26 ± 1.34	26/12200

*All reported values are the average of at least 3 independently synthesized trials. The values for NP size are reported with the standard deviation of the mean. All other values are reported with the standard error.

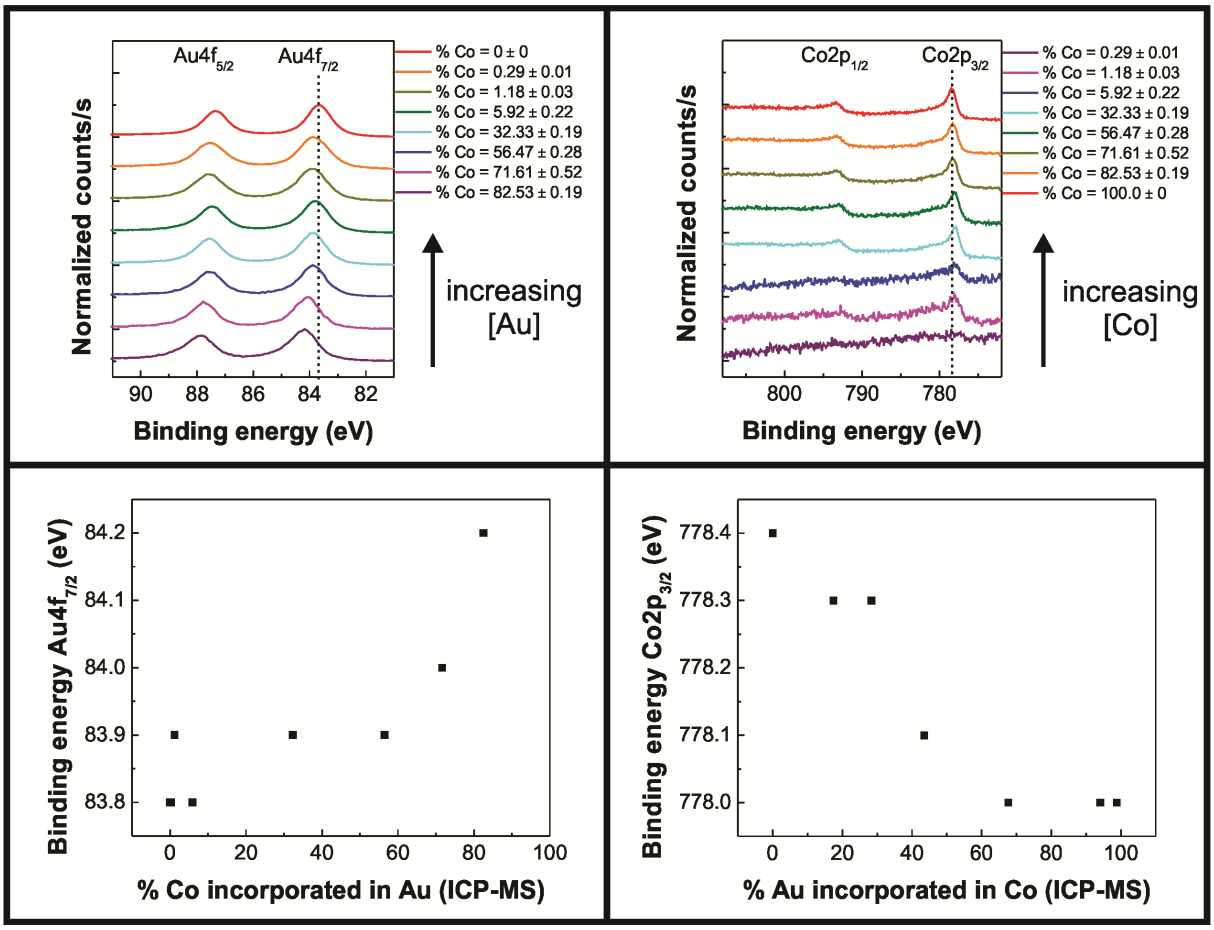

Figure 35. High resolution XPS spectra of Au4f and Co2p regions for all NP compositions (top). Plot of binding energy of $Au4f_{7/2}$ (bottom left) and $Co2p_{3/2}$ (bottom right) as a function of % Co and % Au incorporation in the NP, respectively. Exact % Co and % Au incorporations measured by ICP-MS are reported

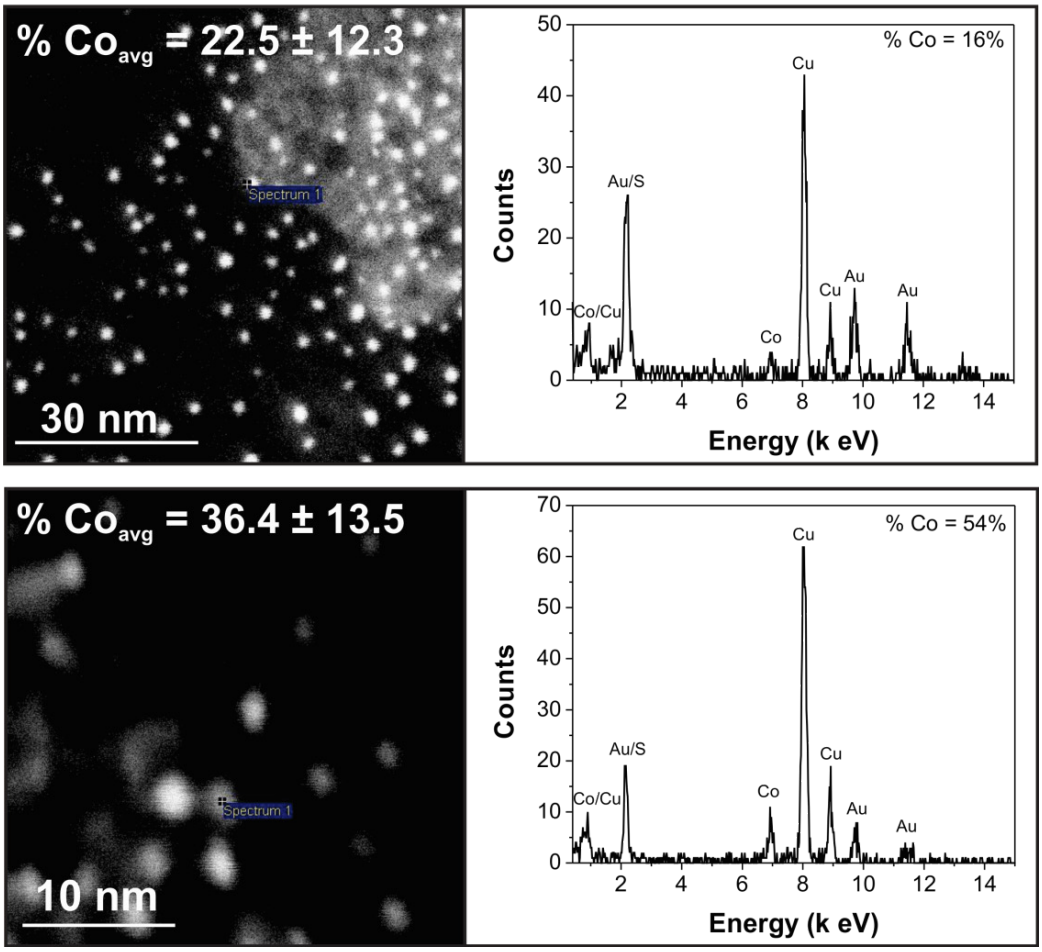

Figure 36. Representative area STEM-HAADF images and corresponding EDS spectra of Au_xCo_yNPs on ultra-thin carbon 3-5 nm copper mesh grid using a JEOL JEM 2100F

Table 3. Comparison of Au_xCo_yNP composition measured by ICP-MS and STEM-EDS

NP composition (% Co) ICP-MS	NP composition (% Co) STEM-EDS
25.7 ± 1.0	22.5 ± 12.3
37.1 ± 0.4	36.4 ± 13.5

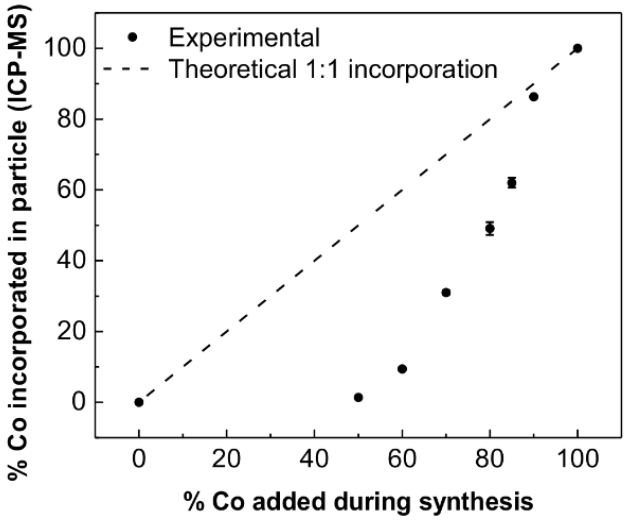

Figure 37. Percent Co incorporated into the final nanoparticle as a function of the initial molar percent Co added during synthesis (as determined by ICP-MS). The data points represent the experimental data, and the dotted line represents the theoretical composition if all metal is incorporated into the final particle

Table 4. Initial molar % Co added during synthesis and final % Co incorporation in the NP by ICP-MS analysis. Error represents the standard error

Co added during synthesis (%)	Co incorporated in final NP (%)
0	0 ± 0
50	1.6 ± 0.1
60	7.7 ± 0.7
70	26.8 ± 2.0
80	48.1 ± 2.7
85	62.0 ± 2.0
90	80.7 ± 2.5
95	89.8 ± 1.2
100	100 ± 0

After analysis of lattice features and general morphology, we use three techniques to analyze elemental composition. ICP-MS and XPS were used to evaluate the metal atom concentrations and oxidation states of the bulk colloid, respectively. STEM-EDS point spectra were used to assess the composition of individual particles (Figures 36-37 and Tables 3-4). ICP-MS analysis indicates that little to no Co incorporation is observed until the initial molar ratio of Co was increased to 50%. At initial molar ratios above 50% Co, the nanoparticles exhibit a continuously tunable stoichiometry, and the final incorporation of Co into the Au nanoparticles was varied from 1.6-89.8% (Figure 37 and Table 2). The initial lag in Co incorporation may be a product of the disparity in reduction potential between Co(II) and Au(III) species[238] which results in less available Co monomer (here, referring to "monomer" as described by LaMer[239]) at the critical concentration for homogeneous nucleation of the particle solid phase. Previous reports indicate that co-reduction during nucleation was a crucial factor in the formation of intermetallics and larger alloyed shells.[235,240,241] Differences in reduction potential are also thought to play a large role in the formation of core-shell particles or incomplete mixing of the two components (e.g., heterogeneous solid solution or "island" formation).[241] Based on the work described in Chapter 2, we hypothesize that above 50% initial molar ratio of Co, no Au(0) is formed prior to nucleation, allowing a threshold amount of Co monomer is to co-nucleate with Au-thiolate monomers (which have a lower reduction potential when compared to $[AuCl_4]^-$,[242] allowing both elements to be incorporated into a single particle.

To analyze the composition of individual particles, we use STEM-EDS point spectra. For a sample of nanoparticles synthesized with a given molar ratio of Au:Co, individual particle compositions were measured by EDS, and spectra were obtained from several different particles to establish an average particle composition. Average compositions agreed well between ICP-

MS and STEM-EDS analysis. However, it is important to note that using STEM-EDS, we observed that particle-to-particle composition was more heterogeneous as % Co increased, and this heterogeneity is consistent with the increased variation for the same initial molar ratios as measured by ICP-MS (i.e., the standard error for composition increases with increasing % Co, Table 2 and Figure 37). Particle-to-particle composition heterogeneity may be a result of our synthetic strategy. For example, the rapid particle nucleation approach can be viewed as an analog to the bulk diffusion-quench processes used to form bulk alloys. In diffusion-quench methods, a given ratio of two metals are heated together and entropy drives metal mixing. The mixture is then cooled to "freeze" the combined state.[208] In our synthesis, instead of cooling, we rapidly increase the solution saturation in metal precursor, which induces nucleation of the solid phase. During this step, there may be limited selectivity for metal incorporation into the particle. Instead, we hypothesize that the local molar ratio of metal precursor in solution determines the ratio of the two metals incorporated into the final nanoparticle architecture. It is important to note that comparison of XRD spectra to determine particle composition was not possible from particles of this size range due to significant line broadening, which is consistent with mathematical predictions of X-ray optics.

To further characterize the composition and oxidation state of the Au_xCo_yNP alloys, all particle compositions were analyzed by XPS (Figure 35). Survey spectra showed the presence of Au, Co, C, O, and S in all samples (with the exception of $Au_{100}NPs$ and $Co_{100}NPs$, which lacked Co and Au peaks, respectively). Previous syntheses using pure Co precursor under similar reaction conditions have also observed boron in the particle products,[243,244] however we do not observe boron signal in any XPS spectra, which indicates that borohydride, borate byproducts or cobalt-boride materials are not present in the purified final nanoparticle products. A shift of the

$Au4f_{7/2}$ peak from Au_{100}NPs at 83.8 eV to higher energy is observed with increasing % Co incorporation, suggesting a continuous change in the Au environment that is consistent with alloy formation.[240,241,245] Analysis of the $Co2p_{3/2}$ peak shows the presence of metallic cobalt as a sharp, narrow band with binding energies ranging from 778.0-778.4 eV, in all cases. From a pure Co phase to an alloyed phase, we observe a shift to lower binding energy of the Co2p features. From a pure Au phase to an alloyed phase, we observe a shift to higher binding energy of the Au4f peaks. These binding energy shifts do not follow trends expected from electronegativity arguments, but instead are consistent with electron density moving from Au to Co. Similar trends have been observed for other Au-transition metal alloys, such as Au-Ni, where $Ni2p_{3/2}$ binding energies decrease and $Au4f_{7/2}$ binding energies increase when comparing the pure metal phase to an alloyed composition.[246] For high concentrations of Co (>60% Co incorporation) a shoulder is present at ~781 eV. This binding energy region is consistent with Co(II) or Co(III) species. However, no corresponding satellite peaks are observed (~786 eV), which indicates that where oxidation is present, the concentration is low (Figure 35). Limited oxidation of the Co, despite a synthesis conducted in air and water, is consistent with stabilizing trends observed in other noble-transition metal alloys such as PtFe[39] and PtCo,[247] where the first row transition metal exhibits enhanced resistance to oxidation when alloyed with a more noble counterpart.

Next, we analyze particle magnetic properties and also use this analysis as an additional metric to assess composition tunability. In order to determine the magnetism of Au_xCo_yNPs, we have used the Evans' method[140] to measure the mass magnetic susceptibility at room temperature. Here, the Evans' method is an alternative to superconducting quantum interference device (SQUID) analysis, which requires significantly more material, especially for small particle sizes where diamagnetic capping ligands can quench the magnetism of surface atoms,[248]

which are a large percentage of total atoms in the sample (~40% for d = 2.2 nm). Using the Evans' approach, we analyzed a series of Au_xCo_yNP compositions (0-100% Co incorporation, Figure 38), to determine the relationship between particle composition and particle susceptibility. Here, we found that by controlling the % Co incorporated in the final Au_xCo_yNPs we could achieve continuously tunable magnetic susceptibility from -0.39×10^{-6} to 11.26×10^{-6} $cm^3g_{NPs}^{-1}$ (Table 2). The reported values represent the total mass magnetic susceptibility of the sample, which is comprised of both the diamagnetic and paramagnetic contributions. The magnetic susceptibility values reported here, as well as relaxivity measurements discussed below, are consistent with previous reports of a variety of superparamagnetic nanoparticles, including AuNi nanoparticles[142] and SPIONs.[225,236,249]

By using a molecular characterization method to analyze our magnetic susceptibility, we were also able to directly observe the ^{1}H NMR spectrum of the NP ligand shell in each sample within a single experiment. Here, ^{1}H NMR spectra show an absence of the thiol proton as well as the directly adjacent CH_2 protons on the PEGSH (Figure 39). The absence of these peaks from the ^{1}H NMR spectra is consistent with signal dephasing, which is expected to be a result of a chemical shift distribution from various PEGSH binding sites as well as conduction electrons at the NP surface and/or being attached to a paramagnetic center (e.g. for NPs with a positive magnetic susceptibility value). The spectral window was expanded to 250 ppm during acquisition to search for hyperfine-shifted peaks present from the formation of high-spin Co(II) complex impurities.[250] No ^{1}H NMR spectral changes in chemical shift were observed. The spectra are consistent with our finding of T_2-enhancing Au_xCo_yNPs and not the result of excess reactant impurities.

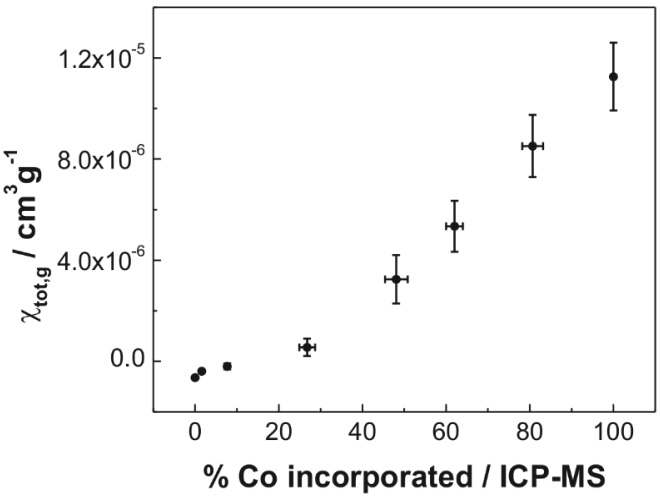

Figure 38. Magnetic susceptibility of Au_xCo_yNPs increases as % Co increases. Error bars in both χ and % Co incorporated represent the standard error of at least 6 independent experiments

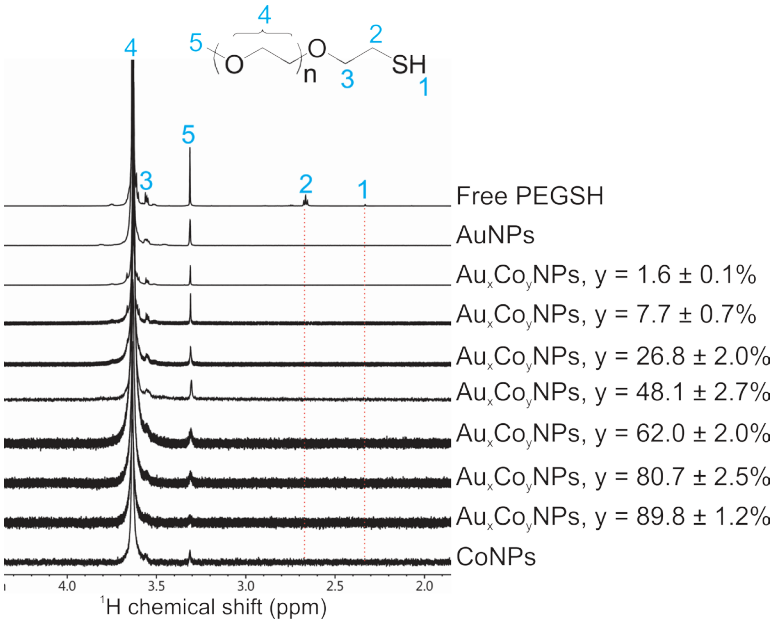

Figure 39. ^1H NMR spectral region containing ^1H NMR resonances of the PEGSH capping ligand. The top spectrum shows the ^1H NMR of free PEGSH in D_2O and the spectra below show the ^1H NMR of PEGSH-capped Au_xCo_yNPs. No free PEGSH is detected in the particle-bound spectra, as indicated by the red dotted line, highlighting the absence of peaks 1 and 2

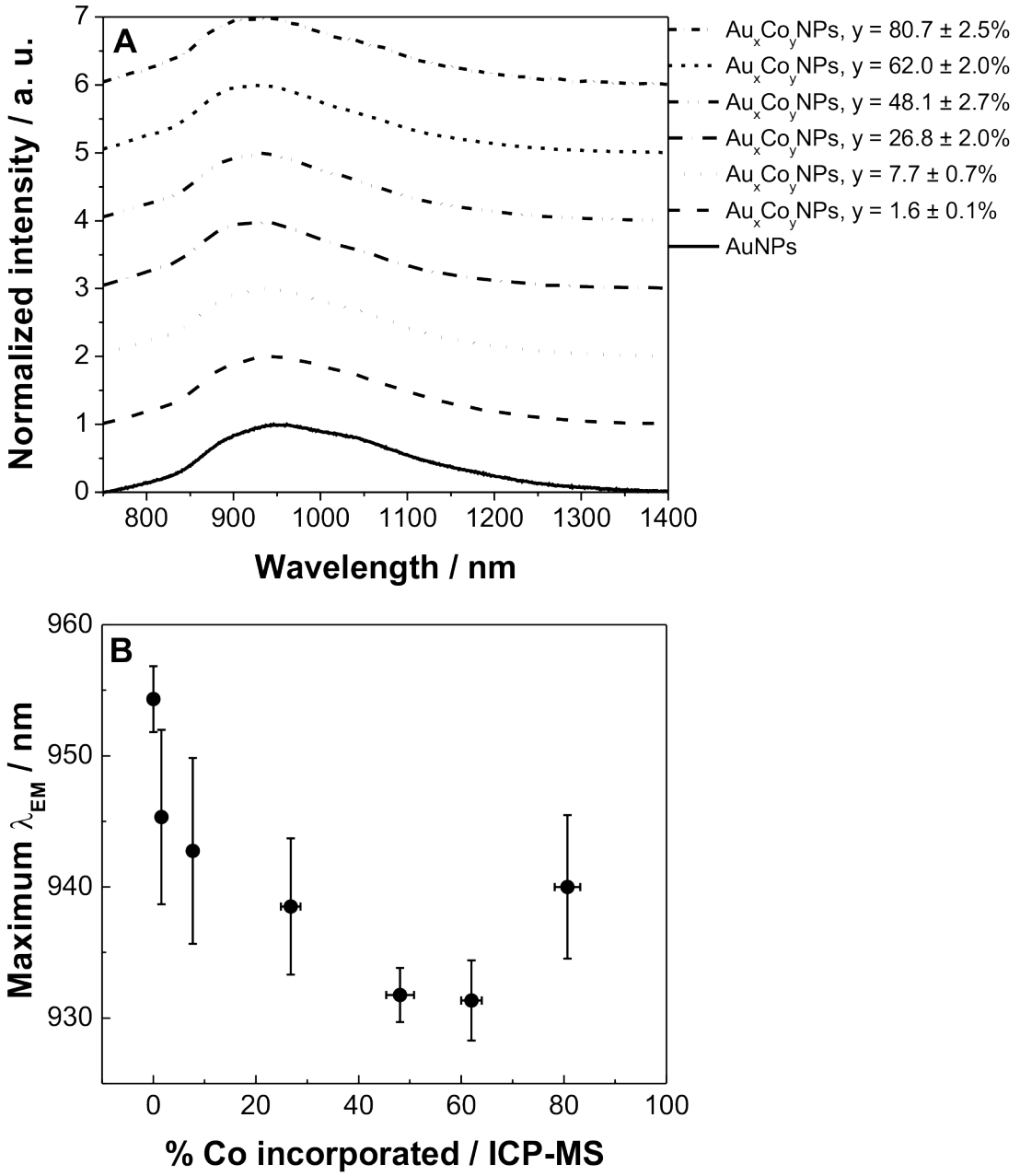

Figure 40. A) Photoluminescence of Au_xCo_yNPs in D_2O showing representative emission spectra. B) Maximum emission wavelength as a function of % Co incorporated

Remarkably, Au_xCo_yNPs also exhibit PL in the NIR spectral region, which to the best of our knowledge, is the first observation of PL from Au-Co alloys at any length scale. Here, all compositions of the Au_xCo_yNPs exhibit NIR PL, with the exception of 100% CoNPs (Table 2). Excitation spectra from these particles are consistent with previous excitation spectra obtained for Au and Au_xCu_yNPs[90] (Figure 30). Interestingly, in the case of Au_xCo_yNPs, a hypsochromic shift (~25 nm) in the maximum emission wavelength relative to 100% AuNPs is observed (Figure 40) with increasing % Co incorporation. This trend is observed until Co concentration in the nanoparticle reaches >60% incorporation. Beyond this concentration, the maximum emission wavelength exhibits a bathochromic shift toward the emission maximum from 100% AuNPs. This % Co composition is also coincident with our observation of increases in Co oxidation via XPS, as well as increases in lattice constants.

Previous work indicates that the NIR emission originates from a surface charge-transfer state comprised of Au-thiolate interactions.[46,251,252] In the case of the Au_xCu_yNPs, we hypothesized that the presence of Cu in the surface region (surface or subsurface layers)[253] changes the energy of this Au-thiolate interaction possibly by replacing one or more of the bonding Au atoms with a Cu atom, consistent with previous reports.[254] The presence of PL from the Au_xCo_yNPs, but less dramatic composition dependence of the maximum λ_{EM} (Figure 40), indicates that the incorporation of Co into the NP either does not significantly alter the energy of the emissive luminophore (excited or ground states), or Co is not proximate to the luminophore. We can further delineate these scenarios as 1) only a small population of Co exists on the NP surface (where the emitting state has been indicated to localize), 2) Co is oxidized on the surface of the particle and therefore does not interact with the luminophore of the NP, 3) Co is segregated into Co "islands" on the surface, 4) Co does not alter the energy of the emissive state

in contrast to Cu in Au_xCu_yNPs and/or 5) Co *does* alter the energy of the emissive state, but at high % Co compositions, compositional heterogeneity and increasing oxidation confounds subsequent interpretation. Mechanism 4 is unlikely, given that all Au_xCo_yNPs exhibit an emission maximum that is blue-shifted from 100% AuNPs. HRTEM analysis indicates that the Au_xCo_yNPs do not exhibit large scale (i.e. observable) metal separation throughout the particle, which seems to eliminate mechanism 3. Based on our current experimental evidence, mechanisms 1 and 5 are the most probable explanations for the composition dependence of the maximum λ_{EM} from Au_xCo_yNPs.

Although the definitive mechanism of PL for these small Au-transition metal NPs is still being determined, standard PL characterization is possible. Quantum yield (Φ) and molar extinction coefficient (ε) measurements were used to calculate particle brightness ($\varepsilon \times \Phi$). The brightness value determines the probability of absorbed and emitted of photons and is a useful figure of merit to compare luminophores.[255] Measured quantum yield values are consistent with those found for other noble metal nanoparticle systems (Table 2). Quantum yield and brightness varied non-linearly (Table 2) as a function of composition with the brightest particles containing ~2% Co. Au_xCo_yNPs exhibit no observable size dependence of optical properties.

Nanoparticle PL was evaluated in both D_2O and H_2O. D_2O was used to eliminate solvent absorption interference, however evaluation in H_2O was also conducted in order to facilitate comparison with other luminophores that have been measured in non-deuterated solvents. All optoelectronic properties were the same, within error, in both solvents. The Au_xCo_yNPs display brightness values that are over an order of magnitude higher than alternative biocompatible probes such as (Yb(III)TsoxMe), a sensitized lanthanide complex evaluated in water (2884 $M^{-1}cm^{-1}$ vs 83 $M^{-1}cm^{-1}$).[256]

The combination of magnetic and optical properties from Au_xCo_yNPs are clearly interesting for application as multimodal MRI contrast agents and therefore the relaxivity properties of each particle composition were also evaluated. Previous reports indicate that metallic Co T_2 relaxivities are both field strength and concentration dependent.[257] To study the effect of field strength, the relaxivity of the Au_xCo_yNPs was measured at 37 °C at two different static fields, 0.47 T (20 MHz proton Larmor frequency) and 7 T (300 MHz proton Larmor frequency) (Figure 41). As a control experiment, the relaxivity of 100% AuNPs was measured, and no effect on relaxivity was observed. For both field strengths, Au_xCo_yNPs had a significant effect on the transverse relaxation time (T_2) of water, and had little to no influence on the longitudinal relaxation time (T_1). These results indicate that Au_xCo_yNPs have the ability to maintain proton T_1 values that are the same as the surrounding tissue (providing essentially no positive contrast properties) while significantly dephasing the transverse magnetization used in MRI signal detection.[258] This property most efficiently produces negative (dark) spots in the final image, making Au_xCo_yNPs attractive negative T_2 contrast agents.

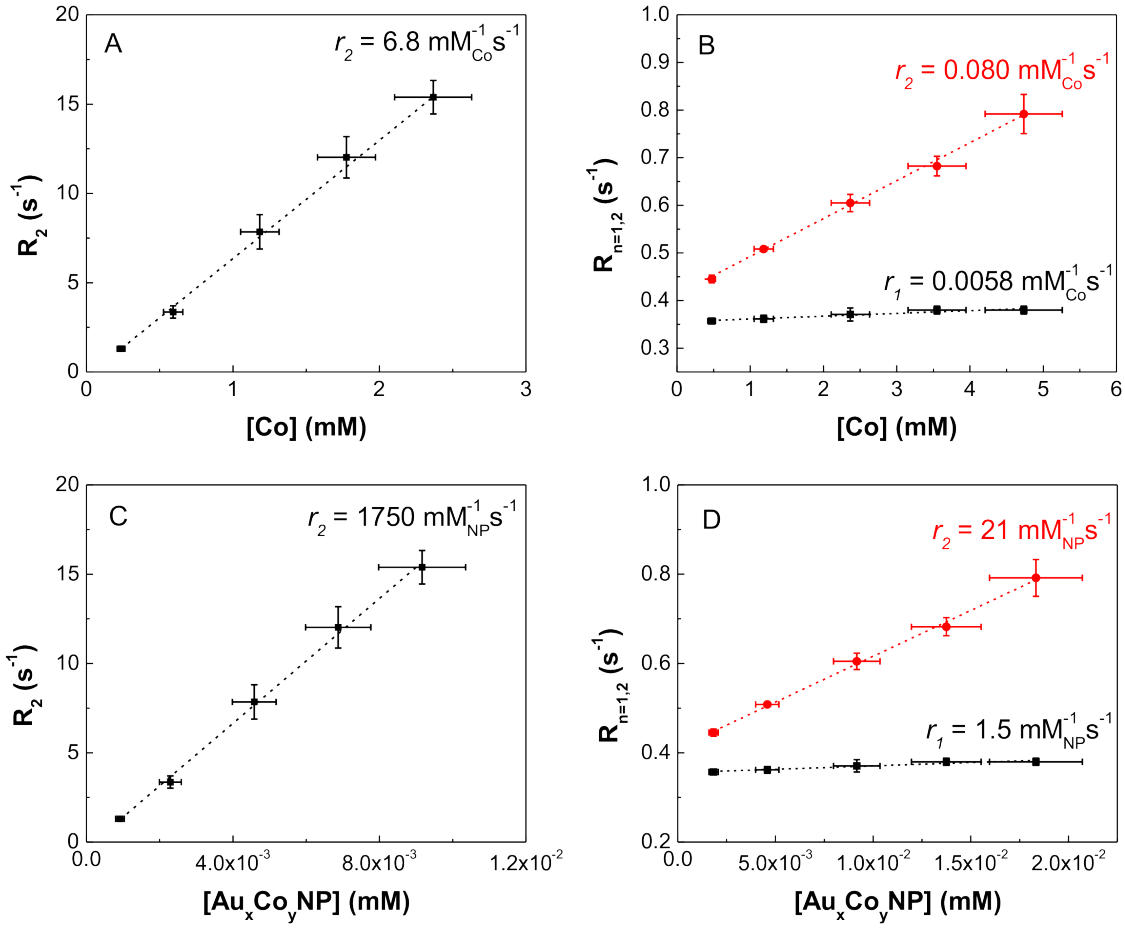

Figure 41. Linear regression plots for Au_xCo_yNPs (y = 48.1 ± 2.7%) relaxivity at 37 °C as a function of per-Co concentration at A) 7 T and B) 0.47 T, and per-particle concentration at C) 7 T and D) 0.47 T. All R^2 values for the linear regression are > 0.99. X and y error bars represent the standard deviation of concentration from ICP-MS and relaxation rates, respectively for three independently synthesized samples of the same initial molar ratio of Co

Even at low field strength, all Au_xCo_yNP compositions show very little effect on T_1, leading to r_2/r_1 values that, in all cases, are either comparable to or larger than those of a clinically available T_2 contrast agent, Ferumoxsil (SPION), which has a diameter nearly 3 times larger than the Au_xCo_yNP alloys reported here.[249] The comparable or in some cases, enhanced, relaxivity for Au_xCo_yNPs (despite their smaller diameter compared to reported SPIONs) is likely the result of the higher saturation magnetization of Co compared to iron oxide (see SI for a full comparison of Au_xCo_yNPs to previously reported iron oxide nanoparticles).[238] Since tissues already have relatively short T_2 times ($\sim 10^2$-10^3 ms),[259] in order to be considered an effective negative T_2 contrast agent, r_2 values must be orders of magnitude larger than r_1 values typically required for positive contrast agents. Further, as field strength is increased, T_1 effects, as well as the efficiency of positive contrast agents, are expected to diminish. As clinical imaging instrumentation moves to higher field strengths to achieve greater resolution, the necessity to develop and implement improved contrast agents for T_2 weighted imaging becomes increasingly important.[260]

Au_xCo_yNP alloys may provide a platform to achieve T_2 enhancements greater than those observed from SPIONs, while maintaining a small particle size for renal clearance.[211] As expected, at 7 T longitudinal relaxation times in the presence of even the most concentrated Au_xCo_yNPs is equal to that of pure water (~6 s at 7 T). Both the per-Co and per-particle T_2 relaxivities at 7 T are listed in Table 2. Relaxivity values are reported as per-particle relaxivity values, in addition to per-Co relaxivity values, to facilitate comparison between nanoparticles of different composition and size.[257] The per-particle comparison is made here due to the difference between superparamagnetic nanoparticles and chelated-metal based contrast agents. For chelated-metal contrast agents, such as commercially available gadolinium-based agents, water

protons bind to a single metal center, and therefore per-metal relaxivities are preferred. For superparamagnetic nanoparticles, the particle itself behaves as a large paramagnetic ion.[261] Therefore, per-particle relaxivities provide a more accurate assessment of contrast agent efficiency in the case of nanoparticles[257] (but with the caveat that larger particles will almost always exhibit higher relaxivities compared with smaller particles of the same material, and this relationship between particle size and per-particle relaxivity is not necessarily linear depending on the particle system).[261] To compare Au_xCo_yNP T_2 relaxivities to other contrast agents, the per-particle relaxivity was calculated for reported earth-abundant metal nanoparticles of comparable size. Indeed, Au_xCo_yNPs exhibit comparable or enhanced per-particle T_2 relaxivities compared to SPIONs, despite the fact that Au_xCo_yNPs are smaller in diameter. Additionally, Au_xCo_yNPs show improved T_2 relaxivities compared to 0D and 1D gold-cobalt ferrite and gold-iron oxide heterostructures.[262] Most relaxivities in the literature are reported as per-metal relaxivities. This figure of merit is important, as biological compatibility and toxicity is likely to be a function of transition metal concentration (for cobalt as well as iron), allowing a more straightforward assessment than particle concentration (although both cobalt and iron are used already in biomedical applications such as surgical implants).[263]

Because a wide range of Au_xCo_yNP compositions can be accessed via the current synthesis, the % Co incorporation parameter was explored to find a composition with both high NIR brightness and high T_2 relaxivity. This optimal composition can be determined by plotting r_2 at 7 T and NIR brightness as a function of % Co incorporation (Figure 42). Particle brightness is highest for Au_xCo_yNPs (y = 1.6 ± 0.1%) and decreases until no NIR PL is observed. For per-particle relaxivity, as % Co incorporated increases, r_2 values become more favorable for negative MRI contrast. The trends for NIR brightness and r_2 intersect at approximately 55% Co

incorporated in the particle. The particle composition closest to this value that retained desirable imaging properties was Au_xCo_yNPs, y = 48.1 ± 2.7%. Even at 48.1 ± 2.7% Co incorporation, the per-particle relaxivity (r_2 = 1750 $mM^{-1}s^{-1}$) remains competitive compared to marketed negative contrast agents[249] and exceeds the relaxivity values for reported iron oxide nanoparticles of similar sizes.[236] Likewise, particle brightness (2322 $M^{-1}cm^{-1}$) also remains high when compared to other biocompatible NIR probes.[264] For this reason, we conclude that 48.1 ± 2.7% Co incorporation is an appropriate composition for a dual NIR-T_2 contrast imaging agent.

3.4 CONCLUSION

In summary, we present a method for preparing a previously inaccessible library of composition tunable Au_xCo_yNP alloys. This method can be used to tailor magnetic susceptibility while maintaining almost identical particle size and surface chemistry. To the best of our knowledge, these particles have also enabled the first observation of photoluminescence from a Au-Co nanoparticle species at any size range or composition. Combined, these magnetic and optical features generate a promising multi-modal agent that exhibits NIR emission and MRI contrast properties that meet or exceed current standards, all at small particle diameters. Taken together, these data suggest that alloying behavior at the nanoscale may deviate significantly from bulk trends and that access to these new stoichiometries should yield an exciting diversity of unique, tunable physical properties useful in applications ranging from multimodal theranostics to heterogeneous catalysis.

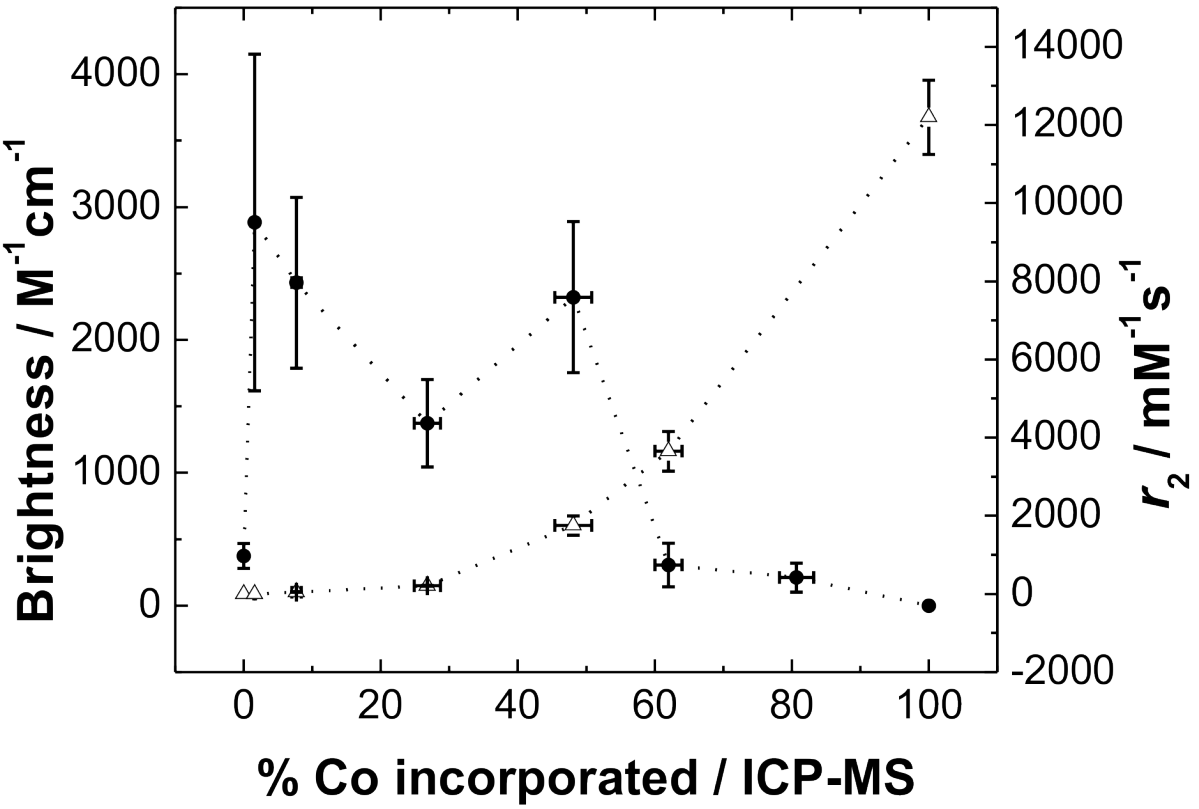

Figure 42. Optimal Au_xCo_yNP composition for bimodal NIR-T_2 contrast imaging occurs at y = 48.1 ± 2.7% Co incorporation

4.0 OBSERVATION OF UNIFORM LIGAND ENVIRONMENTS AND ^{31}P-^{197}AU COUPLING IN PHOSPHINE-TERMINATED GOLD NANOPARTICLES

(Portions of this work were published previously and are reprinted with permission from Marbella, L. E.; Crawford, S. E.; Hartmann, M. J.; Millstone, J. E. *Chemical Communications*, **2016**, *52*, 9020-9023. Copyright 2016 Royal Society of Chemistry)

4.1 INTRODUCTION

Understanding the surface chemistry of nanoparticles is critical to controlling their formation, physical properties, and ultimately their use in applications. NMR spectroscopy has emerged as a promising tool to provide structural,[265,266] electronic,[78,130] and dynamic[63,77] information on the molecular species present at metal nanoparticle surfaces, both in terms of pendant ligands and constituent metal atoms.[267] Yet, certain nanoparticle features exhibit fundamental challenges to characterization by NMR. For example, ^{197}Au and ^{105}Pd exhibit large quadrupole moments, which have prohibited direct, routine NMR characterization of these particle cores thus far. Likewise, the NMR resonances of ligands appended to metal nanoparticles often exhibit broad lineshapes that can be challenging to interpret (however, once interpreted, are a rich source of information on ligand shell arrangement and electronic structure of the underlying particle[59,69,139,267,268]). Here, we use a combination of solution phase and solid-state ^{31}P NMR

spectroscopy to study these ligand architectures using small diameter (d = 1.8 ± 0.2 nm), phosphine-terminated AuNPs. We find that the uniformity of ligand environments on these particles allows the observation of ^{31}P-^{197}Au coupling, which we assign based on a combination of NMR and DFT analyses.

4.2 EXPERIMENTAL

4.2.1 Materials and Methods

4-(diphenylphosphino)benzoic acid (4-DPPBA, 97%), bis(*p*-sulfonatophenyl)phenylphosphine dihydrate dipotassium salt (BSPP, 97%), hydrogen tetrachloroaurate(III) trihydrate ($HAuCl_4$, ≥99.9%), sodium borohydride ($NaBH_4$, ≥99.9%), chloro(triphenylphosphine)gold(I) (Au(I)Cl(PPh_3), ≥ 99.9%), acetic acid (glacial), and phosphoric acid solution (85% H_3PO_4) were purchased from Sigma Aldrich (St. Louis, MO). Deuterium oxide (99.9%) and methylene chloride-d_2 (D, 99.96%) were obtained from Cambridge Isotope Laboratories (Andover, MA). Sodium hydroxide (NaOH, ≥97% Certified ACS) was purchased from Fisher Scientific (Waltham, MA). All chemicals were used as received.

All aqueous solutions were prepared using NANOpure water (Thermo Scientific, >18.2 MΩ·cm). 4-DPPBA was prepared in a 20.0 mM NaOH solution to ensure solubility of the DPPBA ligand. Prior to use, all glassware and Teflon-coated stir bars were washed with aqua regia (3:1 ratio of concentrated HCl to HNO_3) and rinsed with copious amounts of water prior to drying. *Caution: aqua regia is highly toxic and corrosive, and should only be used with proper*

personal protective equipment and training. Aqua regia should be handled only inside a fume hood.

4.2.2 Synthesis of DPPBA-Terminated Gold Nanoparticles

The synthesis of DPPBA-terminated gold nanoparticles has been described previously.[269] Briefly, 81.25 mL of water, 6.75 mL of a 10.0 mM 4-DPPBA solution, and 2.00 mL of a 20.0 mM $HAuCl_4$ solution were combined while stirring. After 20 s, 10.00 mL of a 20.0 mM $NaBH_4$ solution was rapidly injected, yielding a red-orange product. The solution was stirred for 1 min, and the particles were allowed to ripen for 1 h. Afterwards, the particles were centrifuged through 10 kDa molecular weight cut-off filters (Amicon Ultra - 4, Millipore, Inc) for 15 min at 4000 rcf (Eppendorf centrifuge 5804R with swing bucket rotor A-4-44). The particles were rinsed four additional times in a 3.30 mM NaOH solution (~4 mL). Following purification, the particles were analyzed using NMR spectroscopy, high resolution transmission electron microscopy (HRTEM), ultraviolet-visible-near infrared (UV-vis-NIR) spectroscopy, and X-ray photoelectron spectroscopy (XPS).

4.2.3 Solution Phase ^{31}P NMR Spectroscopy

DPPBA-terminated AuNPs were prepared for solution phase ^{31}P NMR spectroscopy by washing twice with 20 mM NaOH in D_2O, resuspending in 500 µL of 20 mM NaOH in D_2O, and loading the colloid into a 5 mm NMR tube. Other solutions that are discussed herein were prepared as follows: BSPP-terminated AuNPs were analyzed after following the same washing procedure as DPPBA-terminated AuNPs, with the exception that only NANOpure water and D_2O were used

for particle resuspension and analysis. DPPBA alone in solution was recorded by preparing a 20 mM solution of DPPBA in 20 mM NaOH in D_2O. The ^{31}P NMR spectrum of Au(I)Cl(PPh_3) was recorded by preparing a 20 mM solution of Au(I)Cl(PPh_3) in CD_2Cl_2. Low temperature ^{31}P NMR measurements of DPPBA-terminated AuNPs were performed by resuspending lyophilized NP powders in CD_2Cl_2 and protonating via dropwise addition of glacial acetic acid.

All solution phase ^{31}P NMR experiments were recorded on a Bruker Avance III 600 MHz (14.1 T) spectrometer with a broadband fluorine observe (BBFO) Plus probe at 25 °C, unless otherwise noted. Temperature was maintained using a Bruker BVT3000 variable temperature system. Low temperature ^{31}P NMR measurements were performed on a Bruker Avance III 400 MHz (9.4 T) spectrometer with a BBFO probe using nitrogen cooling to reach -25 °C. ^{31}P chemical shifts were externally referenced to 85% H_3PO_4 (aq) at 0 ppm. Single pulse ^{31}P spectra were acquired after a $\pi/2$ pulse (typical pulse lengths ~11 μs) with WALTZ-16 ^{1}H decoupling during acquisition. Recycle delays varied for individual samples, but were maintained at $5\times T_1$, which ranged from ~10 s for DPPBA-terminated AuNPs to ~100 s for Au(I)Cl(PPh_3).

^{31}P DOSY of DPPBA-terminated AuNPs and Au(I)Cl(PPh_3) were recorded using a stimulated echo sequence. The response of the ^{31}P NMR signal integration, I, to variation in gradient strength, g, is described by the Stejskal Tanner equation[172]:

$$\frac{I}{I_0} = exp\left(-g^2\gamma^2\delta^2\left(\Delta - \frac{\delta}{3}\right)\cdot D\right) \quad (14)$$

Where I_0 is the integral in the absence of gradients, γ is the gyromagnetic ratio of ^{31}P (108.29×10^6 rad/sT), δ is the length of the gradient pulse, and D is the measured diffusion coefficient. Although ^{31}P diffusion data is reported in the form of DOSY plots, it is important to note that all diffusion coefficients were extracted from linear fits of $\ln(I/I_0)$ data. In addition,

rearrangement of the Stokes-Einstein equation was used to estimate the hydrodynamic size of the DPPBA-terminated AuNPs and Au(I)Cl(PPh_3) as follows:

$$R_H = \frac{k_B T}{6\pi\eta D} \quad (15)$$

Where R_H is the hydrodynamic radius, k_B is Boltzmann's constant, T is temperature, and η is solvent viscosity. A η value of 1.12 mPa·s for semi-heavy water, HDO, was used for the DPPBA-terminated AuNPs and 0.413 mPa·s for CD_2Cl_2. Reported errors were determined from the 2σ value extracted from the fit of the ^{31}P diffusion data.

4.2.4 Solid-State ^{31}P NMR Spectroscopy

DPPBA-terminated AuNPs were prepared for solid-state ^{31}P NMR spectroscopy by lyophilizing nanoparticle solutions overnight. Dried nanoparticle powders and other solids (e.g. DPPBA, Au(I)Cl(PPh_3)) were packed into 4 mm zirconia rotors for analysis with ^{1}H-^{31}P cross-polarization magic-angle spinning (CPMAS) NMR. Prior to each sample analysis, the magic-angle was calibrated with KBr by maximizing the number of rotary echoes observed in the free induction decay (FID) of ^{79}Br while spinning at 8 kHz. ^{1}H-^{31}P CPMAS NMR spectra were recorded on Bruker Avance 600 MHz (14.1 T) and Bruker Avance 500 MHz (11.7 T) spectrometers. Both were equipped with a triple-resonance 4 mm CPMAS probehead operating at a ^{31}P Larmor frequency of 243.11 MHz and 202.45 MHz and ^{1}H Larmor frequency of 600.57 MHz and 500.13 MHz, respectively. Temperature was maintained at 25 °C with either a BCU05 (14.1 T) or BVT3000 (11.7 T) variable temperature unit, unless otherwise noted. ^{1}H-^{31}P Hartmann-Hahn match conditions were optimized using solid DPPBA. ^{1}H 90° pulse widths were ~4 μs at 14.1 T and ~5 μs at 11.7 T and contact times of 3 ms were used in both cases. Two-pulse phase-

modulated (TPPM-20) high power ^{1}H decoupling at 80 kHz was applied during data acquisition. Typical MAS spinning rates between 5-12 kHz were used for all studies. Recycle delays differed for individual samples, which depends on $T_{1H\rho}$, and varied from 3 s for DPPBA-terminated AuNPs to 500 s for Au(I)Cl(PPh_3).

4.2.5 Ab Initio Calculations

Density functional theory (DFT) as implemented in the Amsterdam Density Functional (ADF) code was used to calculate electric field gradient (EFG) tensors, quadrupolar coupling constants, asymmetry parameters, and Euler angles.[270-272] EFG tensors were calculated with the hybrid B1LYP[273] exchange correlation functional with a polarized triple zeta basis set (TZ2P). This combination of functional and basis set has been shown to agree best with experimental results.[274] Relativistic effects for Au were accounted for within the Zeroth-Order Relativistic Approximation (ZORA).[275] In this report, four model systems were examined based on $Au_{11}(PPh_3)_7Cl_3$,[276] the two phosphorous binding sites in $[Au_{39}(PPh_3)_{14}Cl_6]Cl_2$,[277] as well as the single phosphorous binding motif in $Au_{55}(PPh_3)_{12}Cl_6$[278,279] all shown in Figure 43. Calculated parameters used for inputs in spectral simulations are listed in Table 5.

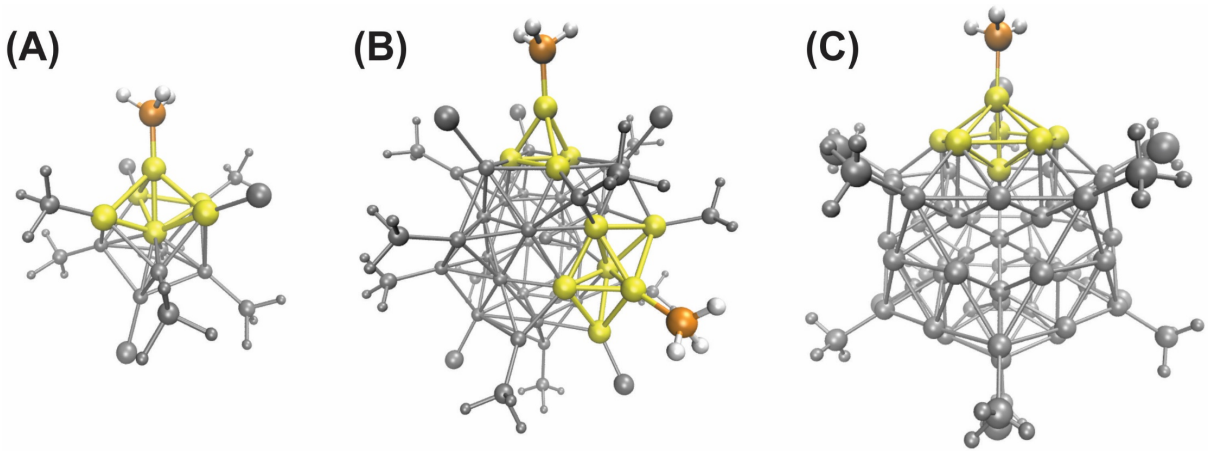

Figure 43. Structures of (A) $Au_{11}(PPh_3)_7Cl_3$ from ref. 276, (B) $[Au_{39}(PPh_3)_{14}Cl_6]Cl_2$ from ref. 277, and (C) $Au_{55}(PPh_3)_{12}Cl_6$ from ref. 278. Orange = Au, Yellow = P, Green = Cl, Dark gray = C, White = H. Clusters are shaded in light gray for emphasis on ligand binding motifs. $[Au_{39}(PPh_3)_{14}Cl_6]Cl_2$ has two binding sites, one with C_1 symmetry and one with C_{3v} symmetry about the Au binding site

Table 5. Nuclear properties of model phosphine binding motifs on AuNPs considered calculated with DFT

Binding site	C_Q (MHz) ^{197}Au	η ^{197}Au	α^D (°)	β^D (°)
Au_{11}	-321.1	0.1996	127.1	5.6
Au_{39}-C_{3v}	-426.6	0.0998	74.5	177.5
Au_{39}-C_1	-279.5	0.2326	179.1	168.8
Au_{55}	-287.5	0.3555	139.3	179.1

4.2.6 Quadrupole Effects in ^{31}P ssNMR Spectra and ^{31}P NMR Simulations

The line positions of spin-1/2 nuclei coupled to a quadrupolar nucleus can be described in terms of four parameters. When the spin-1/2 nucleus, *I*, is ^{31}P and the quadrupolar nucleus, *S*, is ^{197}Au, the relevant parameters are: (*I*) resonance frequency of the *S* nuclei, ^{197}Au (υ_s):

$$\upsilon_s = \gamma_{197Au} B_0 \quad (16)$$

The second, (II), is the ^{197}Au nuclear quadrupole coupling constant, C_Q:

$$C_Q = \frac{e^2 qQ}{h} \quad (17)$$

where *e* is the electronic charge, *q* is the electric field gradient at the ^{197}Au nucleus, and *Q* is the quadrupole moment at the ^{197}Au nucleus. The Euler angles in Table 5 are defined as follows: β^D is the angle between the largest component of the EFG tensor and the internuclear vector, r_{IS}, and α^D is the azimuthal angle. The third relevant coupling constant, (III), is the ^{31}P-^{197}Au dipolar coupling constant, *D*:

$$D = (\mu_0/4\pi)(\gamma_{31P}\gamma_{197Au}/r_{IS}^3)(h/4\pi^2) \quad (18)$$

where r_{IS} is the internuclear vector based on P-Au bond length and μ_0 is the permeability of vacuum. Here, r_{IS} is 2.235 Å for Au(I)Cl(PPh_3)[280] and 2.29 Å for phosphine on a AuNP surface, based on the average bond length observed in $[Au_{39}(PPh_3)_{14}Cl_6]Cl_2$.[277] Based on these bond lengths, *D* = 75 Hz and 70 Hz for Au(I)Cl(PPh_3) and DPPBA-terminated AuNPs, respectively. The values for the ^{197}Au resonance frequency at 14.1 T and 11.7 T are 10.61 MHz and 8.84 MHz, respectively. In this case, C_Q is only known for Au(I)Cl(PPh_3) at 940 MHz,[281] but various possible values of C_Q were calculated with DFT and are considered for DPPBA-terminated AuNPs (*vide supra*, Table 5). Equation 18 represents the direct dipolar coupling, but the spectral

features depend on the effective dipolar coupling constant, which is modulated by anisotropy (ΔJ) in the indirect spin-spin coupling constant tensor, as follows:

$$D_{eff} = D - \frac{\Delta J}{3} \quad (19)$$

Equation 19 assumes axial symmetry in the *J*-coupling tensor and that the *J*-coupling and direct dipolar coupling tensors are coincident with each other. For all simulations we assume that anisotropy is small and that $\Delta J = 0$. We note that large values of ΔJ and deviations from axial symmetry could dramatically change spectral features.

The final coupling constant, (IV), is the isotropic indirect spin-spin coupling constant, J_{iso}. Typical one bond *J*-couplings that have been observed for inorganic complexes range from $^{1}J(^{31}P\text{-}^{197}Au)$ = 120-700 Hz.[282,283]

The form of the spin-1/2 spectrum depends on the ratio, $R = D/J$ and on the dimensionless parameter *K*, which is defined as follows:

$$K = \frac{-3C_Q}{4S(2S-1)Z} \quad (20)$$

We first consider the case of Au(I)Cl(PPh_3), since C_Q is known. For all values of *D* and *J*, $R < 0.5$, and the large value of C_Q = 940 MHz observed for Au(I)Cl(PPh_3), leading to large absolute values of $|K| \approx 23$ and 28 at both 14.1 T and 11.7 T, respectively. Both $R < 0.5$ and the large absolute values of |K| require full diagonalization of the Hamiltonian for accurate spectral description, as outlined by Menger and Veeman.[284] At both field strengths studied, the $^{1}H\text{-}^{31}P$ CPMAS spectrum of Au(I)Cl(PPh_3) is predicted to collapse to the expected quartet to a doublet (Figure 44), and the spacing between the two observed lines is ~1.65 times the $^{1}J(^{197}Au\text{-}^{31}P)$ coupling constant. Changes in lineshape can be due to variation in C_Q, Euler angles, and the magnitude of coupling. For smaller values of C_Q and consequently smaller values of |K|, we find

that first-order perturbation theory may be sufficient to approximate ^{1}H-^{31}P CPMAS spectral lineshapes, especially in the case of partial self-decoupling.

Spectral simulations were performed for both field strengths examined (14.1 T and 11.7 T) using the WSolids software.[285] For the DPPBA-capped AuNPs, we employed first-order perturbation theory, which has been used successfully to approximate spin-1/2 spectra of nuclei coupled to quadrupolar nuclei, even in cases when $C_Q \geq \upsilon_s$.[286-288] The validity of using first-order perturbation theory to simulate the spectra of DPPBA-capped AuNPs was evaluated by comparing the spectral simulation of $[Au(dppey)_2]I$ (dppey = cis-bis(diphenylphosphino)ethylene), for which the crystal structure and ^{1}H-^{31}P CPMAS has been reported.[289] *Ab initio* calculations showed that $[Au(dppey)_2]I$ exhibited a C_Q value similar in magnitude to the particles (C_Q = -265 MHz). Using nuclear parameters from DFT, ^{31}P NMR spectra that resembled the experimental spectrum could be simulated with first-order perturbation theory.

In addition, quadrupolar nuclei that exhibit large C_Q values can exhibit fast quadrupolar T_1 relaxation. As a result of fast quadrupolar relaxation, the spin-1/2 spectrum may not exhibit the expected fine structure, and may be dramatically broadened,[290-292] due to partial self-decoupling. Since no distinct splittings were observed in our ^{31}P NMR spectra, the fast ^{197}Au T_1 relaxation was also taken into account in our simulations and the experimentally observed spectral breadth was simulated with line broadening in both the spectra of DPPBA-capped AuNPs and the ^{31}P NMR spectrum of $Au(I)Cl(PPh_3)$ at both field strengths.

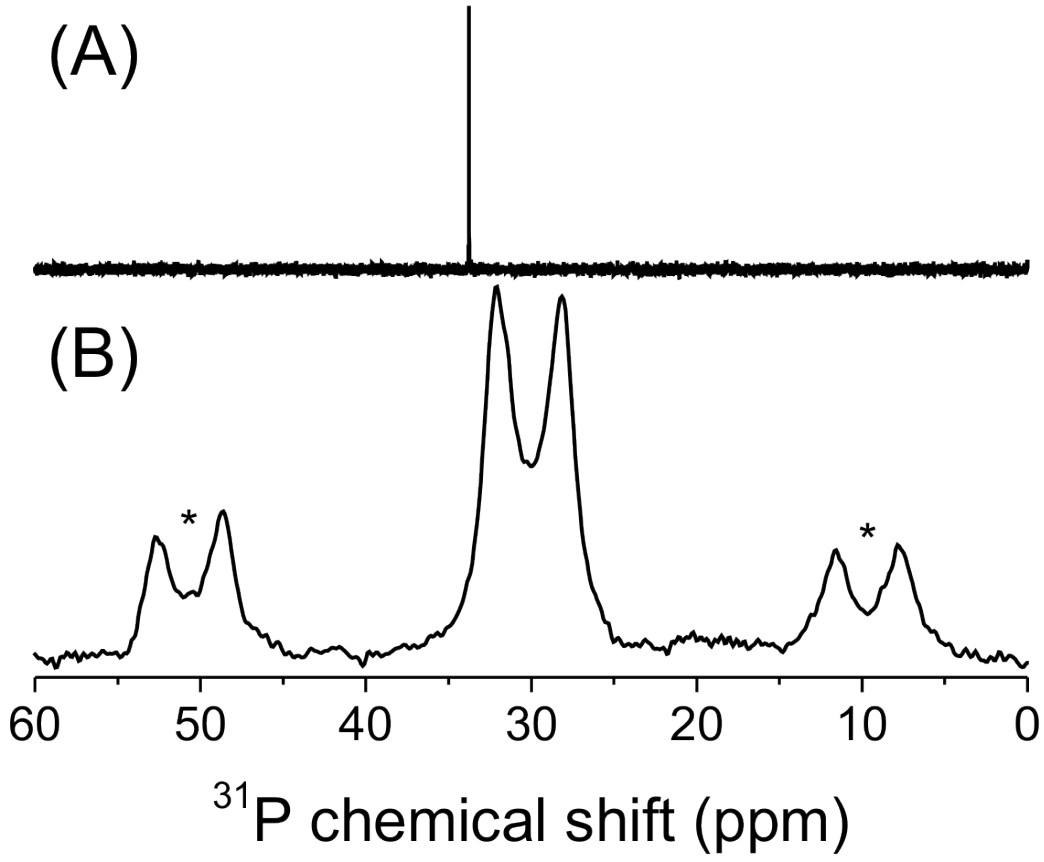

Figure 44. (A) Solution phase ^{31}P (δ = +33.8 ppm) and (B) solid-state ^{1}H-^{31}P CPMAS (δ = +30.2 ppm) NMR spectra of Au(I)Cl(PPh_3) recorded at 14.1 T. Asterisks denote spinning sidebands, MAS = 5 kHz

4.2.7 HRTEM

Purified DPPBA-terminated AuNPs were diluted 1:100 in water, and a 10.0 μL aliquot of the resulting solution was dropcast onto a lacey carbon TEM grid (Ted Pella, Inc.). Samples were allowed to air dry and were then dried under vacuum prior to characterization using a JEOL JEM 2100F operated at 200 kV and equipped with a Gatan Orius camera (Nanoscale Fabrication and Characterization Facility, Petersen Institute of Nanoscience and Engineering, University of Pittsburgh). The size distributions of AuNPs were determined from TEM images, and at least 200 individual AuNPs from various areas of the grid were measured. ImageJ 1.47d (National Institutes of Health, USA).[269]

4.2.8 Absorption Spectroscopy

Purified DPPBA-terminated AuNPs in D_2O were characterized by ultraviolet-visible-near-infrared (UV-vis-NIR) absorption spectroscopy using a Cary 5000 spectrophotometer (Agilent, Inc.) using quartz cuvettes (Hellma, Inc.) with a 1 cm path length. All spectra were baseline corrected with respect to the spectrum of D_2O.

4.2.9 XPS

DPPBA-terminated AuNPs were dropcast directly from the purified colloidal solution in aqueous 20 mM NaOH onto clean (for ultra-high vacuum conditions)[169] 1 cm × 1 cm silicon (*p*-doped (boron)) wafers (University Wafer, Boston, MA). The wafers were allowed to air dry and then were placed under vacuum for at least 24 h prior to analysis with XPS. XPS was performed using

an ESCALAB 250XI XPS with a monochromated, micro-focused Al Kα X-ray source (spot size = 400 μm). Survey and high resolution spectra were collected with a pass energy of 150 eV and 50 eV, respectively. Spectra were collected after Ar ion sputtering (500 eV, 10 seconds) prior to sample analysis. All XPS spectra were charge referenced to the adventitious carbon 1s peak at 284.8 eV.

4.3 RESULTS AND DISCUSSION

Here, we use a combination of solution phase and solid-state ^{31}P NMR spectroscopy to study small diameter (d = 1.8 ± 0.2 nm), phosphine-terminated Au nanoparticles (AuNPs, Figure 45). ^{31}P NMR spectroscopy is a promising route to characterizing metal nanoparticles because ^{31}P exhibits favorable NMR properties (spin-1/2, 100% natural abundance and gyromagnetic ratio, γ = 108.29 × 10^6 rad s^{-1} T^{-1}). Specifically, we use the water-soluble phosphine derivative, 4-(diphenylphosphino)benzoic acid (4-DPPBA), which has advantages for particle stability,[293] toxicity[294,295] and solubility (depending on solution pH). The extinction spectrum of the DPPBA-terminated AuNPs was relatively featureless and consistent with AuNPs in this size regime (Figure 45).

Surprisingly, solution phase ^{31}P NMR spectra of these particles exhibited a sharp (fwhm ~15 Hz) resonance at δ = +57.8 ppm (Figure 46). This ^{31}P NMR peak position was consistent with attachment of the phosphine ligand to a AuNP surface[22,50,77,294,296-304] (shifted 64.1 ppm downfield from the free ligand which resonates at δ = -6.3 ppm, Figure 47). However, the observed linewidth was dramatically more narrow than previous reports studying PPh_3-terminated AuNPs in this size range[50] as well as other similarly sized, water-soluble phosphine-

terminated AuNPs synthesized in our laboratory (see Figure 48 for characterization of bis(*p*-sulfonatophenyl)phenylphosphine (BSPP)-terminated AuNPs). Instead, the observed linewidth resembles spectra of phosphine ligands attached to high symmetry metal clusters (e.g. icosahedral cores = 9-55 metal atoms)[295,303] where the ligand uniformity is attributed to the symmetry of the metal core (*vide infra*).

To confirm that the resonance at +57.8 ppm was associated with AuNPs, ^{31}P diffusion ordered spectroscopy (DOSY) was conducted. These studies revealed that the ^{31}P resonance exhibited a diffusion coefficient consistent with attachment to a 1.8 nm metal core (D_{NP} = 1.5 × 10^{-10} ± 1.0 × 10^{-11} m^2 s^{-1}, d_H = 2.6 ± 0.2 nm, d_{core} = 1.8 ± 0.1 nm) and was not consistent with either a small molecule metal complex or the free ligand (chloro(triphenylphosphine)gold(I), Au(I)Cl(PPh_3), $D_{complex}$ = 1.4 × 10^{-9} ± 5.9 × 10^{-11} m^2 s^{-1}, d_H = 0.74 ± 0.03 nm; D_{ligand} = 4.6 × 10^{-10} ± 2.3 × 10^{-11} m^2 s^{-1}, d_H = 0.76 ± 0.04 nm).

Sharp, isotropic lineshapes can arise in solution phase NMR spectra due to a majority of phosphorus atoms being in the same chemical environment or from inter- or intra-particle dynamics that result in fast exchange between distinct environments, making it appear that ^{31}P sites are in the same environment on the NMR timescale.

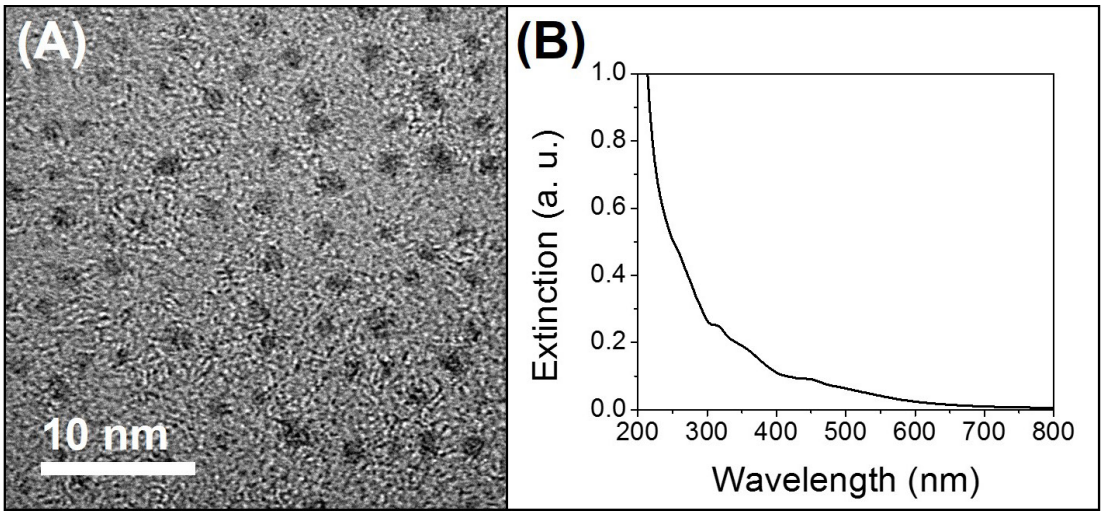

Figure 45. (A) High resolution transmission electron microscopy image of DPPBA-terminated AuNPs, and (B) their corresponding extinction spectrum. Average nanoparticle size: HRTEM = 1.8 ± 0.2 nm, N = 200, DOSY, d_H = 1.8 ± 0.1 nm

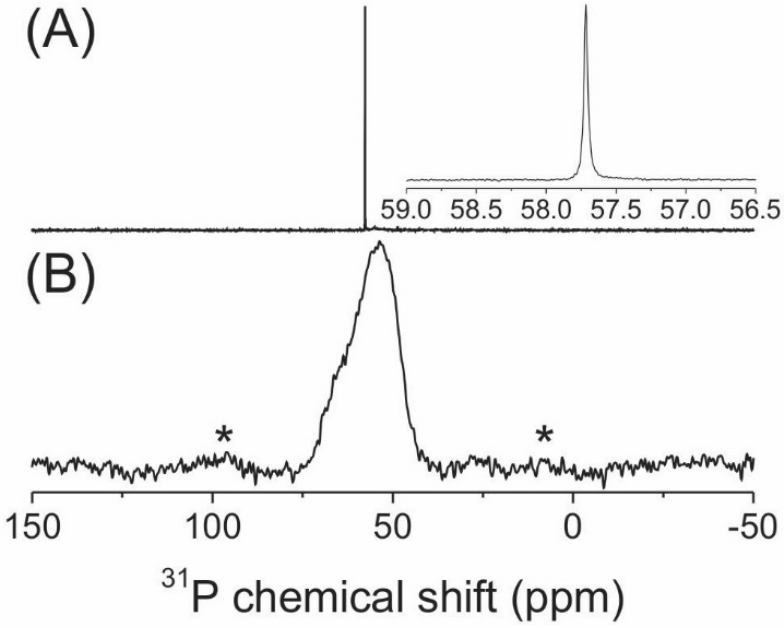

Figure 46. (A) Solution phase ^{31}P NMR with inset showing magnified peak region, and (B) solid-state ^{1}H-^{31}P CPMAS NMR spectra of DPPBA-terminated AuNPs recorded at 14.1 T. Asterisks denote spinning sidebands, MAS = 12 kHz

The most likely cause of inter-particle dynamics in NP systems is equilibrium ligand exchange with the surrounding medium. Previous work measured the rate constant of PPh_3 ligand exchange on d = 1.8 nm AuNPs to be 0.20 min^{-1} (0.003 s^{-1}),[50] which is the same magnitude as the ligand exchange rate constant measured for thiolate-terminated AuNPs.[305] However, from our solid-state ^{31}P NMR measurements (*vide infra*), we would estimate the rate constant of these processes to be on the order of 10^3 s^{-1}, which is dramatically inconsistent with the previously observed rates for equilibrium ligand exchange and indicates that ligand exchange is not the origin of the observed lineshapes. Further, we do not observe a ^{31}P diffusion coefficient that is an average of a population of ligands associated with the AuNP and free in solution, but instead suggests ligands appended to the NP core only.

Next, we consider two possible mechanisms of intra-particle dynamics that can result in isotropic lineshapes in solution NMR: ligand mobility on the NP surface and metal atom rearrangement in the core. Ligand motion has long been reported on the surfaces of small metal NPs, predominantly for di- and tri-atomic gas phase adsorbates.[306] However, 4-DPPBA has three phenyl rings and a carboxylate group that each can participate in interactions with either the Au surface or one another, which will significantly reduce ligand diffusion coefficients on the particle surface and therefore a ligand migration mechanism of line narrowing seems unlikely. Further, ligand mobility on AuNP surfaces is estimated to be slower than ligand exchange with the surrounding medium,[307] which is supported by data showing that ligand exchange of 4-DPPBA with higher affinity, mercaptoalkanoic acid ligands is not complete even after 16 h.[269]

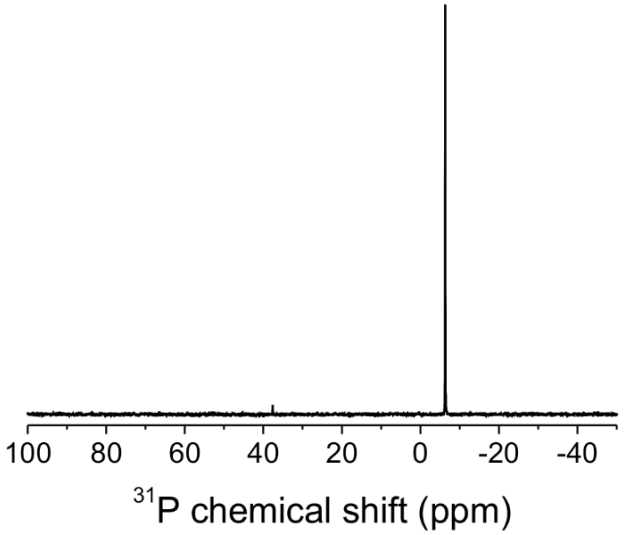

Figure 47. Solution phase ^{31}P NMR spectrum of 20 mM DPPBA (δ = -6.3 ppm) in 20 mM NaOH in D_2O at 14.1 T. The small peak at δ = +37.7 ppm was assigned to oxidized DPPBA, but only accounted for ~2 % of the total sample by signal integration

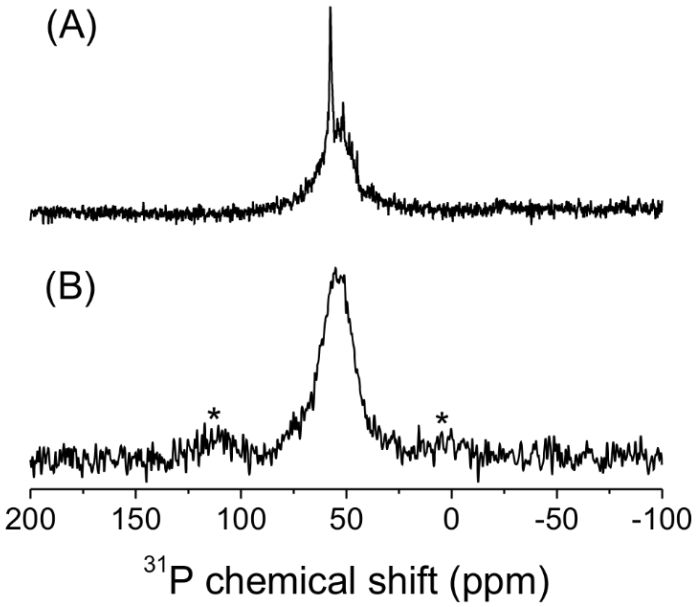

Figure 48. (A) Solution phase ^{31}P (δ sharp peak = +57.6 ppm) and (B) solid-state ^{1}H-^{31}P CPMAS (δ = +55.0 ppm) NMR spectra of BSPP-terminated AuNPs recorded at 14.1 T (A) and 11.7 T (B). Asterisks denote spinning sidebands, MAS = 10 kHz

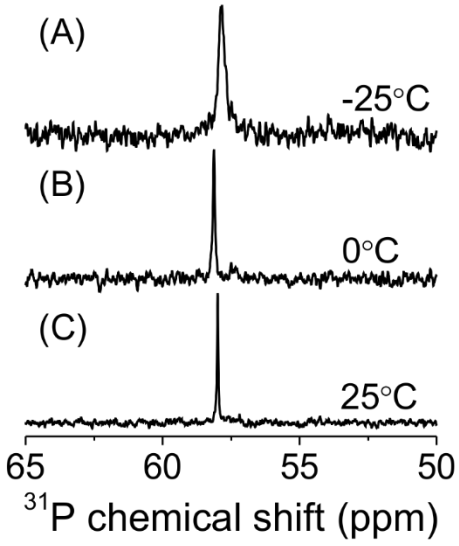

Figure 49. Solution ^{31}P NMR of DPPBA-terminated AuNPs in CD_2Cl_2 recorded at (A) -25 °C, (B) 0 °C, and (C) +25 °C

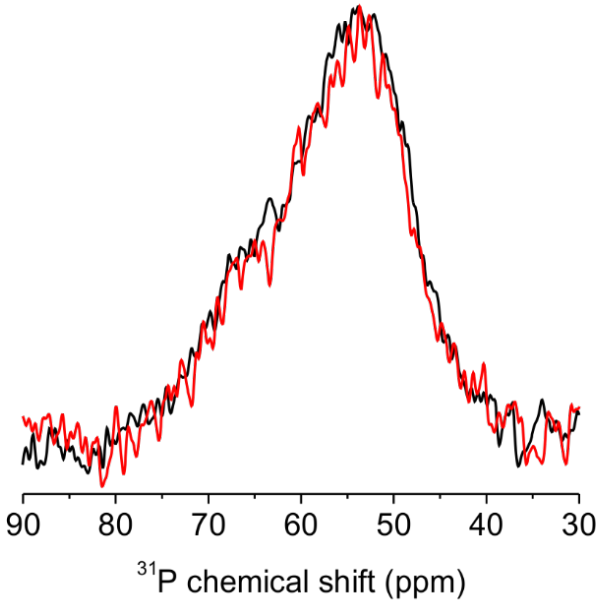

Figure 50. ^{1}H-^{31}P CPMAS NMR spectra of solid DPPBA-terminated AuNPs recorded at 25 °C (black) and 62 °C (red)

The other mode of intra-particle dynamics considered, metal atom rearrangement, has only been directly observed by NMR for metal clusters containing <10 metal atoms.[308] However, no metal atom motion has been observed by NMR for larger particle core sizes.[297,308] The absence of fluxionality with increasing core size is supported by reports on larger (>20 metal atoms) phosphine-[309-311] and thiol-terminated[71,266] NPs in which the solution phase NMR spectrum directly reflects known crystallographic data (e.g. even the particular element that the phosphorus atom is bound to can be discerned in ^{31}P NMR spectra for bimetallic particles[310,311]) and does not exhibit fluxionality on the NMR timescale, making metal atom rearrangement an unlikely source of spectral line narrowing.

To further assess whether inter- or intra-particle fluxionality was the source of the observed lineshapes, we performed both low temperature and high temperature solution phase and solid-state ^{31}P NMR experiments, respectively (-25 °C to 62 °C, Figure 49-50). In the solution phase at -25 °C, the peak at +57.8 ppm does not split into multiple peaks, but broadens as would be expected with increased rotational correlation time. Likewise, at 62 °C, solid-state ^{31}P NMR spectra exhibited no evidence of increased ligand exchange or on-particle mobility, which would be expected to occur if a low activation barrier to ligand or core fluxionality was present.

Taken together, these data uniformly suggest that the observed line narrowing is a result of all observed phosphorus atoms being in the same chemical environment. This phenomenon has also been observed in the ^{1}H NMR spectrum of $Au_{144}(p\text{MBA})_{60}$ clusters[312] (*p*MBA = *para*-mercaptobenzoic acid), suggesting a high degree of symmetry in the particle, but little more can be discerned in the absence of crystallographic data for either the DPPBA-terminated AuNPs reported here or $Au_{144}(p\text{MBA})_{60}$.

However, we note that our particle sample is not a collection of identical particles with respect to size, and chemical intuition would indicate that this particle dispersity (however slight) may lead to some dispersity in ligand environments. It is possible that different phosphine binding motifs can give fortuitously similar ^{31}P chemical shifts or that despite particle size dispersity, a common motif is present on the particle surface - similar to the ‘‘staple’’ motif on thiol-terminated AuNPs.

In order to provide a more robust description of the ^{31}P environment on the DPPBA-terminated AuNPs, ^{1}H-^{31}P cross-polarization magic-angle spinning solid-state NMR (CPMAS ssNMR) experiments were performed. However, unlike the solution phase ^{31}P spectrum, which exhibited a single isotropic resonance, the ^{31}P CPMAS spectrum exhibited a broad (fwhm ~3744 Hz), asymmetric lineshape at approximately +54 ppm (Figure 46), in addition to a small peak centered at approximately +27.5 ppm (peaks are distinct from spinning sidebands (*)). These results are surprising because the ^{1}H-^{31}P CPMAS spectra are acquired under high power ^{1}H decoupling and no ^{31}P-^{31}P homonuclear coupling is observed in the solution spectrum. In order to assign these new features, we conducted a series of variable field ^{31}P CPMAS NMR experiments, and modeled our results using first-order perturbation theory spectral simulations with parameter inputs calculated using density functional theory (DFT).

The difference between the solution and solid-state ^{31}P NMR spectra of DPPBA-terminated AuNPs indicates either that (I) DPPBA ligands undergo a structural rearrangement during solidification that leads to a loss of equivalence (i.e. ^{1}H-^{31}P CPMAS spectrum is the result of a inhomogeneous line broadening from a chemical shift distribution due to various crystallographic sites on the particle surface) or (II) the spin-1/2 ^{31}P nuclei are coupled to the quadrupolar ^{197}Au (spin-3/2, 100% abundant) nuclei of the particle.

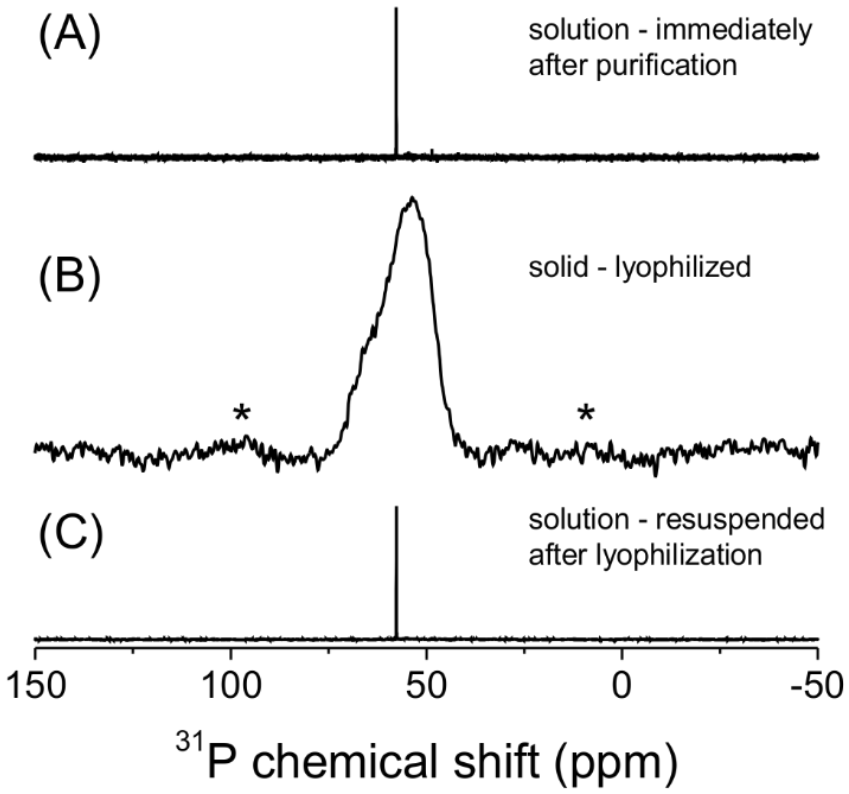

Figure 51. (A) Solution phase ^{31}P NMR of purified DPPBA-terminated AuNPs washed 4× with water and 2× with 20 mM NaOH in D_2O and diluted to volume in 20 mM NaOH in D_2O. (B) ^{1}H-^{31}P CPMAS NMR of purified, lyophilized DPPBA-terminated AuNP powders. MAS = 12 kHz. (C) Solution phase ^{31}P NMR of purified, lyophilized DPPBA-terminated AuNP powders that have been resuspended in 20 mM NaOH in D_2O. The peak position and fwhm in (C) is identical to that in (A). Higher SNR was achieved because the NP solutions were more concentrated after lyophilization and resuspension

In considering possible mechanisms for the first scenario, while it is difficult to envision that ligands have increased mobility in the solid state to adopt new motifs, various modes of particle degradation can be envisioned, especially as a result of mechanical stress when packing the material into a solid-state NMR rotor. Therefore, we conducted experiments in which the colloid was solidified and then resuspended in 20 mM NaOH in D_2O. No spectral changes were observed upon lyophilization and resuspension in either the solution phase ^{31}P or ^{1}H-^{31}P CPMAS spectra, indicating that the particles do not degrade (Figure 51).

The second scenario involves spin-3/2 quadrupolar interactions, which can appear differently in solution state and ssNMR spectra of the same system.[313] In the solution phase, we would expect ^{31}P NMR spectra to result in an isotropic lineshape because molecular tumbling results in rapid reorientation with respect to the external magnetic field, B_0, and facilitates efficient quadrupolar relaxation as well as subsequent ‘‘self-decoupling’’ of the quadrupolar nucleus. However, this self-decoupling effect is attenuated in the solid-state, sometimes dramatically.[313] This attenuation can result in the observation of indirect spin-spin coupling (*J*-coupling) and residual dipolar coupling between the spin-1/2 nuclei and the quadrupolar nuclei.

If ^{31}P-^{197}Au coupling is present in the spin-1/2 ^{1}H-^{31}P CPMAS spectrum, it will not be completely removed by MAS due to second-order quadrupolar effects, which is evident from the geometric factors in the dipolar Hamiltonian $[(3\cos2\theta - 1) + \eta\sin^2\theta \cos^2\beta]$, where θ and β are angles between the principal axis system and B_0. MAS conditions ($\theta = 54.74°$) are only useful at eliminating anisotropic interactions in which the Hamiltonian contains a single geometric factor $(3\cos^2\theta - 1)$, (e.g. chemical shift anisotropy (CSA), ^{31}P-^{1}H dipolar coupling), provided the spinning speed exceeds the magnitude of the interaction.

Since second-order quadrupolar interactions are inversely proportional to B_0, spectral features due to coupling between ^{31}P and ^{197}Au will be expected to increase in magnitude as B_0 is decreased, in ppm.[314] Conversely, for a chemical shift distribution, we would not expect the peak positions or linewidths to change in ppm as a function of B_0. (*N.B.* While spectral hole-burning experiments have been successfully used to distinguish between inhomogeneous and homogeneous sources of line broadening in NPs,[50,69,315] they can only be used in time-independent systems[316] which does not apply to scenario II[314]).

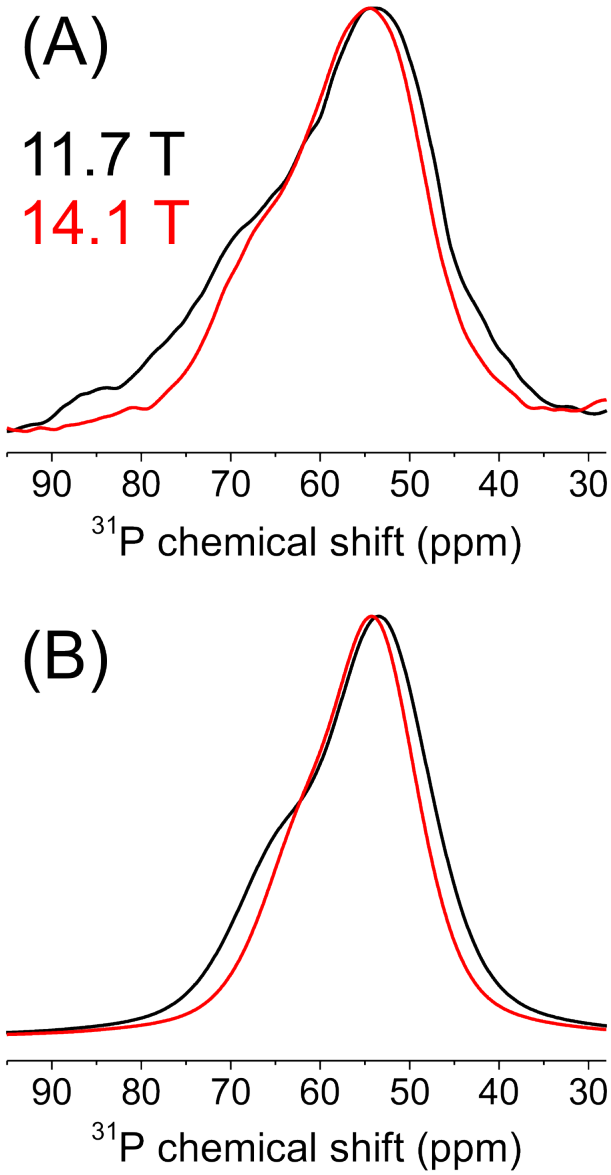

Figure 52. (A) Experimental and (B) simulated ^{1}H-^{31}P CPMAS spectra of DPPBA-terminated AuNPs at 14.1 T (red) and 11.7 T (black). Simulations used the quadrupolar coupling constant, asymmetry parameter, and Euler angles calculated with DFT for the phosphine binding site in $[Au_{39}(PPh_3)_{14}Cl_6]Cl_2$ exhibiting C_1 symmetry. $^{1}J(^{31}P,^{197}Au) = 730$ Hz

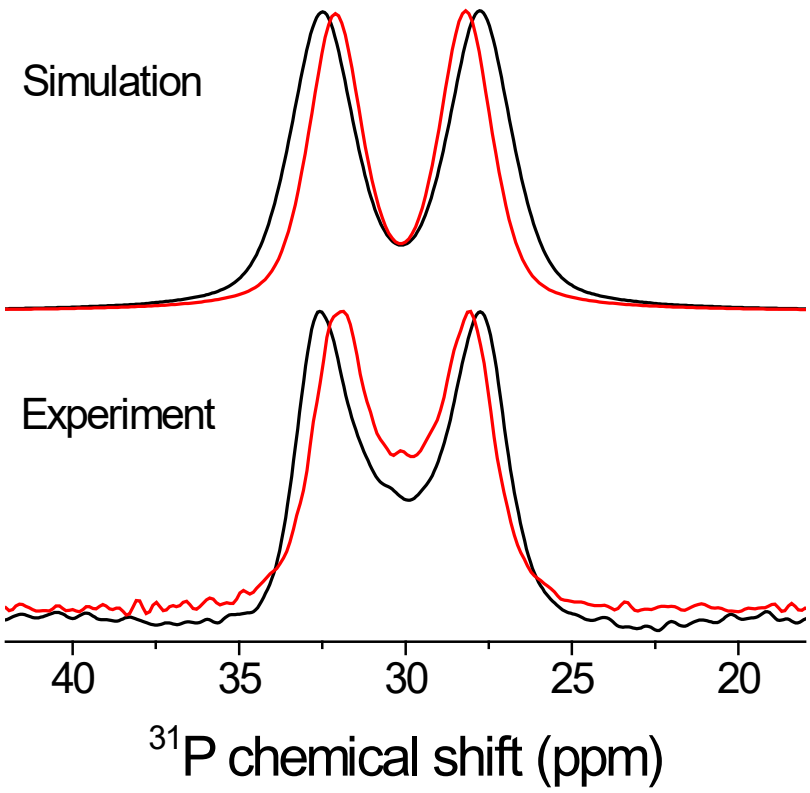

Figure 53. Experimental (bottom) and simulated (top) ^{1}H-^{31}P CPMAS spectra of Au(I)Cl(PPh$_3$) at 14.1 T (red) and 11.7 T (black). Simulation parameters = $^{1}J(^{31}P, ^{197}Au)$ = 575 Hz, LB = 450 Hz

Therefore, in order to determine the physical origin of the broad, asymmetric lineshape in the ^{1}H-^{31}P CPMAS NMR (i.e. scenario I vs. II described above), we also performed ^{1}H-^{31}P CPMAS NMR at a lower field strength (B_0 = 11.7 T) and compared our results with spectral simulations using the WSolids software.[285] For the DPPBA-terminated AuNPs, as B_0 is decreased from 14.1 T to 11.7 T, the spectral breadth of the ^{1}H-^{31}P CPMAS spectra increases slightly, going from 15.4 ppm to 17.9 ppm, respectively (Figure 52A), consistent with the presence of ^{31}P-^{197}Au coupling. This small increase in spectral breadth is also consistent with simulations that include both ^{31}P-^{197}Au scalar and residual dipolar couplings (Figure 52B, spectral breadth increases from 15.2 ppm to 17.9 ppm as B_0 is decreased from 14.1 T to 11.7 T) and ^{31}P-^{197}Au coupling observed in inorganic complexes (Figure 53), but is not consistent with a chemical shift distribution due to different crystallographic sites. Instead, if the change in lineshape upon drying the DPPBA-terminated AuNPs was due to structural rearrangement of the ligands and the ^{197}Au exhibited complete self-decoupling, we would expect to see the ^{1}H-^{31}P CPMAS linewidth to remain the same upon decreasing B_0 in ppm. Taken together, the DPPBA-terminated AuNPs exhibit solution and ssNMR ^{31}P spectral features as well as a B_0 dependence that are each consistent with ^{31}P-^{197}Au coupling and not a chemical shift distribution.

4.4 CONCLUSIONS

Overall, our results indicate that DPPBA-terminated AuNPs exhibit a uniform phosphine ligand environment in the solution phase, and that this homogeneity has allowed us to discern the presence of ^{31}P-^{197}Au coupling in the solid-state ^{1}H-^{31}P CPMAS spectrum. This unexpected finding indicates that indirect spin-spin coupling and/or residual dipolar coupling to spin-1/2

nuclei bound to the surface of quadrupole-containing metal nanoparticles (e.g. ^{197}Au, ^{105}Pd, $^{63/65}$Cu) must be considered (and may also be exploited) as a source of line broadening in ssNMR spectra.

5.0 TOWARD DE NOVO METAL CLUSTER DETERMINATION: IMPACTS OF LOCAL AND GLOBAL STRUCTURE AND DYNAMICS ON NMR SPECTRA

(Portions of this work are being prepared for submission as Marbella, L. E.; Hartmann, M. J.; Geib, S. J.; Millstone, J. E. **2016**, in preparation)

5.1 INTRODUCTION

Metal nanoclusters exhibit fundamentally interesting properties because their core size lies between that of systems with discrete, molecular electronic structure and those with bulk-like or continuous electronic states. This unique electronic structure produces a variety of new physical properties that range from unexpected catalytic behavior[317-321] to emergent optoelectronic phenomena.[251,252,269,322] Currently, our basis for correlating the structural origin of these properties relies primarily on single crystal X-ray diffraction (XRD).[323,324] Unfortunately, not all nanoclusters produce crystals (e.g. because ligands adopt multiple, non-uniform environments) that are suitable for single crystal X-ray studies, motivating the need for alternative characterization tools including combinations of pair distribution function (PDF) analysis,[325,326] X-ray absorption spectroscopy (XAS),[327] advanced transmission electron microscopy techniques,[328,329] and/or computational models.[330] Decades of research from the structural biology community suggest that NMR spectroscopy may also serve as a promising tool for *de*

novo structural characterization[331] and is beginning to be explored in the field of noble metal nanoparticles.[71,266,267,312]

However, before *de novo* structure characterization using NMR spectroscopy can be realized, we must establish a robust correlation between particle structural features and the observed NMR spectra. For metal nanoparticles, several aspects of particle electronic structure may influence the observed NMR spectrum beyond the spectral impacts of basic atomic connectivity within the particle (e.g. Knight shift contributions to adsorbates from free carriers in the underlying particle).[78,130] Interestingly, recent work suggests that symmetry equivalence, or lack thereof, in ligand attachment on thiolated Au clusters may be used to elucidate particle core structures via ^{1}H and ^{13}C solution NMR spectroscopies,[266,312] similar to fullerenes.[332] Understanding the structural features that correlate with specific NMR properties in metal nanoclusters has the potential to allow more rapid structure determination. Using spectroscopic patterns or signatures of various structural features is analogous to the use of chemical shift trends in ^{1}H, ^{13}C, and ^{15}N NMR spectra of biomolecules which can be used to assign secondary structure (e.g. beta sheet vs alpha helix) without two-dimensional NMR analysis.[333,334] Here, we consider two well-characterized Au nanoclusters,[276,335,336] $Au_{11}(PPh_3)_7Cl_3$ and $[Au_{11}(PPh_3)_8Cl_2]Cl$, that differ only in ligand shell composition and arrangement. Both $Au_{11}(PPh_3)_7Cl_3$ and $[Au_{11}(PPh_3)_8Cl_2]Cl$ contain 11 core Au atoms, providing structurally similar core geometries, and the same superatom electron count.[337] Comparison of these two clusters provides a route to study the influence of local and global cluster properties on the NMR signal of nuclei directly bound to the metal as a function of ligand shell composition and arrangement.

Specifically, we use a combination of solution phase and solid-state NMR (ssNMR), single-crystal XRD, absorption spectroscopy, and *ab initio* calculations to reveal the impact of

local vs global structural and dynamic features of $Au_{11}(PPh_3)_7Cl_3$ and $[Au_{11}(PPh_3)_8Cl_2]Cl$ on the observed ^{31}P NMR spectra. We demonstrate that in order to interpret the ^{31}P NMR fingerprints of $Au_{11}(PPh_3)_7Cl_3$ and $[Au_{11}(PPh_3)_8Cl_2]Cl$, both structural and dynamic features of the entire cluster must be considered (i.e. the local coordination environment of the ^{31}P nuclei are not sufficient to accurately predict the experimentally observed scalar couplings and chemical shifts). Ultimately, these studies connect common structural features in metal nanoclusters with their NMR signatures. Just as secondary architecture assignment in proteins yields more rapid and more accurate *de novo* structural characterization by NMR (via constraints in structure minimization), the spectral features reported here are an important step for NMR-based structural determination of nanoclusters.

5.2 EXPERIMENTAL

5.2.1 Materials and Methods

Chloro(triphenylphosphine)gold(I) ($Au(I)Cl(PPh_3)$, ≥ 99.9%), sodium borohydride ($NaBH_4$, ≥ 99.9%), anhydrous methylene chloride (CH_2Cl_2, ≥ 99.8%), hexane (≥ 99%), pentane (≥ 99%), diethyl ether (Et_2O, ≥ 99.7%), methanol (MeOH, ≥ 99.8%) and phosphoric acid solution (85% H_3PO_4) were purchased from Sigma Aldrich (St. Louis, MO). Absolute ethanol (EtOH) was purchased from Thermo Fisher Scientific (Pittsburgh, PA). Methylene chloride-d_2 (CD_2Cl_2, D, 99.96%) was obtained from Cambridge Isotope Laboratories (Andover, MA). All chemicals were used as received.

Prior to use, all glassware and Teflon-coated stir bars were washed with aqua regia (3:1 ratio of concentrated HCl to HNO_3) and rinsed with copious amounts of water prior to use. *Caution: aqua regia is highly toxic and corrosive, and should only be used with proper personal protective equipment and training. Aqua regia should be handled only inside a fume hood.*

5.2.2 Synthesis and Crystallization of $Au_{11}(PPh_3)_7Cl_3$

$Au_{11}(PPh_3)_7Cl_3$ was prepared according to a literature procedure.[335] Briefly, 250 mg (0.5 mmol) of $Au(I)Cl(PPh_3)$ was added to 14 mL of EtOH in a 50 mL round bottom flask, resulting in a cloudy, white solution. While stirring, 19 mg (0.5 mmol) of $NaBH_4$ in 4 mL of EtOH was added to the $Au(I)Cl(PPh_3)$ solution dropwise, resulting in a deep brownish-red solution. The reaction mixture was allowed to stir for 2 h before precipitation in 250 mL of hexane overnight. The supernatant was decanted and the precipitated solid was collected and redissolved in a minimal amount (~3 mL) of CH_2Cl_2. The redissolved product was precipitated in 250 mL of hexane four additional times. The crude product was isolated as an orange-red solid, redissolved in CH_2Cl_2, and filtered over a medium porosity fritted funnel. The solution obtained after filtration was further purified via crystallization. Orange-red needles of $Au_{11}(PPh_3)_7Cl_3$ were afforded by vapor diffusion of Et_2O into solutions of $Au_{11}(PPh_3)_7Cl_3$ in CH_2Cl_2 at -20 °C. Following purification, the crystals were analyzed using NMR spectroscopy, absorption spectroscopy, and single crystal XRD.

5.2.3 Synthesis and Crystallization of $[Au_{11}(PPh_3)_8Cl_2]Cl$

$[Au_{11}(PPh_3)_8Cl_2]Cl$ was prepared according to a literature procedure.[276] Briefly, 250 mg (0.5 mmol) of $Au(I)Cl(PPh_3)$ was dissolved in 10 mL of CH_2Cl_2, to produce a clear solution. While stirring, 5.2 mg (0.14 mmol) of $NaBH_4$ in 1.5 mL of EtOH was rapidly injected into the $Au(I)Cl(PPh_3)$ solution to produce a dark brownish-red solution. The reaction was allowed to stir for 24 h prior to solvent removal and resuspension in CH_2Cl_2 (~5 mL). The crude product was precipitated from ~100 mL of pentane. The supernatant was discarded and precipitation was repeated. The resulting solid was redissolved in a minimal amount of CH_2Cl_2 and purified by column chromatography. The crude product was added to a silica gel column that was prepared with a solvent mixture of 25:1 CH_2Cl_2:MeOH. The solvent mixture was gradually adjusted to 15:1 CH_2Cl_2:MeOH to elute a dark orange band containing $[Au_{11}(PPh_3)_8Cl_2]Cl$ and was monitored by UV-visible spectroscopy. Following elution, the solvent was removed from fractions containing $[Au_{11}(PPh_3)_8Cl_2]Cl$. The desired product was further purified via crystallization from slow evaporation of CH_2Cl_2/octane (5/1, v/v) at room temperature. Orange-red plates of $[Au_{11}(PPh_3)_8Cl_2]Cl$ were removed from the light yellow mother liquor and further characterized with NMR spectroscopy, absorption spectroscopy, and single crystal XRD.

5.2.4 Absorption Spectroscopy

Crystals of $Au_{11}(PPh_3)_7Cl_3$ and $[Au_{11}(PPh_3)_8Cl_2]Cl$ were dissolved in CH_2Cl_2 and characterized by ultraviolet-visible (UV-vis) absorption spectroscopy using a Cary 5000 spectrophotometer (Agilent, Inc.) using quartz cuvettes (Hellma, Inc.) with a 1 cm path length. All spectra were baseline corrected with respect to the spectrum of CH_2Cl_2.

5.2.5 Solution Phase NMR Spectroscopy

Crystals of $Au_{11}(PPh_3)_7Cl_3$ and $[Au_{11}(PPh_3)_8Cl_2]Cl$ were dissolved in methylene chloride-d_2 and loaded into Teflon-sleeved NMR tubes. Teflon sleeved NMR tubes were used because organo-soluble phosphine-terminated Au nanoparticles are known to decompose on glass.[50] Room temperature ^1H and ^{31}P NMR experiments were recorded on a Bruker Avance III 600 MHz (14.1 T) spectrometer with a broadband fluorine observe (BBFO) Plus probe at 25 °C. Temperature was maintained using a Bruker BVT3000 variable temperature system. ^1H chemical shifts were referenced to the residual solvent peak. ^{31}P chemical shifts were externally referenced to 85% H_3PO_4 (aq) at 0 ppm. Single pulse ^1H NMR spectra were acquired after a $\pi/6$ pulse with a recycle delay of 5 s. Single pulse ^{31}P spectra were acquired after a $\pi/2$ pulse with WALTZ-16 ^1H decoupling during acquisition with a recycle delay of 60 s. Low temperature (temperatures ranged from -77 to 0 °C) solution ^{31}P NMR spectra were collected on a Bruker Avance 500 MHz (11.7 T) spectrometer. Temperature was maintained with a BVT3000 variable temperature unit equipped with nitrogen cooling.

5.2.6 Solid-State NMR Spectroscopy

Crystals of $Au_{11}(PPh_3)_7Cl_3$ and $[Au_{11}(PPh_3)_8Cl_2]Cl$ were packed into 4 mm zirconia rotors for analysis with ^1H-^{31}P cross-polarization magic-angle spinning (CPMAS) NMR techniques. Prior to each sample analysis, the magic-angle was calibrated with KBr by maximizing the number of rotary echoes observed in the FID of the ^{79}Br NMR spectrum while spinning at 8 kHz. All ^1H-^{31}P CPMAS NMR spectra were recorded on a Bruker Avance 500 MHz (11.7 T) spectrometer, equipped with a triple-resonance 4 mm CPMAS probehead operating at a ^{31}P Larmor frequency

of 202.45 MHz and ^{1}H Larmor frequency of 500.13 MHz. Temperature was maintained with a BVT3000 variable temperature unit. ^{1}H-^{31}P Hartmann-Hahn match conditions were as follows: ^{1}H 90° pulse widths were ~5 μs with a contact time of 2 ms. Two-pulse phase-modulated (TPPM-20) high power ^{1}H decoupling at 80 kHz was applied during data acquisition. MAS spinning rates of 10 kHz and recycle delays of 5 s were used for all studies.

5.2.7 Single Crystal XRD

X-ray intensity data for $Au_{11}(PPh_3)_7Cl_3$ and $[Au_{11}(PPh_3)_8Cl_2]Cl$ were collected on a Bruker Apex II CCD system equipped with a Cu IMuS micro-focus source (λ = 1.54178 Å). For $Au_{11}(PPh_3)_7Cl_3$, the total exposure time was 28.14 hours. The frames were integrated with the Bruker SAINT software package using a narrow-frame algorithm. The integration of the data using a monoclinic unit cell yielded a total of 37787 reflections to a maximum θ angle of 50.45° (1.00 Å resolution), of which 6829 were independent (average redundancy 5.533, completeness = 99.0%, R_{int} = 57.85%, R_{sig} = 54.09%) and 1943 (28.45%) were greater than $2\sigma(F^2)$. The final cell constants of a = 16.011(5) Å, b = 26.339(8) Å, c = 16.467(5) Å, β = 112.685(10) °, volume = 6407.(3) $Å^3$, are based upon the refinement of the XYZ-centroids of 164 reflections above 20 σ(I) with 5.815° < 2θ < 46.67°. Data were corrected for absorption effects using the multi-scan method (SADABS). The ratio of minimum to maximum apparent transmission was 0.521. The calculated minimum and maximum transmission coefficients (based on crystal size) are 0.3900 and 0.7500.

The structure was solved and refined using the Bruker SHELXTL Software Package, using the space group *P*1 $2_1/m$ 1, with Z = 2 for the formula unit, $C_{126}H_{105}Au_{11}Cl_3P_7$. The final anisotropic full-matrix least-squares refinement on F^2 with 112 variables converged at R1 =

14.05%, for the observed data and wR2 = 38.49% for all data. The goodness-of-fit was 1.216. The largest peak in the final difference electron density synthesis was 3.348 $e^-/Å^3$ and the largest hole was -2.457 $e^-/Å^3$ with an RMS deviation of 0.423 $e^-/Å^3$. On the basis of the final model, the calculated density was 2.130 g/cm^3 and F(000), 3772 e^-.

For $[Au_{11}(PPh_3)_8Cl_2]Cl$, The frames were integrated with the Bruker SAINT software package using a narrow-frame algorithm. The integration of the data using a monoclinic unit cell yielded a total of 76942 reflections to a maximum θ angle of 46.95° (1.05 Å resolution), of which 12651 were independent (average redundancy 6.082, completeness = 98.7%, R_{int} = 18.48%, R_{sig} = 11.21%) and 9163 (72.43%) were greater than $2\sigma(F^2)$. The final cell constants of a = 22.5966(10) Å, b = 18.5467(8) Å, c = 34.5033(14) Å, β = 96.123(3)°, volume = 14377.6(11) $Å^3$, are based upon the refinement of the XYZ-centroids of reflections above 20 σ(I). Data were corrected for absorption effects using the multi-scan method (SADABS).

The structure was solved and refined using the Bruker SHELXTL Software Package, using the space group *P*1 $2_1/c$ 1, with Z = 4 for the formula unit, $C_{144}H_{120}Au_{11}Cl_2P_8$. The final anisotropic full-matrix least-squares refinement on F^2 with 490 variables converged at R1 = 10.16%, for the observed data and wR2 = 27.11% for all data. The goodness-of-fit was 1.785. The largest peak in the final difference electron density synthesis was 9.292 $e^-/Å^3$ and the largest hole was -3.700 $e^-/Å^3$ with an RMS deviation of 0.465 $e^-/Å^3$. On the basis of the final model, the calculated density was 2.003 g/cm^3 and F(000), 8028 e^-.

5.2.8 Ab Initio Calculations

Calculations were performed using density functional theory (DFT) as implemented in grid-based projector augmented wave code (GPAW).[338,339] Structural optimizations we preformed

within the local density approximation (LDA), with a grid spacing of 0.2 Å, a convergence criterion of 0.05 eV/Å for the residual force, were performed without a symmetry constraint, and scalar relativistic corrections were included for the Au atoms. The LDA exchange correlation (XC) functional is known to reproduce empirically determined Au-Au bond lengths more accurately than higher level functionals, an important parameter for the simulation of absorption spectra.[340,341] The optical absorption calculations were performed from the relaxed structures using Casida's formulation of linear response time dependent density functional theory (LR-TDDFT),[342] as implemented by GPAW using the Perdew-Burke-Ernzerhof (PBE) XC. HOMO-LUMO gaps calculated with PBE exhibit good agreement with experiment for small Au nanocluster systems at low costs compared to other XC functionals.[343] Calculated, discrete transitions were broadened with Gaussian functions having widths of 0.08 eV to simulate experimental absorption spectra.

Table 6. Nuclear properties for $Au_{11}(PMe_3)_7Cl_3$ calculated with DFT

^{31}P site	C_Q (MHz) ^{197}Au	η ^{197}Au	α^D (°)	β^D (°)	J_{iso} (Hz) ^{31}P-^{197}Au	ΔJ (Hz) ^{31}P-^{197}Au	D (Hz) ^{31}P-^{197}Au	δ (ppm) ^{31}P
P1	-439.9	0.342	24.1	176.3	378.8	174.8	74.1	54.5
P2	-445.3	0.379	139.9	177.9	378.3	174.8	68.6	55.2
P3	-435.4	0.339	152.7	176.0	385.7	175.1	68.6	55.4
P4	-438.4	0.333	11.3	4.5	378.3	174.8	65.6	54.5
P5	-492.2	0.020	149.6	177.8	206.0	154.8	57.0	51.8
P6	-440.8	0.365	163.2	178.1	360.5	171.9	68.6	58.4
P7	-452.6	0.313	152.0	1.5	347.8	171.6	65.6	57.5

Table 7. Nuclear properties for $[Au_{11}(PMe_3)_8Cl_2]Cl$ calculated with DFT

^{31}P site	C_Q (MHz) ^{197}Au	η ^{197}Au	α^D (°)	β^D (°)	J_{iso} (Hz) ^{31}P-^{197}Au	ΔJ (Hz) ^{31}P-^{197}Au	D (Hz) ^{31}P-^{197}Au	δ (ppm) ^{31}P
P1	-426.7	0.256	113.0	175.6	412.1	183.7	74.3	57.0
P2	-424.4	0.400	135.9	178.8	391.4	180.4	70.4	49.5
P3	-468.6	0.240	45.8	174.6	339.2	173.9	74.0	49.1
P4	-475.5	0.255	170.1	172.4	348.8	176.4	74.5	45.6
P5	-505.0	0.178	168.2	176.2	298.3	171.1	70.5	46.3
P6	-473.0	0.128	49.3	3.4	297.0	166.9	68.3	50.4
P7	-449.8	0.218	25.6	1.4	321.9	170.1	72.3	60.4
P8	-506.3	0.030	89.8	1.7	263.1	164.6	68.0	45.8

Density functional theory (DFT) as implemented in the Amsterdam Density Functional (ADF) code was used to calculate chemical shielding tensors, electric field gradient (EFG) tensors, **J** tensors, quadrupolar coupling constants, asymmetry parameters, and Euler angles[270-272] of geometrically optimized $Au_{11}(PMe_3)_7Cl_3$ and $[Au_{11}(PMe_3)_8Cl_2]Cl$. Results from DFT calculations on the entire clusters were compared to individual phosphine binding sites, which were modeled as the immediate coordination complex. All NMR parameters were calculated with the hybrid BLYP[344,345] exchange correlation functional using a polarized triple zeta basis set (TZ2P). Spin orbit relativistic effects for Au were accounted for within the Zeroth-Order Relativistic Approximation (ZORA).[275] Isotropic ^{31}P chemical shielding values were converted to ^{31}P chemical shifts by using 223.0 ppm as the ^{31}P reference shielding value, in order to achieve the chemical shift range observed experimentally. Calculated parameters used for inputs in spectral simulations are listed in Tables 6 and 7.

5.2.9 Spectral Simulations

Spectral simulations of the geometrically relaxed $Au_{11}(PMe_3)_7Cl_3$ and $[Au_{11}(PMe_3)_8Cl_2]Cl$ were performed using the WSolids software[285] using full matrix diagonalization and compared to experimental ^{1}H-^{31}P CPMAS spectra of $Au_{11}(PMe_3)_7Cl_3$ and $[Au_{11}(PMe_3)_8Cl_2]Cl$ and a 50:50 mixed Lorentzian:Gaussian line broadening of 300 Hz. Small alterations that maintained the qualitative trends of isotropic chemical shielding and *J*-coupling outputs calculated from DFT were able to successfully simulate the experimentally observed ^{31}P NMR spectra.

5.3 RESULTS

After crystallization, the isolation of $Au_{11}(PPh_3)_7Cl_3$ and $[Au_{11}(PPh_3)_8Cl_2]Cl$ was confirmed with single crystal XRD (Figure 54, see Appendix Tables 16-24 for crystallographic data), solution ^{1}H and ^{31}P NMR spectroscopy (Figure 55A and B, respectively), and UV-visible spectroscopy (Figure 56). Based on single crystal XRD (Figure 54), both clusters have nearly identical core structures, allowing us to determine the influence of ligand arrangement on NMR spectra of the appended ligands.

First, the optoelectronic features of $Au_{11}(PPh_3)_7Cl_3$ and $[Au_{11}(PPh_3)_8Cl_2]Cl$ were analyzed with absorption spectroscopy (Figure 56) to understand the influence of the ligand shell on observed optoelectronic behaviors. Both clusters display distinct peaks, characteristic of discrete electronic transitions expected for Au cores at this size range.[346] In the visible region of the absorption spectrum, $Au_{11}(PPh_3)_7Cl_3$ and $[Au_{11}(PPh_3)_8Cl_2]Cl$ have an onset of absorption at approximately 600 nm, a broad peak at 512 nm, as well as sharp transitions at 415 and 420 nm, respectively ($|E_{Au11(PPh3)7Cl3}-E_{[Au11(PPh3)8Cl2]Cl}| = \Delta = 0.036$ eV, Table 8). Here, the similar onset of absorption at approximately 600 nm is consistent with the HOMO-LUMO gaps derived from first-principle calculations of 2.076 and 2.057 eV for $Au_{11}(PPh_3)_7Cl_3$ and $[Au_{11}(PPh_3)_8Cl_2]Cl$, respectively.

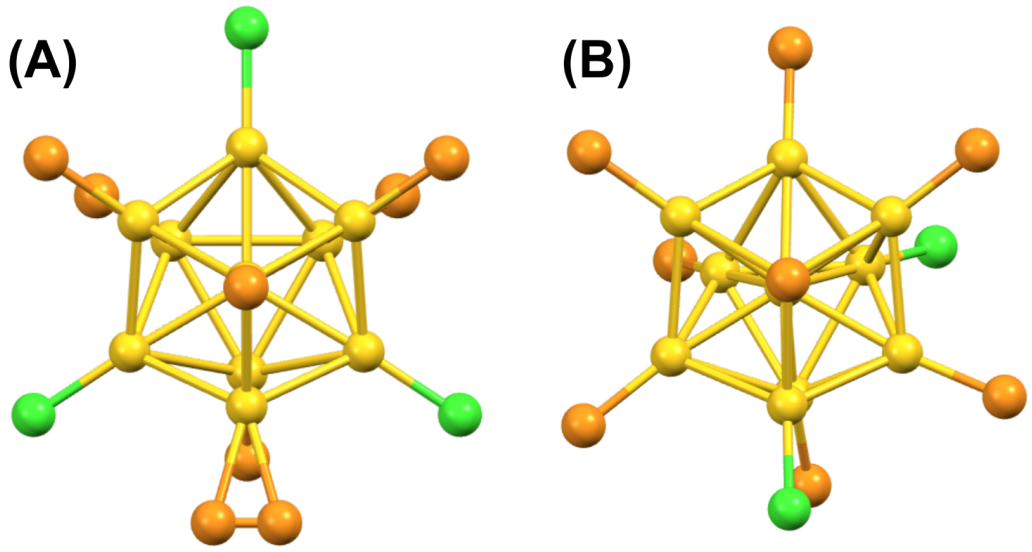

Figure 54. Structure of (A) $Au_{11}(PPh_3)_7Cl_3$ and (B) $[Au_{11}(PPh_3)_8Cl_2]Cl$ derived from single-crystal XRD data. Organic components (C and H) are eliminated for clarity. Orange = P, green = Cl, yellow = Au

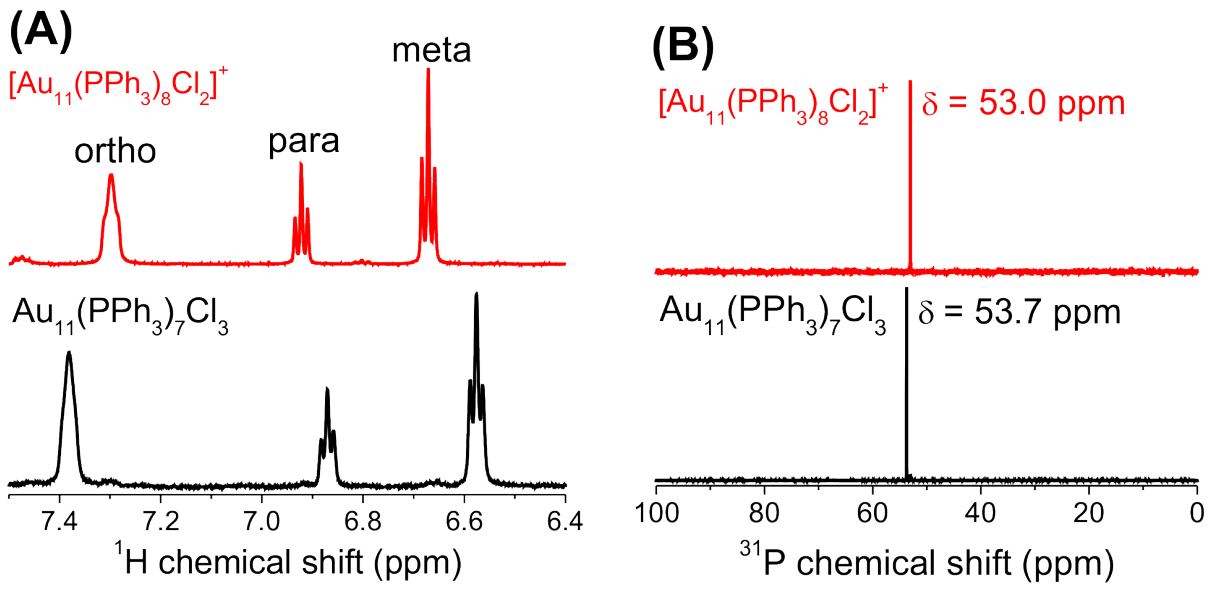

Figure 55. Solution (A) ^{1}H NMR and (B) ^{31}P NMR characterization of $Au_{11}(PPh_3)_7Cl_3$ (black) and $[Au_{11}(PPh_3)_8Cl_2]Cl$ (red) in CD_2Cl_2 recorded at 14.1 T at 25 °C

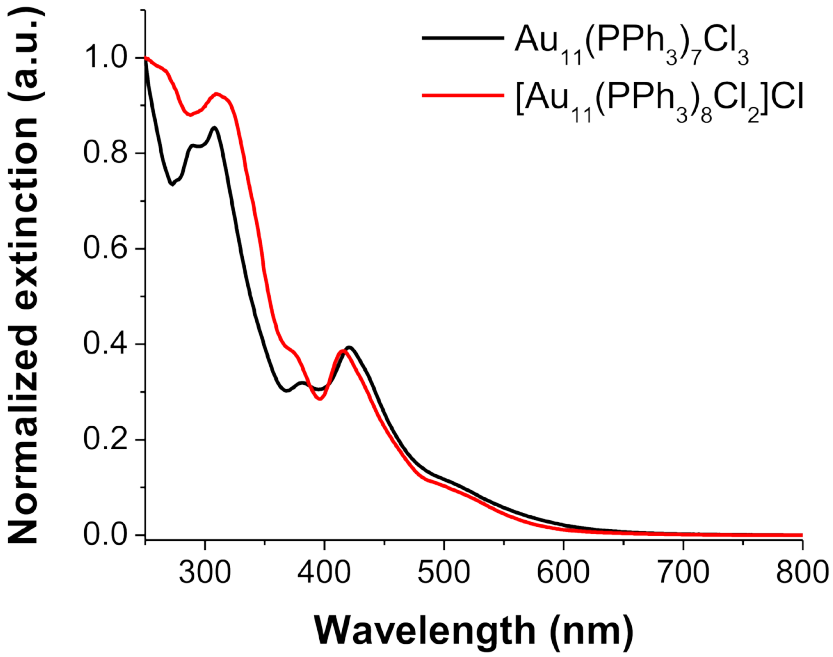

Figure 56. UV-visible spectra of $Au_{11}(PPh_3)_7Cl_3$ (black) and $[Au_{11}(PPh_3)_8Cl_2]Cl$ (red) in CH_2Cl_2

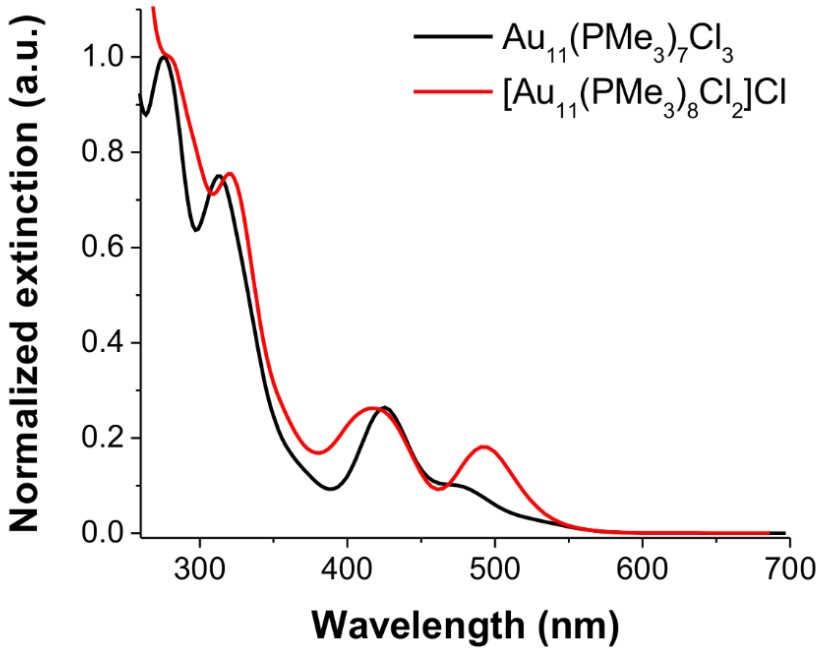

Figure 57. Simulated absorption spectra of $Au_{11}(PMe_3)_7Cl_3$ (black) and $[Au_{11}(PMe_3)_8Cl_2]Cl$ (red)

By simulating the absorption spectra (Figure 57), the remaining peaks in the visible region (512, 420, and 415 nm) can be assigned to transitions that are primarily localized within the 11 Au atoms that compose the core of each cluster (Figures 58-59). Since the core structures are similar between $Au_{11}(PPh_3)_7Cl_3$ and $[Au_{11}(PPh_3)_8Cl_2]Cl$, it is reasonable to expect these core-to-core transitions to show similar energies. Calculated absorption spectra are sensitive to the level of theory used for both the structural optimization and the LR-TDDFT calculation, each of which can lead to small differences between calculated and experimental absorption spectra.[340] For each cluster, the absorption spectra derived from first principles are in qualitative agreement with experimental spectra, allowing the assignment of each transition.

Conversely, larger deviations in transition energies between the two clusters are observed in the UV region of the absorption spectrum. In the UV range, $Au_{11}(PPh_3)_7Cl_3$ has three peaks at 381, 308, and 289 nm, while $[Au_{11}(PPh_3)_8Cl_2]Cl$ exhibits three separate peaks at 374, 320, and 309 nm (Table 8). Assignment of these peaks with LR-TDDFT revealed that the higher energy transitions include more participation from surface states than the lower energy transitions (Figures 59-60). These assignments suggest that the most drastic deviations in the absorption spectra can be attributed to differences in the composition and arrangement of ligands appended to the cluster. Single crystal XRD indicates that $Au_{11}(PPh_3)_7Cl_3$ and $[Au_{11}(PPh_3)_8Cl_2]Cl$ contain different local crystallographic environments with respect to ligand binding sites, which is consistent with spectroscopic deviation in this region.

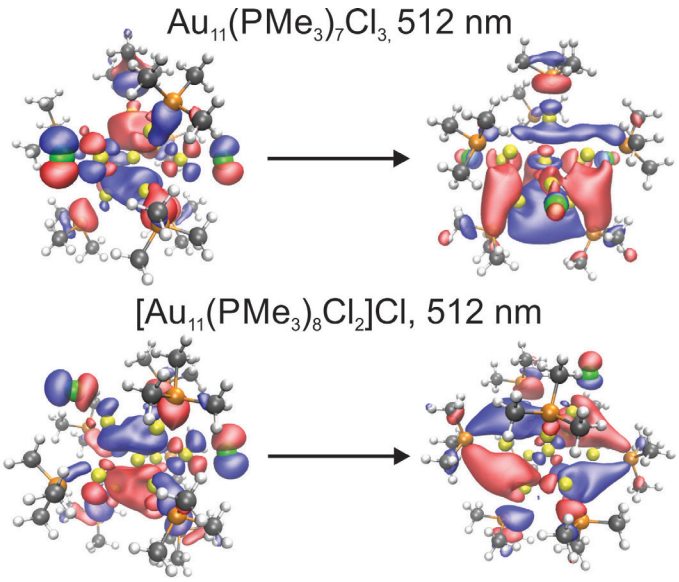

Figure 58. Representative orbitals of the before (left) and after (right) the transitions at 512 nm for $Au_{11}(PMe_3)_7Cl_3$ (top) and $[Au_{11}(PMe_3)_8Cl_2]Cl$ (bottom). The transitions primarily contain core-to-core character

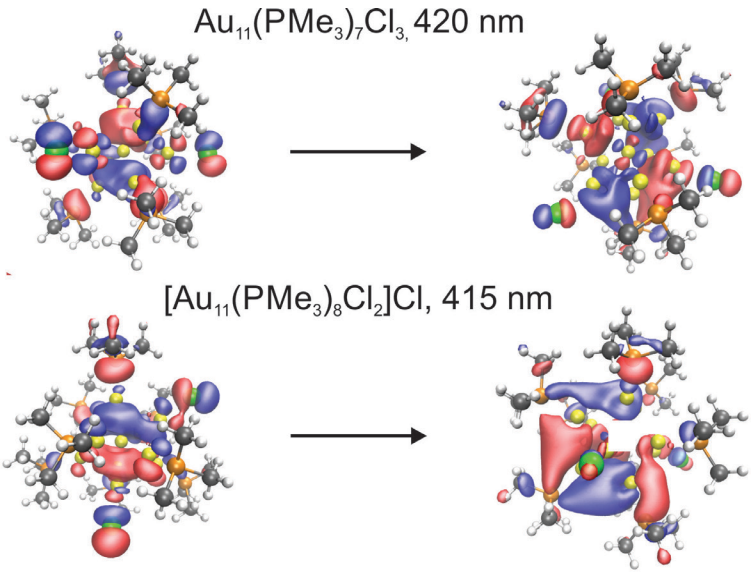

Figure 59. Representative orbitals of the before (left) and after (right) the transitions at 420 nm for $Au_{11}(PMe_3)_7Cl_3$ (top) and 415 nm $[Au_{11}(PMe_3)_8Cl_2]Cl$ (bottom). The transitions primarily contain core-to-core character

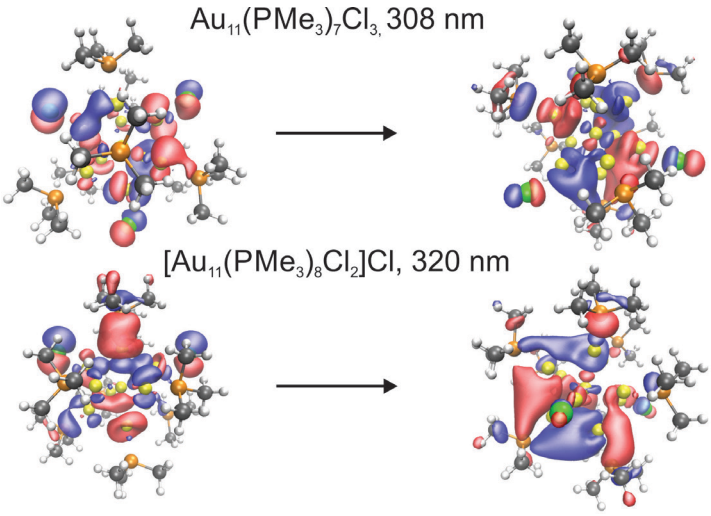

Figure 60. Representative orbitals of the before (left) and after (right) the transitions at 308 nm for $Au_{11}(PMe_3)_7Cl_3$ (top) and 320 nm $[Au_{11}(PMe_3)_8Cl_2]Cl$ (bottom). The transitions primarily contain ligand-to-core character

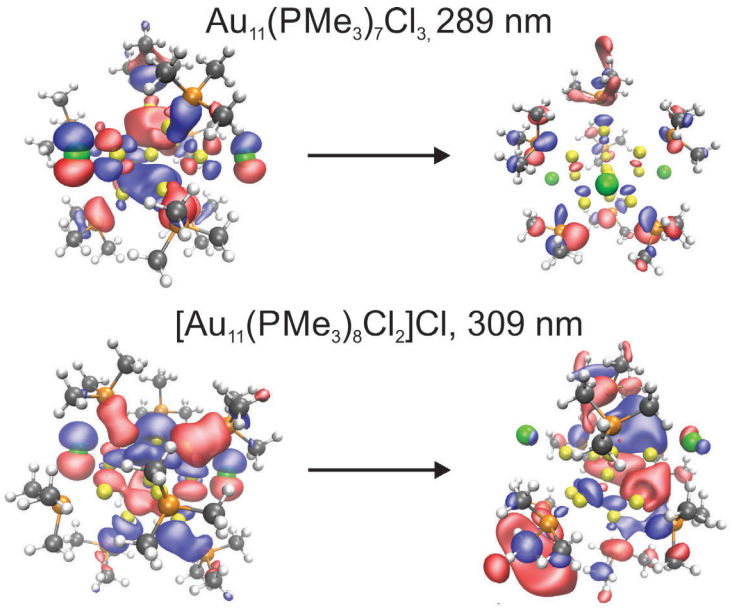

Figure 61. Representative orbitals of the before (left) and after (right) the transitions at 289 nm for $Au_{11}(PMe_3)_7Cl_3$ (top) and 309 nm $[Au_{11}(PMe_3)_8Cl_2]Cl$ (bottom). The transitions primarily contain ligand-to-ligand character

Table 8. Transitions observed in absorption spectra for $Au_{11}(PPh_3)_7Cl_3$ and $[Au_{11}(PPh_3)_8Cl_2]Cl$

λ_{max} (nm) $Au_{11}(PPh_3)_7Cl_3$	λ_{max} (nm) $[Au_{11}(PPh_3)_8Cl_2]Cl$	E (eV) $Au_{11}(PPh_3)_7Cl_3$	E (eV) $[Au_{11}(PPh_3)_8Cl_2]Cl$	$\lvert\Delta E\rvert$ (eV)
512	512	2.422	2.422	0
415	420	2.988	2.952	0.036
381	374	3.254	3.315	0.061
308	320	4.025	3.875	0.150
289	309	4.290	4.012	0.278

Likewise, solution ^{1}H and ^{31}P NMR spectroscopy show differences in the resonances corresponding to PPh_3 for both clusters. Although distinct chemical shifts are observed for each cluster, only one resonance is observed for each position on the ring (e.g. ortho, meta, para) for both $Au_{11}(PPh_3)_7Cl_3$ and $[Au_{11}(PPh_3)_8Cl_2]Cl$ in the solution ^{1}H NMR spectra. Similar results are observed in the ^{31}P NMR spectra, where only one resonance is observed at room temperature for each cluster, albeit at different chemical shifts. To determine the physical origin of the magnetic equivalence observed in the solution phase spectra, $Au_{11}(PPh_3)_7Cl_3$ and $[Au_{11}(PPh_3)_8Cl_2]Cl$ are also studied with low temperature (-80 °C) solution and solid-state ^{31}P NMR spectroscopy (Figure 62). For $[Au_{11}(PPh_3)_8Cl_2]Cl$, both low temperature (-80 °C) solution ^{31}P NMR spectroscopy and solid-state ^{1}H-^{31}P CPMAS of $[Au_{11}(PPh_3)_8Cl_2]Cl$ are consistent with independent ^{31}P environments on the cluster surface (Figure 62B) present in the crystallographic data. The spread in ^{31}P frequencies increases in the solid state compared to the distribution in solution, likely due to the presence of ^{31}P-^{197}Au coupling.[283,289,347-349] From single crystal XRD, we know that $[Au_{11}(PPh_3)_8Cl_2]Cl$ shows an overall C_1 cluster symmetry. The low cluster symmetry of $[Au_{11}(PPh_3)_8Cl_2]Cl$ combined with a relatively ordered ligand shell (*vide infra*), results in the observation of multiple ^{31}P resonances in both the low temperature solution and ssNMR spectra.[350] Interestingly, the presence of only a single ^{31}P resonance in the room temperature solution ^{31}P NMR spectrum of $[Au_{11}(PPh_3)_8Cl_2]Cl$ indicates that intra-cluster motion may be responsible for dynamic averaging, perhaps due to intra-ligand dynamics (e.g. P-C and P-M bond rotations are on the order of 2 kcal/mol in solution[351]) and/or metal atom displacement in the core at room temperature in solution (*vide infra*).[298]

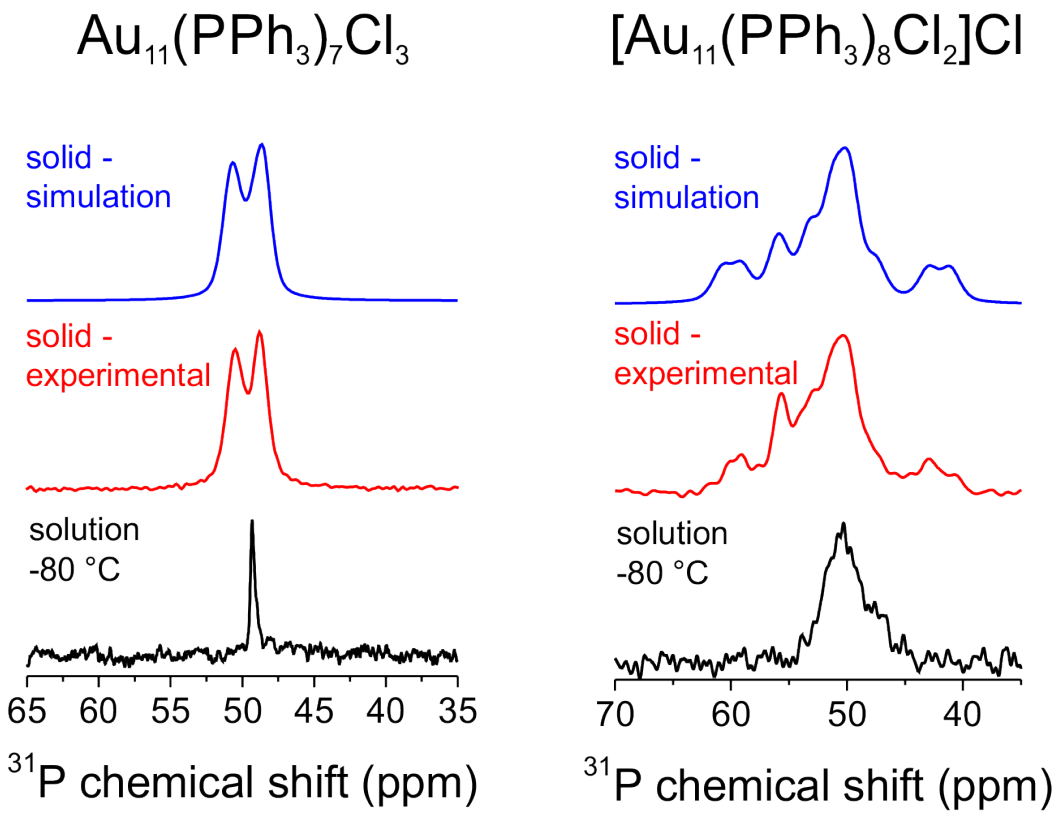

Figure 62. Low temperature (-80 °C) solution phase ^{31}P NMR in CD_2Cl_2 (black), experimental ^{1}H-^{31}P CPMAS ssNMR (red, MAS = 10 kHz), and simulated ^{1}H-^{31}P CPMAS ssNMR (blue) of $Au_{11}(PPh_3)_7Cl_3$ (left) and $[Au_{11}(PPh_3)_8Cl_2]Cl$ (right)

The influence of thermal vibration on the observed NMR features can be distinguished by comparing to the spectra obtained for $Au_{11}(PPh_3)_7Cl_3$. Here, single crystal XRD indicates that structural disorder may be present in the ligand shell of $Au_{11}(PPh_3)_7Cl_3$ relative to $[Au_{11}(PPh_3)_8Cl_2]Cl$. Specifically, the entire ligand shell of $[Au_{11}(PPh_3)_8Cl_2]Cl$ can be resolved in single crystal XRD, but disorder in the ligand moieties of $Au_{11}(PPh_3)_7Cl_3$ prohibited structural determination of the phenyl rings as well as disorder in one of the phosphorus substituents (Figure 54A). Further, fitting of the thermal ellipsoids in the crystallographic data indicates that more atomic displacement is present in both the core and the ligand layer of $Au_{11}(PPh_3)_7Cl_3$ compared to $[Au_{11}(PPh_3)_8Cl_2]Cl$ (Figure 63). Ignoring the phenyl rings and contributions from thermal vibration, a cluster symmetry of C_{3v} is observed for $Au_{11}(PPh_3)_7Cl_3$, resulting in three crystallographically unique ^{31}P sites, consistent with previous reports in which the crystallographic architecture of the phenyl rings has been determined.[276,335] The discrepancy in X-ray determination may be due to differences in data collection. Previous determinations were performed at 150 K (vs 293 K for our measurements),[276,335] and in some cases, required a synchrotron source.[276] Despite collecting the data at a beamline at 150 K, the authors still observed distortion in the phenyl ring positions[276] that was not present in $[Au_{11}(PPh_3)_8Cl_2]Cl$, suggesting greater motional freedom in the ligand shell of $Au_{11}(PPh_3)_7Cl_3$.

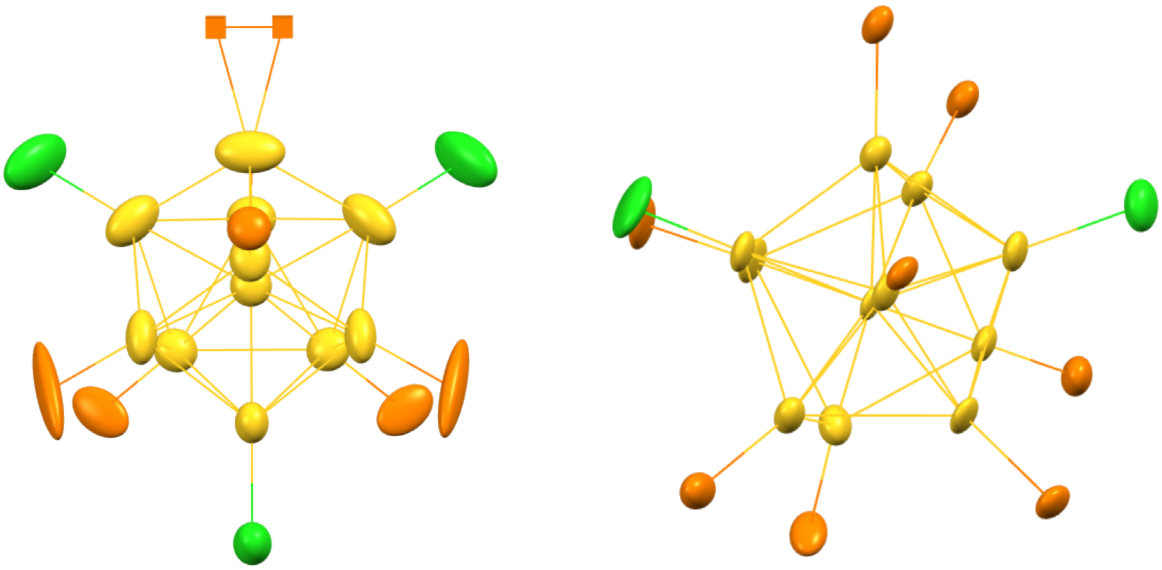

Figure 63. Atomic displacement parameters represented as thermal ellipsoids obtained from single crystal X-ray diffraction data from (A) $Au_{11}(PPh_3)_7Cl_3$ and (B) $[Au_{11}(PPh_3)_8Cl_2]Cl$

In $Au_{11}(PPh_3)_7Cl_3$, a single ^{31}P site is observed in both room temperature and low temperature (-80 °C) solution ^{31}P NMR (Figure 62A). The presence of only a single ^{31}P site for $Au_{11}(PPh_3)_7Cl_3$ is unexpected because three independent PPh_3 sites exist on the cluster according to the symmetry observed in single crystal XRD (*vide supra*), unless all independent ^{31}P sites fortuitously overlap. However, the resolution of multiple ^{31}P sites in $[Au_{11}(PPh_3)_8Cl_2]Cl$, which exhibits similar Au-P bond lengths and bond angles, would make the possibility of fortuitous overlap in $Au_{11}(PPh_3)_7Cl_3$ unlikely. In addition, the single ^{31}P chemical shift for $Au_{11}(PPh_3)_7Cl_3$, within the resolution of the experiment is not consistent with DFT predictions for PMe_3 structural analogues. Here, DFT was used to calculate the nuclear properties of the underlying Au clusters, chemical shielding tensors of each ^{31}P site, and scalar coupling constants. Dipolar coupling constants were calculated from the Au-P bond lengths observed in single-crystal XRD. For all DFT calculations, geometrically relaxed $Au_{11}(PMe_3)_7Cl_3$ and $[Au_{11}(PMe_3)_8Cl_2]Cl$ models based on the coordinates found in the crystal structures were used. Experimental spectra can be accurately simulated when taking into account five primary electronic features from the underlying Au cluster including the quadrupolar coupling constants, asymmetry parameters, Euler angles that describe the Au-P bond vector with respect to the electric field gradient tensor of ^{197}Au, the effective dipolar coupling constants, and scalar coupling constants with minor adjustments (Figure 62, blue spectra). Relative to the experimental data, DFT systematically overestimated *J*-coupling constants, therefore *J*-coupling values were reduced by multiplying by approximately 0.7 before being used as input for spectral simulation.[352]

In the reported simulations that strongly resemble the experimental data, chemical shift variations between ^{31}P sites for $Au_{11}(PPh_3)_7Cl_3$ ($\leq$0.8 ppm) were smaller than predicted with DFT for $Au_{11}(PMe_3)_7Cl_3$ (6.6 ppm, 157% difference), but *J*-coupling constants were

representative and varied by 125.8 Hz in experimental simulations vs 179.7 Hz for DFT (35% difference). Conversely, for $[Au_{11}(PPh_3)_8Cl_2]Cl$, the span of chemical shifts was more accurately represented in DFT calculations of $[Au_{11}(PMe_3)_8Cl_2]Cl$ (17.6 ppm in experiment vs 14.8 ppm in DFT, 19% difference) and similar consistency was obtained for $^1J(^{31}P, ^{197}Au)$ values (169 Hz in experiment vs 149 Hz in DFT, 13% difference). All calculated and experimental figures of merit are listed in Tables 9 and 10. Despite some discrepancy for $Au_{11}(PPh_3)_7Cl_3$, averaging of the ^{31}P chemical shielding values for both clusters indicated that $[Au_{11}(PMe_3)_8Cl_2]Cl$ should resonate at lower frequency than $Au_{11}(PMe_3)_7Cl_3$, which matches observations from room temperature solution phase data. If the calculated ^{31}P chemical shifts are averaged they reproduce the experimental trends in chemical shift, which is consistent with the conclusion that the experimental spectra reflect an average chemical shift from multiple ^{31}P sites.

Table 9. Simulated and theoretical ^{31}P chemical shift and $^{1}J(^{31}P, ^{197}Au)$ values for $Au_{11}(PMe_3)_7Cl_3$

^{31}P site	Simulated δ (ppm)	Calculated δ (ppm)	Simulated J_{iso} (Hz)	Calculated J_{iso} (Hz)
P1	49.4	54.5	265.1	378.8
P2	49.5	55.2	264.8	378.3
P3	49.6	55.4	270.0	385.7
P4	49.4	54.5	264.8	378.3
P5	49.2	51.8	144.2	206.0
P6	50.0	58.4	252.4	360.5
P7	50.0	57.5	243.4	347.8

Table 10. Simulated and theoretical ^{31}P chemical shift and $^{1}J(^{31}P, ^{197}Au)$ values for $[Au_{11}(PMe_3)_8Cl_2]Cl$

^{31}P site	Simulated δ (ppm)	Calculated δ (ppm)	Simulated J_{iso} (Hz)	Calculated J_{iso} (Hz)
P1	54.5	57.0	372.0	412.1
P2	48.8	49.5	350.0	391.4
P3	54.6	49.1	309.0	339.2
P4	42	45.6	249.0	348.8
P5	50.7	46.3	208.0	298.3
P6	50.3	50.4	211.0	297.0
P7	59.9	60.4	222.0	321.9
P8	50.4	45.8	203.0	263.1

The observation of an average ^{31}P environment can be a result of metal/ligand atom movement as well as intra-ligand motion in the PPh_3 substituents. Such dynamics are consistent with the thermal ellipsoids observed in single crystal XRD and with ^{2}H NMR studies that showed PPh_3 on gold nanoparticles can undergo fast phenyl ring flips, even in the solid state.[77] (*N.B.* preliminary ^{31}P spin-lattice relaxation measurements suggest this motion is reduced in $[Au_{11}(PPh_3)_8Cl_2]Cl$ (T_1 = 67 ± 12 s) compared to $Au_{11}(PPh_3)_7Cl_3$ (T_1 = 20 ± 6 s), probably as a result of steric differences). The solid-state ^{1}H-^{31}P CPMAS spectrum of $Au_{11}(PPh_3)_7Cl_3$ also shows only a single ^{31}P resonance (similar to the solution spectrum) which is split into a doublet due to ^{31}P-^{197}Au coupling. Intra-ligand and intra-core motion can persist in the solid state, and therefore a single resonance may be observed due to this dynamic averaging.

5.4 DISCUSSION

Chemical intuition would suggest that differences in the local coordination environment[353] and different crystallographic sites[354] of the ^{31}P nucleus would result in changes in chemical shift. However, we have established that the observed single resonance in the solution and solid-state ^{31}P NMR of $Au_{11}(PPh_3)_7Cl_3$ is not consistent with the presence of three crystallographically unique ^{31}P environments.

In order to explain the ^{31}P chemical shift observations from the low temperature solution and ssNMR spectrum of $Au_{11}(PPh_3)_7Cl_3$, we first examined the atomic displacement parameters present in X-ray crystallography which indicate that atomic motion due to thermal vibrations may be responsible for the average ^{31}P chemical shift. As a result of the greater steric hindrance due to the additional PPh_3 ligand in $[Au_{11}(PPh_3)_8Cl_2]Cl$, the activation barrier to atomic

displacement is presumably increased, allowing the observation of multiple ^{31}P crystallographic environments on the cluster surface in the low temperature solution NMR and ssNMR spectra, consistent with DFT calculations. The differences between $Au_{11}(PPh_3)_7Cl_3$ and $[Au_{11}(PPh_3)_8Cl_2]Cl$ due to ligand shell composition and arrangement indicate that dynamics must be taken into consideration when evaluating the structural properties that can be obtained from NMR spectra.

Importantly, this data is not consistent with the proposed "trans-effect" of the central Au atom in small clusters, on the ^{31}P resonances of appended phosphorus-based ligands.[304] In the proposed "trans-effect" theory, the trans influence is an analogy to bipyramidal structures observed in coordination chemistry, where the Au atom bound to phosphorous can be thought of as the central atom in the complex, the peripheral gold atoms are cis to the phosphorous, and the center atom of the cluster is trans to the phosphorous. The hypothesis of a trans-effect was supported by the observation of a single ^{31}P chemical shift in solution for $Au_{11}(PPh_3)_7(SCN)_3$ vs $[Au_{11}(PPh_3)_8(SCN)_2]^+$, implying that the substitution of a single ligand affected all other ^{31}P resonances equally, as transmitted through the central Au atom, meaning that cis-substituents (peripheral Au atoms and appended ligands) had little influence on observed ^{31}P chemical shifts.[304] However, $Au_{11}(PPh_3)_7(SCN)_3$ and $[Au_{11}(PPh_3)_8(SCN)_2]^+$ should be isostructural analogues to the clusters studied here, and we *do* observe differences in the low temperature solution and solid-state ^{31}P NMR spectra of $Au_{11}(PPh_3)_7Cl_3$ and $[Au_{11}(PPh_3)_8Cl_2]Cl$.

The discrepancies between our results and the previous studies could be due to the difference in external magnetic field strength (40.5 vs 202.45 MHz), resulting in lower resolution in the prior work. In the high resolution solution and ssNMR spectra reported here, we have demonstrated that crystallographic information pertaining to the ^{31}P coordination environment as

well as the properties of the underlying ^{197}Au nuclei via ^{31}P-^{197}Au interactions can be determined from ^{31}P NMR spectra if thermal vibrations are suitably minimized (the case for ^{31}P ssNMR of $[Au_{11}(PPh_3)_8Cl_2]Cl$). Conversely, atomic displacement due to thermal motion (as observed in $Au_{11}(PPh_3)_7Cl_3$ and room temperature solution phase $[Au_{11}(PPh_3)_8Cl_2]Cl$ spectra) produces an averaging mechanism of the local crystallographic environments on small Au clusters, and leads to the observation of only a single ^{31}P chemical shift for appended ligands. We note that despite this motion, ^{31}P-^{197}Au coupling is still not entirely averaged out and is observed in the ^{31}P ssNMR of $Au_{11}(PPh_3)_7Cl_3$, and likely represents an average coordination environment. In this case, it is possible that both the large quadrupolar coupling constant and atomic motion of Au atoms lead to fast ^{197}Au T_1 relaxation, and collapse of the expected quartet pattern to a doublet, whereas for $[Au_{11}(PPh_3)_8Cl_2]Cl$, the large quadrupolar coupling constant is likely the dominating factor for producing the observed doublet. The contribution of fast quadrupolar relaxation has recently been observed in inorganic Cu complexes, where $^{63/65}$Cu is coupled to ^{31}P.[292] In this report, the authors also only resolve a single ^{31}P chemical shift for two different crystallographic environments, indicating that the principles of how molecular motion can influence NMR spectra can be extended to both small molecules and metal nanoparticles.

Here, we have considered the smallest possible metal cluster containing a single central atom surrounded by a single layer of metal atoms. Interestingly, even at this size, we find that both local *and* global features of the entire cluster are necessary to interpret the NMR spectra.

Table 11. Bond lengths and bond angles for $Au_{11}(PPh_3)_7Cl_3$/$[Au_{11}(PPh_3)_8Cl_2]^+$ from single crystal XRD

Cluster	Au-P (Å)	Au_m-Au-P (°)	Au_m-Au-P (Å)	Au_s-Au-P (°)	Au_s-Au-P (Å)
Average $Au_{11}(PPh_3)_7Cl_3$/ $[Au_{11}(PPh_3)_8Cl_2]^+$	2.346/ 2.292	174.3/ 174.4	2.664/ 2.689	124.2/ 123.5	2.949/ 2.964
Standard deviation $Au_{11}(PPh_3)_7Cl_3$/ $[Au_{11}(PPh_3)_8Cl_2]^+$	0.063/ 0.028	2.2/ 3.4	0.026/ 0.029	4.5/ 5.1	0.054/ 0.088

Table 12. Theoretical ^{31}P chemical shift and $^{1}J(^{31}P, ^{197}Au)$ values for $Au_{11}(PMe_3)_7Cl_3$ vs local coordination sites

^{31}P site	σ_{iso} (ppm) cluster	σ_{iso} (ppm) coordination site	J_{iso} (Hz) cluster	J_{iso} (Hz) coordination site
P1	277.5	348.2	378.8	639.2
P2	278.2	255.4	378.3	634.0
P3	278.4	348.9	385.7	636.2
P4	277.5	336.1	378.3	638.0
P5	274.8	195.9	206.0	165.8
P6	281.4	367.3	360.5	586.7
P7	280.5	379.9	347.8	595.5
Range	6.6	183.8	179.7	473.4

Table 13. Theoretical ^{31}P chemical shift and $^{1}J(^{31}P, ^{197}Au)$ values for $[Au_{11}(PMe_3)_8Cl_2]Cl$ vs local coordination sites

^{31}P site	σ_{iso} (ppm) cluster	σ_{iso} (ppm) coordination site	J_{iso} (Hz) cluster	J_{iso} (Hz) coordination site
P1	280.0	352.3	412.1	623.9
P2	272.5	236.3	391.4	581.2
P3	272.1	316.0	339.2	522.7
P4	268.6	301.3	348.8	490.8
P5	269.3	152.8	298.3	423.1
P6	273.4	295.3	297.0	522.3
P7	283.4	344.0	321.9	584.3
P8	268.8	122.0	263.1	140.4
Range	14.8	230.3	149.0	483.5

5.5 CONCLUSIONS

Overall, we have demonstrated that the NMR spectra of ligands bound to nanoclusters can serve as a sensitive readout on the local crystallographic features (e.g. ligand binding mode, packing, and arrangement) as well as the overall cluster structure (e.g. global cluster symmetry and dynamics) in $Au_{11}(PPh_3)_7Cl_3$ and $[Au_{11}(PPh_3)_8Cl_2]Cl$. Because these aspects of particle surface chemistry are universal, these NMR principles are expected to apply to larger clusters as well. An evaluation of the literature suggests that multinuclear NMR studies have the potential to allow total structure determination, together with other characterization tools. This atomistic understanding of these technologically relevant nanomaterials will significantly enhance our ability to understand and design materials for systems such as subsurface alloys in heterogeneous catalytic activity[221,222,355] and subtle composition-dependent optical features.[90,356]

6.0 METALLICITY, CARRIER DENSITY, AND STRUCTURAL EVOLUTION IN PLASMONIC $Cu_{2-x}Se$ NANOPARTICLES

(Portions of this work are being prepared for submission as Marbella, L. E.; Gan, X. Y.; Millstone, J. E. **2016**, in preparation)

6.1 INTRODUCTION

Plasmonic materials have been shown to enhance or enable a myriad of technologies including biomedical imaging,[357] heterogeneous catalysis,[204] water purification,[358] and photovoltaic device design.[359] However, the fast majority of these demonstrations use noble metal (e.g. Au and Ag) nanoparticles, and these materials introduce inherent drawbacks in terms of cost and therefore limit the translation of the materials into broader use. This translation gap has motivated the study of cost-effective alternative materials[360,361] such as Al-based NPs,[362] degenerately doped metal chalcogenide and metal oxide NPs,[363,364] and carbon-based nanomaterials.[365] However, the synthesis of these materials is significantly more challenging than their noble metal counterparts, and therefore there is a need to not only produce the alternative plasmonic particles but also to understand and control their properties once formed.

When exploring the diversity of materials that exhibit a localized surface plasmon resonance (LSPR), a number of new research directions emerge. For example, in non-noble

metal plasmonic nanomaterials, the charge carrier density can be manipulated via doping, providing an additional handle (alongside particle morphology and surface chemistry) that can tune the wavelength of maximum emission,[366] and is readily monitored with absorption spectroscopy. Further, in many degenerately doped plasmonic nanoparticles, the carrier density is approximately an order of magnitude lower than traditional metal nanoparticles,[364] resulting in changes in carrier properties (e.g. carrier heat capacity and effective carrier temperature), which in turn may influence scattering and absorption cross sections as well as subsequent electromagnetic field enhancements.[367] Unfortunately, the high concentration of stabilizing ligands on the particle surface typically prohibits evaluation of free carrier properties via traditional figures of merit such Seebeck coefficients and the Hall effect that are more suitable for analysis of non-colloidal materials.[368] In place of these traditional methods, absorption spectroscopy may be used to determine carrier density using a variety of approaches, most commonly, the Drude model.[369-372] However, there are drawbacks to using the absorption spectrum to determine carrier densities, because a variety of intrinsic and extrinsic system parameters may influence the position and intensity of features in a given absorption spectrum.

In concert, X-ray diffraction (XRD) and electron microscopy (EM) are typically used to determine the crystallographic features and shape of the material, which are particle parameters that can also influence plasmonic figures of merit.[373] For example, the crystalline anisotropy in hexagonal cesium-doped tungsten oxide nanorods results in an anisotropic dielectric function in the material.[373] The authors found that this crystalline anisotropy produced splitting of the LSPR, and that both plasmon modes displayed a 400-fold near-field enhancement, providing uniformity in near-field enhancement that is not achievable in metal nanoparticles. Further, upon oxidation of the NPs, computer simulations of the resulting LSPR features were consistent with an

inhomogeneous depletion of carrier density (with a lower carrier density at the surface compared to the core), suggesting surface-driven oxidation of the NPs. The structural changes at the surface responsible for the resulting LSPR properties were not observed in powder X-ray diffraction (PXRD), suggesting that long-range materials characterization techniques may not be sufficient to characterize structural changes that dictate the observed optoelectronic behaviors. In order to explore the influence of parameters such as particle size and shape on non-noble metal NPs for plasmonic applications, we must first provide a robust correlation between LSPR features and material properties, such as carrier density and crystalline architecture. Therefore, an ideal analytical tool to characterize plasmonic nanoparticles would be able to simultaneously evaluate charge carrier density and the structure of the particle.

To our knowledge, the only technique that is able to distinguish between metallic, semiconducting, and molecular behavior as well as provide a direct probe of chemical structure is solid-state NMR (ssNMR) spectroscopy. Further, once the semiconducting/metallic behavior of the system has been established, the carrier density,[374-376] electronic heterogeneity in the material,[375-378] and even the type of free carriers (electrons vs holes)[379] can be determined by analyzing ssNMR data. An additional advantage of ssNMR is the ability to perform *in situ* measurements to monitor these features as a function of time, chemical environment, or external stimuli.

Here, we use ^{77}Se ssNMR spectroscopy to evaluate the local structural changes at the atomic level that lead to the emergence of a near-infrared LSPR band in a well-studied,[364,366,370,380-383] degenerately doped semiconductor NP system, $Cu_{2-x}Se$. Specifically, we use ^{77}Se phase adjusted sideband separation (PASS) experiments to determine the short-range chemical structure of $Cu_{2-x}Se$ NPs as a function of air exposure and compare to PXRD patterns.

Then, we perform variable temperature ^{77}Se spin-lattice relaxation (T_1) measurements to confirm metallicity and determine carrier density according to an NMR phenomenon known as the Korringa relationship,[7] and correlate these results with absorbance spectroscopy and material structure.

6.2 EXPERIMENTAL

6.2.1 Materials and Methods

Copper(I) chloride (CuCl, 99.995%), selenium powder (Se, ≥ 99.5%), octadecene (90%, technical grade), oleylamine (70%, technical grade), hexane (≥ 99.9%), anhydrous toluene (99.8%), and dimethyl selenide (Me_2Se, 99%) were purchased from Sigma Aldrich (St. Louis, MO). Absolute ethanol (EtOH) was purchased from Thermo Fisher Scientific (Pittsburgh, PA). Anhydrous solvents were freeze-pump-thawed at least three times before use. All other chemicals were used as received. Prior to use, all glassware and Teflon-coated stir bars were washed with aqua regia (3:1 ratio of concentrated HCl to HNO_3) and rinsed with copious amounts of water prior to drying. *Caution: aqua regia is highly toxic and corrosive, and should only be used with proper personal protective equipment and training. Aqua regia should be handled only inside a fume hood.*

6.2.2 Synthesis of $Cu_{2-x}Se$ Nanoparticles

$Cu_{2-x}Se$ (x ~ 0-0.2) NPs were prepared according to a modified literature procedure[380] using standard air-free techniques. Briefly, 80 mg (1 mmol) of Se powder was added to 1 mL of octadecene and 2 mL of oleylamine and heated to 195 °C overnight in a round bottom flask. In a separate flask, 200 mg (2 mmol) of CuCl was added to 5 mL of octadecene and 5 mL of oleylamine in a three neck flask. While stirring, the mixture was heated to 120 °C under vacuum. After holding at 120 °C for 30 min, the mixture was heated to 285 °C under Ar. The Se-octadecene mixture was rapidly injected into the CuCl-octadecene-oleylamine mixture, which led to a temperature drop to 275 °C. The resulting $Cu_{2-x}Se$ (x ~ 0) NPs were allowed to grow for 10 min before removing the heating mantle and cooling to room temperature.

The $Cu_{2-x}Se$ (x ~ 0) NP product was purified via centrifugation. The as-synthesized NPs were cannula-transferred to air-free centrifuge tubes containing 10 mL of EtOH and centrifuged in an Eppendorf 5804R centrifuge with a swing bucket rotor (A-44-4) (Eppendorf, Inc.) at a force of 2850 rcf at 20 °C for 5 min. The resulting supernatant was removed and the pellet was resuspended in a small amount of hexane or toluene for additional centrifugation in another 5 mL of EtOH. This washing procedure was repeated once. Stoichiometric $Cu_{2-x}Se$ (x ~ 0) NPs were either transferred to the glovebox for air-free characterization preparation or resuspended in hexane or toluene and exposed to air to produce oxidized $Cu_{2-x}Se$ (x ~ 0.2) NPs that could be handled outside the glovebox. All purified NPs were then characterized by electron microscopy techniques, UV-visible-near infrared (UV-vis-NIR) spectroscopy, PXRD, and ^{77}Se ssNMR spectroscopy.

6.2.3 Absorption Spectroscopy

Purified $Cu_{2-x}Se$ (x ~ 0-0.2) NPs in toluene were characterized by ultraviolet-visible-near-infrared (UV-vis-NIR) absorption spectroscopy using a Cary 5000 spectrophotometer (Agilent, Inc.) in air-free quartz cuvettes (Starna Cells, Inc.) with a 1 cm path length modified with a high vacuum straight valve and PTFE plug (Kimble Chase). All spectra were baseline corrected with respect to the spectrum of toluene.

6.2.4 Electron Microscopy

Samples were prepared for electron microscopy by drop casting an aliquot of purified NC solution (diluted 1:10 or 1:100 with toluene) onto Formvar-coated copper transmission electron microscopy grids (Ted Pella, Inc.) or thin film (<10 nm) molybdenum 400 mesh carbon grids (Pacific Grid Tech, Inc.) for high resolution characterization. Air-free $Cu_{2-x}Se$ (x ~ 0) nanoparticles were drop cast inside the glovebox and stored in an air-tight container used to transport the sample to the microscope. Transmission electron microscopy (TEM) characterization was performed on an FEI Morgagni transmission electron microscope at 80 kV. The size distributions of the NPs were determined from TEM images of at least 200 NPs from various areas of the grid using ImageJ 1.47d (National Institutes of Health, USA). High resolution transmission electron microscopy (HRTEM) characterization was performed using a FEI Tecnai G2 F20 S-Twin TMP microscope operating at 200 kV (Mechanical Engineering and Materials Science Department, University of Pittsburgh).

6.2.5 Powder X-ray Diffraction

For air-free preparations, $Cu_{2-x}Se$ (x ~ 0-0.2) NPs powders were packed in a 0.50 mm capillary tubes (Hampton Research) in the glovebox and flame sealed for PXRD characterization. PXRD patterns were collected on a Bruker X8 Prospector Ultra (Department of Chemistry, University of Pittsburgh) at 45 kV, 0.65 mA equipped with a IμS micro-focus CuKα X-ray source (λ = 1.54178 Å) with a scan speed of 0.5 s/step from 12 to 108° with a step size of 0.02°. Oxidized $Cu_{2-x}Se$ (x ~ 0.2) NPs were characterized by PXRD using a Bruker AXS D8 Discover XRD (NanoScale Fabrication and Characterization Facility, Petersen Institute of NanoScience and Engineering, Pittsburgh, PA) at 40 kV, 40 mA for CuKα (λ = 1.5406 Å) X-ray source with a scan speed of 0.5 s/step from 10 to 90° with a step size of 0.02°. Samples were prepared by drop casting an aliquot of purified NC solution (diluted 1:10 or 1:100 with toluene) on a piece of microscope glass slide (Fisher Scientific).

6.2.6 Solid-State NMR Spectroscopy

Dried $Cu_{2-x}Se$ (x ~ 0-0.2) NPs were packed into 4 mm zirconia rotors with inserts and air-free Vespel caps for analysis with ssNMR. All ssNMR spectra were recorded on a Bruker Avance 500 MHz (11.7 T) spectrometer, equipped with a triple-resonance 4 mm CPMAS probehead operating at a ^{77}Se Larmor frequency of 95.38 MHz. ^{77}Se chemical shifts were externally referenced to Me_2Se at 0 ppm. Temperature was maintained with a BVT3000 variable temperature unit and nitrogen cooling was used for all low temperature measurements.

Static ^{77}Se NMR spectra of $Cu_{2-x}Se$ (x ~ 0-0.2) NPs was recorded using a standard $(\pi/2)_x$-τ-$(\pi)_y$-acquire spin echo sequence. In general, π/2 pulse lengths were ~2.5 μs and τ = 30 μs.

Typical recycle delays ranged from 50-200 ms, depending on the T_1 of the sample. Static T_1 measurements were collected from at approximately 175-350 K using a previously described inversion-recovery sequence.[384] Here, a composite-π pulse was used to achieve inversion as follows: $(\pi/2)_x$-$(3\pi/2)_y$-$(\pi/2)_x$-vd-$(\pi/2)_x$-τ-$(\pi)_y$-τ-acquire. ^{77}Se PASS spectra were collected at 298 K using a modified PASS sequence[385] with 32 or 64 t_1 slices. Typical MAS spinning speeds of 1.2-2 kHz were employed. Spinning sideband patterns were fit in dmfit[386] to extract chemical shift tensors and are described with the Haeberlen convention as follows:

$$|\delta_{33} - \delta_{iso}| \geq |\delta_{11} - \delta_{iso}| \geq |\delta_{22} - \delta_{iso}| \quad (21)$$

$$\eta = \frac{\delta_{11} - \delta_{22}}{\delta_{33} - \delta_{iso}} \quad (22)$$

$$\delta_{iso} = \frac{1}{3}(\delta_{11} + \delta_{22} + \delta_{33}) \quad (23)$$

$$\Delta = \delta_{33} - \delta_{iso} \quad (24)$$

Where η is the asymmetry parameter, δ_{iso} is the isotropic shift, and Δ is the reduced anisotropy.

6.3 RESULTS AND DISCUSSION

$Cu_{2-x}Se$ (x ~ 0-0.2) NPs were synthesized via a hot injection method using standard air-free techniques. Upon exposure to air, $Cu_{2-x}Se$ (x ~ 0) acquired Cu vacancies that produced holes in the valence band, leading to a degenerately doped, non-stoichiometric $Cu_{2-x}Se$ (x > 0) phase[387-390] in the NP. Transmission electron micrographs showed average particle diameters of 14.2 ± 2.1 nm and 13.6 ± 1.8 nm for oxidized and air-free samples (Figures 64), respectively, indicating that air exposure did not result in dramatic changes in particle size. Analysis with selected area electron diffraction (SAED) showed a lattice contraction (Figure 65) of the $Cu_{2-x}Se$ NPs upon

exposure to air and subsequent increase in x (x > 0). Similarly, PXRD patterns of $Cu_{2-x}Se$ NPs showed that oxidized particles exhibited a cubic structure (Figures 66-67), characteristic of $Cu_{1.8}Se$ (PDF card 06-0680). If the samples were kept in an inert environment post-synthesis, the PXRD patterns were consistent with stoichiometric Cu_2Se (reference patterns PDF cards 27-1131 and 029-0575) and the lattice expansion observed in SAED (Figures 65-67). However, there is conflict in the literature assignment of the reduced Cu_2Se NPs to either monoclinic[383] or tetragonal[382] structures, since both exhibit similar PXRD and SAED patterns. Further complicating structural assignment is the fact that many of the bulk Cu_2Se phases have not been solved by single crystal analysis, prohibiting definitive assignment of atomic positions. In structures that have been proposed, some peaks in the PXRD pattern cannot be assigned from the single crystal data,[391] suggesting the presence of additional structural variation that is present in the bulk material, but not crystallized. To address this issue, computational approaches using genetic algorithms show promise for determining atom positions in the most likely structures of Cu_2Se.[392]

Therefore, all diffraction analyses were complemented with static ^{77}Se spin echo NMR measurements and PASS experiments to provide additional insight into the local coordination environments of the Se nuclei. By comparing static ^{77}Se spin echo NMR spectra of $Cu_{2-x}Se$ (x ~ 0-0.2) NPs with the corresponding PXRD, we observe that the ^{77}Se frequency depends on the chemical composition, with more oxidized structures resonating at higher frequencies (Figure 68). (*N.B.* all NPs a ^{77}Se NMR signal that is consistent with the most deshielded peak upon exposure to air). A progressive deshielding of ^{77}Se nuclei is observed as x is increased from 0 to 0.2 in $Cu_{2-x}Se$ (x ~ 0-0.2) NPs, which is likely a result of an increasing Knight shift contribution due to changes in free carrier (hole) density.

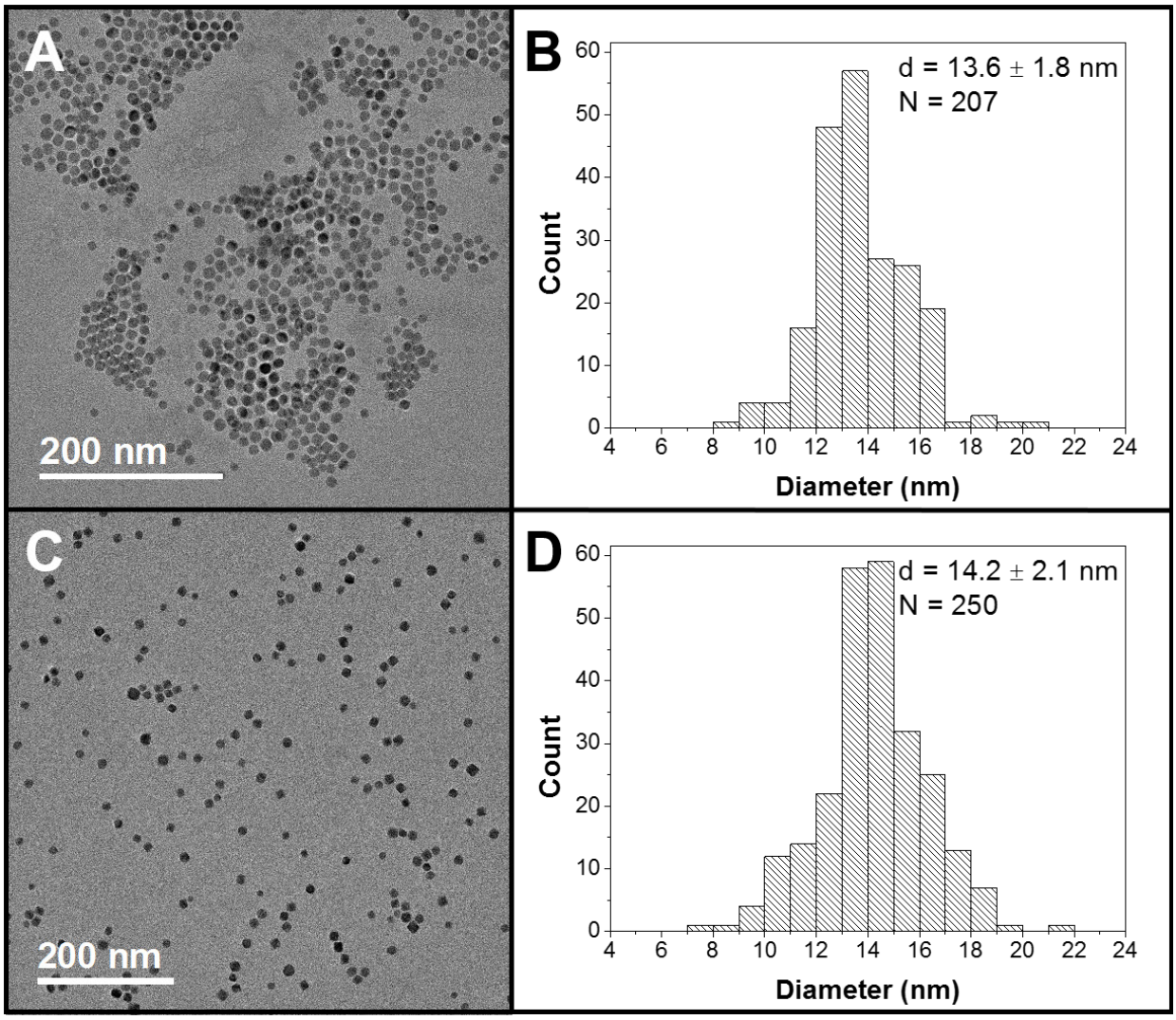

Figure 64. Transmission electron micrographs (A, C) and corresponding size histograms (B, D) for air-free (A, B) and air-exposed (C, D) $Cu_{2-x}Se$ NPs

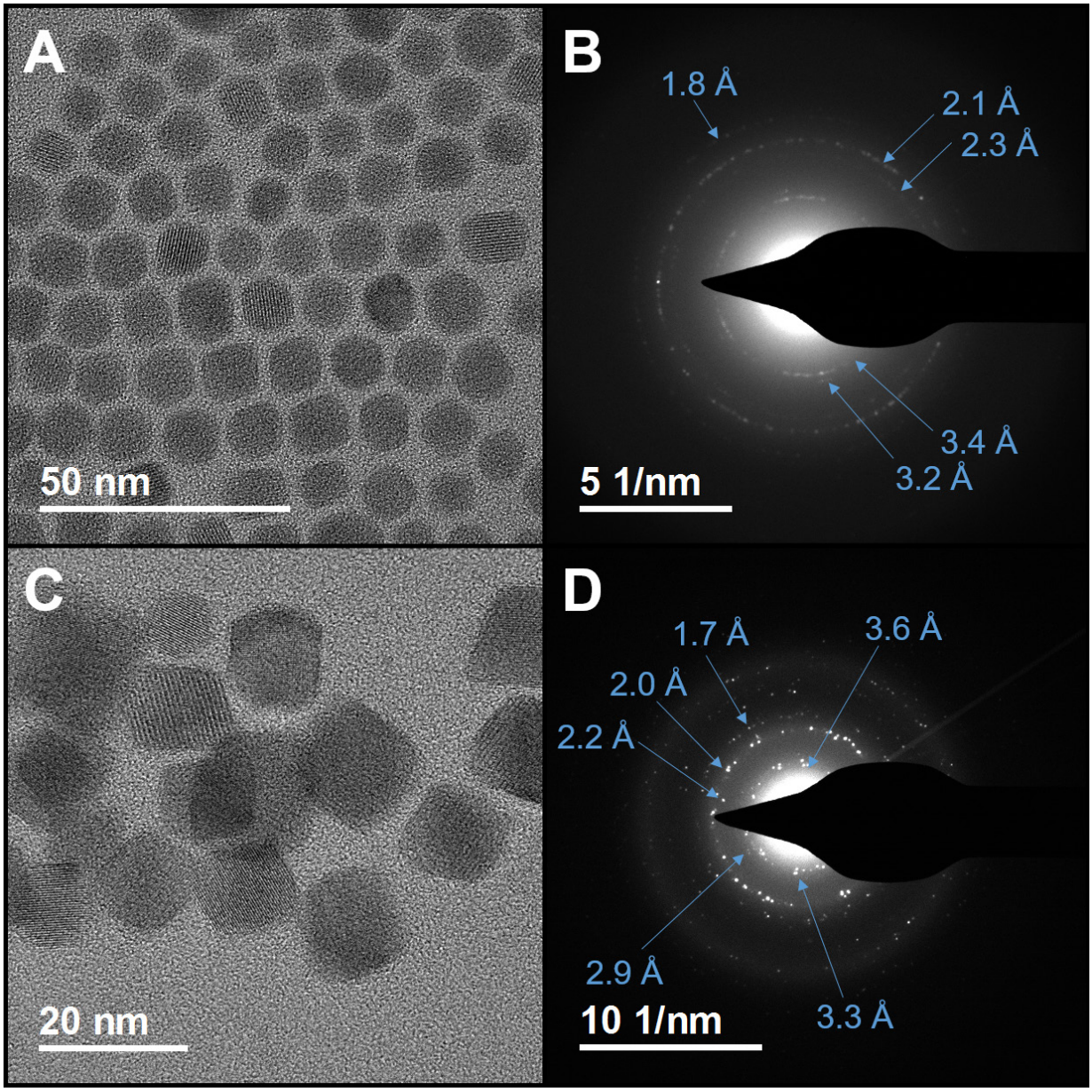

Figure 65. HRTEM micrographs (A, C) and corresponding SAED patterns (B, D) for air-free (A, B) and air-exposed (C, D) $Cu_{2-x}Se$ NPs

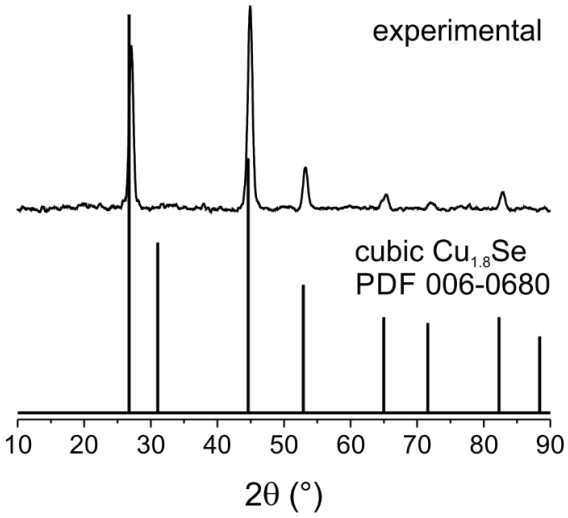

Figure 66. Experimental PXRD of $Cu_{2-x}Se$ (x ~ 0.2) NPs after oxidation (top) compared to PDF card 006-0680 for cubic $Cu_{1.8}Se$ (bottom)

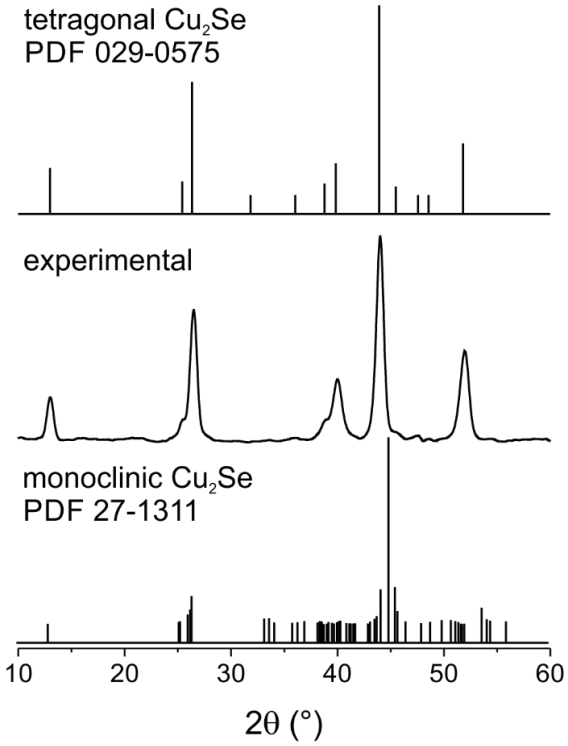

Figure 67. Experimental PXRD of $Cu_{2-x}Se$ (x ~ 0) NPs prepared in the glovebox (middle) compared to PDF cards 029-0575 (top) and 27-1311 (bottom) for tetragonal and monoclinic Cu_2Se, respectively

Interestingly, the linewidth of the ^{77}Se peaks varies non-linearly in the spin echo NMR spectra, possibly due to compositional and structural changes as the amount of Cu varies in the $Cu_{2-x}Se$ NPs. Specifically, these line broadening changes may produce nuclear coupling to excess free carriers that have a short T_{1h} and/or from chemical shielding anisotropy in the ^{77}Se coordination environment. In order to investigate the source of line broadening, ^{77}Se PASS experiments were performed on three representative $Cu_{2-x}Se$ (x ~ 0-0.2) NP samples that exhibit distinct ^{77}Se frequencies (e.g. different carrier densities) and linewidths. For the most deshielded sample (δ = 1126 ppm), which was intentionally exposed to air (thus creating Cu vacancies), ^{77}Se isotropic projections indicate that more than one ^{77}Se environment is present in the $Cu_{2-x}Se$ (x ~ 0.2) NPs (Figure 69). For simplicity, we analyzed the spinning sideband patterns at the center of gravity of two peaks fit with Gaussians (δ_{iso} = 1133 and 1267 ppm) from the isotropic projection. Each of the ^{77}Se chemical shifts provided distinct spinning sideband patterns that were fit to determine the chemical shift anisotropies. From these fits, we determined that the major peak showed smaller anisotropy and a larger asymmetry parameter than the minor peak (Δ = -25.1 vs -35.3 ppm, and η = 0.85 vs 0.55, Table 14). This sample is expected to exhibit the highest carrier density because it was intentionally exposed to air, permitting an assignment of the major peak at δ_{iso} = 1133 ppm to fully coordinated ^{77}Se nuclei and the minor peak at δ_{iso} = 1267 ppm to ^{77}Se nuclei adjacent to Cu vacancies. This model is consistent with electronic structure investigations, in which each Cu atom contributes one electron to the valence band and the absence of Cu atoms produces holes (*vide infra*).[393] From the patterns observed in the PXRD, we expect fully Cu-coordinated cubic ^{77}Se sites to show little to no chemical shift anisotropy, due to the cubic symmetry of the local coordination environment. In principle, a perfect cubic symmetry would produce no chemical shift anisotropy. In practice, some broadening and anisotropy is observed

due to local distortions of bond lengths and/or angles as a result of deviation from the expected value and/or the presence of crystallographic defects.[394] As Cu atoms are removed to form vacancies in oxidized structures, the local ^{77}Se environment deviates from symmetric coordination, and we expect to observe larger Δ values at these sites. In addition, we also expect that for Se sites adjacent to vacancies, the asymmetry parameter would exhibit uniaxial symmetry ($\eta = 0$).[395] The observed asymmetry parameter of $\eta = 0.55$ for ^{77}Se next to a vacancy may deviate from uniaxial symmetry due to factors including vacancy distribution in the material and/or dynamics, and an investigation of these parameters will be the subject of a separate report. Therefore, ^{77}Se NMR offers short-range structural information at positions near defect sites in the crystal lattice, which also provides site-specific electronic information, a level of detail that is remarkable for conductive materials, due to the extreme line broadening that is observed.

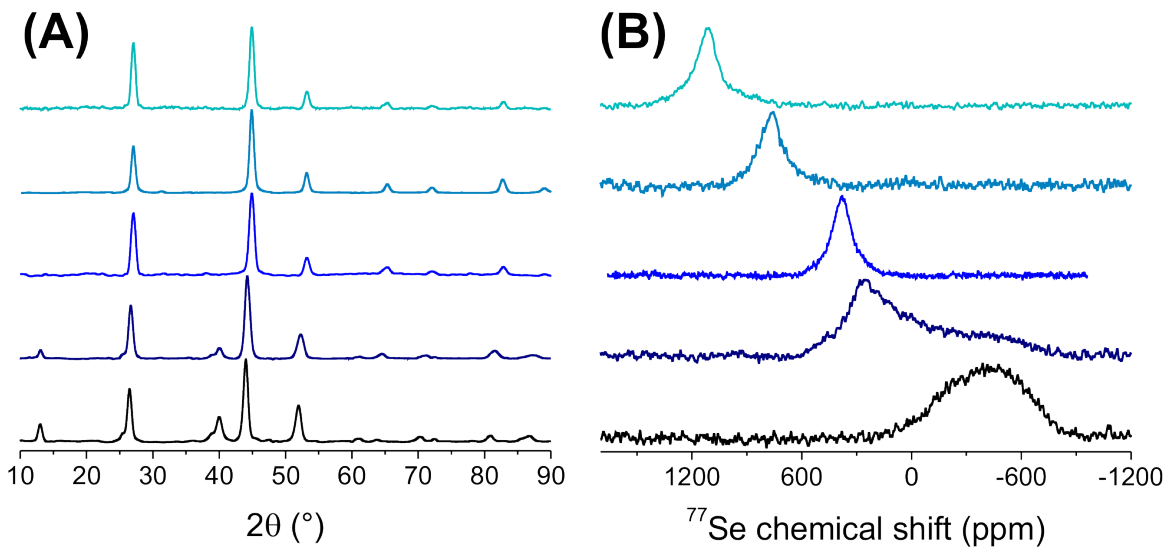

Figure 68. (A) Experimental PXRD patterns and corresponding (B) static ^{77}Se spin echo NMR spectra for $Cu_{2-x}Se$ NPs as a function of composition. Representative $Cu_{2-x}Se$ (x ~ 0) NPs (black, bottom) are progressively oxidized to $Cu_{2-x}Se$ (x ~ 0.2) NPs (cyan, top)

Table 14. ^{77}Se chemical shift tensor values for $Cu_{2-x}Se$ (x ~ 0-0.2) NPs

^{77}Se site	δ_{iso} (ppm)	Δ (ppm)	η
Se-Cu_8 (cubic)	1133	-25.1	0.85
Se-Cu_{8-x} (x = vacancy), cubic	1267	-35.3	0.55
Se-Cu_8 (cubic)	370	23.9	0.85
Se monoclinic	-445	-375.3	0.70

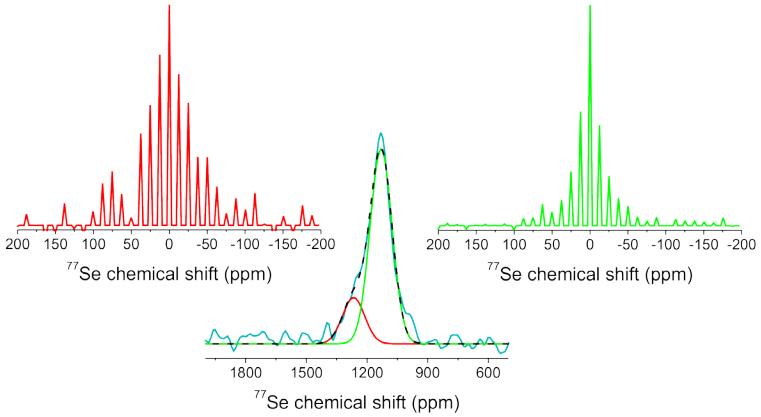

Figure 69. ^{77}Se isotropic projection (middle) of oxidized cubic $Cu_{2-x}Se$ (x ~ 0.2) NPs and corresponding spinning sideband patterns at MAS = 1.2 kHz

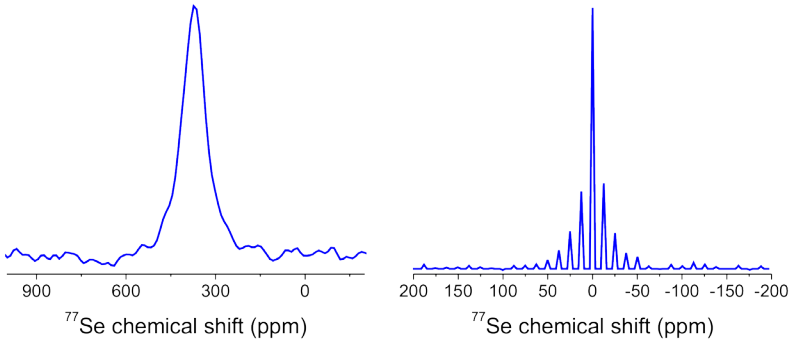

Figure 70. ^{77}Se isotropic projection (left) of partially oxidized cubic $Cu_{2-x}Se$ (x > 0) NPs and corresponding spinning sideband pattern at MAS = 1.2 kHz (right)

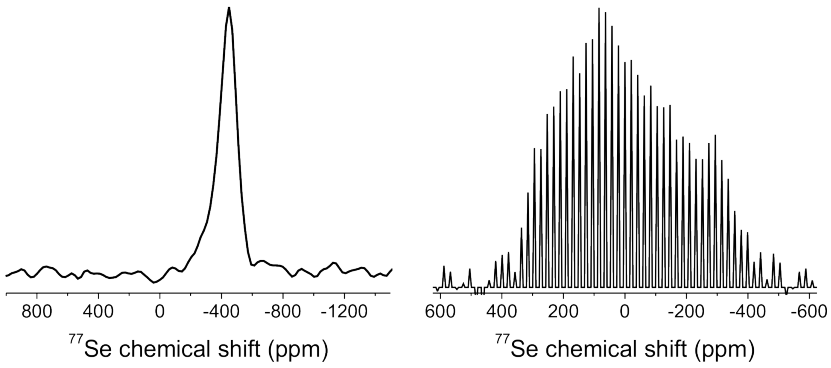

Figure 71. ^{77}Se isotropic projection (left) of stoichiometric $Cu_{2-x}Se$ (x ~ 0) NPs and corresponding spinning sideband pattern at MAS = 2 kHz (right)

As we move down in frequency, the static ^{77}Se NMR peak at 382 ppm shows a narrower lineshape than the fully oxidized sample (fwhm ~10.8 kHz vs 13.4 kHz). This sample was maintained in an air-free environment, but PXRD analysis indicates that these $Cu_{2-x}Se$ NPs may have a composition with $x > 0$ because they have a similar cubic crystal structure when compared to the oxidized sample, perhaps due to non-stoichiometric incorporations in the initial synthesis. ^{77}Se PASS analysis indicates that only one major species is present in the isotropic projection (Figure 70). Although other ^{77}Se peaks may be present, peaks from lower population environments remain unresolved due to low signal to noise. For this reason, only one spinning sideband pattern was characterized. Fitting of the sidebands revealed that the chemical shift anisotropy and asymmetry parameters at δ_{iso} = 370 ppm are comparable to that of δ_{iso} = 1133 ppm (Table 14), consistent with PXRD. This observation suggests that the ^{77}Se coordination environment at δ_{iso} = 370 ppm is similar to that of δ_{iso} = 1133 ppm. However, the difference in δ_{iso} together with the absence of additional Se sites, is consistent with a lower concentration of Cu atom vacancies and subsequently lower carrier density for these particles.

Finally, the static ^{77}Se peak with a center of mass at -397 ppm displays a considerable linewidth of 56.5 kHz with a more asymmetric lineshape than the other $Cu_{2-x}Se$ NP samples. Both the ^{77}Se frequency and PXRD indicates that this sample, which was maintained in an air-free atmosphere, more closely resembles stoichiometric Cu_2Se NPs. PXRD assignments are consistent with a tetragonal or monoclinic environment, both of which would be expected to show greater chemical shift anisotropy than cubic environments. Based on known crystal structures,[391] the ^{77}Se environments in monoclinic unit cells are expected to exhibit a more significant increase in Δ compared to tetragonal and cubic unit cells.[394] Indeed, ^{77}Se PASS experiments show that multiple ^{77}Se sites are present in this sample, as indicated by the

downfield shoulder on the isotropic projection, with chemical shift anisotropies that are over an order of magnitude larger (Figure 71 and Table 14) than samples with higher carrier densities. This magnitude in Δ is consistent with the lower symmetry structures observed in PXRD. Taken together, we conclude that ^{77}Se PASS experiments are sensitive to changes in local crystallographic environment as a function of x value (i.e. charge carrier density) in $Cu_{2-x}Se$ NPs and have the potential to provide insight in electronic heterogeneities in nanomaterials.

The relationship between ^{77}Se Knight shift and carrier density in $Cu_{2-x}Se$ NPs was confirmed using variable temperature ^{77}Se T_1 measurements and absorbance spectroscopy. The UV-vis-NIR extinction spectra of all three $Cu_{2-x}Se$ (x ~ 0-0.2) NPs show characteristic optical features (Figure 72A) that are consistent with the composition and structure changes assigned in diffraction and ^{77}Se NMR spectroscopy. The most oxidized sample showed the largest Knight shift and the most intense, blue-shifted LSPR band at ~1100 nm. The intermediate sample showed a ^{77}Se resonance at δ_{iso} = 370 ppm and LSPR at ~1600 nm. The stoichiometric Cu_2Se NPs do not show an LSPR band in the optical window examined here, but display a tail that may indicate an LSPR at lower energy (λ_{max} > 2100 nm). According to the Drude model, the red shift in the absorption spectrum from non-stoichiometric, cubic NPs to stoichiometric monoclinic NPs is the result of a progressive decrease in carrier density, that is consistent with variable temperature T_1 measurements showing a larger Korringa product (*vide infra*).

The increase in carriers at the Fermi level as x approaches 0.2 in $Cu_{2-x}Se$ NPs can be directly monitored with variable temperature ^{77}Se T_1 measurements. In the metallic regime, the spin-lattice relaxation rate (T_1^{-1}) exhibits a linear relationship with temperature (T), with an intercept through zero, whereas T_1^{-1} in semiconductors shows a linear relationship with $T^{1/2}$.[396] The linear relationship between T_1^{-1} and T is known as Korringa behavior,[7] which indicates that

there are free carriers that couple to nuclei, resulting in behavior that follows Fermi-Dirac statistics (while semiconductors follow Boltzmann statistics).[396] Therefore, variable temperature ^{77}Se T_1 measurements provide a direct readout of the band structure in materials.

Surprisingly, we find that all three $Cu_{2-x}Se$ (x ~ 0-0.2) NPs show a linear relationship between ^{77}Se T_1^{-1} and T, characteristic of Korringa behavior (Figure 72B). The presence of Korringa behavior indicates that all samples examined exhibit some population of free carriers. However, the slope of the line varies between $Cu_{2-x}Se$ (x ~ 0-0.2) NPs. From the slope of the line, we can extract the Korringa product, T_1T, which is inversely proportional to the local density of states at the Fermi level (E_f-LDOS). Based on this analysis, the most oxidized cubic $Cu_{2-x}Se$ NPs with δ_{iso} = 1133 and 1267 ppm, have the lowest Korringa product (i.e. highest E_f-LDOS (Ry^{-1} $atom^{-1}$)) with T_1T = 0.68 ± 0.01 sK, followed by the cubic sample at δ_{iso} = 370 ppm and T_1T = 1.17 ± 0.01 sK, and the monoclinic $Cu_{2-x}Se$ NPs at δ_{iso} = -445 ppm and T_1T = 12.39 ± 0.10 sK.

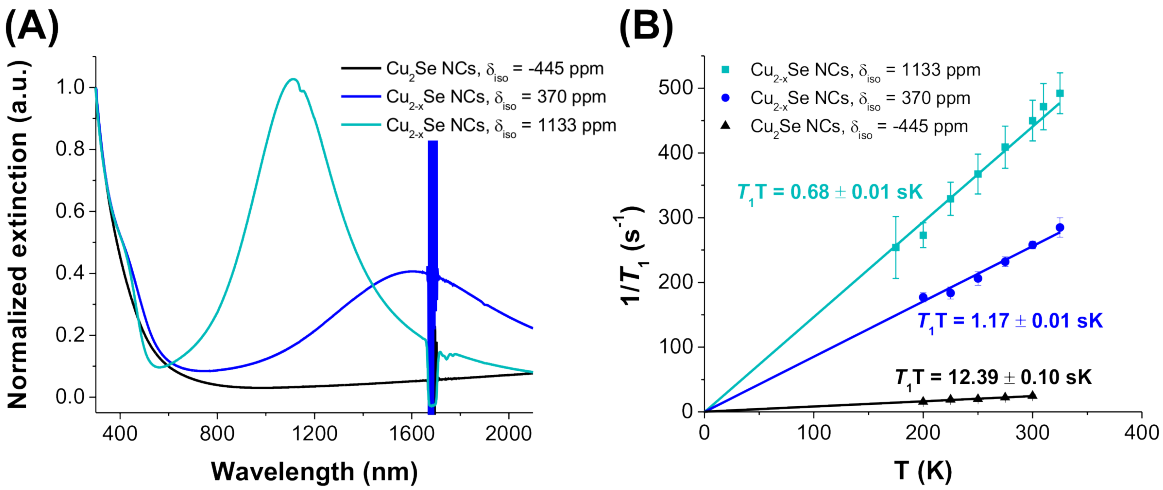

Figure 72. Characteristic (A) extinction spectra and (B) Korringa behavior for $Cu_{2-x}Se$ (x ~ 0-0.2) NPs with various compositions

Additionally, by comparing to a standard sample with similar composition and known carrier properties, the carrier density of each $Cu_{2-x}Se$ NPs can be estimated by analyzing the relaxation data. In order to determine the carrier density from NMR data, the following relationship can be used:

$$N_{h,s} = \left[\frac{(m_r^*)^2 N_{h,r}^{2/3}}{(m_s^*)^2}\left(\frac{T_{1,r}}{T_{1,s}}\right)\right]^{3/2} \qquad (25)$$

Where N_h is the carrier density, m^* is the effective mass of the free carriers, and T_1 are the measured spin-lattice relaxation rates. The subscripts *s* and *r* refer to the unknown sample of interest and the reference material, respectively. Here, we used the carrier densities found from the Drude model for oxidized $Cu_{2-x}Se$ (x ~ 0.2) NPs for our reference compound, with the following parameters at room temperature: $m_h^* = 0.336m_0$, $N_h = 4.2 \times 10^{21}$ cm^{-3}, and $T_1 = 2.1 \pm 0.1$ ms. The effective mass for each $Cu_{2-x}Se$ NP was adjusted based on the compositional changes[389] observed in PXRD and ssNMR. Using this approach, we find that the carrier densities of the $Cu_{2-x}Se$ NPs are generally consistent with those found using the Drude model (Table 15) – with the important exception that NMR can approximate carrier densities even in cases where no absorption band is observed. As expected for metallic systems that follow Fermi-Dirac statistics, a plot of δ_{iso} (which contains contributions from the chemical shift and Knight shift) as a function of $N_h^{1/3}$ results in a linear relationship (Figure 73). By analyzing $Cu_{2-x}Se$ NPs with NMR spectroscopy we able to determine that all particle compositions exhibit Korringa behavior and subsequently measure the carrier density for comparison with the Drude model. Importantly, we were able to provide a robust structural analysis of short- and long-range order in $Cu_{2-x}Se$ NPs using a combination of PXRD, SAED, and ssNMR spectroscopy to correlate optoelectronic features with structural and compositional changes in the NPs.

Table 15. Carrier densities calculated with the Drude model and ssNMR and associated parameters

Sample	m_h^*/m_0	T_1 (ms)	N_h (cm^{-3}, Drude)	N_h (cm^{-3}, ssNMR)
$Cu_{2-x}Se$ (x ~ 0.2) NPs (δ_{iso} = 1133 ppm)	0.336	2.1 ± 0.1	4.2×10^{21}	N/A – reference
$Cu_{2-x}Se$ (x > 0) NPs (δ_{iso} = 370 ppm)	0.445	3.9 ± 0.1	2.6×10^{21}	7.9×10^{20}
$Cu_{2-x}Se$ (x ~ 0) NPs (δ_{iso} = -445 ppm)	1.1	40.6 ± 2.9	N/A	1.4×10^{18}

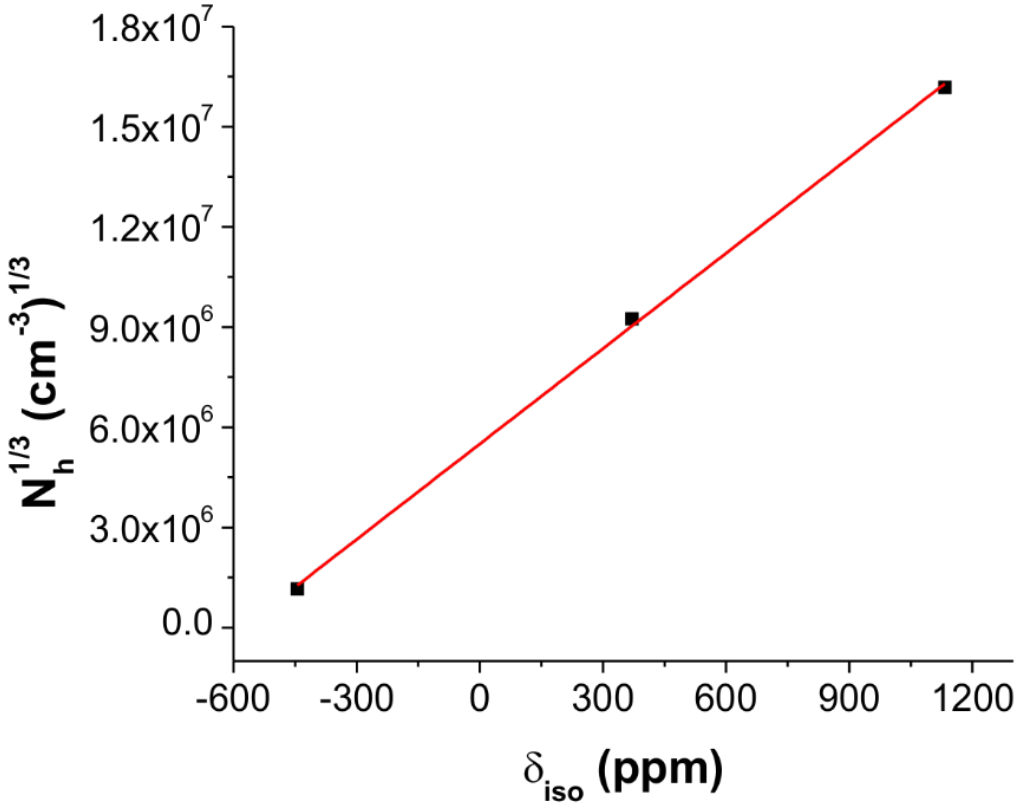

Figure 73. Isotropic ^{77}Se chemical shift as a function of $N_h^{1/3}$ for $Cu_{2-x}Se$ (x ~ 0-0.2) NPs showing linear behavior that is consistent with metallicity

6.4 CONCLUSIONS

In conclusion, we describe the local structural transformations induced by oxygen exposure for $Cu_{2-x}Se$ NPs and correlate those structural features with the electronic properties of the resulting NPs. Interestingly, even $Cu_{2-x}Se$ NP compositions that did not exhibit a LSPR in the optical window examined, still showed a non-zero local density of states at the Fermi level, consistent with metallic behavior. Using a combination of absorption spectroscopy and ssNMR, the carrier density of each sample was determined and found to correlate with both structure and the Korringa product. Based on these results, ssNMR spectroscopy provides previously inaccessible local structural and electronic properties that dictate the emergence of plasmonic behavior in non-noble metal nanomaterials, and should become a powerful tool in designing and testing next generation plasmonic materials.

APPENDIX A

CRYSTALLOGRAPHIC DATA

Table 16. Atomic coordinates and equivalent isotropic atomic displacement parameters ($Å^2$) for $Au_{11}(PPh_3)_7Cl_3$. U(eq) is defined as one third of the trace of the orthogonalized U_{ij} tensor

	x/a	y/b	z/c	U(eq)
Au1	0.2214(4)	0.25	0.1128(3)	0.0549(17)
Cl1	0.062(2)	0.25	0.073(2)	0.072(10)
Au2	0.4019(4)	0.25	0.1575(3)	0.0563(18)
Cl2	0.580(2)	0.4106(11)	0.2494(18)	0.128(12)
Au3	0.3938(4)	0.25	0.9961(3)	0.0622(19)
P3	0.395(2)	0.25	0.859(2)	0.066(11)
Au4	0.3507(3)	0.30694(15)	0.2650(2)	0.0641(14)
P4	0.2946(19)	0.3634(10)	0.3400(14)	0.086(10)
Au5	0.5279(4)	0.25	0.3231(3)	0.070(2)
P5	0.647(2)	0.25	0.4600(18)	0.079(13)
Au6	0.3162(3)	0.33158(14)	0.0686(3)	0.0722(15)
P6	0.230(3)	0.4009(10)	0.989(2)	0.18(2)
Au7	0.4944(3)	0.33820(18)	0.2029(3)	0.0941(18)
Au8	0.5646(4)	0.25	0.1494(4)	0.106(3)
P8	0.718(3)	0.2749(15)	0.147(3)	0.068(17)

Table 17. Bond lengths (Å) for $Au_{11}(PPh_3)_7Cl_3$

Au1-Cl1	2.38(3)	Au1-Au2	2.694(8)
Au1-Au6	2.881(5)	Au1-Au6	2.881(5)
Au1-Au4	2.969(6)	Au1-Au4	2.969(6)
Au2-Au3	2.611(7)	Au2-Au8	2.659(9)
Au2-Au6	2.664(5)	Au2-Au6	2.664(5)
Au2-Au4	2.678(5)	Au2-Au4	2.678(5)
Au2-Au5	2.694(7)	Au2-Au7	2.701(5)
Au2-Au7	2.701(5)	Cl2-Au7	2.30(3)

Au3-P3	2.27(3)	Au3-Au8	2.920(8)
Au3-Au6	2.954(5)	Au3-Au6	2.954(5)
Au4-P4	2.32(2)	Au4-Au7	2.972(6)
Au4-Au4	2.999(8)	Au4-Au5	3.021(7)
Au4-Au6	3.132(5)	Au5-P5	2.32(3)
Au5-Au7	2.963(6)	Au5-Au7	2.963(6)
Au5-Au4	3.021(7)	Au5-Au8	3.134(8)
Au6-P6	2.36(3)	Au6-Au7	2.863(6)
Au7-Au8	2.864(6)	Au8-P8	2.55(5)
Au8-P8	2.55(5)	Au8-Au7	2.864(6)
P8-P8	1.31(8)		

Table 18. Bond angles (°) for $Au_{11}(PPh_3)_7Cl_3$

Cl1-Au1-Au2	179.7(8)	Cl1-Au1-Au6	122.9(4)
Au2-Au1-Au6	56.96(14)	Cl1-Au1-Au6	122.9(4)
Au2-Au1-Au6	56.96(14)	Au6-Au1-Au6	96.4(2)
Cl1-Au1-Au4	124.0(6)	Au2-Au1-Au4	56.21(14)
Au6-Au1-Au4	64.71(13)	Au6-Au1-Au4	109.0(2)
Cl1-Au1-Au4	124.0(6)	Au2-Au1-Au4	56.21(14)
Au6-Au1-Au4	109.0(2)	Au6-Au1-Au4	64.71(13)
Au4-Au1-Au4	60.68(18)	Au3-Au2-Au8	67.3(2)
Au3-Au2-Au6	68.12(14)	Au8-Au2-Au6	106.21(17)
Au3-Au2-Au6	68.12(14)	Au8-Au2-Au6	106.21(17)
Au6-Au2-Au6	107.5(2)	Au3-Au2-Au4	139.90(16)
Au8-Au2-Au4	126.1(2)	Au6-Au2-Au4	71.78(14)
Au6-Au2-Au4	126.2(2)	Au3-Au2-Au4	139.90(16)
Au8-Au2-Au4	126.1(2)	Au6-Au2-Au4	126.2(2)
Au6-Au2-Au4	71.78(14)	Au4-Au2-Au4	68.1(2)
Au3-Au2-Au1	95.4(2)	Au8-Au2-Au1	162.7(3)
Au6-Au2-Au1	65.07(15)	Au6-Au2-Au1	65.07(15)
Au4-Au2-Au1	67.10(17)	Au4-Au2-Au1	67.10(17)
Au3-Au2-Au5	138.9(3)	Au8-Au2-Au5	71.7(2)
Au6-Au2-Au5	125.61(12)	Au6-Au2-Au5	125.61(12)
Au4-Au2-Au5	68.43(16)	Au4-Au2-Au5	68.43(16)
Au1-Au2-Au5	125.6(2)	Au3-Au2-Au7	95.08(16)
Au8-Au2-Au7	64.59(15)	Au6-Au2-Au7	163.2(2)

Au6-Au2-Au7	64.50(14)	Au4-Au2-Au7	125.0(2)
Au4-Au2-Au7	67.08(14)	Au1-Au2-Au7	119.45(15)
Au5-Au2-Au7	66.63(15)	Au3-Au2-Au7	95.08(16)
Au8-Au2-Au7	64.59(15)	Au6-Au2-Au7	64.50(14)
Au6-Au2-Au7	163.2(2)	Au4-Au2-Au7	67.08(14)
Au4-Au2-Au7	125.0(2)	Au1-Au2-Au7	119.45(15)
Au5-Au2-Au7	66.63(15)	Au7-Au2-Au7	118.7(3)
P3-Au3-Au2	176.8(9)	P3-Au3-Au8	119.7(9)
Au2-Au3-Au8	57.1(2)	P3-Au3-Au6	124.7(4)
Au2-Au3-Au6	56.79(13)	Au8-Au3-Au6	92.88(17)
P3-Au3-Au6	124.7(4)	Au2-Au3-Au6	56.79(13)
Au8-Au3-Au6	92.88(17)	Au6-Au3-Au6	93.3(2)
P4-Au4-Au2	171.6(6)	P4-Au4-Au1	119.0(7)
Au2-Au4-Au1	56.70(17)	P4-Au4-Au7	121.0(7)
Au2-Au4-Au7	56.82(14)	Au1-Au4-Au7	103.29(17)
P4-Au4-Au4	129.8(7)	Au2-Au4-Au4	55.95(10)
Au1-Au4-Au4	59.66(9)	Au7-Au4-Au4	106.08(12)
P4-Au4-Au5	131.1(6)	Au2-Au4-Au5	56.03(16)
Au1-Au4-Au5	106.29(16)	Au7-Au4-Au5	59.25(15)
Au4-Au4-Au5	60.23(10)	P4-Au4-Au6	117.8(6)
Au2-Au4-Au6	53.89(12)	Au1-Au4-Au6	56.30(13)
Au7-Au4-Au6	55.87(14)	Au4-Au4-Au6	101.96(10)
Au5-Au4-Au6	101.51(16)	P5-Au5-Au2	174.5(9)
P5-Au5-Au7	121.2(4)	Au2-Au5-Au7	56.79(12)
P5-Au5-Au7	121.2(4)	Au2-Au5-Au7	56.79(12)
Au7-Au5-Au7	103.3(2)	P5-Au5-Au4	128.7(7)
Au2-Au5-Au4	55.54(15)	Au7-Au5-Au4	105.8(2)
Au7-Au5-Au4	59.55(14)	P5-Au5-Au4	128.7(7)
Au2-Au5-Au4	55.54(15)	Au7-Au5-Au4	59.55(14)
Au7-Au5-Au4	105.8(2)	Au4-Au5-Au4	59.53(19)
P5-Au5-Au8	120.9(9)	Au2-Au5-Au8	53.65(19)
Au7-Au5-Au8	55.95(12)	Au7-Au5-Au8	55.95(12)
Au4-Au5-Au8	101.24(18)	Au4-Au5-Au8	101.24(18)
P6-Au6-Au2	175.6(11)	P6-Au6-Au7	125.4(11)
Au2-Au6-Au7	58.37(16)	P6-Au6-Au1	117.6(11)
Au2-Au6-Au1	57.97(16)	Au7-Au6-Au1	108.39(19)
P6-Au6-Au3	125.8(7)	Au2-Au6-Au3	55.09(15)
Au7-Au6-Au3	84.69(19)	Au1-Au6-Au3	84.50(15)

P6-Au6-Au4	124.6(7)	Au2-Au6-Au4	54.33(14)
Au7-Au6-Au4	59.24(14)	Au1-Au6-Au4	58.99(14)
Au3-Au6-Au4	109.42(16)	Cl2-Au7-Au2	176.2(9)
Cl2-Au7-Au6	126.6(9)	Au2-Au7-Au6	57.12(15)
Cl2-Au7-Au8	121.3(8)	Au2-Au7-Au8	57.00(18)
Au6-Au7-Au8	96.04(19)	Cl2-Au7-Au5	119.8(8)
Au2-Au7-Au5	56.58(16)	Au6-Au7-Au5	109.76(19)
Au8-Au7-Au5	65.04(18)	Cl2-Au7-Au4	123.8(7)
Au2-Au7-Au4	56.10(15)	Au6-Au7-Au4	64.89(14)
Au8-Au7-Au4	109.21(19)	Au5-Au7-Au4	61.19(16)
P8-Au8-P8	29.7(16)	P8-Au8-Au2	165.0(8)
P8-Au8-Au2	165.0(8)	P8-Au8-Au7	106.8(9)
P8-Au8-Au7	134.9(8)	Au2-Au8-Au7	58.41(15)
P8-Au8-Au7	134.9(8)	P8-Au8-Au7	106.8(9)
Au2-Au8-Au7	58.41(15)	Au7-Au8-Au7	108.4(3)
P8-Au8-Au3	124.9(9)	P8-Au8-Au3	124.9(9)
Au2-Au8-Au3	55.57(19)	Au7-Au8-Au3	85.31(18)
Au7-Au8-Au3	85.31(18)	P8-Au8-Au5	122.1(10)
P8-Au8-Au5	122.1(10)	Au2-Au8-Au5	54.69(18)
Au7-Au8-Au5	59.01(14)	Au7-Au8-Au5	59.01(14)
Au3-Au8-Au5	110.3(3)	P8-P8-Au8	75.1(8)

Table 19. Anisotropic atomic displacement parameters ($Å^2$) for $Au_{11}(PPh_3)_7Cl_3$. The anisotropic atomic displacement factor exponent takes the form: $-2\pi^2[h^2 a^{*2} U_{11} + ... + 2 h k a^* b^* U_{12}]$

	U_{11}	U_{22}	U_{33}	U_{23}	U_{13}	U_{12}
Au1	0.067(4)	0.046(4)	0.050(4)	0	0.020(3)	0
Cl1	0.07(3)	0.06(2)	0.08(3)	0	0.02(2)	0
Au2	0.069(4)	0.071(4)	0.030(3)	0	0.019(3)	0
Cl2	0.14(3)	0.16(3)	0.11(2)	-0.09(2)	0.07(2)	-0.08(2)
Au3	0.088(5)	0.070(4)	0.030(3)	0	0.025(3)	0
P3	0.08(3)	0.08(3)	0.04(2)	0	0.03(2)	0
Au4	0.078(3)	0.079(3)	0.038(2)	-0.006(2)	0.025(2)	0.003(3)
P4	0.11(2)	0.13(2)	0.028(15)	0.037(16)	0.036(16)	0.050(19)
Au5	0.076(5)	0.100(5)	0.032(4)	0	0.018(3)	0
P5	0.08(3)	0.15(4)	0.001(18)	0	0.011(19)	0
Au6	0.129(4)	0.041(2)	0.060(3)	-0.002(2)	0.052(3)	-0.003(3)
P6	0.45(7)	0.04(2)	0.17(3)	0.05(2)	0.24(4)	0.08(3)
Au7	0.111(4)	0.118(4)	0.062(3)	-0.034(3)	0.042(3)	-0.054(3)

Au8	0.074(5)	0.204(8)	0.045(4)	0	0.027(4)	0
P8	0.06(3)	0.06(3)	0.05(3)	0.00(2)	-0.02(2)	0.06(2)

Table 20. Atomic coordinates and equivalent isotropic atomic displacement parameters ($Å^2$) for $[Au_{11}(PPh_3)_8Cl_2]Cl$. U(eq) is defined as one third of the trace of the orthogonalized U_{ij} tensor

	x/a	**y/b**	**z/c**	**U(eq)**
Au1	0.71773(7)	0.68970(8)	0.63083(4)	0.0263(4)
Au2	0.65256(8)	0.79406(8)	0.59114(4)	0.0323(5)
Au3	0.74515(8)	0.70614(9)	0.55734(4)	0.0343(5)
Au4	0.66881(8)	0.57146(8)	0.65950(4)	0.0353(5)
Au5	0.68890(8)	0.80506(9)	0.67357(4)	0.0367(5)
Au6	0.60226(8)	0.70150(8)	0.64652(5)	0.0347(5)
Au7	0.75191(8)	0.56279(9)	0.60222(4)	0.0352(5)
Au8	0.63661(8)	0.63261(9)	0.57634(4)	0.0372(5)
Au9	0.75048(9)	0.67908(9)	0.70656(4)	0.0419(5)
Au10	0.78137(8)	0.81029(9)	0.62175(5)	0.0383(5)
Au11	0.83421(8)	0.66755(10)	0.64013(5)	0.0433(5)
P2	0.5918(5)	0.8763(5)	0.5589(3)	0.034(3)
P3	0.7594(5)	0.7157(6)	0.4924(3)	0.040(3)
P5	0.5095(5)	0.6981(5)	0.6654(3)	0.036(3)
P6	0.6319(5)	0.4665(5)	0.6804(3)	0.038(3)
P7	0.7780(6)	0.6792(6)	0.7735(3)	0.056(4)
P8	0.7822(5)	0.4526(6)	0.5807(3)	0.048(3)
P10	0.9363(5)	0.6455(7)	0.6460(3)	0.051(3)
P11	0.8295(5)	0.9186(7)	0.6275(3)	0.051(3)
Cl1	0.5650(5)	0.5830(6)	0.5286(3)	0.058(3)
Cl2	0.6630(6)	0.9060(7)	0.7095(3)	0.081(4)
C1	0.6823(9)	0.9197(14)	0.5176(6)	0.042(11)
C2	0.7064(9)	0.9496(15)	0.4859(8)	0.090(18)
C3	0.6702(13)	0.9628(14)	0.4514(7)	0.057(13)
C4	0.6100(12)	0.9461(14)	0.4487(6)	0.078(16)
C5	0.5859(8)	0.9162(13)	0.4805(7)	0.035(10)
C6	0.6220(10)	0.9030(12)	0.5149(6)	0.021(9)
C7	0.5616(12)	0.0257(13)	0.5645(5)	0.051(12)
C8	0.5445(12)	0.0853(11)	0.5850(7)	0.050(12)
C9	0.5435(13)	0.0813(12)	0.6251(7)	0.061(13)
C10	0.5597(13)	0.0177(15)	0.6448(5)	0.074(15)
C11	0.5769(12)	0.9581(11)	0.6243(7)	0.045(11)
C12	0.5778(12)	0.9621(11)	0.5841(7)	0.037(10)
C13	0.4699(13)	0.8850(10)	0.5346(8)	0.058(13)
C14	0.4150(11)	0.8563(13)	0.5204(8)	0.046(11)
C15	0.4091(10)	0.7827(14)	0.5136(8)	0.060(13)
C16	0.4582(12)	0.7377(10)	0.5209(8)	0.047(11)
C17	0.5132(10)	0.7663(14)	0.5351(8)	0.057(13)
C18	0.5190(10)	0.8400(15)	0.5419(9)	0.068(14)

C19	0.8333(15)	0.8301(18)	0.5100(7)	0.089(18)
C20	0.8674(15)	0.8886(18)	0.5007(10)	0.11(2)
C21	0.8666(14)	0.9108(15)	0.4622(12)	0.13(3)
C22	0.8315(15)	0.8744(17)	0.4329(8)	0.077(16)
C23	0.7974(13)	0.8158(15)	0.4422(7)	0.060(13)
C24	0.7982(13)	0.7936(13)	0.4808(9)	0.041(11)
C25	0.6389(14)	0.7356(15)	0.4735(6)	0.068(14)
C26	0.5861(10)	0.7324(16)	0.4489(9)	0.074(15)
C27	0.5866(10)	0.7095(16)	0.4106(8)	0.086(18)
C28	0.6399(13)	0.6898(14)	0.3969(6)	0.061(14)
C29	0.6927(10)	0.6929(13)	0.4215(8)	0.049(12)
C30	0.6922(10)	0.7158(15)	0.4598(7)	0.046(11)
C31	0.8543(11)	0.6519(13)	0.4578(8)	0.049(12)
C32	0.8810(11)	0.5931(17)	0.4416(9)	0.072(15)
C33	0.8536(15)	0.5259(14)	0.4408(9)	0.11(2)
C34	0.7997(15)	0.5174(12)	0.4563(10)	0.11(2)
C35	0.7731(11)	0.5762(16)	0.4724(9)	0.065(14)
C36	0.8004(11)	0.6434(13)	0.4732(8)	0.036(10)
C37	0.7417(12)	0.4445(14)	0.7198(8)	0.057(13)
C38	0.7820(9)	0.4193(18)	0.7501(10)	0.11(2)
C39	0.7625(14)	0.3752(18)	0.7787(8)	0.096(19)
C40	0.7027(15)	0.3563(15)	0.7771(7)	0.086(17)
C41	0.6625(10)	0.3815(14)	0.7468(8)	0.061(13)
C42	0.6820(11)	0.4256(13)	0.7182(7)	0.028(9)
C43	0.6270(12)	0.3252(13)	0.6494(6)	0.044(11)
C44	0.6111(13)	0.2745(10)	0.6205(8)	0.062(14)
C45	0.5839(14)	0.2965(14)	0.5844(7)	0.084(17)
C46	0.5725(13)	0.3692(16)	0.5773(6)	0.074(15)
C47	0.5884(12)	0.4199(11)	0.6062(8)	0.057(13)
C48	0.6156(12)	0.3979(12)	0.6423(7)	0.033(10)
C49	0.5185(12)	0.4152(12)	0.6976(7)	0.044(11)
C50	0.4709(10)	0.4152(13)	0.7200(8)	0.060(13)
C51	0.4655(11)	0.4700(16)	0.7469(8)	0.068(15)
C52	0.5077(13)	0.5247(13)	0.7514(7)	0.072(15)
C53	0.5553(11)	0.5247(12)	0.7289(8)	0.040(11)
C54	0.5607(10)	0.4699(14)	0.7020(7)	0.051(12)
C55	0.5635(9)	0.7077(13)	0.7401(7)	0.035(10)
C56	0.5657(10)	0.7147(14)	0.7803(7)	0.062(14)
C57	0.5132(13)	0.7201(15)	0.7978(5)	0.064(14)
C58	0.4586(10)	0.7184(15)	0.7750(8)	0.077(16)
C59	0.4565(8)	0.7114(14)	0.7348(7)	0.047(12)
C60	0.5090(11)	0.7061(13)	0.7173(5)	0.030(10)
C61	0.4258(13)	0.5851(16)	0.6650(7)	0.056(13)
C62	0.3951(12)	0.5261(16)	0.6480(9)	0.12(2)
C63	0.4104(13)	0.4981(13)	0.6131(9)	0.068(14)
C64	0.4565(14)	0.5290(15)	0.5951(7)	0.069(15)

C65	0.4872(11)	0.5880(15)	0.6121(8)	0.055(13)
C66	0.4718(12)	0.6160(12)	0.6470(8)	0.043(11)
C67	0.4052(12)	0.7580(12)	0.6238(8)	0.049(12)
C68	0.3666(11)	0.8147(16)	0.6133(8)	0.078(16)
C69	0.3794(13)	0.8835(14)	0.6278(9)	0.077(16)
C70	0.4307(14)	0.8955(11)	0.6529(9)	0.076(16)
C71	0.4693(11)	0.8388(15)	0.6635(8)	0.070(15)
C72	0.4565(11)	0.7700(12)	0.6489(8)	0.032(10)
C73	0.6863(12)	0.4522(13)	0.5261(8)	0.050(12)
C74	0.6523(10)	0.4293(15)	0.4924(8)	0.073(15)
C75	0.6717(12)	0.3722(16)	0.4709(7)	0.062(13)
C76	0.7252(13)	0.3380(13)	0.4832(8)	0.080(16)
C77	0.7592(10)	0.3610(14)	0.5169(8)	0.051(12)
C78	0.7398(12)	0.4181(15)	0.5383(7)	0.059(13)
C79	0.8765(18)	0.516(2)	0.5515(11)	0.041(11)
C80	0.930(2)	0.530(3)	0.5391(15)	0.086(18)
C81	0.966(2)	0.462(3)	0.5382(14)	0.076(16)
C82	0.940(3)	0.394(3)	0.5527(17)	0.10(2)
C83	0.887(2)	0.394(2)	0.5677(13)	0.059(13)
C84	0.8532(18)	0.455(2)	0.5639(11)	0.039(10)
C85	0.7576(14)	0.3197(18)	0.6086(8)	0.078(16)
C86	0.7657(15)	0.2642(14)	0.6358(11)	0.087(17)
C87	0.8056(18)	0.2726(17)	0.6690(10)	0.10(2)
C88	0.8373(15)	0.337(2)	0.6751(8)	0.14(3)
C89	0.8292(14)	0.3920(15)	0.6480(10)	0.070(15)
C90	0.7893(15)	0.3836(15)	0.6147(9)	0.063(14)
C91	0.6940(13)	0.5768(15)	0.7860(6)	0.047(12)
C92	0.6533(12)	0.5424(12)	0.8072(8)	0.062(13)
C93	0.6435(12)	0.5680(15)	0.8438(8)	0.078(16)
C94	0.6744(13)	0.6281(15)	0.8592(6)	0.056(13)
C95	0.7151(12)	0.6625(13)	0.8380(8)	0.062(14)
C96	0.7249(12)	0.6369(15)	0.8014(8)	0.065(14)
C97	0.7426(13)	0.815(2)	0.7854(9)	0.094(19)
C98	0.7393(14)	0.8789(17)	0.8064(11)	0.11(2)
C99	0.7821(17)	0.8939(14)	0.8374(10)	0.090(18)
C100	0.8281(14)	0.8453(19)	0.8473(8)	0.10(2)
C101	0.8313(13)	0.7818(16)	0.8263(9)	0.070(15)
C102	0.7886(15)	0.7668(14)	0.7954(9)	0.060(13)
C103	0.9576(18)	0.561(3)	0.8070(13)	0.14(3)
C104	0.9567(16)	0.625(3)	0.7860(13)	0.14(3)
C105	0.903(2)	0.6608(18)	0.7763(11)	0.12(2)
C106	0.8506(16)	0.633(2)	0.7877(11)	0.077(16)
C107	0.8516(18)	0.569(2)	0.8087(12)	0.13(3)
C108	0.905(2)	0.5327(18)	0.8183(11)	0.16(3)
C109	0.8446(13)	0.8951(13)	0.7087(9)	0.065(14)
C110	0.8600(14)	0.9151(15)	0.7472(8)	0.058(13)

C111	0.8806(14)	0.9845(17)	0.7561(7)	0.079(16)
C112	0.8858(15)	0.0338(13)	0.7263(11)	0.11(2)
C113	0.8705(16)	0.0137(16)	0.6877(9)	0.090(18)
C114	0.8499(15)	0.9444(18)	0.6789(7)	0.072(15)
C115	0.7331(12)	0.0116(15)	0.6238(7)	0.043(11)
C116	0.6954(11)	0.0658(16)	0.6080(9)	0.095(19)
C117	0.7065(14)	0.0991(14)	0.5734(10)	0.098(19)
C118	0.7551(16)	0.0782(16)	0.5546(7)	0.096(19)
C119	0.7927(12)	0.0240(16)	0.5704(8)	0.067(14)
C120	0.7817(11)	0.9907(13)	0.6050(8)	0.037(10)
C121	0.9284(15)	0.9944(13)	0.6050(9)	0.077(16)
C122	0.9861(16)	0.9952(16)	0.5946(10)	0.094(19)
C123	0.0150(11)	0.931(2)	0.5884(11)	0.16(3)
C124	0.9862(13)	0.8655(16)	0.5926(9)	0.082(17)
C125	0.9284(13)	0.8647(13)	0.6030(8)	0.047(12)
C126	0.8995(11)	0.9292(16)	0.6092(9)	0.059(13)
C127	0.9329(11)	0.6905(16)	0.5696(10)	0.067(14)
C128	0.9583(15)	0.7081(16)	0.5359(8)	0.095(19)
C129	0.0187(16)	0.6964(17)	0.5339(8)	0.086(18)
C130	0.0536(11)	0.6671(17)	0.5656(10)	0.094(19)
C131	0.0282(13)	0.6495(15)	0.5994(8)	0.071(15)
C132	0.9678(14)	0.6612(15)	0.6013(7)	0.053(12)
C133	0.9861(15)	0.5089(17)	0.6400(7)	0.061(13)
C134	0.0019(14)	0.4410(16)	0.6546(9)	0.087(17)
C135	0.9848(16)	0.4193(14)	0.6904(10)	0.078(16)
C136	0.9519(16)	0.4656(19)	0.7114(8)	0.11(2)
C137	0.9361(14)	0.5335(17)	0.6968(9)	0.083(17)
C138	0.9532(14)	0.5552(13)	0.6610(10)	0.074(15)
C139	0.9559(12)	0.7692(17)	0.6887(9)	0.085(17)
C140	0.9922(18)	0.8171(13)	0.7113(10)	0.084(17)
C141	0.0495(17)	0.7968(19)	0.7258(10)	0.14(3)
C142	0.0705(12)	0.729(2)	0.7177(11)	0.11(2)
C143	0.0343(15)	0.6806(15)	0.6951(10)	0.092(19)
C144	0.9769(13)	0.7009(15)	0.6806(8)	0.039(11)

Table 21. Bond lengths (Å) for $[Au_{11}(PPh_3)_8Cl_2]Cl$

Au1-Au9	2.646(2)	Au1-Au11	2.649(3)
Au1-Au3	2.691(2)	Au1-Au4	2.691(2)
Au1-Au10	2.695(2)	Au1-Au7	2.697(2)
Au1-Au8	2.698(2)	Au1-Au2	2.713(2)
Au1-Au5	2.717(2)	Au1-Au6	2.730(2)
Au2-P2	2.264(10)	Au2-Au5	2.882(2)
Au2-Au6	2.890(2)	Au2-Au3	2.986(2)

Au2-Au10	3.004(3)	Au2-Au8	3.052(2)
Au3-P3	2.304(10)	Au3-Au8	2.941(3)
Au3-Au10	2.992(2)	Au3-Au7	3.072(2)
Au4-P6	2.265(10)	Au4-Au6	2.852(2)
Au4-Au7	2.872(2)	Au4-Au9	3.064(2)
Au4-Au8	3.099(2)	Au5-Cl2	2.354(11)
Au5-Au6	2.829(2)	Au5-Au9	2.890(2)
Au5-Au10	2.893(2)	Au6-P5	2.262(11)
Au6-Au8	2.915(2)	Au7-P8	2.303(11)
Au7-Au11	2.903(2)	Au7-Au8	2.961(2)
Au8-Cl1	2.368(11)	Au9-P7	2.328(10)
Au9-Au11	3.131(3)	Au10-P11	2.283(12)
Au10-Au11	2.945(2)	Au11-P10	2.329(11)
P2-C6	1.80(2)	P2-C18	1.82(2)
P2-C12	1.86(2)	P3-C24	1.76(2)
P3-C30	1.79(2)	P3-C36	1.80(2)
P5-C60	1.80(2)	P5-C66	1.83(2)
P5-C72	1.84(2)	P6-C42	1.80(2)
P6-C48	1.84(2)	P6-C54	1.85(2)
P7-C102	1.80(3)	P7-C96	1.80(2)
P7-C106	1.87(3)	P8-C90	1.73(3)
P8-C84	1.76(4)	P8-C78	1.78(2)
P10-C144	1.76(3)	P10-C138	1.78(3)
P10-C132	1.79(3)	P11-C126	1.78(3)
P11-C120	1.84(2)	P11-C114	1.85(3)
C1-C2	1.39	C1-C6	1.39
C1-H1A	0.94	C2-C3	1.39
C2-H2A	0.94	C3-C4	1.39
C3-H3A	0.94	C4-C5	1.39
C4-H4A	0.94	C5-C6	1.39
C5-H5A	0.94	C7-C8	1.39
C7-C12	1.39	C7-H7A	0.94
C8-C9	1.39	C8-H8A	0.94
C9-C10	1.39	C9-H9A	0.94
C10-C11	1.39	C10-H10A	0.94
C11-C12	1.39	C11-H11A	0.94
C13-C14	1.39	C13-C18	1.39
C13-H13A	0.94	C14-C15	1.39

C14-H14A	0.94	C15-C16	1.39
C15-H15A	0.94	C16-C17	1.39
C16-H16A	0.94	C17-C18	1.39
C17-H17A	0.94	C19-C20	1.39
C19-C24	1.39	C19-H19A	0.94
C20-C21	1.39	C20-H20A	0.94
C21-C22	1.39	C21-H21A	0.94
C22-C23	1.39	C22-H22A	0.94
C23-C24	1.39	C23-H23A	0.94
C25-C26	1.39	C25-C30	1.39
C25-H25A	0.94	C26-C27	1.39
C26-H26A	0.94	C27-C28	1.39
C27-H27A	0.94	C28-C29	1.39
C28-H28A	0.94	C29-C30	1.39
C29-H29A	0.94	C31-C32	1.39
C31-C36	1.39	C31-H31A	0.94
C32-C33	1.39	C32-H32A	0.94
C33-C34	1.39	C33-H33A	0.94
C34-C35	1.39	C34-H34A	0.94
C35-C36	1.39	C35-H35A	0.94
C37-C38	1.39	C37-C42	1.39
C37-H37A	0.94	C38-C39	1.39
C38-H38A	0.94	C39-C40	1.39
C39-H39A	0.94	C40-C41	1.39
C40-H40A	0.94	C41-C42	1.39
C41-H41A	0.94	C43-C44	1.39
C43-C48	1.39	C43-H43A	0.94
C44-C45	1.39	C44-H44A	0.94
C45-C46	1.39	C45-H45A	0.94
C46-C47	1.39	C46-H46A	0.94
C47-C48	1.39	C47-H47A	0.94
C49-C50	1.39	C49-C54	1.39
C49-H49A	0.94	C50-C51	1.39
C50-H50A	0.94	C51-C52	1.39
C51-H51A	0.94	C52-C53	1.39
C52-H52A	0.94	C53-C54	1.39
C53-H53A	0.94	C55-C56	1.39
C55-C60	1.39	C55-H55A	0.94

C56-C57	1.39	C56-H56A	0.94
C57-C58	1.39	C57-H57A	0.94
C58-C59	1.39	C58-H58A	0.94
C59-C60	1.39	C59-H59A	0.94
C61-C62	1.39	C61-C66	1.39
C61-H61A	0.94	C62-C63	1.39
C62-H62A	0.94	C63-C64	1.39
C63-H63A	0.94	C64-C65	1.39
C64-H64A	0.94	C65-C66	1.39
C65-H65A	0.94	C67-C68	1.39
C67-C72	1.39	C67-H67A	0.94
C68-C69	1.39	C68-H68A	0.94
C69-C70	1.39	C69-H69A	0.94
C70-C71	1.39	C70-H70A	0.94
C71-C72	1.39	C71-H71A	0.94
C73-C74	1.39	C73-C78	1.39
C73-H73A	0.94	C74-C75	1.39
C74-H74A	0.94	C75-C76	1.39
C75-H75A	0.94	C76-C77	1.39
C76-H76A	0.94	C77-C78	1.39
C77-H77A	0.94	C79-C84	1.34(5)
C79-C80	1.36(6)	C79-H79A	0.94
C80-C81	1.49(7)	C80-H80A	0.94
C81-C82	1.50(7)	C81-H81A	0.94
C82-C83	1.37(7)	C82-H82A	0.94
C83-C84	1.36(5)	C83-H83A	0.94
C85-C86	1.39	C85-C90	1.39
C85-H85A	0.94	C86-C87	1.39
C86-H86A	0.94	C87-C88	1.39
C87-H87A	0.94	C88-C89	1.39
C88-H88A	0.94	C89-C90	1.39
C89-H89A	0.94	C91-C92	1.39
C91-C96	1.39	C91-H91A	0.94
C92-C93	1.39	C92-H92A	0.94
C93-C94	1.39	C93-H93A	0.94
C94-C95	1.39	C94-H94A	0.94
C95-C96	1.39	C95-H95A	0.94
C97-C98	1.39	C97-C102	1.39

C97-H97A	0.94	C98-C99	1.39
C98-H98A	0.94	C99-C100	1.39
C99-H99A	0.94	C100-C101	1.39
C100-H10B	0.94	C101-C102	1.39
C101-H10C	0.94	C103-C104	1.39
C103-C108	1.39	C103-H10D	0.94
C104-C105	1.39	C104-H10E	0.94
C105-C106	1.39	C105-H10F	0.94
C106-C107	1.39	C107-C108	1.39
C107-H10G	0.94	C108-H10H	0.94
C109-C110	1.39	C109-C114	1.39
C109-H10I	0.94	C110-C111	1.39
C110-H11B	0.94	C111-C112	1.39
C111-H11C	0.94	C112-C113	1.39
C112-H11D	0.94	C113-C114	1.39
C113-H11E	0.94	C115-C116	1.39
C115-C120	1.39	C115-H11F	0.94
C116-C117	1.39	C116-H11G	0.94
C117-C118	1.39	C117-H11H	0.94
C118-C119	1.39	C118-H11I	0.94
C119-C120	1.39	C119-H11J	0.94
C121-C122	1.39	C121-C126	1.39
C121-H12A	0.94	C122-C123	1.39
C122-H12B	0.94	C123-C124	1.39
C123-H12C	0.94	C124-C125	1.39
C124-H12D	0.94	C125-C126	1.39
C125-H12E	0.94	C127-C128	1.39
C127-C132	1.39	C127-H12F	0.94
C128-C129	1.39	C128-H12G	0.94
C129-C130	1.39	C129-H12H	0.94
C130-C131	1.39	C130-H13B	0.94
C131-C132	1.39	C131-H13C	0.94
C133-C134	1.39	C133-C138	1.39
C133-H13D	0.94	C134-C135	1.39
C134-H13E	0.94	C135-C136	1.39
C135-H13F	0.94	C136-C137	1.39
C136-H13G	0.94	C137-C138	1.39
C137-H13H	0.94	C139-C140	1.39

C139-C144	1.39	C139-H13I	0.94
C140-C141	1.39	C140-H14B	0.94
C141-C142	1.39	C141-H14C	0.94
C142-C143	1.39	C142-H14D	0.94
C143-C144	1.39	C143-H14E	0.94

Table 22. Bond angles (°) for $[Au_{11}(PPh_3)_8Cl_2]Cl$

Au9-Au1-Au11	72.50(7)	Au9-Au1-Au3	150.54(9)
Au11-Au1-Au3	78.81(7)	Au9-Au1-Au4	70.05(6)
Au11-Au1-Au4	105.72(8)	Au3-Au1-Au4	125.71(7)
Au9-Au1-Au10	94.59(7)	Au11-Au1-Au10	66.88(7)
Au3-Au1-Au10	67.49(6)	Au4-Au1-Au10	164.59(8)
Au9-Au1-Au7	103.63(7)	Au11-Au1-Au7	65.76(6)
Au3-Au1-Au7	69.53(6)	Au4-Au1-Au7	64.42(6)
Au10-Au1-Au7	120.30(8)	Au9-Au1-Au8	139.16(8)
Au11-Au1-Au8	128.01(8)	Au3-Au1-Au8	66.14(6)
Au4-Au1-Au8	70.20(6)	Au10-Au1-Au8	125.16(7)
Au7-Au1-Au8	66.57(6)	Au9-Au1-Au2	129.13(8)
Au11-Au1-Au2	130.58(8)	Au3-Au1-Au2	67.09(6)
Au4-Au1-Au2	123.01(8)	Au10-Au1-Au2	67.47(6)
Au7-Au1-Au2	126.81(7)	Au8-Au1-Au2	68.68(6)
Au9-Au1-Au5	65.20(6)	Au11-Au1-Au5	110.43(8)
Au3-Au1-Au5	120.99(7)	Au4-Au1-Au5	108.09(7)
Au10-Au1-Au5	64.62(6)	Au7-Au1-Au5	168.67(8)
Au8-Au1-Au5	120.19(8)	Au2-Au1-Au5	64.12(6)
Au9-Au1-Au6	89.01(7)	Au11-Au1-Au6	161.22(8)
Au3-Au1-Au6	119.93(8)	Au4-Au1-Au6	63.49(6)
Au10-Au1-Au6	119.32(7)	Au7-Au1-Au6	117.37(8)
Au8-Au1-Au6	64.97(6)	Au2-Au1-Au6	64.15(6)
Au5-Au1-Au6	62.58(6)	P2-Au2-Au1	175.6(3)
P2-Au2-Au5	122.1(2)	Au1-Au2-Au5	58.01(5)
P2-Au2-Au6	117.6(3)	Au1-Au2-Au6	58.21(6)
Au5-Au2-Au6	58.69(6)	P2-Au2-Au3	126.2(2)
Au1-Au2-Au3	56.10(5)	Au5-Au2-Au3	106.63(7)
Au6-Au2-Au3	105.98(7)	P2-Au2-Au10	128.3(3)
Au1-Au2-Au10	55.98(6)	Au5-Au2-Au10	58.84(6)

Au6-Au2-Au10	105.17(7)	Au3-Au2-Au10	59.93(6)
P2-Au2-Au8	121.6(3)	Au1-Au2-Au8	55.43(5)
Au5-Au2-Au8	104.52(6)	Au6-Au2-Au8	58.69(5)
Au3-Au2-Au8	58.27(6)	Au10-Au2-Au8	104.47(7)
P3-Au3-Au1	174.3(3)	P3-Au3-Au8	117.3(3)
Au1-Au3-Au8	57.05(6)	P3-Au3-Au2	120.9(3)
Au1-Au3-Au2	56.81(5)	Au8-Au3-Au2	61.99(6)
P3-Au3-Au10	128.1(3)	Au1-Au3-Au10	56.32(5)
Au8-Au3-Au10	107.60(7)	Au2-Au3-Au10	60.32(6)
P3-Au3-Au7	123.5(3)	Au1-Au3-Au7	55.33(5)
Au8-Au3-Au7	58.95(6)	Au2-Au3-Au7	105.96(6)
Au10-Au3-Au7	100.92(6)	P6-Au4-Au1	175.3(3)
P6-Au4-Au6	124.8(3)	Au1-Au4-Au6	58.91(6)
P6-Au4-Au7	117.4(3)	Au1-Au4-Au7	57.89(6)
Au6-Au4-Au7	108.16(7)	P6-Au4-Au9	127.8(3)
Au1-Au4-Au9	54.28(5)	Au6-Au4-Au9	79.05(6)
Au7-Au4-Au9	90.01(7)	P6-Au4-Au8	123.4(3)
Au1-Au4-Au8	55.01(5)	Au6-Au4-Au8	58.49(5)
Au7-Au4-Au8	59.30(6)	Au9-Au4-Au8	108.72(6)
Cl2-Au5-Au1	178.9(3)	Cl2-Au5-Au6	120.8(4)
Au1-Au5-Au6	58.93(6)	Cl2-Au5-Au2	121.0(3)
Au1-Au5-Au2	57.87(5)	Au6-Au5-Au2	60.79(6)
Cl2-Au5-Au9	124.9(3)	Au1-Au5-Au9	56.22(5)
Au6-Au5-Au9	82.43(7)	Au2-Au5-Au9	113.95(7)
Cl2-Au5-Au10	122.4(4)	Au1-Au5-Au10	57.33(6)
Au6-Au5-Au10	109.81(7)	Au2-Au5-Au10	62.68(6)
Au9-Au5-Au10	85.50(7)	P5-Au6-Au1	171.9(3)
P5-Au6-Au5	123.7(3)	Au1-Au6-Au5	58.49(6)
P5-Au6-Au4	114.9(2)	Au1-Au6-Au4	57.60(6)
Au5-Au6-Au4	100.80(7)	P5-Au6-Au2	130.5(3)
Au1-Au6-Au2	57.65(6)	Au5-Au6-Au2	60.51(6)
Au4-Au6-Au2	111.60(7)	P5-Au6-Au8	124.3(3)
Au1-Au6-Au8	56.99(6)	Au5-Au6-Au8	109.59(8)
Au4-Au6-Au8	64.99(6)	Au2-Au6-Au8	63.44(6)
P8-Au7-Au1	177.4(3)	P8-Au7-Au4	120.7(3)
Au1-Au7-Au4	57.69(6)	P8-Au7-Au11	122.8(3)
Au1-Au7-Au11	56.33(6)	Au4-Au7-Au11	94.99(7)
P8-Au7-Au8	124.9(3)	Au1-Au7-Au8	56.74(6)

Au4-Au7-Au8	64.17(6)	Au11-Au7-Au8	110.12(7)
P8-Au7-Au3	127.3(3)	Au1-Au7-Au3	55.14(5)
Au4-Au7-Au3	107.30(7)	Au11-Au7-Au3	69.07(6)
Au8-Au7-Au3	58.31(6)	Cl1-Au8-Au1	179.7(3)
Cl1-Au8-Au6	121.7(3)	Au1-Au8-Au6	58.03(6)
Cl1-Au8-Au3	123.3(3)	Au1-Au8-Au3	56.81(6)
Au6-Au8-Au3	106.51(7)	Cl1-Au8-Au7	123.6(3)
Au1-Au8-Au7	56.70(6)	Au6-Au8-Au7	104.17(7)
Au3-Au8-Au7	62.74(6)	Cl1-Au8-Au2	123.9(3)
Au1-Au8-Au2	55.89(5)	Au6-Au8-Au2	57.88(5)
Au3-Au8-Au2	59.74(6)	Au7-Au8-Au2	107.11(7)
Cl1-Au8-Au4	125.3(3)	Au1-Au8-Au4	54.79(5)
Au6-Au8-Au4	56.52(5)	Au3-Au8-Au4	104.89(7)
Au7-Au8-Au4	56.53(5)	Au2-Au8-Au4	101.08(6)
P7-Au9-Au1	175.6(3)	P7-Au9-Au5	117.2(3)
Au1-Au9-Au5	58.58(6)	P7-Au9-Au4	127.5(3)
Au1-Au9-Au4	55.66(5)	Au5-Au9-Au4	94.62(7)
P7-Au9-Au11	127.4(4)	Au1-Au9-Au11	53.80(6)
Au5-Au9-Au11	94.01(6)	Au4-Au9-Au11	86.81(6)
P11-Au10-Au1	167.2(3)	P11-Au10-Au5	110.1(3)
Au1-Au10-Au5	58.05(6)	P11-Au10-Au11	126.4(3)
Au1-Au10-Au11	55.82(6)	Au5-Au10-Au11	98.03(7)
P11-Au10-Au3	136.3(3)	Au1-Au10-Au3	56.19(5)
Au5-Au10-Au3	106.20(7)	Au11-Au10-Au3	69.64(6)
P11-Au10-Au2	123.6(3)	Au1-Au10-Au2	56.54(6)
Au5-Au10-Au2	58.49(6)	Au11-Au10-Au2	109.94(7)
Au3-Au10-Au2	59.74(6)	P10-Au11-Au1	177.8(3)
P10-Au11-Au7	120.2(3)	Au1-Au11-Au7	57.91(6)
P10-Au11-Au10	123.5(3)	Au1-Au11-Au10	57.31(6)
Au7-Au11-Au10	106.21(7)	P10-Au11-Au9	128.1(3)
Au1-Au11-Au9	53.70(6)	Au7-Au11-Au9	88.13(7)
Au10-Au11-Au9	80.41(6)	C6-P2-C18	103.9(13)
C6-P2-C12	105.0(12)	C18-P2-C12	106.1(14)
C6-P2-Au2	109.5(9)	C18-P2-Au2	112.9(10)
C12-P2-Au2	118.2(9)	C24-P3-C30	105.4(14)
C24-P3-C36	103.8(14)	C30-P3-C36	101.9(13)
C24-P3-Au3	114.2(11)	C30-P3-Au3	114.5(11)
C36-P3-Au3	115.6(10)	C60-P5-C66	111.2(13)

C60-P5-C72	100.1(12)	C66-P5-C72	103.5(13)
C60-P5-Au6	112.9(9)	C66-P5-Au6	109.6(10)
C72-P5-Au6	118.9(10)	C42-P6-C48	106.7(12)
C42-P6-C54	103.2(13)	C48-P6-C54	101.4(13)
C42-P6-Au4	111.6(10)	C48-P6-Au4	114.9(9)
C54-P6-Au4	117.8(10)	C102-P7-C96	103.7(15)
C102-P7-C106	103.5(18)	C96-P7-C106	106.1(18)
C102-P7-Au9	115.2(12)	C96-P7-Au9	114.1(11)
C106-P7-Au9	113.2(13)	C90-P8-C84	102.4(18)
C90-P8-C78	107.0(16)	C84-P8-C78	99.6(17)
C90-P8-Au7	116.5(12)	C84-P8-Au7	113.6(14)
C78-P8-Au7	115.6(11)	C144-P10-C138	105.8(16)
C144-P10-C132	105.2(15)	C138-P10-C132	108.0(16)
C144-P10-Au11	113.4(12)	C138-P10-Au11	111.8(12)
C132-P10-Au11	112.2(12)	C126-P11-C120	105.9(14)
C126-P11-C114	99.9(16)	C120-P11-C114	107.1(15)
C126-P11-Au10	120.0(12)	C120-P11-Au10	110.5(10)
C114-P11-Au10	112.3(12)	C2-C1-C6	120.0
C2-C1-H1A	120.0	C6-C1-H1A	120.0
C1-C2-C3	120.0	C1-C2-H2A	120.0
C3-C2-H2A	120.0	C4-C3-C2	120.0
C4-C3-H3A	120.0	C2-C3-H3A	120.0
C5-C4-C3	120.0	C5-C4-H4A	120.0
C3-C4-H4A	120.0	C4-C5-C6	120.0
C4-C5-H5A	120.0	C6-C5-H5A	120.0
C5-C6-C1	120.0	C5-C6-P2	121.9(14)
C1-C6-P2	117.5(14)	C8-C7-C12	120.0
C8-C7-H7A	120.0	C12-C7-H7A	120.0
C7-C8-C9	120.0	C7-C8-H8A	120.0
C9-C8-H8A	120.0	C8-C9-C10	120.0
C8-C9-H9A	120.0	C10-C9-H9A	120.0
C9-C10-C11	120.0	C9-C10-H10A	120.0
C11-C10-H10A	120.0	C12-C11-C10	120.0
C12-C11-H11A	120.0	C10-C11-H11A	120.0
C11-C12-C7	120.0	C11-C12-P2	116.3(14)
C7-C12-P2	123.2(14)	C14-C13-C18	120.0
C14-C13-H13A	120.0	C18-C13-H13A	120.0
C15-C14-C13	120.0	C15-C14-H14A	120.0

C13-C14-H14A	120.0	C14-C15-C16	120.0
C14-C15-H15A	120.0	C16-C15-H15A	120.0
C17-C16-C15	120.0	C17-C16-H16A	120.0
C15-C16-H16A	120.0	C16-C17-C18	120.0
C16-C17-H17A	120.0	C18-C17-H17A	120.0
C17-C18-C13	120.0	C17-C18-P2	119.1(17)
C13-C18-P2	120.9(17)	C20-C19-C24	120.0
C20-C19-H19A	120.0	C24-C19-H19A	120.0
C19-C20-C21	120.0	C19-C20-H20A	120.0
C21-C20-H20A	120.0	C22-C21-C20	120.0
C22-C21-H21A	120.0	C20-C21-H21A	120.0
C23-C22-C21	120.0	C23-C22-H22A	120.0
C21-C22-H22A	120.0	C22-C23-C24	120.0
C22-C23-H23A	120.0	C24-C23-H23A	120.0
C23-C24-C19	120.0	C23-C24-P3	120.3(19)
C19-C24-P3	119.6(19)	C26-C25-C30	120.0
C26-C25-H25A	120.0	C30-C25-H25A	120.0
C25-C26-C27	120.0	C25-C26-H26A	120.0
C27-C26-H26A	120.0	C26-C27-C28	120.0
C26-C27-H27A	120.0	C28-C27-H27A	120.0
C27-C28-C29	120.0	C27-C28-H28A	120.0
C29-C28-H28A	120.0	C30-C29-C28	120.0
C30-C29-H29A	120.0	C28-C29-H29A	120.0
C29-C30-C25	120.0	C29-C30-P3	120.3(17)
C25-C30-P3	119.6(17)	C32-C31-C36	120.0
C32-C31-H31A	120.0	C36-C31-H31A	120.0
C31-C32-C33	120.0	C31-C32-H32A	120.0
C33-C32-H32A	120.0	C34-C33-C32	120.0
C34-C33-H33A	120.0	C32-C33-H33A	120.0
C33-C34-C35	120.0	C33-C34-H34A	120.0
C35-C34-H34A	120.0	C34-C35-C36	120.0
C34-C35-H35A	120.0	C36-C35-H35A	120.0
C35-C36-C31	120.0	C35-C36-P3	115.5(17)
C31-C36-P3	124.4(17)	C38-C37-C42	120.0
C38-C37-H37A	120.0	C42-C37-H37A	120.0
C37-C38-C39	120.0	C37-C38-H38A	120.0
C39-C38-H38A	120.0	C40-C39-C38	120.0
C40-C39-H39A	120.0	C38-C39-H39A	120.0

C41-C40-C39	120.0	C41-C40-H40A	120.0
C39-C40-H40A	120.0	C42-C41-C40	120.0
C42-C41-H41A	120.0	C40-C41-H41A	120.0
C41-C42-C37	120.0	C41-C42-P6	122.7(17)
C37-C42-P6	117.1(17)	C44-C43-C48	120.0
C44-C43-H43A	120.0	C48-C43-H43A	120.0
C43-C44-C45	120.0	C43-C44-H44A	120.0
C45-C44-H44A	120.0	C46-C45-C44	120.0
C46-C45-H45A	120.0	C44-C45-H45A	120.0
C47-C46-C45	120.0	C47-C46-H46A	120.0
C45-C46-H46A	120.0	C46-C47-C48	120.0
C46-C47-H47A	120.0	C48-C47-H47A	120.0
C47-C48-C43	120.0	C47-C48-P6	118.2(15)
C43-C48-P6	121.7(15)	C50-C49-C54	120.0
C50-C49-H49A	120.0	C54-C49-H49A	120.0
C51-C50-C49	120.0	C51-C50-H50A	120.0
C49-C50-H50A	120.0	C50-C51-C52	120.0
C50-C51-H51A	120.0	C52-C51-H51A	120.0
C53-C52-C51	120.0	C53-C52-H52A	120.0
C51-C52-H52A	120.0	C54-C53-C52	120.0
C54-C53-H53A	120.0	C52-C53-H53A	120.0
C53-C54-C49	120.0	C53-C54-P6	115.9(15)
C49-C54-P6	123.2(15)	C56-C55-C60	120.0
C56-C55-H55A	120.0	C60-C55-H55A	120.0
C57-C56-C55	120.0	C57-C56-H56A	120.0
C55-C56-H56A	120.0	C56-C57-C58	120.0
C56-C57-H57A	120.0	C58-C57-H57A	120.0
C57-C58-C59	120.0	C57-C58-H58A	120.0
C59-C58-H58A	120.0	C60-C59-C58	120.0
C60-C59-H59A	120.0	C58-C59-H59A	120.0
C59-C60-C55	120.0	C59-C60-P5	122.3(15)
C55-C60-P5	117.7(15)	C62-C61-C66	120.0
C62-C61-H61A	120.0	C66-C61-H61A	120.0
C61-C62-C63	120.0	C61-C62-H62A	120.0
C63-C62-H62A	120.0	C64-C63-C62	120.0
C64-C63-H63A	120.0	C62-C63-H63A	120.0
C65-C64-C63	120.0	C65-C64-H64A	120.0
C63-C64-H64A	120.0	C66-C65-C64	120.0

C66-C65-H65A	120.0	C64-C65-H65A	120.0
C65-C66-C61	120.0	C65-C66-P5	117.6(17)
C61-C66-P5	122.2(17)	C68-C67-C72	120.0
C68-C67-H67A	120.0	C72-C67-H67A	120.0
C67-C68-C69	120.0	C67-C68-H68A	120.0
C69-C68-H68A	120.0	C68-C69-C70	120.0
C68-C69-H69A	120.0	C70-C69-H69A	120.0
C69-C70-C71	120.0	C69-C70-H70A	120.0
C71-C70-H70A	120.0	C72-C71-C70	120.0
C72-C71-H71A	120.0	C70-C71-H71A	120.0
C71-C72-C67	120.0	C71-C72-P5	116.7(16)
C67-C72-P5	123.2(16)	C74-C73-C78	120.0
C74-C73-H73A	120.0	C78-C73-H73A	120.0
C75-C74-C73	120.0	C75-C74-H74A	120.0
C73-C74-H74A	120.0	C74-C75-C76	120.0
C74-C75-H75A	120.0	C76-C75-H75A	120.0
C77-C76-C75	120.0	C77-C76-H76A	120.0
C75-C76-H76A	120.0	C76-C77-C78	120.0
C76-C77-H77A	120.0	C78-C77-H77A	120.0
C77-C78-C73	120.0	C77-C78-P8	122.6(17)
C73-C78-P8	117.4(17)	C84-C79-C80	131.(5)
C84-C79-H79A	114.5	C80-C79-H79A	114.5
C79-C80-C81	111.(5)	C79-C80-H80A	124.7
C81-C80-H80A	124.7	C80-C81-C82	118.(5)
C80-C81-H81A	120.9	C82-C81-H81A	120.9
C83-C82-C81	122.(6)	C83-C82-H82A	119.1
C81-C82-H82A	119.1	C84-C83-C82	117.(5)
C84-C83-H83A	121.3	C82-C83-H83A	121.3
C79-C84-C83	120.(4)	C79-C84-P8	121.(3)
C83-C84-P8	118.(3)	C86-C85-C90	120.0
C86-C85-H85A	120.0	C90-C85-H85A	120.0
C85-C86-C87	120.0	C85-C86-H86A	120.0
C87-C86-H86A	120.0	C88-C87-C86	120.0
C88-C87-H87A	120.0	C86-C87-H87A	120.0
C87-C88-C89	120.0	C87-C88-H88A	120.0
C89-C88-H88A	120.0	C90-C89-C88	120.0
C90-C89-H89A	120.0	C88-C89-H89A	120.0
C89-C90-C85	120.0	C89-C90-P8	119.(2)

C85-C90-P8	121.(2)	C92-C91-C96	120.0
C92-C91-H91A	120.0	C96-C91-H91A	120.0
C91-C92-C93	120.0	C91-C92-H92A	120.0
C93-C92-H92A	120.0	C94-C93-C92	120.0
C94-C93-H93A	120.0	C92-C93-H93A	120.0
C95-C94-C93	120.0	C95-C94-H94A	120.0
C93-C94-H94A	120.0	C94-C95-C96	120.0
C94-C95-H95A	120.0	C96-C95-H95A	120.0
C95-C96-C91	120.0	C95-C96-P7	121.2(17)
C91-C96-P7	118.8(17)	C98-C97-C102	120.0
C98-C97-H97A	120.0	C102-C97-H97A	120.0
C97-C98-C99	120.0	C97-C98-H98A	120.0
C99-C98-H98A	120.0	C100-C99-C98	120.0
C100-C99-H99A	120.0	C98-C99-H99A	120.0
C99-C100-C101	120.0	C99-C100-H10B	120.0
C101-C100-H10B	120.0	C102-C101-C100	120.0
C102-C101-H10C	120.0	C100-C101-H10C	120.0
C101-C102-C97	120.0	C101-C102-P7	124.(2)
C97-C102-P7	115.(2)	C104-C103-C108	120.0
C104-C103-H10D	120.0	C108-C103-H10D	120.0
C103-C104-C105	120.0	C103-C104-H10E	120.0
C105-C104-H10E	120.0	C106-C105-C104	120.0
C106-C105-H10F	120.0	C104-C105-H10F	120.0
C105-C106-C107	120.0	C105-C106-P7	120.(3)
C107-C106-P7	120.(3)	C106-C107-C108	120.0
C106-C107-H10G	120.0	C108-C107-H10G	120.0
C107-C108-C103	120.0	C107-C108-H10H	120.0
C103-C108-H10H	120.0	C110-C109-C114	120.0
C110-C109-H10I	120.0	C114-C109-H10I	120.0
C109-C110-C111	120.0	C109-C110-H11B	120.0
C111-C110-H11B	120.0	C110-C111-C112	120.0
C110-C111-H11C	120.0	C112-C111-H11C	120.0
C111-C112-C113	120.0	C111-C112-H11D	120.0
C113-C112-H11D	120.0	C114-C113-C112	120.0
C114-C113-H11E	120.0	C112-C113-H11E	120.0
C113-C114-C109	120.0	C113-C114-P11	120.(2)
C109-C114-P11	120.(2)	C116-C115-C120	120.0
C116-C115-H11F	120.0	C120-C115-H11F	120.0

C117-C116-C115	120.0	C117-C116-H11G	120.0
C115-C116-H11G	120.0	C118-C117-C116	120.0
C118-C117-H11H	120.0	C116-C117-H11H	120.0
C117-C118-C119	120.0	C117-C118-H11I	120.0
C119-C118-H11I	120.0	C118-C119-C120	120.0
C118-C119-H11J	120.0	C120-C119-H11J	120.0
C119-C120-C115	120.0	C119-C120-P11	122.4(17)
C115-C120-P11	117.6(17)	C122-C121-C126	120.0
C122-C121-H12A	120.0	C126-C121-H12A	120.0
C121-C122-C123	120.0	C121-C122-H12B	120.0
C123-C122-H12B	120.0	C124-C123-C122	120.0
C124-C123-H12C	120.0	C122-C123-H12C	120.0
C123-C124-C125	120.0	C123-C124-H12D	120.0
C125-C124-H12D	120.0	C126-C125-C124	120.0
C126-C125-H12E	120.0	C124-C125-H12E	120.0
C125-C126-C121	120.0	C125-C126-P11	114.3(19)
C121-C126-P11	125.4(19)	C128-C127-C132	120.0
C128-C127-H12F	120.0	C132-C127-H12F	120.0
C127-C128-C129	120.0	C127-C128-H12G	120.0
C129-C128-H12G	120.0	C130-C129-C128	120.0
C130-C129-H12H	120.0	C128-C129-H12H	120.0
C131-C130-C129	120.0	C131-C130-H13B	120.0
C129-C130-H13B	120.0	C130-C131-C132	120.0
C130-C131-H13C	120.0	C132-C131-H13C	120.0
C131-C132-C127	120.0	C131-C132-P10	120.(2)
C127-C132-P10	120.(2)	C134-C133-C138	120.0
C134-C133-H13D	120.0	C138-C133-H13D	120.0
C135-C134-C133	120.0	C135-C134-H13E	120.0
C133-C134-H13E	120.0	C134-C135-C136	120.0
C134-C135-H13F	120.0	C136-C135-H13F	120.0
C137-C136-C135	120.0	C137-C136-H13G	120.0
C135-C136-H13G	120.0	C138-C137-C136	120.0
C138-C137-H13H	120.0	C136-C137-H13H	120.0
C137-C138-C133	120.0	C137-C138-P10	117.(2)
C133-C138-P10	123.(2)	C140-C139-C144	120.0
C140-C139-H13I	120.0	C144-C139-H13I	120.0
C141-C140-C139	120.0	C141-C140-H14B	120.0
C139-C140-H14B	120.0	C142-C141-C140	120.0

C142-C141-H14C	120.0	C140-C141-H14C	120.0
C141-C142-C143	120.0	C141-C142-H14D	120.0
C143-C142-H14D	120.0	C144-C143-C142	120.0
C144-C143-H14E	120.0	C142-C143-H14E	120.0
C143-C144-C139	120.0	C143-C144-P10	119.(2)
C139-C144-P10	120.(2)		

Table 23. Anisotropic atomic displacement parameters ($Å^2$) for $[Au_{11}(PPh_3)_8Cl_2]Cl$. The anisotropic atomic displacement factor exponent takes the form: $-2\pi^2[h^2 a^{*2} U_{11} + ... + 2 h k a^* b^* U_{12}]$

	U_{11}	U_{22}	U_{33}	U_{23}	U_{13}	U_{12}
Au1	0.0400(11)	0.0324(10)	0.0062(8)	-0.0013(6)	0.0000(7)	0.0020(8)
Au2	0.0525(12)	0.0320(10)	0.0122(9)	0.0033(7)	0.0025(8)	0.0020(9)
Au3	0.0536(12)	0.0402(10)	0.0100(9)	0.0002(7)	0.0067(8)	-0.0003(9)
Au4	0.0562(12)	0.0286(10)	0.0229(10)	0.0013(7)	0.0123(9)	-0.0015(9)
Au5	0.0530(12)	0.0406(11)	0.0159(9)	-0.0083(7)	0.0002(8)	0.0018(9)
Au6	0.0486(12)	0.0329(10)	0.0235(10)	0.0021(7)	0.0072(8)	0.0006(9)
Au7	0.0483(12)	0.0388(11)	0.0189(10)	-0.0086(7)	0.0054(8)	-0.0004(9)
Au8	0.0535(12)	0.0403(11)	0.0170(9)	-0.0053(7)	-0.0005(8)	-0.0019(9)
Au9	0.0690(14)	0.0476(11)	0.0079(9)	0.0008(7)	-0.0021(9)	0.0044(10)
Au10	0.0528(12)	0.0393(10)	0.0235(10)	-0.0005(7)	0.0074(9)	-0.0063(9)
Au11	0.0387(12)	0.0479(12)	0.0415(11)	-0.0078(8)	-0.0050(9)	0.0032(9)
P2	0.042(7)	0.044(7)	0.017(6)	0.001(5)	0.007(5)	0.006(5)
P3	0.048(7)	0.055(7)	0.018(6)	0.002(5)	0.010(5)	-0.002(6)
P5	0.056(7)	0.028(6)	0.024(6)	0.001(4)	0.009(5)	0.004(5)
P6	0.055(7)	0.032(6)	0.028(6)	-0.002(5)	0.011(5)	0.003(6)
P7	0.094(11)	0.059(8)	0.015(6)	-0.010(5)	-0.003(6)	-0.006(7)
P8	0.056(8)	0.051(7)	0.037(7)	-0.013(5)	0.007(6)	-0.008(6)
P10	0.032(7)	0.061(8)	0.057(8)	-0.017(6)	-0.007(6)	0.025(6)
P11	0.048(8)	0.078(9)	0.029(7)	-0.004(6)	0.004(6)	-0.012(7)
Cl1	0.070(8)	0.059(7)	0.040(7)	-0.007(5)	-0.016(6)	0.003(6)
Cl2	0.106(11)	0.088(10)	0.050(8)	-0.035(7)	0.009(8)	0.042(9)

Table 24. Hydrogen atomic coordinates and isotropic atomic displacement parameters ($Å^2$) for $[Au_{11}(PPh_3)_8Cl_2]Cl$

	x/a	y/b	z/c	U(eq)
H1A	0.7067	0.9108	0.5409	0.051

H2A	0.7471	0.9609	0.4877	0.108
H3A	0.6866	0.9830	0.4300	0.068
H4A	0.5855	0.9550	0.4254	0.093
H5A	0.5451	0.9049	0.4787	0.042
H7A	0.5623	1.0284	0.5373	0.061
H8A	0.5335	1.1283	0.5717	0.06
H9A	0.5319	1.1216	0.6390	0.073
H10A	0.5590	1.0150	0.6719	0.089
H11A	0.5878	0.9151	0.6376	0.054
H13A	0.4738	0.9348	0.5392	0.07
H14A	0.3817	0.8867	0.5155	0.056
H15A	0.3720	0.7633	0.5040	0.071
H16A	0.4543	0.6878	0.5163	0.056
H17A	0.5464	0.7359	0.5400	0.068
H19A	0.8339	0.8151	0.5361	0.107
H20A	0.8911	0.9133	0.5205	0.137
H21A	0.8897	0.9504	0.4559	0.156
H22A	0.8309	0.8894	0.4069	0.092
H23A	0.7737	0.7912	0.4224	0.072
H25A	0.6385	0.7511	0.4994	0.082
H26A	0.5500	0.7457	0.4582	0.089
H27A	0.5509	0.7073	0.3940	0.103
H28A	0.6403	0.6743	0.3710	0.073
H29A	0.7288	0.6796	0.4122	0.059
H31A	0.8728	0.6973	0.4583	0.059
H32A	0.9174	0.5988	0.4311	0.087
H33A	0.8716	0.4862	0.4299	0.127
H34A	0.7812	0.4720	0.4558	0.127
H35A	0.7366	0.5705	0.4829	0.079
H37A	0.7549	0.4743	0.7004	0.069
H38A	0.8224	0.4321	0.7511	0.135
H39A	0.7897	0.3582	0.7992	0.116
H40A	0.6896	0.3265	0.7965	0.103
H41A	0.6221	0.3687	0.7458	0.074
H43A	0.6454	0.3103	0.6739	0.053
H44A	0.6187	0.2253	0.6254	0.075
H45A	0.5731	0.2622	0.5649	0.101
H46A	0.5541	0.3841	0.5529	0.088
H47A	0.5808	0.4691	0.6013	0.069
H49A	0.5221	0.3781	0.6794	0.053
H50A	0.4423	0.3782	0.7170	0.072
H51A	0.4333	0.4701	0.7621	0.082
H52A	0.5041	0.5618	0.7696	0.086
H53A	0.5839	0.5617	0.7320	0.048
H55A	0.5990	0.7041	0.7282	0.042
H56A	0.6026	0.7159	0.7957	0.074

H57A	0.5146	0.7248	0.8250	0.076
H58A	0.4231	0.7221	0.7868	0.093
H59A	0.4196	0.7103	0.7194	0.056
H61A	0.4154	0.6040	0.6886	0.067
H62A	0.3640	0.5052	0.6601	0.139
H63A	0.3897	0.4582	0.6016	0.081
H64A	0.4669	0.5101	0.5715	0.083
H65A	0.5183	0.6089	0.5999	0.066
H67A	0.3965	0.7115	0.6139	0.058
H68A	0.3319	0.8066	0.5963	0.093
H69A	0.3533	0.9219	0.6207	0.093
H70A	0.4394	0.9420	0.6628	0.091
H71A	0.5040	0.8469	0.6804	0.085
H73A	0.6731	0.4909	0.5406	0.06
H74A	0.6161	0.4524	0.4841	0.088
H75A	0.6487	0.3567	0.4482	0.074
H76A	0.7384	0.2994	0.4687	0.096
H77A	0.7954	0.3378	0.5252	0.061
H79A	0.8511	0.5562	0.5514	0.049
H80A	0.9435	0.5758	0.5320	0.104
H81A	1.0036	0.4626	0.5289	0.092
H82A	0.9614	0.3509	0.5514	0.122
H83A	0.8735	0.3524	0.5802	0.07
H85A	0.7306	0.3140	0.5861	0.094
H86A	0.7442	0.2210	0.6316	0.105
H87A	0.8111	0.2351	0.6873	0.118
H88A	0.8643	0.3422	0.6976	0.169
H89A	0.8507	0.4352	0.6521	0.084
H91A	0.7006	0.5594	0.7612	0.056
H92A	0.6324	0.5017	0.7968	0.074
H93A	0.6160	0.5447	0.8582	0.093
H94A	0.6678	0.6454	0.8840	0.067
H95A	0.7360	0.7032	0.8484	0.074
H97A	0.7137	0.8052	0.7645	0.112
H98A	0.7083	0.9117	0.7997	0.134
H99A	0.7799	0.9369	0.8516	0.108
H10B	0.8570	0.8555	0.8683	0.119
H10C	0.8624	0.7490	0.8330	0.084
H10D	0.9938	0.5364	0.8135	0.163
H10E	0.9922	0.6438	0.7783	0.174
H10F	0.9025	0.7041	0.7621	0.147
H10G	0.8161	0.5497	0.8163	0.159
H10H	0.9058	0.4894	0.8325	0.193
H10I	0.8307	0.8482	0.7027	0.077
H11B	0.8564	0.8818	0.7674	0.07
H11C	0.8909	0.9980	0.7821	0.094

H11D	0.8998	1.0807	0.7322	0.13
H11E	0.8741	1.0471	0.6675	0.109
H11F	0.7256	0.9891	0.6472	0.051
H11G	0.6625	1.0800	0.6207	0.114
H11H	0.6810	1.1357	0.5627	0.118
H11I	0.7626	1.1007	0.5312	0.116
H11J	0.8257	1.0098	0.5577	0.081
H12A	0.9089	1.0380	0.6092	0.093
H12B	1.0057	1.0393	0.5918	0.113
H12C	1.0541	0.9313	0.5814	0.189
H12D	1.0057	0.8218	0.5884	0.098
H12E	0.9089	0.8205	0.6058	0.056
H12F	0.8920	0.6984	0.5709	0.08
H12G	0.9347	0.7279	0.5144	0.114
H12H	1.0359	0.7082	0.5111	0.104
H13B	1.0944	0.6592	0.5643	0.112
H13C	1.0518	0.6297	0.6208	0.086
H13D	0.9977	0.5236	0.6158	0.074
H13E	1.0241	0.4097	0.6404	0.105
H13F	0.9955	0.3734	0.7003	0.094
H13G	0.9403	0.4510	0.7356	0.132
H13H	0.9139	0.5648	0.7110	0.099
H13I	0.9171	0.7829	0.6789	0.102
H14B	0.9779	0.8632	0.7167	0.101
H14C	1.0740	0.8292	0.7410	0.165
H14D	1.1093	0.7148	0.7275	0.126
H14E	1.0485	0.6345	0.6897	0.11

REFERENCES

(1) *Solid State NMR*; Springer-Verlag: Berlin, 2012; Vol. 306.

(2) Opella, S. J.; Marassi, F. M. *Chem. Rev.* **2004**, *104*, 3587.

(3) Grey, C. P.; Dupré, N. *Chem. Rev.* **2004**, *104*, 4493.

(4) Knight, W. D. *Phys. Rev.* **1949**, *76*, 1259.

(5) Knight, W. D.; Kobayashi, S.-I. In *eMagRes*; John Wiley & Sons, Ltd: 2007.

(6) Bloembergen, N. *Can. J. Phys.* **1956**, *34*, 1299.

(7) Korringa, J. *Physica* **1950**, *16*, 601.

(8) *Spin Dynamics: Basics of Nuclear Magnetic Resonance*; 2nd ed.; John Wiley & Sons Ltd: Chichester, 2001.

(9) Jameson, C. J.; Mason, J. In *Multinuclear NMR*; Mason, J., Ed.; Plenum Press: New York, 1987.

(10) *Solid State NMR Spectroscopy: Principles and Applications*; Blackwell Science: Oxford, 2002.

(11) Widdifield, C. M.; Schurko, R. W. *Concept Magn. Reson. A* **2009**, *34A*, 91.

(12) *Solid-State NMR in Materials Science: Principles and Applications*; CRC Press: Boca Raton, 2011.

(13) Brust, M.; Walker, M.; Bethell, D.; Schiffrin, D. J.; Whyman, R. *J. Chem. Soc., Chem. Comm.* **1994**, 801.

(14) Goulet, P. J. G.; Leonardi, A.; Lennox, R. B. *J. Phys. Chem. C* **2012**, *116*, 14096.

(15) Li, Y.; Zaluzhna, O.; Xu, B.; Gao, Y.; Modest, J. M.; Tong, Y. J. *J. Am. Chem. Soc.* **2011**, *133*, 2092.

(16) Li, Y.; Zaluzhna, O.; Tong, Y. J. *Langmuir* **2011**, *27*, 7366.

(17) Brust, M.; Fink, J.; Bethell, D.; Schiffrin, D. J.; Kiely, C. *J. Chem. Soc., Chem. Commun.* **1995**, 1655.

(18) Whetten, R. L.; Khoury, J. T.; Alvarez, M. M.; Murthy, S.; Vezmar, I.; Wang, Z. L.; Stephens, P. W.; Cleveland, C. L.; Luedtke, W. D.; Landman, U. *Adv. Mater.* **1996**, *8*, 428.

(19) Simpson, C. A.; Farrow, C. L.; Tian, P.; Billinge, S. J. L.; Huffman, B. J.; Harkness, K. M.; Cliffel, D. E. *Inorg. Chem.* **2010**, *49*, 10858.

(20) Barngrover, B. M.; Aikens, C. M. *J. Phys. Chem. Lett.* **2011**, *2*, 990.

(21) Mpourmpakis, G.; Caratzoulas, S.; Vlachos, D. G. *Nano Lett.* **2010**, *10*, 3408.

(22) Stefanescu, D. M.; Glueck, D. S.; Siegel, R.; Wasylishen, R. E. *Langmuir* **2004**, *20*, 10379.

(23) Turkevich, J.; Stevenson, P. C.; Hillier, J. *Discuss. Faraday Soc.* **1951**, *11*, 55.

(24) Frens, G. *Nature* **1973**, *241*, 20.

(25) Doyen, M.; Bartik, K.; Bruylants, G. *J. Colloid Interf. Sci.* **2013**, *399*, 1.
(26) Debouttière, P.-J.; Coppel, Y.; Behra, P.; Chaudret, B.; Fajerwerg, K. *Gold Bull* **2013**, *46*, 291.
(27) Ott, L. S.; Cline, M. L.; Deetlefs, M.; Seddon, K. R.; Finke, R. G. *J. Am. Chem. Soc.* **2005**, *127*, 5758.
(28) Polte, J.; Tuaev, X.; Wuithschick, M.; Fischer, A.; Thuenemann, A. F.; Rademann, K.; Kraehnert, R.; Emmerling, F. *ACS Nano* **2012**, *6*, 5791.
(29) Jones, L. C.; Buras, Z.; Gordon, M. J. *J. Phys. Chem. C* **2012**, *116*, 12982.
(30) Mallissery, S. K.; Gudat, D. *Dalton Trans.* **2010**, *39*, 4280.
(31) Penner, G. H.; Li, W. *Inorg. Chem.* **2004**, *43*, 5588.
(32) Liu, C. W.; Lin, Y.-R.; Fang, C.-S.; Latouche, C.; Kahlal, S.; Saillard, J.-Y. *Inorg. Chem.* **2013**, *52*, 2070.
(33) Pellechia, P. J.; Gao, J.; Gu, Y.; Ploehn, H. J.; Murphy, C. J. *Inorg. Chem.* **2004**, *43*, 1421.
(34) Straney, P. J.; Marbella, L. E.; Andolina, C. M.; Nuhfer, N. T.; Millstone, J. E. *J. Am. Chem. Soc.* **2014**, *136*, 7873.
(35) Ismail, I. M.; Kerrison, S. J. S.; Sadler, P. J. *J. Chem. Soc., Chem. Commun.* **1980**, 1175.
(36) Gerber, W. J.; Murray, P.; Koch, K. R. *Dalton Trans.* **2008**, 4113.
(37) Hubbard, A. T.; Anson, F. C. *Anal. Chem.* **1966**, *38*, 1887.
(38) Chen, C.; Kang, Y.; Huo, Z.; Zhu, Z.; Huang, W.; Xin, H. L.; Snyder, J. D.; Li, D.; Herron, J. A.; Mavrikakis, M.; Chi, M.; More, K. L.; Li, Y.; Markovic, N. M.; Somorjai, G. A.; Yang, P.; Stamenkovic, V. R. *Science* **2014**, *343*, 1339.
(39) Sun, S.; Murray, C. B.; Weller, D.; Folks, L.; Moser, A. *Science* **2000**, *287*, 1989.
(40) Anderson, N. C.; Hendricks, M. P.; Choi, J. J.; Owen, J. S. *J. Am. Chem. Soc.* **2013**, *135*, 18536.
(41) Hens, Z.; Martins, J. C. *Chem. Mater.* **2013**, *25*, 1211.
(42) Tagliazucchi, M.; Tice, D. B.; Sweeney, C. M.; Morris-Cohen, A. J.; Weiss, E. A. *ACS Nano* **2011**, *5*, 9907.
(43) Valdez, C. N.; Schimpf, A. M.; Gamelin, D. R.; Mayer, J. M. *ACS Nano* **2014**, *8*, 9463.
(44) Gentilini, C.; Franchi, P.; Mileo, E.; Polizzi, S.; Lucarini, M.; Pasquato, L. *Angew. Chem. Int. Ed.* **2009**, *48*, 3060.
(45) McIntosh, C. M.; Esposito, E. A.; Boal, A. K.; Simard, J. M.; Martin, C. T.; Rotello, V. M. *J. Am. Chem. Soc.* **2001**, *123*, 7626.
(46) Wang, G.; Guo, R.; Kalyuzhny, G.; Choi, J.-P.; Murray, R. W. *J. Phys. Chem. B* **2006**, *110*, 20282.
(47) Zaupa, G.; Mora, C.; Bonomi, R.; Prins, L. J.; Scrimin, P. *Chem. Eur. J.* **2011**, *17*, 4879.
(48) Hostetler, M. J.; Wingate, J. E.; Zhong, C.-J.; Harris, J. E.; Vachet, R. W.; Clark, M. R.; Londono, J. D.; Green, S. J.; Stokes, J. J.; Wignall, G. D.; Glish, G. L.; Porter, M. D.; Evans, N. D.; Murray, R. W. *Langmuir* **1998**, *14*, 17.
(49) Zelakiewicz, B. S.; de Dios, A. C.; Tong, Y. J. *J. Am. Chem. Soc.* **2002**, *125*, 18.
(50) Sharma, R.; Holland, G. P.; Solomon, V. C.; Zimmermann, H.; Schiffenhaus, S.; Amin, S. A.; Buttry, D. A.; Yarger, J. L. *J. Phys. Chem. C* **2009**, *113*, 16387.

(51) Smith, A. M.; Marbella, L. E.; Johnston, K. A.; Hartmann, M. J.; Crawford, S. E.; Kozycz, L. M.; Seferos, D. S.; Millstone, J. E. *Anal. Chem.* **2015**, *87*, 2771.
(52) Barantin, L.; Le Pape, A.; Akoka, S. *Magn. Reson. Med.* **1997**, *38*, 179.
(53) Zhou, H.; Du, F.; Li, X.; Zhang, B.; Li, W.; Yan, B. *J. Phys. Chem. C* **2008**, *112*, 19360.
(54) Calzolai, L.; Franchini, F.; Gilliland, D.; Rossi, F. *Nano Lett.* **2010**, *10*, 3101.
(55) Guarino, G.; Rastrelli, F.; Mancin, F. *Chem. Commun.* **2012**, *48*, 1523.
(56) Guarino, G.; Rastrelli, F.; Scrimin, P.; Mancin, F. *J. Am. Chem. Soc.* **2012**, *134*, 7200.
(57) Solomon, I. *Phys. Rev.* **1955**, *99*, 559.
(58) Bloembergen, N. *J. Chem. Phys.* **1957**, *27*, 572.
(59) Liu, X.; Yu, M.; Kim, H.; Mameli, M.; Stellacci, F. *Nat. Commun.* **2012**, *3*, 1182.
(60) Gullion, T.; Schaefer, J. *J. Magn. Reson.* **1989**, *81*, 196.
(61) Abraham, A.; Mihaliuk, E.; Kumar, B.; Legleiter, J.; Gullion, T. *J. Phys. Chem. C* **2010**, *114*, 18109.
(62) Abraham, A.; Ilott, A. J.; Miller, J.; Gullion, T. *J. Phys. Chem. B* **2012**, *116*, 7771.
(63) Badia, A.; Lennox, R. B.; Reven, L. *Acc. Chem. Res.* **2000**, *33*, 475.
(64) Soederlind, E.; Stilbs, P. *Langmuir* **1993**, *9*, 1678.
(65) Badia, A.; Gao, W.; Singh, S.; Demers, L.; Cuccia, L.; Reven, L. *Langmuir* **1996**, *12*, 1262.
(66) Badia, A.; Cuccia, L.; Demers, L.; Morin, F.; Lennox, R. B. *J. Am. Chem. Soc.* **1997**, *119*, 2682.
(67) Schmitt, H.; Badia, A.; Dickinson, L.; Reven, L.; Lennox, R. B. *Adv. Mater.* **1998**, *10*, 475.
(68) Fiurasek, P.; Reven, L. *Langmuir* **2007**, *23*, 2857.
(69) Badia, A.; Demers, L.; Dickinson, L.; Morin, F. G.; Lennox, R. B.; Reven, L. *J. Am. Chem. Soc.* **1997**, *119*, 11104.
(70) Wu, Z.; Gayathri, C.; Gil, R. R.; Jin, R. *J. Am. Chem. Soc.* **2009**, *131*, 6535.
(71) Qian, H.; Zhu, M.; Gayathri, C.; Gil, R. R.; Jin, R. *ACS Nano* **2011**, *5*, 8935.
(72) Nealon, G. L.; Donnio, B.; Greget, R.; Kappler, J.-P.; Terazzi, E.; Gallani, J.-L. *Nanoscale* **2012**, *4*, 5244.
(73) Venzo, A.; Antonello, S.; Gascón, J. A.; Guryanov, I.; Leapman, R. D.; Perera, N. V.; Sousa, A.; Zamuner, M.; Zanella, A.; Maran, F. *Anal. Chem.* **2011**, *83*, 6355.
(74) Dainese, T.; Antonello, S.; Gascón, J. A.; Pan, F.; Perera, N. V.; Ruzzi, M.; Venzo, A.; Zoleo, A.; Rissanen, K.; Maran, F. *ACS Nano* **2014**, *8*, 3904.
(75) Chandrakumar, N. *Spin-1 NMR*; Springer: Berlin, 1996.
(76) Schmidt-Rohr, K.; Rawal, A.; Fang, X.-W. *J. Chem. Phys.* **2007**, *126*.
(77) Sharma, R.; Taylor, R. E.; Bouchard, L.-S. *J. Phys. Chem. C* **2011**, *115*, 3297.
(78) Slichter, C. P. *Annu. Rev. Phys. Chem.* **1986**, *37*, 25.
(79) Engelke, F.; Bhatia, S.; King, T. S.; Pruski, M. *Phys. Rev. B* **1994**, *49*, 2730.
(80) Pery, T.; Pelzer, K.; Buntkowsky, G.; Philippot, K.; Limbach, H.-H.; Chaudret, B. *Chem. Phys. Chem.* **2005**, *6*, 605.
(81) Duncan, T. M.; Yates, J. T.; Vaughan, R. W. *J. Chem. Phys.* **1980**, *73*, 975.
(82) Kobayashi, T.; Babu, P. K.; Gancs, L.; Chung, J. H.; Oldfield, E.; Wieckowski, A. *J. Am. Chem. Soc.* **2005**, *127*, 14164.

(83) Babu, P. K.; Kim, H. S.; Kuk, S. T.; Chung, J. H.; Oldfield, E.; Wieckowski, A.; Smotkin, E. S. *J. Phys. Chem. B* **2005**, *109*, 17192.

(84) Terrill, R. H.; Postlethwaite, T. A.; Chen, C.-h.; Poon, C.-D.; Terzis, A.; Chen, A.; Hutchison, J. E.; Clark, M. R.; Wignall, G.; Londono, J. D.; Superfine, R.; Falvo, M.; Johnson Jr., C. S.; Samulski, E. T.; Murray, R. W. *J. Am. Chem. Soc.* **1995**, *117*, 12537.

(85) Gomez, M. V.; Guerra, J.; Myers, V. S.; Crooks, R. M.; Velders, A. H. *J. Am. Chem. Soc.* **2009**, *131*, 14634.

(86) Perrone, B.; Springhetti, S.; Ramadori, F.; Rastrelli, F.; Mancin, F. *J. Am. Chem. Soc.* **2013**, *135*, 11768.

(87) Salvia, M.-V.; Ramadori, F.; Springhetti, S.; Diez-Castellnou, M.; Perrone, B.; Rastrelli, F.; Mancin, F. *J. Am. Chem. Soc.* **2015**, *137*, 886.

(88) Canzi, G.; Mrse, A. A.; Kubiak, C. P. *J. Phys. Chem. C* **2011**, *115*, 7972.

(89) Provencher, S. W. *Comput. Phys. Commun.* **1982**, *27*, 229.

(90) Andolina, C. M.; Dewar, A. C.; Smith, A. M.; Marbella, L. E.; Hartmann, M. J.; Millstone, J. E. *J. Am. Chem. Soc.* **2013**, *135*, 5266.

(91) Marbella, L. E.; Andolina, C. M.; Smith, A. M.; Hartmann, M. J.; Dewar, A. C.; Johnston, K. A.; Daly, O. H.; Millstone, J. E. *Adv. Funct. Mater.* **2014**, *24*, 6532.

(92) Salorinne, K.; Lahtinen, T.; Malola, S.; Koivisto, J.; Häkkinen, H. *Nanoscale* **2014**, *6*, 7823.

(93) van der Klink, J. J.; Brom, H. B. *Prog. Nucl. Mag. Res. Sp.* **2000**, *36*, 89.

(94) Lovingood, D. D.; Achey, R.; Paravastu, A. K.; Strouse, G. F. *J. Am. Chem. Soc.* **2010**, *132*, 3344.

(95) Cadars, S.; Smith, B. J.; Epping, J. D.; Acharya, S.; Belman, N.; Golan, Y.; Chmelka, B. F. *Phys. Rev. Lett.* **2009**, *103*, 136802.

(96) Bercier, J. J.; Jirousek, M.; Graetzel, M.; van der Klink, J. J. *J. Phys.: Condens. Matter* **1993**, *5*, L571.

(97) Mastikhin, V. M.; Mudrakovsky, I. L.; Goncharova, S. N.; Balzhinimaev, B. S.; Noskova, S. P.; Zaikovsky, V. I. *React Kinet Catal Lett* **1992**, *48*, 425.

(98) Plischke, J. K.; Benesi, A. J.; Vannice, M. A. *J. Phys. Chem.* **1992**, *96*, 3799.

(99) Son, K.; Jang, Z. *Journal of the Korean Physical Society* **2013**, *62*, 292.

(100) Suits, B. H.; Siegel, R. W.; Liao, Y. X. *Nanostruct. Mater.* **1993**, *2*, 597.

(101) Vuissoz, P. A.; Yonezawa, T.; Yang, D.; Kiwi, J.; van der Klink, J. J. *Chem. Phys. Lett.* **1997**, *264*, 366.

(102) Kobayashi, S.; Takahashi, T.; Sasaki, W. *J. Phys. Soc. Jpn.* **1972**, *32*, 1234.

(103) Tunstall, D. P.; Edwards, P. P.; Todd, J.; Williams, M. J. *J. Phys.: Condens. Matter* **1994**, *6*, 1791.

(104) Williams, M. J.; Edwards, P. P.; Tunstall, D. P. *Faraday Discuss.* **1991**, *92*, 199.

(105) Yee, P.; Knight, W. D. *Phys. Rev. B* **1975**, *11*, 3261.

(106) Yu, I.; Gibson, A.; Hunt, E.; Halperin, W. *Phys. Rev. Lett.* **1980**, *44*, 348.

(107) Rhodes, H. E.; Wang, P.-K.; Stokes, H. T.; Slichter, C. P.; Sinfelt, J. H. *Phys. Rev. B* **1982**, *26*, 3559.

(108) Slichter, C. P. *Surf. Sci.* **1981**, *106*, 382.

(109) Bucher, J.; van der Klink, J. J. *Phys. Rev. B* **1988**, *38*, 11038.

(110) Bucher, J. P.; Buttet, J.; van der Klink, J. J.; Graetzel, M. *Surf. Sci.* **1989**, *214*, 347.

(111) van der Klink, J. J.; Buttet, J.; Graetzel, M. *Phys. Rev. B* **1984**, *29*, 6352.

(112) Weinert, M.; Freeman, A. *Phys. Rev. B* **1983**, *28*, 6262.

(113) Bucher, J. P.; Buttet, J.; van der Klink, J. J.; Graetzel, M.; Newson, E.; Truong, T. B. *Colloids Surf.* **1989**, *36*, 155.

(114) Rees, G. J.; Orr, S. T.; Barrett, L. O.; Fisher, J. M.; Houghton, J.; Spikes, G. H.; Theobald, B. R. C.; Thompsett, D.; Smith, M. E.; Hanna, J. V. *Phys. Chem. Chem. Phys.* **2013**, *15*, 17195.

(115) Tong, Y. J.; Rice, C.; Wieckowski, A.; Oldfield, E. *J. Am. Chem. Soc.* **2000**, *122*, 11921.

(116) Yano, H.; Inukai, J.; Uchida, H.; Watanabe, M.; Babu, P. K.; Kobayashi, T.; Chung, J. H.; Oldfield, E.; Wieckowski, A. *Phys. Chem. Chem. Phys.* **2006**, *8*, 4932.

(117) Kleis, J.; Greeley, J.; Romero, N. A.; Morozov, V. A.; Falsig, H.; Larsen, A. H.; Lu, J.; Mortensen, J. J.; Dułak, M.; Thygesen, K. S.; Nørskov, J. K.; Jacobsen, K. W. *Catal Lett* **2011**, *141*, 1067.

(118) Tong, Y. J.; Martin, G. A.; van der Klink, J. J. *J. Phys.: Condens. Matter* **1994**, *6*, L533.

(119) Tong, Y. J.; Zelakiewicz, B. S.; Dy, B. M.; Pogozelski, A. R. *Chem. Phys. Lett.* **2005**, *406*, 137.

(120) van der Putten, D.; Brom, H. B.; Witteveen, J.; de Jongh, L. J.; Schmid, G. *Z Phys D - Atoms, Molecules and Clusters* **1993**, *26*, 21.

(121) Wang, Z.; Ansermet, J.-P.; Slichter, C. P.; Sinfelt, J. H. *J. Chem. Soc., Faraday Trans. 1* **1988**, *84*, 3785.

(122) Tong, Y. J.; Yonezawa, T.; Toshima, N.; van der Klink, J. J. *J. Phys. Chem.* **1996**, *100*, 730.

(123) Babu, P. K.; Kim, H. S.; Oldfield, E.; Wieckowski, A. *J. Phys. Chem. B* **2003**, *107*, 7595.

(124) Danberry, A. L.; Du, B.; Park, I.-S.; Sung, Y.-E.; Tong, Y. J. *J. Am. Chem. Soc.* **2007**, *129*, 13806.

(125) Atienza, D. O.; Allison, T. C.; Tong, Y. J. *J. Phys. Chem. C* **2012**, *116*, 26480.

(126) Massiot, D.; Farnan, I.; Gautier, N.; Trumeau, D.; Trokiner, A.; Coutures, J. P. *Solid State Nucl. Magn. Reson.* **1995**, *4*, 241.

(127) MacGregor, A. W.; O'Dell, L. A.; Schurko, R. W. *J. Magn. Reson.* **2011**, *208*, 103.

(128) Wang, P. K.; Ansermet, J. P.; Rudaz, S. L.; Wang, Z.; Shore, S.; Slichter, C. P.; Sinfelt, J. H. *Science* **1986**, *234*, 35.

(129) Rudaz, S. L.; Ansermet, J.-P.; Wang, P.-K.; Slichter, C. P.; Sinfelt, J. H. *Phys. Rev. Lett.* **1985**, *54*, 71.

(130) Tong, Y. J.; Rice, C.; Godbout, N.; Wieckowski, A.; Oldfield, E. *J. Am. Chem. Soc.* **1999**, *121*, 2996.

(131) Becerra, L.; Slichter, C.; Sinfelt, J. *Phys. Rev. B* **1995**, *52*, 11457.

(132) MacDonald, A.; Daams, J.; Vosko, S.; Koelling, D. *Phys. Rev. B* **1981**, *23*, 6377.

(133) Rice, C.; Tong, Y. J.; Oldfield, E.; Wieckowski, A.; Hahn, F.; Gloaguen, F.; Léger, J.-M.; Lamy, C. *J. Phys. Chem. B* **2000**, *104*, 5803.

(134) Hammer, B.; Morikawa, Y.; Nørskov, J. *Phys. Rev. Lett.* **1996**, *76*, 2141.

(135) Tong, Y. J.; Oldfield, E.; Wieckowski, A. *Anal. Chem.* **1998**, *70*, 518A.

(136) Kobayashi, H.; Yamauchi, M.; Kitagawa, H.; Kubota, Y.; Kato, K.; Takata, M. *J. Am. Chem. Soc.* **2010**, *132*, 5576.

(137) Kobayashi, H.; Yamauchi, M.; Ikeda, R.; Kitagawa, H. *Chem. Commun.* **2009**, 4806.

(138) Kusada, K.; Yamauchi, M.; Kobayashi, H.; Kitagawa, H.; Kubota, Y. *J. Am. Chem. Soc.* **2010**, *132*, 15896.

(139) Zelakiewicz, B. S.; Yonezawa, T.; Tong, Y. J. *J. Am. Chem. Soc.* **2004**, *126*, 8112.

(140) Evans, D. F. *J. Chem. Soc.* **1959**, 2003.

(141) Live, D. H.; Chan, S. I. *Anal. Chem.* **1970**, *42*, 791.

(142) Auten, B. J.; Hahn, B. P.; Vijayaraghavan, G.; Stevenson, K. J.; Chandler, B. D. *J. Phys. Chem. C* **2008**, *112*, 5365.

(143) Bain, G. A.; Berry, J. F. *J. Chem. Ed.* **2008**, *85*, 532.

(144) Tedsree, K.; Chan, C. W. A.; Jones, S.; Cuan, Q.; Li, W.-K.; Gong, X.-Q.; Tsang, S. C. E. *Science* **2011**, *332*, 224.

(145) Tedsree, K.; Kong, A. T. S.; Tsang, S. C. *Angew. Chem. Int. Ed.* **2009**, *48*, 1443.

(146) Hanna, J. V.; Smith, M. E. *Solid State Nucl. Mag.* **2010**, *38*, 1.

(147) Schurko, R. W. *Acc. Chem. Res.* **2013**, *46*, 1985.

(148) Ni, Q. Z.; Daviso, E.; Can, T. V.; Markhasin, E.; Jawla, S. K.; Swager, T. M.; Temkin, R. J.; Herzfeld, J.; Griffin, R. G. *Acc. Chem. Res.* **2013**, *46*, 1933.

(149) Guidez, E. B.; Mäkinen, V.; Häkkinen, H.; Aikens, C. M. *J. Phys. Chem. C* **2012**, *116*, 20617.

(150) Hartmann, M. J.; Häkkinen, H.; Millstone, J. E.; Lambrecht, D. S. *J. Phys. Chem. C* **2015**, *119*, 8290.

(151) Yamazoe, S.; Kurashige, W.; Nobusada, K.; Negishi, Y.; Tsukuda, T. *J. Phys. Chem. C* **2014**, *118*, 25284.

(152) Zhang, L.; Anderson, R. M.; Crooks, R. M.; Henkelman, G. *Surf. Sci.* **2015**, *640*, 65.

(153) Cortie, M. B.; McDonagh, A. M. *Chem. Rev.* **2011**, *111*, 3713.

(154) Malola, S.; Lehtovaara, L.; Häkkinen, H. *J. Phys. Chem. C* **2014**, *118*, 20002.

(155) Riccardo, F. *J. Phys. Condens. Matt.* **2015**, *27*, 013003.

(156) Bhattarai, N.; Black, D. M.; Boppidi, S.; Khanal, S.; Bahena, D.; Tlahuice-Flores, A.; Bach, S. B. H.; Whetten, R. L.; Jose-Yacaman, M. *J. Phys. Chem. C* **2015**, *119*, 10935.

(157) Fields-Zinna, C. A.; Crowe, M. C.; Dass, A.; Weaver, J. E. F.; Murray, R. W. *Langmuir* **2009**, *25*, 7704.

(158) Jiang, D.-e.; Dai, S. *Inorg. Chem.* **2009**, *48*, 2720.

(159) Malola, S.; Hartmann, M. J.; Häkkinen, H. *J. Phys. Chem. Lett.* **2015**, *6*, 515.

(160) Qian, H.; Jiang, D.-e.; Li, G.; Gayathri, C.; Das, A.; Gil, R. R.; Jin, R. *J. Am. Chem. Soc.* **2012**, *134*, 16159.

(161) Wuithschick, M.; Birnbaum, A.; Witte, S.; Sztucki, M.; Vainio, U.; Pinna, N.; Rademann, K.; Emmerling, F.; Kraehnert, R.; Polte, J. *ACS Nano* **2015**, *9*, 7052.

(162) Gary, D. C.; Terban, M. W.; Billinge, S. J. L.; Cossairt, B. M. *Chem. Mater.* **2015**, *27*, 1432.

(163) Essinger-Hileman, E. R.; DeCicco, D.; Bondi, J. F.; Schaak, R. E. *J. Mater. Chem.* **2011**, *21*, 11599.

(164) Archer, P. I.; Santangelo, S. A.; Gamelin, D. R. *J. Am. Chem. Soc.* **2007**, *129*, 9808.

(165) Dharmaratne, A. C.; Dass, A. *Chem. Commun.* **2014**, *50*, 1722.

(166) Yang, H.; Wang, Y.; Yan, J.; Chen, X.; Zhang, X.; Häkkinen, H.; Zheng, N. *J. Am. Chem. Soc.* **2014**, *136*, 7197.

(167) He, R.; Wang, Y.-C.; Wang, X.; Wang, Z.; Liu, G.; Zhou, W.; Wen, L.; Li, Q.; Wang, X.; Chen, X.; Zeng, J.; Hou, J. G. *Nat. Commun.* **2014**, *5*, 4327.

(168) Motl, N. E.; Ewusi-Annan, E.; Sines, I. T.; Jensen, L.; Schaak, R. E. *J. Phys. Chem. C* **2010**, *114*, 19263.

(169) Straney, P. J.; Andolina, C. M.; Millstone, J. E. *Isr. J. Chem.* **2015**, DOI: 10.1002/ijch.201500033.

(170) Latour, L. L.; Li, L. M.; Sotak, C. H. *J. Magn. Reson., Ser. B* **1993**, *101*, 72.

(171) Tanner, J. E. *J. Chem. Phys.* **1970**, *52*, 2523.

(172) Stejskal, E. O.; Tanner, J. E. *J. Chem. Phys.* **1965**, *42*, 288.

(173) Sekhar, A.; Vallurupalli, P.; Kay, L. E. *Proc. Natl. Acad. Sci.* **2013**, *110*, 11391.

(174) Cabrita, E. J.; Berger, S. *Magn. Res. Chem.* **2001**, *39*, S142.

(175) Ankudinov, A. L.; Ravel, B.; Rehr, J. J.; Conradson, S. D. *Phys. Rev. B* **1998**, *58*, 7565.

(176) Newville, M.; Boyanov, B.; Sayers, D. *J. Synchrotron Rad.* **1999**, *6*, 264.

(177) Freeman, F.; Angeletakis, C. N.; Maricich, T. J. *Org. Magn. Resonance* **1981**, *17*, 53.

(178) Holewinski, A.; Idrobo, J.-C.; Linic, S. *Nat. Chem.* **2014**, *6*, 828.

(179) McKone, J. R.; Sadtler, B. F.; Werlang, C. A.; Lewis, N. S.; Gray, H. B. *ACS Catal.* **2013**, *3*, 166.

(180) Goulet, P. J. G.; Lennox, R. B. *J. Am. Chem. Soc.* **2010**, *132*, 9582.

(181) Ohyama, J.; Teramura, K.; Higuchi, Y.; Shishido, T.; Hitomi, Y.; Kato, K.; Tanida, H.; Uruga, T.; Tanaka, T. *ChemPhysChem* **2011**, *12*, 127.

(182) Heaven, M. W.; Dass, A.; White, P. S.; Holt, K. M.; Murray, R. W. *J. Am. Chem. Soc.* **2008**, *130*, 3754.

(183) Jadzinsky, P. D.; Calero, G.; Ackerson, C. J.; Bushnell, D. A.; Kornberg, R. D. *Science* **2007**, *318*, 430.

(184) Desireddy, A.; Conn, B. E.; Guo, J.; Yoon, B.; Barnett, R. N.; Monahan, B. M.; Kirschbaum, K.; Griffith, W. P.; Whetten, R. L.; Landman, U.; Bigioni, T. P. *Nature* **2013**, *501*, 399.

(185) Yang, H.; Wang, Y.; Huang, H.; Gell, L.; Lehtovaara, L.; Malola, S.; Häkkinen, H.; Zheng, N. *Nat. Commun.* **2013**, *4*, 2422.

(186) Santra, A. K.; Subbanna, G. N.; Rao, C. N. R. *Surf. Sci.* **1994**, *317*, 259.

(187) Vijayakrishnan, V.; Rao, C. N. R. *Surf. Sci.* **1991**, *255*, L516.

(188) Toshima, N.; Wang, Y. *Langmuir* **1994**, *10*, 4574.

(189) Manisha, K.; Tsuyoshi, H.; Kazuya, T.; Kazuhiro, Y.; Masakazu, A. *Sci. Technol. Adv. Mat.* **2008**, *9*, 035011.

(190) Buonsanti, R.; Milliron, D. J. *Chem. Mater.* **2013**, *25*, 1305.

(191) Grzelczak, M.; Pérez-Juste, J.; Mulvaney, P.; Liz-Marzán, L. M. *Chem. Soc. Rev.* **2008**, *37*, 1783.

(192) Lohse, S. E.; Murphy, C. J. *Chem. Mater.* **2013**, *25*, 1250.

(193) Murray, C. B.; Kagan, C. R.; Bawendi, M. G. *Annu. Rev. Mater. Sci.* **2000**, *30*, 545.

(194) Xia, Y.; Xiong, Y.; Lim, B.; Skrabalak, S. E. *Angew. Chem. Int. Ed.* **2009**, *48*, 60.

(195) Alivisatos, A. P. *J. Phys. Chem.* **1996**, *100*, 13226.

(196) Beckers, N. A.; Huynh, S.; Zhang, X.; Luber, E. J.; Buriak, J. M. *ACS Catal.* **2012**, *2*, 1524.
(197) Dehm, N. A.; Zhang, X.; Buriak, J. M. *Inorg. Chem.* **2010**, *49*, 2706.
(198) Eustis, S.; El-Sayed, M. A. *Chem. Soc. Rev.* **2006**, *35*, 209.
(199) Kelly, K. L.; Coronado, E.; Zhao, L. L.; Schatz, G. C. *J. Phys. Chem. B* **2002**, *107*, 668.
(200) Luk'yanchuk, B.; Zheludev, N. I.; Maier, S. A.; Halas, N. J.; Nordlander, P.; Giessen, H.; Chong, C. T. *Nat. Mater.* **2010**, *9*, 707.
(201) McLaurin, E. J.; Fataftah, M. S.; Gamelin, D. R. *Chem. Comm.* **2013**, *49*, 39.
(202) Dreaden, E. C.; El-Sayed, M. A. *Acc. Chem. Res.* **2012**, *45*, 1854.
(203) Giljohann, D. A.; Seferos, D. S.; Daniel, W. L.; Massich, M. D.; Patel, P. C.; Mirkin, C. A. *Angew. Chem. Int. Ed.* **2010**, *49*, 3280.
(204) Linic, S.; Christopher, P.; Ingram, D. B. *Nat. Mater.* **2011**, *10*, 911.
(205) Sun, J.; Zhong, D. K.; Gamelin, D. R. *Energ. Environ. Sci.* **2010**, *3*, 1252.
(206) Talapin, D. V.; Lee, J.-S.; Kovalenko, M. V.; Shevchenko, E. V. *Chem. Rev.* **2009**, *110*, 389.
(207) Zhong, D. K.; Gamelin, D. R. *J. Am. Chem. Soc.* **2010**, *132*, 4202.
(208) Walter, J. L.; Jackson, M. R.; Sims, C. T. *Alloying*; ASM International: Metals Park, Ohio, 1988.
(209) Wilkes, P. *Solid State Theory in Metallurgy*; Cambridge University Press: New York, New York, 1973.
(210) Woodruff, D. P. *The Chemical Physics of Solid Surfaces: Surface Alloys and Alloy Surfaces*; Elsevier Science: Amsterdam, The Netherlands, 2002; Vol. 10.
(211) Choi, H. S.; Liu, W.; Misra, P.; Tanaka, E.; Zimmer, J. P.; Ipe, B. I.; Bawendi, M. G.; Frangioni, J. V. *Nat. Biotechol.* **2007**, *25*, 1165.
(212) Cuenya, B. R. *Thin Solid Films* **2010**, *518*, 3127.
(213) Haruta, M. *Catal. Today* **1997**, *36*, 153.
(214) Kim, D.; Park, S.; Lee, J. H.; Jeong, Y. Y.; Jon, S. *J. Am. Chem. Soc.* **2007**, *129*, 7661.
(215) Longmire, M.; Choyke, P. L.; Kobayashi, H. *Nanomedicine* **2008**, *3*, 703.
(216) Zhang, Y.; Cui, X.; Shi, F.; Deng, Y. *Chem. Rev.* **2011**, *112*, 2467.
(217) Ferrando, R.; Jellinek, J.; Johnston, R. L. *Chem. Rev.* **2008**, *108*, 845.
(218) Ghosh Chaudhuri, R.; Paria, S. *Chem. Rev.* **2011**, *112*, 2373.
(219) Lattuada, M.; Hatton, T. A. *Nano Today* **2011**, *6*, 286.
(220) Cui, C.; Gan, L.; Heggen, M.; Rudi, S.; Strasser, P. *Nat. Mater.* **2013**, *12*, 765.
(221) Greeley, J.; Mavrikakis, M. *Nat. Mater.* **2004**, *3*, 810.
(222) Greeley, J.; Nørskov, J. K.; Mavrikakis, M. *Annu. Rev. Phys. Chem.* **2002**, *53*, 319.
(223) Kitchin, J. R.; Norskov, J. K.; Barteau, M. A.; Chen, J. G. *J. Chem. Phys.* **2004**, *120*, 10240.
(224) Ho, D.; Sun, X.; Sun, S. *Acc. Chem. Res.* **2011**, *44*, 875.
(225) Hu, F.; Joshi, H. M.; Dravid, V. P.; Meade, T. J. *Nanoscale* **2010**, *2*, 1884.
(226) Na, H. B.; Song, I. C.; Hyeon, T. *Adv. Mater.* **2009**, *21*, 2133.
(227) Blaber, M. G.; Arnold, M. D.; Ford, M. J. *J. Phys.: Condens. Matter* **2010**, *22*, 143201.

(228) Franke, P.; Neuschütz, D. In *Binary Systems. Part 5: Binary Systems Supplement 1*; Franke, P., Neuschütz, D., Eds.; Springer Berlin Heidelberg: 2007; Vol. 19B5, p 1.

(229) Okamoto, H.; Massalski, T. B.; Nishizawa, T.; Hasebe, M. *Bulletin of Alloy Phase Diagrams* **1985**, *6*, 449.

(230) Okamoto, H.; Massalski, T. B.; Swartzendruber, L. J.; Beck, P. A. *Bulletin of Alloy Phase Diagrams* **1984**, *5*, 592.

(231) Bochicchio, D.; Ferrando, R. *Phys. Rev. B* **2013**, *87*, 165435.

(232) Nilekar, A. U.; Ruban, A. V.; Mavrikakis, M. *Surf. Sci.* **2009**, *603*, 91.

(233) Christensen, A.; Stoltze, P.; Norskov, J. K. *J. Phys.: Condens. Matter* **1995**, *7*, 1047.

(234) Bondi, J. F.; Misra, R.; Ke, X.; Sines, I. T.; Schiffer, P.; Schaak, R. E. *Chem. Mater.* **2010**, *22*, 3988.

(235) Vasquez, Y.; Luo, Z.; Schaak, R. E. *J. Am. Chem. Soc.* **2008**, *130*, 11866.

(236) Park, J. Y.; Choi, E. S.; Baek, M. J.; Lee, G. H.; Woo, S.; Chang, Y. *Eur. J. Inorg. Chem.* **2009**, *2009*, 2477.

(237) Hyeon, T. *Chem. Comm.* **2003**, 927.

(238) Haynes, W. M.; Lide, D. R. *CRC Handbook of Chemistry and Physics*; 92nd ed.; CRC Press: Boca Raton, Fla., 2011.

(239) LaMer, V. K.; Dinegar, R. H. *J. Am. Chem. Soc.* **1950**, *72*, 4847.

(240) DeSantis, C. J.; Sue, A. C.; Bower, M. M.; Skrabalak, S. E. *ACS Nano* **2012**, *6*, 2617.

(241) Zhou, S.; Jackson, G. S.; Eichhorn, B. *Adv. Func. Mater.* **2007**, *17*, 3099.

(242) Pacheco, E. A.; Tiekink, E. R. T.; Whitehouse, M. W. In *Gold Chemistry*; Wiley-VCH Verlag GmbH & Co. KGaA: 2009, p 283.

(243) Glavee, G. N.; Klabunde, K. J.; Sorensen, C. M.; Hadjipanayis, G. C. *Langmuir* **1993**, *9*, 162.

(244) Klabunde, K. J.; Stark, J. V.; Koper, O.; Mohs, C.; Khaleel, A.; Glavee, G.; Zhang, D.; Sorensen, C. M.; Hadjipanayis, G. C. In *Nanophase Materials*; Hadjipanayis, G., Siegel, R., Eds.; Springer Netherlands: 1994; Vol. 260.

(245) Vasquez, Y.; Sra, A. K.; Schaak, R. E. *J. Am. Chem. Soc.* **2005**, *127*, 12504.

(246) Rousset, J. L.; Cadete Santos Aires, F. J.; Sekhar, B. R.; Mélinon, P.; Prevel, B.; Pellarin, M. *J. Phys. Chem. B* **2000**, *104*, 5430.

(247) Zsoldos, Z.; Hoffer, T.; Guczi, L. *J. Phys. Chem.* **1991**, *95*, 798.

(248) Knecht, M. R.; Garcia-Martinez, J. C.; Crooks, R. M. *Chem. Mater.* **2006**, *18*, 5039.

(249) Jung, C. W.; Jacobs, P. *Magn. Res. Imaging* **1995**, *13*, 661.

(250) Bertini, I.; Turano, P.; Vila, A. J. *Chem. Rev.* **1993**, *93*, 2833.

(251) Zheng, J.; Zhang, C.; Dickson, R. M. *Phys. Rev. Lett.* **2004**, *93*, 077402.

(252) Zheng, J.; Zhou, C.; Yu, M.; Liu, J. *Nanoscale* **2012**, *4*, 4073.

(253) Christensen, A.; Ruban, A.; Stoltze, P.; Jacobsen, K. W.; Skriver, H. L.; Nørskov, J. K.; Besenbacher, F. *Phys. Rev. B* **1997**, *56*, 5822.

(254) Crespo, O.; Gimeno, M. C.; Laguna, A.; Larraz, C.; Villacampa, M. D. *Chem. Eur. J.* **2007**, *13*, 235.

(255) Hänninen, P.; Härmä, H. *Lanthanide Luminescence: Photophysical, Analytical, and Biological Aspects*, 2011.

(256) Comby, S.; Imbert, D.; Chauvin, A.-S.; Bünzli, J.-C. G. *Inorg. Chem.* **2006**, *45*, 732.

(257) Bouchard, L. S.; Anwar, M. S.; Liu, G. L.; Hann, B.; Xie, Z. H.; Gray, J. W.; Wang, X.; Pines, A.; Chen, F. F. *P. Natl. Acad. Sci.* **2009**, *106*, 4085.

(258) Lauffer, R. B. *Chem. Rev.* **1987**, *87*, 901.

(259) Stanisz, G. J.; Odrobina, E. E.; Pun, J.; Escaravage, M.; Graham, S. J.; Bronskill, M. J.; Henkelman, R. M. *Magn. Res. Med.* **2005**, *54*, 507.

(260) Klemm, P. J.; Floyd III, W. C.; Andolina, C. M.; Fréchet, J. M. J.; Raymond, K. N. *Eur. J. Inorg. Chem.* **2012**, *2012*, 2108.

(261) Jun, Y.-w.; Seo, J.-w.; Cheon, J. *Acc. Chem. Res.* **2008**, *41*, 179.

(262) Jaganathan, H.; Gieseck, R. L.; Ivanisevic, A. *J. Phys. Chem. C* **2010**, *114*, 22508.

(263) Disegi, J. A.; Kennedy, R. L.; Pilliar, R. *Cobalt-base alloys for biomedical applications*; ASTM International, 1999.

(264) Comby, S.; Imbert, D.; Chauvin, A.-S.; Bünzli, J.-C. G. *Inorg. Chem.* **2005**, *45*, 732.

(265) Karki, I.; Wang, H.; Geise, N. R.; Wilson, B. W.; Lewis, J. P.; Gullion, T. *J. Phys. Chem. B* **2015**, *119*, 11998.

(266) Salorinne, K.; Malola, S.; Wong, O. A.; Rithner, C. D.; Chen, X.; Ackerson, C. J.; Hakkinen, H. *Nat. Commun.* **2016**, *7*.

(267) Marbella, L. E.; Millstone, J. E. *Chem. Mater.* **2015**, *27*, 2721.

(268) Li, Y.; Zelakiewicz, B. S.; Allison, T. C.; Tong, Y. J. *ChemPhysChem* **2015**, *16*, 747.

(269) Crawford, S. E.; Andolina, C. M.; Smith, A. M.; Marbella, L. E.; Johnston, K. A.; Straney, P. J.; Hartmann, M. J.; Millstone, J. E. *J. Am. Chem. Soc.* **2015**, *137*, 14423.

(270) Autschbach, J.; Zheng, S.; Schurko, R. W. *Concept Magn. Res. A* **2010**, *36A*, 84.

(271) Autschbach, J.; Ziegler, T. *J. Chem. Phys.* **2000**, *113*, 9410.

(272) te Velde, G.; Bickelhaupt, F. M.; Baerends, E. J.; Fonseca Guerra, C.; van Gisbergen, S. J. A.; Snijders, J. G.; Ziegler, T. *J. Comput. Chem.* **2001**, *22*, 931.

(273) Adamo, C.; Barone, V. *Chem. Phys. Lett.* **1997**, *274*, 242.

(274) Dwan, J. R. Thesis, University of Alberta, 2011.

(275) Lenthe, E. v.; Baerends, E. J.; Snijders, J. G. *J. Chem. Phys.* **1993**, *99*, 4597.

(276) McKenzie, L. C.; Zaikova, T. O.; Hutchison, J. E. *J. Am. Chem. Soc.* **2014**, *136*, 13426.

(277) Teo, B. K.; Shi, X.; Zhang, H. *J. Am. Chem. Soc.* **1992**, *114*, 2743.

(278) Pei, Y.; Shao, N.; Gao, Y.; Zeng, X. C. *ACS Nano* **2010**, *4*, 2009.

(279) Schmid, G.; Pfeil, R.; Boese, R.; Bandermann, F.; Meyer, S.; Calis, G. H. M.; van der Velden, J. W. A. *Chem. Ber.* **1981**, *114*, 3634.

(280) Baenziger, N. C.; Bennett, W. E.; Soborofe, D. M. *Acta Crystallogr. Sect. B* **1976**, *32*, 962.

(281) Jones, P. G.; Maddock, A. G.; Mays, M. J.; Muir, M. M.; Williams, A. F. *J. Chem. Soc., Dalton Trans.* **1977**, 1434.

(282) Baker, L.-J.; Bowmaker, G. A.; Healy, P. C.; Skelton, B. W.; White, A. H. *J. Chem. Soc., Dalton Trans.* **1992**, 989.

(283) Berners-Price, S. J.; Colquhoun, L. A.; Healy, P. C.; Byriel, K. A.; Hanna, J. V. *J. Chem. Soc., Dalton Trans.* **1992**, 3357.

(284) Menger, E. M.; Veeman, W. S. *J. Magn. Reson.* **1982**, *46*, 257.

(285) Eichele, K.; ver. 1.21.3 ed. Universitat Tubingen, 2015.
(286) Alarcón, S. H.; Olivieri, A. C.; Harris, R. K. *Solid State Nucl. Magn. Reson.* **1993**, *2*, 325.
(287) Hexem, J. G.; Frey, M. H.; Opella, S. J. *J. Chem. Phys.* **1982**, *77*, 3847.
(288) Olivieri, A. C. *J. Magn. Reson. A* **1993**, *101*, 313.
(289) Healy, P. C.; Loughrey, B. T.; Bowmaker, G. A.; Hanna, J. V. *Dalton Trans.* **2008**, 3723.
(290) Schurko, R. W.; Wasylishen, R. E.; Nelson, J. H. *J. Phys. Chem.* **1996**, *100*, 8057.
(291) Szalontai, G. In *Current Developments in Solid State NMR Spectroscopy*; Müller, N., Madhu, P., Eds.; Springer Vienna: 2003, p 95.
(292) Yu, H.; Tan, X.; Bernard, G. M.; Terskikh, V. V.; Chen, J.; Wasylishen, R. E. *J. Phys. Chem. A* **2015**, *119*, 8279.
(293) Schmid, G. In *Clusters*; Springer Berlin Heidelberg: 1985; Vol. 62, p 51.
(294) Gutrath, B. S.; Merkens, C.; Schiefer, F.; Englert, U.; Schmid, G.; Simon, U. *znb* **2013**, *68*, 569.
(295) Schmid, G.; Klein, N.; Korste, L.; Kreibig, U.; Schönauer, D. *Polyhedron* **1988**, *7*, 605.
(296) Bos, W.; Kanters, R. P. F.; Van Halen, C. J.; Bosman, W. P.; Behm, H.; Smits, J. M. M.; Beurskens, P. T.; Bour, J. J.; Pignolet, L. H. *J. Organomet. Chem.* **1986**, *307*, 385.
(297) Clayden, N. J.; Dobson, C. M.; Hall, K. P.; Mingos, D. M. P.; Smith, D. J. *J. Chem. Soc., Dalton Trans.* **1985**, 1811.
(298) Copley, R. C. B.; Mingos, D. M. P. *J. Chem. Soc., Dalton Trans.* **1996**, 479.
(299) Diesveld, J. W.; Menger, E. M.; Edzes, H. T.; Veeman, W. S. *J. Am. Chem. Soc.* **1980**, *102*, 7935.
(300) Kolbert, A. C.; Groot, H. J. M.; Putten, D.; Brom, H. B.; Jongh, L. J.; Schmid, G.; Krautscheid, H.; Fenske, D. *Z. Phys. D*, *26*, 24.
(301) Stefanescu, D. M.; Glueck, D. S.; Siegel, R.; Wasylishen, R. E. *J. Clust. Sci.* **2008**, *19*, 445.
(302) Van der Velden, J. W. A.; Beurskens, P. T.; Bour, J. J.; Bosman, W. P.; Noordik, J. H.; Kolenbrander, M.; Buskes, J. A. K. M. *Inorg. Chem.* **1984**, *23*, 146.
(303) van der Velden, J. W. A.; Bour, J. J.; Steggerda, J. J.; Beurskens, P. T.; Roseboom, M.; Noordik, J. H. *Inorg. Chem.* **1982**, *21*, 4321.
(304) Vollenbroek, F. A.; Van den Berg, J. P.; Van der Velden, J. W. A.; Bour, J. J. *Inorg. Chem.* **1980**, *19*, 2685.
(305) Donkers, R. L.; Song, Y.; Murray, R. W. *Langmuir* **2004**, *20*, 4703.
(306) Band, E.; Muetterties, E. L. *Chem. Rev.* **1978**, *78*, 639.
(307) Song, Y.; Harper, A. S.; Murray, R. W. *Langmuir* **2005**, *21*, 5492.
(308) Gansow, O. A.; Gill, D. S.; Bennis, F. J.; Hutchinson, J. R.; Vidal, J. L.; Schoening, R. C. *J. Am. Chem. Soc.* **1980**, *102*, 2449.
(309) Erickson, J. D.; Mednikov, E. G.; Ivanov, S. A.; Dahl, L. F. *J. Am. Chem. Soc.* **2016**, *138*, 1502.
(310) Mednikov, E. G.; Dahl, L. F. *Angew. Chem.* **2013**, *125*, 7967.
(311) Mednikov, E. G.; Dahl, L. F. *Inorg. Chem.* **2015**, *54*, 1145.
(312) Wong, O. A.; Heinecke, C. L.; Simone, A. R.; Whetten, R. L.; Ackerson, C. J. *Nanoscale* **2012**, *4*, 4099.
(313) Bohm, J.; Fenzke, D.; Pfeifer, H. *J. Magn. Reson.* **1983**, *55*, 197.

(314) Harris, R. K.; Olivieri, A. C. *Prog. Nucl. Magn. Reson. Spectrosc.* **1992**, *24*, 435.
(315) Hens, Z.; Moreels, I.; Martins, J. C. *ChemPhysChem* **2005**, *6*, 2578.
(316) Frydman, L. *Annu. Rev. Phys. Chem.* **2001**, *52*, 463.
(317) Daniel, M.-C.; Astruc, D. *Chem. Rev.* **2004**, *104*, 293.
(318) Li, G.; Jin, R. *Acc. Chem. Res.* **2013**, *46*, 1749.
(319) Turner, M.; Golovko, V. B.; Vaughan, O. P. H.; Abdulkin, P.; Berenguer-Murcia, A.; Tikhov, M. S.; Johnson, B. F. G.; Lambert, R. M. *Nature* **2008**, *454*, 981.
(320) Valden, M.; Lai, X.; Goodman, D. W. *Science* **1998**, *281*, 1647.
(321) Nilius, N.; Risse, T.; Shaikhutdinov, S.; Sterrer, M.; Freund, H.-J. In *Gold Clusters, Colloids and Nanoparticles II*; Mingos, P. D. M., Ed.; Springer International Publishing: Cham, 2014, p 91.
(322) Parker, J. F.; Fields-Zinna, C. A.; Murray, R. W. *Acc. Chem. Res.* **2010**, *43*, 1289.
(323) Ni, T. W.; Tofanelli, M. A.; Ackerson, C. J. In *Protected Metal Clusters: From Fundamentals to Applications*; Tsukuda, T., Häkkinen, H., Eds.; Elsevier: 2015.
(324) Zeng, C.; Jin, R. In *Gold Clusters, Colloids and Nanoparticles I*; Mingos, P. D. M., Ed.; Springer International Publishing: Cham, 2014, p 87.
(325) Billinge, S. J. L.; Levin, I. *Science* **2007**, *316*, 561.
(326) Jensen, K. M. O.; Juhas, P.; Tofanelli, M. A.; Heinecke, C. L.; Vaughan, G.; Ackerson, C. J.; Billinge, S. J. L. *Nat. Commun.* **2016**, *7*.
(327) Chevrier Daniel, M.; Yang, R.; Chatt, A.; Zhang, P. In *Nanotech. Rev.* 2015; Vol. 4, p 193.
(328) Azubel, M.; Koivisto, J.; Malola, S.; Bushnell, D.; Hura, G. L.; Koh, A. L.; Tsunoyama, H.; Tsukuda, T.; Pettersson, M.; Häkkinen, H.; Kornberg, R. D. *Science* **2014**, *345*, 909.
(329) Bahena, D.; Bhattarai, N.; Santiago, U.; Tlahuice, A.; Ponce, A.; Bach, S. B. H.; Yoon, B.; Whetten, R. L.; Landman, U.; Jose-Yacaman, M. *J. Phys. Chem. Lett.* **2013**, *4*, 975.
(330) Lopez-Acevedo, O.; Akola, J.; Whetten, R. L.; Grönbeck, H.; Häkkinen, H. *J. Phys. Chem. C* **2009**, *113*, 5035.
(331) Wüthrich, K. *NMR in structural biology: a collection of papers by Kurt Wüthrich*; World Scientific, 1995; Vol. 5.
(332) Ajie, H.; Alvarez, M. M.; Anz, S. J.; Beck, R. D.; Diederich, F.; Fostiropoulos, K.; Huffman, D. R.; Kraetschmer, W.; Rubin, Y.; et al. *J. Phys. Chem.* **1990**, *94*, 8630.
(333) Wishart, D. S.; Sykes, B. D. *J. Biomol. NMR* **1994**, *4*, 171.
(334) Wishart, D. S.; Sykes, B. D.; Richards, F. M. *Biochemistry* **1992**, *31*, 1647.
(335) Gutrath, B. S.; Englert, U.; Wang, Y.; Simon, U. *Eur. J. Inorg. Chem.* **2013**, *2013*, 2002.
(336) Anderson, D. P.; Alvino, J. F.; Gentleman, A.; Qahtani, H. A.; Thomsen, L.; Polson, M. I. J.; Metha, G. F.; Golovko, V. B.; Andersson, G. G. *Phys. Chem. Chem. Phys.* **2013**, *15*, 3917.
(337) Walter, M.; Akola, J.; Lopez-Acevedo, O.; Jadzinsky, P. D.; Calero, G.; Ackerson, C. J.; Whetten, R. L.; Grönbeck, H.; Häkkinen, H. *P. Natl. Acad. Sci.* **2008**, *105*, 9157.
(338) Enkovaara, J.; Rostgaard, C.; Mortensen, J. J.; Chen, J.; Dułak, M.; Ferrighi, L.; Gavnholt, J.; Glinsvad, C.; Haikola, V.; Hansen, H. A.; Kristoffersen, H. H.; Kuisma, M.; Larsen, A. H.; Lehtovaara, L.; Ljungberg, M.; Lopez-Acevedo, O.; Moses, P. G.; Ojanen, J.; Olsen, T.; Petzold, V.; Romero, N. A.; Stausholm-Møller, J.; Strange, M.; Tritsaris, G. A.;

Vanin, M.; Walter, M.; Hammer, B.; Häkkinen, H.; Madsen, G. K. H.; Nieminen, R. M.; Nørskov, J. K.; Puska, M.; Rantala, T. T.; Schiøtz, J.; Thygesen, K. S.; Jacobsen, K. W. *J. Phys.: Condens. Matter* **2010**, *22*, 253202.

(339) Mortensen, J. J.; Hansen, L. B.; Jacobsen, K. W. *Phys. Rev. B* **2005**, *71*, 035109.

(340) Aikens, C. M. *J. Phys. Chem. A* **2009**, *113*, 10811.

(341) Akola, J.; Walter, M.; Whetten, R. L.; Häkkinen, H.; Grönbeck, H. *J. Am. Chem. Soc.* **2008**, *130*, 3756.

(342) Casida, M. E. *Recent Advances in Density Functional Methods* **1995**, *1*, 1.

(343) Muniz-Miranda, F.; Menziani, M. C.; Pedone, A. *J. Phys. Chem. C* **2014**, *118*, 7532.

(344) Becke, A. D. *Phys. Rev. A* **1988**, *38*, 3098.

(345) Moruzzi, V. L.; Janak, J. F.; Schwarz, K. *Phys. Rev. B* **1988**, *37*, 790.

(346) Negishi, Y.; Nakazaki, T.; Malola, S.; Takano, S.; Niihori, Y.; Kurashige, W.; Yamazoe, S.; Tsukuda, T.; Häkkinen, H. *J. Am. Chem. Soc.* **2015**, *137*, 1206.

(347) Angermair, K.; Bowmaker, G. A.; de Silva, E. N.; Healy, P. C.; Jones, B. E.; Schmidbaur, H. *J. Chem. Soc., Dalton Trans.* **1996**, 3121.

(348) Barron, P. F.; Engelhardt, L. M.; Healy, P. C.; Oddy, J.; White, A. H. *Aust. J. Chem.* **1987**, *40*, 1545.

(349) Marbella, L. E.; Crawford, S. E.; Hartmann, M. J.; Millstone, J. E. *Chem. Commun.* **2016**.

(350) Fyfe, C. A. *Solid State NMR for Chemists*; C.F.C. Press, 1983.

(351) Brock, C. P.; Ibers, J. A. *Acta Cryst. B* **1973**, *29*, 2426.

(352) Autschbach, J. In *Principles and Applications of Density Functional Theory in Inorganic Chemistry I*; Springer Berlin Heidelberg: Berlin, Heidelberg, 2004, p 1.

(353) Verkade, J. G.; Quin, L. D. *Phosphorus-31 NMR Spectroscopy in Stereochemical Analysis*; VCH Publishers, 1987.

(354) Penner, G. H.; Wasylishen, R. E. *Can. J. Chem.* **1989**, *67*, 1909.

(355) Stamenkovic, V. R.; Mun, B. S.; Arenz, M.; Mayrhofer, K. J. J.; Lucas, C. A.; Wang, G.; Ross, P. N.; Markovic, N. M. *Nat. Mater.* **2007**, *6*, 241.

(356) Gaudry, M.; Cottancin, E.; Pellarin, M.; Lermé, J.; Arnaud, L.; Huntzinger, J. R.; Vialle, J. L.; Broyer, M.; Rousset, J. L.; Treilleux, M.; Mélinon, P. *Phys. Rev. B* **2003**, *67*, 155409.

(357) Chinen, A. B.; Guan, C. M.; Ferrer, J. R.; Barnaby, S. N.; Merkel, T. J.; Mirkin, C. A. *Chem. Rev.* **2015**, *115*, 10530.

(358) Neumann, O.; Urban, A. S.; Day, J.; Lal, S.; Nordlander, P.; Halas, N. J. *ACS Nano* **2013**, *7*, 42.

(359) Atwater, H. A.; Polman, A. *Nat. Mater.* **2010**, *9*, 205.

(360) Boltasseva, A.; Atwater, H. A. *Science* **2011**, *331*, 290.

(361) Naik, G. V.; Shalaev, V. M.; Boltasseva, A. *Adv. Mater.* **2013**, *25*, 3264.

(362) Knight, M. W.; King, N. S.; Liu, L.; Everitt, H. O.; Nordlander, P.; Halas, N. J. *ACS Nano* **2014**, *8*, 834.

(363) Kanehara, M.; Koike, H.; Yoshinaga, T.; Teranishi, T. *J. Am. Chem. Soc.* **2009**, *131*, 17736.

(364) Luther, J. M.; Jain, P. K.; Ewers, T.; Alivisatos, A. P. *Nat. Mater.* **2011**, *10*, 361.

(365) Ju, L.; Geng, B.; Horng, J.; Girit, C.; Martin, M.; Hao, Z.; Bechtel, H. A.; Liang, X.; Zettl, A.; Shen, Y. R.; Wang, F. *Nat. Nano.* **2011**, *6*, 630.

(366) Hsu, S.-W.; On, K.; Tao, A. R. *J. Am. Chem. Soc.* **2011**, *133*, 19072.

(367) Scotognella, F.; Della Valle, G.; Srimath Kandada, A. R.; Dorfs, D.; Zavelani-Rossi, M.; Conforti, M.; Miszta, K.; Comin, A.; Korobchevskaya, K.; Lanzani, G.; Manna, L.; Tassone, F. *Nano Lett.* **2011**, *11*, 4711.

(368) Yesinowski, J. P. In *Solid State NMR*; Chan, C. J. C., Ed.; Springer Berlin Heidelberg: Berlin, Heidelberg, 2012, p 229.

(369) Faucheaux, J. A.; Stanton, A. L. D.; Jain, P. K. *J. Phys. Chem. Lett.* **2014**, *5*, 976.

(370) Mendelsberg, R. J.; Garcia, G.; Li, H.; Manna, L.; Milliron, D. J. *J. Phys. Chem. C* **2012**, *116*, 12226.

(371) Schimpf, A. M.; Thakkar, N.; Gunthardt, C. E.; Masiello, D. J.; Gamelin, D. R. *ACS Nano* **2014**, *8*, 1065.

(372) Zhang, H.; Kulkarni, V.; Prodan, E.; Nordlander, P.; Govorov, A. O. *J. Phys. Chem. C* **2014**, *118*, 16035.

(373) Kim, J.; Agrawal, A.; Krieg, F.; Bergerud, A.; Milliron, D. J. *Nano Lett.* **2016**, *16*, 3879.

(374) Levin, E. M. *Phys. Rev. B* **2016**, *93*, 045209.

(375) Levin, E. M.; Cook, B. A.; Ahn, K.; Kanatzidis, M. G.; Schmidt-Rohr, K. *Phys. Rev. B* **2009**, *80*, 115211.

(376) Levin, E. M.; Heremans, J. P.; Kanatzidis, M. G.; Schmidt-Rohr, K. *Physical Review B* **2013**, *88*, 115211.

(377) Koumoulis, D.; Taylor, R. E.; King, D.; Bouchard, L. S. *Phys. Rev. B* **2014**, *90*, 125201.

(378) Taylor, R. E.; Alkan, F.; Koumoulis, D.; Lake, M. P.; King, D.; Dybowski, C.; Bouchard, L.-S. *J. Phys. Chem. C* **2013**, *117*, 8959.

(379) Senturia, S. D.; Smith, A. C.; Hewes, C. R.; Hofmann, J. A.; Sagalyn, P. L. *Phys. Rev. B* **1970**, *1*, 4045.

(380) Deka, S.; Genovese, A.; Zhang, Y.; Miszta, K.; Bertoni, G.; Krahne, R.; Giannini, C.; Manna, L. *J. Am. Chem. Soc.* **2010**, *132*, 8912.

(381) Dorfs, D.; Härtling, T.; Miszta, K.; Bigall, N. C.; Kim, M. R.; Genovese, A.; Falqui, A.; Povia, M.; Manna, L. *J. Am. Chem. Soc.* **2011**, *133*, 11175.

(382) Kriegel, I.; Jiang, C.; Rodríguez-Fernández, J.; Schaller, R. D.; Talapin, D. V.; da Como, E.; Feldmann, J. *J. Am. Chem. Soc.* **2012**, *134*, 1583.

(383) Riha, S. C.; Johnson, D. C.; Prieto, A. L. *J. Am. Chem. Soc.* **2011**, *133*, 1383.

(384) Tong, Y. J.; Rice, C.; Wieckowski, A.; Oldfield, E. *J. Am. Chem. Soc.* **2000**, *122*, 1123.

(385) Walder, B. J.; Dey, K. K.; Kaseman, D. C.; Baltisberger, J. H.; Grandinetti, P. J. *J. Chem. Phys.* **2013**, *138*, 174203.

(386) Massiot, D.; Fayon, F.; Capron, M.; King, I.; Le Calvé, S.; Alonso, B.; Durand, J.-O.; Bujoli, B.; Gan, Z.; Hoatson, G. *Magn. Res. Chem.* **2002**, *40*, 70.

(387) El Akkad, F.; Mansour, B.; Hendeya, T. *Mat. Res. Bull.* **1981**, *16*, 535.

(388) Gorbachev, V. V.; Putilin, I. M. *Phys. Stat. Sol. A* **1973**, *16*, 553.

(389) Mansour, B. A.; Demian, S. E.; Zayed, H. A. *J. Mater. Sci. Mater. Electron.* **1992**, *3*, 249.

(390) Voskamyan, A. A.; Inglizyan, P. N.; Lalykin, S. P.; Plyutto, I. A.; Shevchenko, Y. M. *Fiz. Tekh. Poluprovodn.* **1978**, *12*, 2096.

(391) Gulay, L.; Daszkiewicz, M.; Strok, O.; Pietraszko, A. *Chem. Met. Alloys* **2011**, *4*, 200.

(392) Nguyen, M. C.; Choi, J.-H.; Zhao, X.; Wang, C.-Z.; Zhang, Z.; Ho, K.-M. *Phys. Rev. Lett.* **2013**, *111*, 165502.

(393) Garba, E. J. D.; Jacobs, R. L. *Physica B+C* **1986**, *138*, 253.

(394) Harris, R. K.; Wasylishen, R. E.; Duer, M. J. *NMR Crystallography*; Wiley, 2012.

(395) Sen, S.; Edwards, T.; Kim, S. K.; Kim, S. *Chem. Mater.* **2014**, *26*, 1918.

(396) Selbach, H.; Kanert, O.; Wolf, D. *Phys. Rev. B* **1979**, *19*, 4435.